

Springer Proceedings in Energy

Vinod Kumar Jain
Vikram Kumar
Abhishek Verma *Editors*

Advances in Solar Power Generation and Energy Harvesting

Select Proceedings of ESPGEH 2019

 Springer

Springer Proceedings in Energy

The series Springer Proceedings in Energy covers a broad range of multidisciplinary subjects in those research fields closely related to present and future forms of energy as a resource for human societies. Typically based on material presented at conferences, workshops and similar scientific meetings, volumes published in this series will constitute comprehensive state-of-the-art references on energy-related science and technology studies. The subjects of these conferences will fall typically within these broad categories:

- Energy Efficiency
- Fossil Fuels
- Nuclear Energy
- Policy, Economics, Management & Transport
- Renewable and Green Energy
- Systems, Storage and Harvesting
- Materials for Energy

eBook Volumes in the Springer Proceedings in Energy will be available online in the world's most extensive eBook collection, as part of the Springer Energy eBook Collection. Please send your proposals/inquiry to Dr. Loyola DSilva, Senior Publishing Editor, Springer (loyola.dsilva@springer.com).

More information about this series at <http://www.springer.com/series/13370>

Vinod Kumar Jain · Vikram Kumar ·
Abhishek Verma
Editors

Advances in Solar Power Generation and Energy Harvesting

Select Proceedings of ESPGEH 2019

 Springer

Editors

Vinod Kumar Jain
Amity Institute for Advanced Research
and Studies (Materials & Devices)
Amity University
Noida, India

Vikram Kumar
Solid State Physics Laboratory (SSPL)
Defence Research & Development
Organization (DRDO)
Centre for Laboratory Accreditation
New Delhi, India

Abhishek Verma
Amity Institute for Advanced Research
and Studies (Materials & Devices)
Amity University
Noida, India

ISSN 2352-2534

Springer Proceedings in Energy

ISBN 978-981-15-3634-2

<https://doi.org/10.1007/978-981-15-3635-9>

ISSN 2352-2542 (electronic)

ISBN 978-981-15-3635-9 (eBook)

© Springer Nature Singapore Pte Ltd. 2020, corrected publication 2020

This work is subject to copyright. All rights are reserved by the Publisher, whether the whole or part of the material is concerned, specifically the rights of translation, reprinting, reuse of illustrations, recitation, broadcasting, reproduction on microfilms or in any other physical way, and transmission or information storage and retrieval, electronic adaptation, computer software, or by similar or dissimilar methodology now known or hereafter developed.

The use of general descriptive names, registered names, trademarks, service marks, etc. in this publication does not imply, even in the absence of a specific statement, that such names are exempt from the relevant protective laws and regulations and therefore free for general use.

The publisher, the authors and the editors are safe to assume that the advice and information in this book are believed to be true and accurate at the date of publication. Neither the publisher nor the authors or the editors give a warranty, expressed or implied, with respect to the material contained herein or for any errors or omissions that may have been made. The publisher remains neutral with regard to jurisdictional claims in published maps and institutional affiliations.

This Springer imprint is published by the registered company Springer Nature Singapore Pte Ltd. The registered company address is: 152 Beach Road, #21-01/04 Gateway East, Singapore 189721, Singapore

Preface

The Sun is the biggest source of energy for mankind, which is playing an essential role in compensating the need of electrical energy, due to escalation in demand and declining trends of conventional source of energies, like petroleum, coal and natural gases. Therefore, an effective energy solution should be able to address the long-term issues by utilizing renewable energy sources. However, the main issue is the conversion efficiencies for harnessing them and the costs involved in the processes. Currently, the science and technology of the twenty-first century in the field of solar energy is relying heavily on the development of new materials, technologies, structures, policies and their implementations. The latest research is directed towards developing more efficient systems to not only convert solar radiations into electricity but also store thermal energy during the day time.

The recent trends in solar energy generation and harvesting are to decrease the cost of the energy generation, either by introducing the low-cost processing techniques or to increase the efficiency of the solar cells. Thus, this industry is rapidly becoming an inexpensive, low-carbon technology to harness renewable energy from the Sun. With the new investigations and research, the cost of solar electricity has substantially fallen down such that the number of grid-connected solar PV plants has grown into millions of solar power stations with hundreds of megawatts capacity. Further, many new technologies including photo-electrochemical cells, polymer solar cells, quantum dot, tandem/multi-junction solar cells, up-conversion and down-conversion, surface plasmonic, nano-crystal solar cells and other novel inventions and innovations are also underway.

In order to deliberate on the current trends in solar power generation, its storage, harnessing and related issues, *Amity Institute of Advanced Research and Studies (Materials & Devices)* has organized an “International Conference on Efficient Solar Power Generation and Energy Harvesting” (ESPGEH) at Amity University Uttar Pradesh, Noida, India, from 12 to 14 February 2019. The conference was being organized with the aim to provide a platform for scientists to promote, share and discuss various new issues and developments in the area of solar energy and its

applications. During this, a common platform was provided for eminent scientists, technologists, entrepreneurs and scholars from various disciplines to present their work and discuss the latest advances and innovations in this exciting area of research. The purpose and objective of this meeting were also to share the vast knowledge and latest investigations with the scientific industrial community and how to include in the production to get more efficient solar cells or systems. It was felt that planning and policies of the authorities are very much effective especially when industries must compete internationally cost- and efficiency-wise. A special session was organized in which scientists, industrialists and representatives from the government agencies participated and presented their views. The main objective was to understand the problems of each and how to solve these. The best outcome can come only if all the three, scientists, industries and planners, work together in a coordinated way.

The book *Advances in Solar Power Generation and Energy Harvesting* comprises selected peer-reviewed scientific contributions from different veins of renewable energy generation, harvesting and the related technologies. The contribution has been made by different researchers and eminent scientists, who presented their papers in the ESPGEH 2019. The chapters of the book include various latest and significant topics, i.e. *Solar Photovoltaics, Solar Thermal, Solar Energy Harvesting, Hybrid Renewable Energy Plant, On-Grid and Off-Grid Power Plant, Batteries, along with Energy Management and Policies*. The book gives the cutting-edge technologies and other significant aspects related to solar energy generation and harvesting. It includes the latest findings of eminent scientists discussing the synthesis, optimization and characterization of different materials related to efficient energy devices; investigation into thermo-physical properties nano-enhanced phase change materials for solar thermal energy storage applications; degradation analysis of photovoltaic panels and PERC solar cells; new morphology for dye-sensitized solar cells; study on efficient tubular daylighting devices; solar parabolic concentrators; electronic properties in perovskite solar cells; hybrid renewable power plant; and apart from this, the book also includes the chapters having Intelligent Energy Information and Management System for Academic Institutes and Indian scenario on solar power generation.

These contributory papers were full of new scientific knowledge, thought-provoking ideas, skills, brainstorming discussions and exchange of ideas. Through this, every latest findings and researches will go ahead to our scientific world. We are sure that all the latest results and findings reported here will be useful to the young researchers or scientists working in these areas and will serve as an important document for all those associated with solar energy research, development and its use.

We are indebted to all of them who have given their guidance and support. Although it is difficult to name all of our colleagues, we would like to thank each one.

We wish to place on record our appreciation to Dr. Ashok K. Chauhan, Founder President, Amity University, Noida, for his guidance, support and encouragement to organize this important conference. We are also highly thankful to Prof. (Dr.) Balvinder Shukla, Vice Chancellor, Amity University, for her tremendous support at every step in making this conference a great success. Our sincere gratitude goes to Dr. Suman, Dr. Amit Kumar and all the members of the organizing committee, for their valuable support.

Noida, India
February 2019

Vinod Kumar Jain
Abhishek Verma

Contents

1 Optimization of Ag NP's Fabrication Using RTP for Polycrystalline Si Solar Cell Application	1
Bidyut Barman, Hrishikesh Dhasmana, Amit Kumar, Abhishek Verma and V. K. Jain	
2 Aligned Zinc Oxide Nanostructures for Dye-Sensitized Solar Cells: A Review	9
Rakhi Grover, Nidhi Gupta, Omita Nanda and Kanchan Saxena	
3 Investigation of Heat Transfer Characteristics of Al₂O₃-Embedded Magnesium Nitrate Hexahydrate-Based Nanocomposites for Thermal Energy Storage	17
Neeraj Gupta, Vivek Kumar, Hrishikesh Dhasmana, Avshish Kumar, Prashant Shukla, Amit Kumar, Abhishek Verma, S. K. Dhawan and Vinod Kumar Jain	
4 Theoretical Analysis of Temperature-Dependent Electrical Parameters of Si Solar Cell Integrated with Carbon-Based Thermal Cooling Layer	27
Vivek Kumar, Hrishikesh Dhasmana, Apurv Yadav, Amit Kumar, Abhishek Verma, P. K. Bhatnagar and Vinod Kumar Jain	
5 Studies of MWCNT-PEDOT:PSS Nanocomposites for Power Generation	37
Omita Nanda, Nidhi Gupta, Rakhi Grover and Kanchan Saxena	
6 Improving Thermal Comfort in Helmet Using Phase Change Nanocomposite Material	45
Neeraj Gupta, Vivek Kumar, Hrishikesh Dhasmana, Abhishek Verma, Avshish Kumar, Prashant Shukla, Amit Kumar, S. K. Dhawan and Vinod Kumar Jain	

7	Impact of Light- and Elevated Temperature-Induced Degradation on PERC Solar Cells	53
	Arati Joshi and Hasan Iqbal	
8	Facile Fabrication of 1-D Hierarchical TiO₂ Nanomorphology and Its Application in Dye Sensitized Solar Cell	65
	Asha Anish Madhavan	
9	Study and Analysis of Parameters Affecting Tubular Daylighting Device	73
	Devendra Singh Bisht, Harry Garg, R. R. Shravana Kumar and Vinod Karar	
10	Optimization of Electron Transport Layer Based on Cadmium Sulfide for Perovskite Solar Cells	93
	Nidhi Gupta, Shivansh Rastogi, Jampana Gayathri, Omita Nanda and Kanchan Saxena	
11	Intelligent Energy Information and Management System for Academic Institutes	99
	Maneesha, Praveen Kant Pandey and Sachin Kumar	
12	Thermal Performance Enhancement of Flat-Plate Solar Collector Using CeO₂-Water Nanofluid	109
	Shubham Sharma, Sandeep Tiwari, Arun Kumar Tiwari, Gopal Nandan and Ravi Prakash	
13	Study of Hybrid Photovoltaic-Thermoelectric System for Efficiency Enhancement of Solar Cells	119
	Sahitya Singh, Akshaj Arora, Vivek Kumar, Abhishek Verma, Hrishikesh Dhasmana, Amit Kumar and V. K. Jain	
14	Periodical Imaging of Microstructure During Temperature Regulated Electrical Conductivity Measurements of Supercritically Synthesized Polypyrrole	127
	Anjali Bisht, Rekha Sati, Kavita Singhal, Sameena Mehtab and M. G. H. Zaidi	
15	Thermal Efficiency Enhancement of Solar Parabolic Trough Collector Using Nanofluids: A Recent Review	137
	Gopal Nandan	
16	Structural Transformations in Fullerene C₇₀ Thin Film by 65 MeV Ni Ion Beam Irradiation	149
	Ritu Vishnoi, Vaishali Singh and Rahul Singhal	

17 Enhancement of Incident Solar Energy on Panels and Indoor Load Leveling Due to Seasonal Adjustment of Rooftop Solar PV Arrays 159
Prakhar Duggal, R. K. Tomar and N. D. Kaushika

18 Overview of Heat Transfer Augmentation Techniques for Parabolic Solar Concentrator Receiver 167
Milind S. Patil and Sanjay Pratapsingh Shekhawat

19 Synthesis of ZnO Nanostructures Using RTCVD, Suitable for Various Applications 191
Ravi Keshwar Kumar, Avshish Kumar, Samina Husain, M. Husain and M. Zulfequar

20 Role of Nanostructures in Development of Energy-Efficient Electrochemical Non-enzymatic Glucose Sensors 199
Vijay Kumar Anand, B. Archana, Amit Wason, G. S. Viridi and Rakesh Goyal

Correction to: Study and Analysis of Parameters Affecting Tubular Daylighting Device C1
Devendra Singh Bisht, Harry Garg, R. R. Shravana Kumar and Vinod Karar

About the Editors

Prof. Vinod Kumar Jain obtained his Ph.D. in Solid State Physics from IIT Delhi, India. He joined Solid State Physics Laboratory and worked as Director Grade scientist. He was the head of the silicon devices and Micro Electro Mechanical Systems (MEMS) division, and has developed many new technologies. He has also developed the technology for space quality silicon solar cells and among these technologies a few have been transferred to industries. His work on electro-luminescence in porous silicon was considered as the first international observation and was reported as NEWS by Photonics spectra USA, Electronics Asia. Dr. Jain was also associated with the National Programme on Smart materials & MEMS technology from the beginning. He has published more than 160 papers in national and international journals, edited a few books and has filed 40 patents. He also worked as Emeritus Scientist of CSIR at NPL up to June 2007. He got the Award in 2012 from “Power of Ideas” (DST programme) and from Royal Academy of U.K. “On the pocket friendly reusable water purification system” based on nanomaterials. His areas of interest include solar energy, sensors, bio-sensors, water purification. He has started two new institutes at Amity University – Amity Institute for Advanced Research and Studies (Materials & Devices) & Amity Institute of Renewable and Alternative Energy, where he is working as a Distinguished Scientist & Professor.

Prof. Vikram Kumar is well known in the area of semiconductor materials, characterization and device technology. His extensive work towards the understanding of electronic defects and interface states in silicon, III-V and II-VI semiconductors led to the prestigious Shanti Swarup Bhatnagar Award in 1992. He led the setting up of GaAs Enabling Technology Centre (GAETEC) foundry at Hyderabad for pilot production of monolithic microwave integrated circuits (MMIC). Prof. Kumar is currently Chairman, Centre for Laboratory Accreditation, & Dr. Raja Ramanna Distinguished DRDO Fellow at SSPL, DRDO. He was formerly Emeritus Professor, IIT-Delhi; Professor, IIT Delhi; Director, National Physical Laboratory CSIR; and Director, Solid State Physics Laboratory, DRDO. He has been responsible for setting up the Nanoscale Research Facility at IIT Delhi.

He has published over 190 papers in peer reviewed journals. He is a Fellow of the NASI, INAE and IETE in addition to being a member of several professional societies, some of which he is presiding. He was recognized as the Distinguished Materials Scientist of the Year 2012 by the Materials Research Society of India. He has received an honorary DSc from the Indian Institute of Engineering Science and Technology (IEST), Howrah. He has been chair or member of several committees for DST, DIT, MNRE, MEITY, DRDO and other scientific agencies.

Dr. Abhishek Verma completed his Ph.D. in Electronic Science from Delhi University in 2009. He further joined National University of Singapore, Singapore, as a post-doctoral researcher in the area of solar cells. Presently, he is working as an Assistant Professor at Amity University Uttar Pradesh, Noida, India, where he is teaching at Amity Institute of Renewable & Alternative Energy and pursuing his research activities at Amity Institute for Advanced Research & Studies (Materials & Devices). His areas of interest are organic and inorganic third generation solar cells, nanomaterial characterization, nano-enhanced phase change materials, agrivoltaics, clean energy generation using ferro-fluids, quantum dots and sensors. He has handled various R & D projects, and he has also organized three prestigious international conferences. He has filed 15 patents and 1 granted. He has also edited 3 books and published more than 60 papers in peer-reviewed international journals and conference proceedings.

Chapter 1

Optimization of Ag NP's Fabrication Using RTP for Polycrystalline Si Solar Cell Application



Bidyut Barman, Hrishikesh Dhasmana, Amit Kumar, Abhishek Verma and V. K. Jain

Abstract The light coupling and scattering property of silver (Ag) nanoparticles (NPs) depend on Ag NPs' size, shape and interparticle distance of adjacent Ag NPs on the respective silicon (Si) substrate surface. In this Ag NPs' arrangement onto the Si surface, least surface coverage is always required to minimize the parasitic resistance and enhance light transmission into Si layer which helps to enhance Si solar cell efficiency. In this work, fabrication and optimization of silver (Ag) nanoparticles onto the polycrystalline silicon (pc-Si) have been discussed for enhancing light trapping into Si substrate. Silver NPs of different sizes have been fabricated by using rapid thermal annealing (RTP) of RF deposited Ag thin film on pc-Si surface at RTP temperature of 200, 250, 300, 350 and 400 °C for various annealing durations. A shrinkage force generated at the interface due to the difference in thermal expansion coefficient between Ag thin film and pc-Si surface is responsible for the formation of these Ag NPs. The magnitude of RTP temperature and amount of RTP heat treatment helps in reshaping of Ag NPs, and accordingly, surface coverage by Ag NPs changes onto the pc-Si surface. Experimental results show that minimum surface coverage of 12.17% can be achieved at 400 °C for 35 min RTP treatment which can be utilized for enhancing light trapping property into Si surface.

Keywords Rapid thermal annealing · Ag nanoparticles · Shrinkage force · Surface area coverage

1.1 Introduction

In recent times, the light extinction (absorption + scattering) property of metal nanoparticles (MNPs) has been studied extensively to increase light trapping and

B. Barman · H. Dhasmana (✉) · A. Kumar · A. Verma · V. K. Jain
Amity Institute of Renewable and Alternate Energy, Amity University, Noida, UP, India
e-mail: hrishikeshd07@gmail.com

H. Dhasmana · A. Kumar · A. Verma · V. K. Jain
Amity Institute of Advance Research and Studies (Material & Devices), Amity University,
Noida, Uttar Pradesh 201303, India

© Springer Nature Singapore Pte Ltd. 2020
V. K. Jain et al. (eds.), *Advances in Solar Power Generation and Energy Harvesting*, Springer Proceedings in Energy,
https://doi.org/10.1007/978-981-15-3635-9_1

scattering for silicon (Si) as well as for thin-film solar cells. For MNPs, scattering and coupling efficiency of incoming electromagnetic radiation depend on nanoparticles' (NPs) size, shape, interparticle distance and surface coverage [1–5]. For MNPs such as Ag NPs, a comparatively higher scattering efficiency can be observed with NPs' size of around 100 nm diameter [2]. Amongst all of the MNPs, silver (Ag) NPs possess better optical property for light trapping application into Si surface. The interparticle distance along with area surface coverage has a significant role in light trapping capacity of Ag NPs' arrangement. The surface area coverage of Ag NPs should be optimized to increase light transmission into the absorber layer of Si and increase light collection in the active layer of the Si semiconductor. Thus, higher interparticle distance along with lower surface area coverage is desirable for Si solar cell as it will increase light transmission which eventually increases light trapping of the solar cell. In our previous studies, we discussed low-temperature fabrication of Ag NPs exhibiting surface plasmonic behaviour for reflectance reduction of pc-Si surface [6]. In this study, optimization of Ag NPs' arrangement onto the Si surface by RTP annealing is discussed for polycrystalline solar cell (pc-Si) applications.

1.2 Experimental Methodology

The Ag NPs' arrays were fabricated on polycrystalline silicon (pc-Si) substrate using RF sputtering unit (model: HHV—12" MSPT) operated at 13.56 MHz followed by rapid thermal annealing/processing (RTA/RTP) (model: MTI—EQ-OTF-1200X-4-RTP-HV). Prior to deposition, the pc-Si samples were cleaned ultrasonically by using de-ionized water, acetone and isopropyl alcohol, respectively, for 15 min each. A non-continuous thin Ag film (thickness of ~8 nm) with 99.999% purity was deposited on these cleaned substrates. During the deposition process, the deposition conditions were maintained at a base pressure of 2.6×10^{-6} mbar and operating pressure of 6×10^{-2} mbar in an argon gas atmosphere at a constant gas pressure of 2 kg/cm². The deposition conditions in RF sputtering were maintained at the same power rate of 75 W for 10 s at room temperature. The distance between target and substrate was kept at 2 inches for all the depositions. As prepared samples were subjected to RTP treatment at temperature of 200, 250, 300, 350 and 400 °C for various RTP durations of 5–35 min. After that, the samples were cooled naturally to get back the substrates' temperature to room temperature.

The surface morphology of fabricated Ag NPs onto the pc-Si substrates was studied using a (Zeiss—EVO-18) scanning electron microscopy (SEM) and field emission electron microscopy (FE-SEM, model: TESCAN-MIRA). The average particle sizes and surface area coverage of Ag NPs in SEM images were calculated by using ImageJ v1.45 software [7].

1.3 Results and Discussions

The RTP treatment of as-sputtered flattened non-continuous Ag particles layer results into the formation of Ag NPs of different size and shape onto the pc-Si substrates. The as-sputtered Ag thin films were subjected to RTP heat treatment for 5, 10, 15, 20, 30 and 35 min at a temperature of 200, 250, 300, 350 and 400 °C. The fabricated Ag NPs with different sizes are observed on pc-Si substrates, and the average particle size is calculated using J-image software. It is observed that with an increase in RTP time duration, average particle size and surface coverage reduce for 20 min and then again these parameters start to rise for 30 min RTP temperature corresponding to 200, 250, 300 °C. The RTP treatment at 350 and 400 °C results into formation of different sizes of Ag NPs, and minimum average particle size is observed corresponding to 35 min. Figure 1.1a shows the FE-SEM image of Ag-coated pc-Si surface which clearly shows flattened Ag particles onto the Si surface with a surface coverage of highest surface coverage. Figure 1.1b–f shows the SEM image corresponding to minimum average particle size and lowest area coverage of Ag NPs at 200 °C, 250 °C, 300 °C, 350 °C and 400 °C, respectively.

The ultimate size, shape and interparticle distance of the so-formed Ag NPs on pc-Si depend on the amount of shrinkage force (thermal stress) generated at the interface of thin-film and substrate surface due to natural cooling of the RTP-treated samples

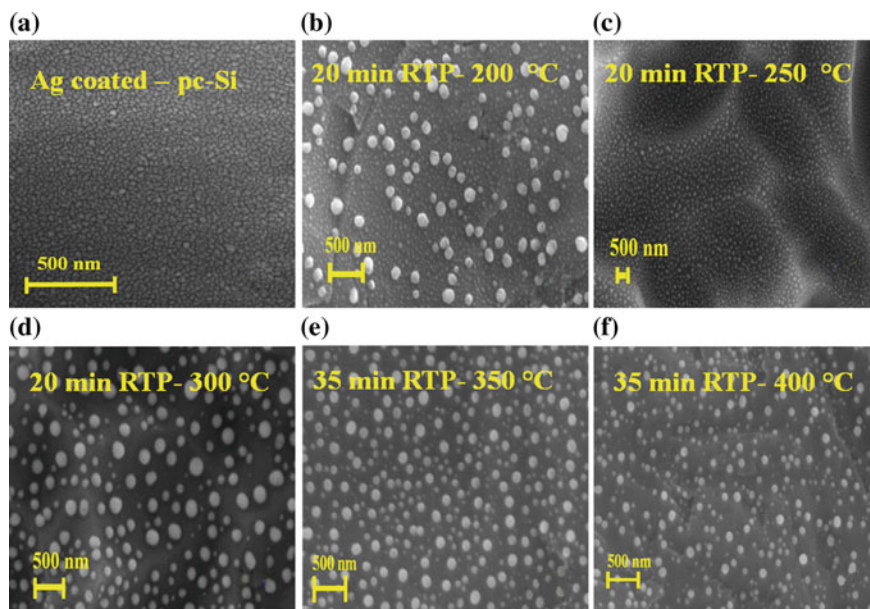


Fig. 1.1 a FE-SEM image of Ag-coated pc-Si surface; SEM image corresponding to minimum average particle size and lowest area coverage of Ag NPs at **b** 200 °C, **c** 250 °C, **d** 300 °C, **e** 350 °C and **f** 400 °C, respectively

[8]. Upon cooling of RTP-treated Ag-coated pc-Si samples, thermal compressive stress garnered at the interface of thin Ag film and pc-Si surface due to mismatching in thermal expansion coefficient of both the surfaces. The generation of shrinkage force between the interfaces of two surface results shrinkage of the Ag thin film, which leads to the formation of Ag NPs. The generated thermal stress or shrinkage force value can be calculated by using the following equation [9]

$$\sigma = \frac{F_f}{d_f w} = \frac{(\alpha_s - \alpha_f) \Delta T E_f}{(1 - \nu_f)} \quad (1.1)$$

Here, α_s -thermal expansion coefficient of substrate, α_f -thermal expansion coefficient of film (Ag), ν_s -Poisson's ratio of substrate, E_f -Young's modulus of film, ν_f -Poisson's ratio of film and ΔT -temperature difference.

The thermal expansion coefficient of pc-Si substrate and Ag is $2.6 \times 10^{-6}/\text{K}$ and $19 \times 10^{-6}/\text{K}$, respectively [10, 11]. Young's modulus of elasticity and Poisson's ratio of Ag film are reported as 82.5 GPa and 0.364, respectively [12].

The RTP treatment of as-sputtered non-continuous Ag thin film causes reduction in % surface area coverage of Ag particles due to the presence of shrinkage force at the interface which is reshaping the particles into Ag NPs. For pc-Si surface, the surface area coverage by RF sputtered Ag thin film is about 45.39%. Using RTP treatment, the % surface coverage reduced significantly and attained minimum value for 20-min RTP duration at 200, 250, 300 °C and for 35-min RTP duration at 350 °C and 400 °C, respectively. During RTP treatment, the thermal compressive force generated at the interface reshapes the so-formed Ag NPs with varying RTP duration which reduces surface coverage and increases the vertical height of the Ag NPs. Table 1.1 shows the minimum average Ag NPs' size along with generated thermal stress and respective least area surface coverage at all annealing temperature.

Table 1.1 shows that at 400 °C for 35-min RTA duration, surface area coverage of Ag NPs becomes minimum (12.17%) amongst all temperatures. There is a decrease in existing area surface converge (45.39%) of Ag films which are around 67.27%, 68.28%, 58.33% and 67.07%, respectively, at RTP temperature of 200, 250, 300, 350 °C corresponding to minimum Ag NPs' size. Thus, around 73.18% decrease in existing area coverage is achieved at 400 °C for 35 min. This table clearly depicts

Table 1.1 Minimum average Ag NPs' size (nm) with respective % surface area coverage and corresponding generated shrinkage force at various RTP temperatures

RTP temp. (°C)	Particle size (nm)	% surface area coverage	Magnitude of shrinkage force (GPa/K)
200	48.9	14.87	0.368
250	53.54	16.21	0.474
300	95.97	18.91	0.58
350	98.32	14.96	0.687
400	104.21	12.17	0.793

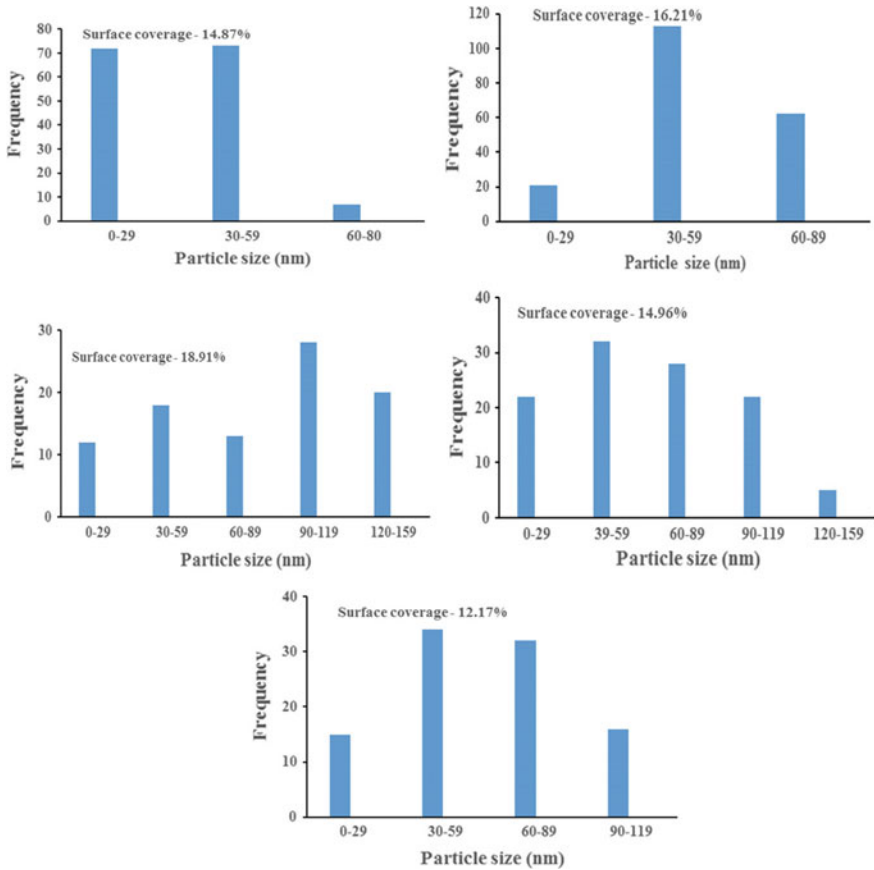


Fig. 1.2 Ag NPs' size distribution onto pc-Si surfaces corresponding to minimum particle size at all RTP temperatures

that with the increase in RTP temperature, the average particle size is increasing. The higher average Ag NPs' size with RTP temperature can be attributed to higher values of generated shrinkage force. At higher RTP temperature, the values of generated shrinkage force increase surface diffusion and neighbouring Ag NPs merge with each other which increase size of average Ag NPs. Thus higher shrinkage force present at the interface of film and substrate increases the aspect ratio of Ag NPs. This shrinkage force can decrease lateral coverage and increase the vertical height of Ag NPs which eventually lead to reduce surface area coverage of Ag NPs. Figure shows the histogram of pc-Si surfaces SEM images corresponding to a minimum particle size at all RTP temperatures. Histogram shows that maximum numbers of Ag NPs lie in the range of 40 nm which favours higher light scattering [13]. So, on increasing RTP temperature, the average size of particles is increasing and promoting light scattering phenomenon dominating over plasmonic effect in Ag NPs.

Thus, SEM image (shown in Fig. 1.2) and Table 1.1 reveal that the irregular arrangement of size distribution of Ag NPs started becomes regular with RTP treatment due to grain refinement during recrystallization process in annealing and attained minimum value for 20-min RTP duration at 200, 250, 300 °C and for 35-min RTP duration at 350 °C and 400 °C, respectively. Also, the % surface area coverage by Ag NPs also reduces with average particles size of Ag NPs considerably by changing the RTP parameters that can be beneficial for enhanced light trapping in Si-based solar cell (Fig. 1.2).

1.4 Conclusion

This study described the fabrication and optimization of Ag NPs using rapid thermal annealing of Ag thin film at RTP temperature of 200, 250, 300, 350 and 400 °C at various annealing duration. The generated thermal stress or shrinkage force at particular temperature arises due to mismatch in thermal expansion coefficients between substrate and thin-film material. The RTP treatment helps in reshaping irregular arrangement of so fabricated Ag NPs into more uniform distribution of Ag NPs along with decreasing the surface coverage of Ag NPs onto the substrate. After the optimization of RTP durations and RTP temperatures in the range of 5–35 min and 200–400 °C, respectively, least surface area coverage up to 12.17% is achieved at 400 °C for 35-min annealing duration. This reduction and optimization of Ag NPs' area coverage onto the pc-Si surface can be used for pc-Si solar cell application and so increased light trapping into the Si absorber layer and can increase short-circuit current density of the Pc-Si solar cells.

Acknowledgements Authors are thankful to the Department of Science and Technology (DST), Govt. of India, for financially supporting this research work. Authors also wish to thank Dr. D. N. Singh, CTO, IndoSolar Pvt. Ltd., for his valuable time and support. Authors also wish to acknowledge Dr. Ashok K. Chauhan, Founder President, Amity University, Noida, for his continuous encouragement and kind support to carry out present research.

References

1. K.R. Catchpole, A. Polman, *Appl. Phys. Lett.* **93**(19), 191113 (2008)
2. K.L. Kelly, E. Coronado, L.L. Zhao, G.C. Schatz, *J. Phys. Chem. B* **107**, 668–677 (2003)
3. D.M. Schaadt, B. Feng, E.T. Yu, *Appl. Phys. Lett.* **86**(6), 063106 (2005)
4. S. Pillai, K.R. Catchpole, T. Trupke, M.A. Green, *J. Appl. Phys.* **101**(9), 093105 (2007)
5. E. Thouti, N. Chander, V. Dutta, V.K. Komarala, *J. Opt.* **15**(3), 035005 (2013)
6. B. Barman, H. Dhasmana, A. Verma, A. Kumar, S.P. Chaudhary, V.K. Jain, *Adv. Nat. Sci. Nanosci. Nanotechnol.* **8**(3), 1–8 (2017)
7. W.S. Rasband, ImageJ. US National Institutes of Health (Bethesda, MD, 2016). <http://rsb.info.nih.gov/ij/>. Accessed 12 July 2017
8. N. Marechal, E. Quesnel, Y. Pauleau, *Thin Solid Films* **241**, 34 (1994)

9. M. Ohring, *The Material Science of Thin Films* (Academic Press Inc, New York, 1992)
10. M. Gad-El-Hak (ed.), *The MEMS Handbook* (CRC Press, Boca Raton, Florida, 2001)
11. C.Y. Ho, R.E. Taylor (eds.), *Thermal Expansion of Solids* (ASM International, Materials Park, OH, USA, 1998)
12. D.R. Smith, F.R. Fickett, *J. Res. Nat. Inst. Stand. Technol.* **100**, 119 (1995)
13. C. Noguez, *J. Phys. Chem. C* **111**(10), 3806–3819 (2007)

Chapter 2

Aligned Zinc Oxide Nanostructures for Dye-Sensitized Solar Cells: A Review



Rakhi Grover, Nidhi Gupta, Omita Nanda and Kanchan Saxena

Abstract The optoelectronic and electrical properties of zinc oxide (ZnO) nanostructures are dependent on the morphology and dimensions at the nanoscale. The present work explains different methods to grow zinc oxide nanostructures to be applied in dye-sensitized solar cells (DSSCs). The importance of aligned nanostructures of ZnO has been described with advantages specific to DSSC applications. The aligned ZnO nanostructures are generally helpful in reducing recombination instances and faster electron collection rates when used as photoanode in DSSCs. This helps to enhance short-circuit current density and open-circuit voltage which result in increased efficiency of the devices. The significance of optimization of the thickness of the photoanode has also been explained to achieve these advantages.

Keywords Zinc oxide · Aligned nanostructures · Dye-sensitized solar cells

2.1 Introduction

Semiconductor oxide-based nanostructures have been researched in detail for their unique optoelectronic applications [1, 2]. Zinc oxide (ZnO) is a wide band gap II–VI semiconductor exhibiting a number of properties including electronic, semiconducting and piezoelectric properties with high thermal and mechanical stability [3, 4]. Especially, large band gap energy (3.37 eV) at room temperature and large exciton binding energy (60 meV) of ZnO promote its use in optoelectronic applications [5, 6]. It can be used as a transparent conductive oxide (TCO) electrode due to its transparency in the visible region of electromagnetic spectrum [7, 8]. The polar surface of ZnO helps to achieve different morphologies. ZnO nanostructures are reported to be synthesized in one-dimensional (e.g., nanorods, wires, needles, etc.), two-dimensional (e.g., nanosheets) or three-dimensional structures (e.g., nanoflowers)

R. Grover (✉) · N. Gupta · O. Nanda · K. Saxena

Amity Institute of Advanced Research and Studies (Materials & Devices), Amity Institute of Renewable and Alternative Energy, Amity University, Sector 125, Noida, Uttar Pradesh 201303, India

e-mail: rgrover1@amity.edu

[9]. ZnO nanostructures can be synthesized using physical vapor deposition (PVD), chemical vapor deposition (CVD), electrodeposition and a number of other methods as reported in the literature [9].

PVD is a quite simple technique to grow ZnO nanostructures and is based on the evaporation, transportation and condensation of metal oxide on the substrate. In this method, the flow rate of the carrier gas, deposition temperature and pressure are the key factors determining final yield on the substrate [10].

In CVD techniques, thin film of material is deposited by the decomposition of chemicals in the vapor phase onto a substrate surface. Vapor transport process involves transportation and reaction of zinc and oxygen vapors forming ZnO nanostructures or heating zinc powder in the presence of oxygen flow. This requires precise control over vapor pressure of both constituents. Ma et al. have reported [11] the synthesis of aligned ZnO nanowires on polycrystalline Zn_2GeO_4 : Mn substrates by CVD technique. The density of nanowires was varied by optimizing the lateral distance between the substrate and source powder in the tube furnace.

The solution-based synthesis of ZnO nanostructures makes use of a zinc precursor, e.g., zinc chloride/nitrate/acetate along with reducing and stabilizing agents. These solution-based methods include electrodeposition, hydrothermal, solvothermal, precipitation and sol-gel. Hydrothermal and electrochemical deposition methods are quite simple techniques for the growth of nanostructures. Hydrothermal synthesis of ZnO nanostructures is a low-temperature process with easily controllable particle size. This method offers easy control over different growth parameters, e.g., temperature, concentration ratio of precursors and reaction time, etc. to produce different morphologies of nanostructures [12].

Electrochemical deposition or electrodeposition is an easy and cost-effective method to grow ZnO nanostructures at comparatively low temperatures. Two electrodes: one acting as cathode and another as anode are dipped into electrolyte solution to which an appropriate electric field is applied. The size and morphology of ZnO nanostructures are dependent on electrolyte concentration, applied potential, temperature and electrodeposition duration [9]. Template-assisted electrodeposition methods allow well-aligned ZnO nanostructure arrays under an applied electric field. Recently, we have grown ZnO nanostructures by electrodeposition on silicon substrate in an electrochemical cell placed in a water bath maintained at 75–80 °C. In this electrochemical cell, a zinc sheet was used as anode and ZnO nanostructures were grown on Si substrate fixed to another electrode made up of copper. The electrolyte solution was made using zinc nitrate hexahydrate aqueous solution. Figure 2.1 shows the SEM micrograph of the nanostructures fabricated. Randomly oriented ZnO nanorods with 600 nm–1 μm length and hexagonal ends (130–190 nm) were obtained (as shown in Fig. 2.1). The size and morphology of these nanostructures are being further optimized for DSSC applications.

Recently, Boda et al. [13] demonstrated the growth of hybrid ZnO nanostructures by a facile combined method based on electrodeposition and chemical bath deposition (CBD). The hybrid ZnO-based photoanode resulted in increased current density by 43% as compared to the bare ZnO nanostructures which were attributed to increased crystallinity and reduced charge transfer resistance.

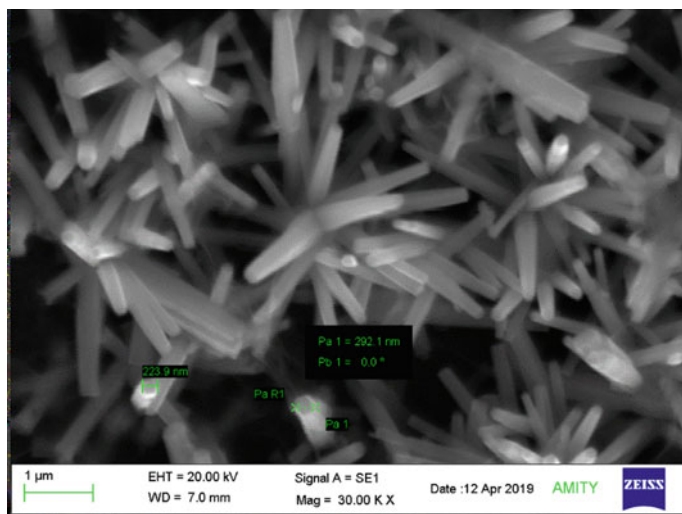


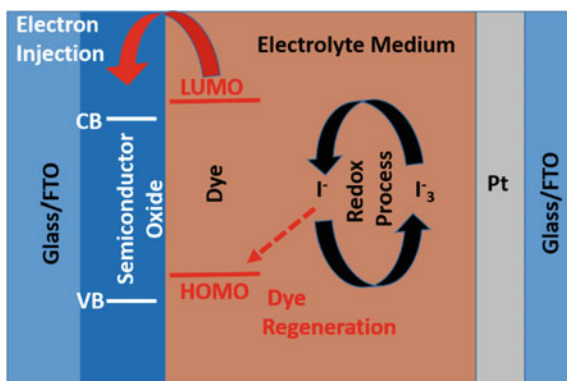
Fig. 2.1 SEM micrograph of the ZnO nanostructured film fabricated

The morphology and dimensions of ZnO nanostructures significantly affect their optoelectronic and electrical properties and therefore the efficiency of the final devices. One-dimensional nanostructures in the form of nanorods, nanowire and nanotubes, etc. offer efficient charge carrier transport when used inside the photovoltaic devices. These nanostructures provide interconnected network with a large surface-to-volume ratio which is highly desirable to form a large interfacial area with dyes for solar cell applications. In DSSCs, a mesoporous network of ZnO is desirable to function as a photoanode and/or counter electrode. A typical DSSC consists of a wide band gap semiconductor oxide (SO), e.g., ZnO or TiO₂ coated with dye molecules to absorb sufficient part of the electromagnetic spectrum. This sensitizer is regenerated by an electrolyte medium which acts as a mediator between photoanode and the counter electrode (CE). This architecture is fabricated as glass/FTO/SO/Dye/Electrolyte/CE as shown in Fig. 2.2.

2.2 Aligned ZnO Nanostructures for Dye-Sensitized Solar Cells (DSSCs) Applications

DSSCs are based on wide band gap semiconductor oxides with mesoporous structures for maximum dye adsorption. Dyes when illuminated with light undergo excitation and transfer an electron to the adjoining semiconductor oxide (generally TiO₂ or ZnO). The dye is then regenerated by the redox electrolyte which itself gets its electron back from the counter electrode via the electrolyte medium as depicted in Fig. 2.2.

Fig. 2.2 Schematic diagram showing significant electrochemical processes inside DSSC



Well-aligned ZnO nanostructures can be used as photoanodes in DSSCs where the efficiency of the device can be tuned by adjusting morphology, orientation and the energy level alignment of these nanostructures with the sensitizer being used. For example, increasing nanorods length from 2.6 to 10.8 μm resulted in an enhanced efficiency from 0.94 to 1.69% in the devices [14]. The higher electron mobility of ZnO, that is, 200–300 $\text{cm}^2 \text{V}^{-1} \text{s}^{-1}$ for bulk material as compared to conventional TiO_2 (0.1–4 $\text{cm}^2 \text{V}^{-1} \text{s}^{-1}$) [15], makes it a significant alternative to function as a photoanode in DSSCs. Further, solution processability of ZnO layer at room temperature makes it an ideal choice to be used in low-cost dye-based solar cells with reduced recombination losses [16].

Several designs of photoanodes are possible with varied possible morphologies of ZnO nanostructures. ZnO-based photoanodes in DSSCs are intended to work as efficient light absorbers as well as to enable fast electron transfer rates to reduce the recombination events inside DSSCs. Randomly oriented ZnO nanostructures exhibit electron transport via charge carrier hopping to arrive at the electrode, but this electron transport is limited by a number of nanoparticle or nanostructure boundaries in the random network.

However, aligned 1D nanostructures of ZnO favor direct electron pathways and reduced recombination events which can result in high photocurrents and open-circuit voltages and hence improved efficiency of the final devices. These aligned nanostructures require optimized thickness for effective electron diffusion length in the devices for better charge collection at the electrodes. Hence, the charge carrier diffusion length should be greater than the total film thickness. Apart from the photoanode applications of aligned ZnO nanorods in DSSCs, these nanostructures have also been explored as counter electrodes and scattering layers in DSSCs for significant improvements in efficiency values. A number of authors have reported various applications of aligned ZnO nanostructures in DSSCs. Table 2.1 shows some of the significant achievements in this direction.

Gonzalez-Valls and Cantu research group [17] reported vertically aligned ZnO nanorods (NRs) and studied physisorption/chemisorption of the dye molecules on

Table 2.1 Some of the significant achievements in applications of aligned ZnO nanostructures in DSSCs

Authors, year	Method adopted	Highest PCE (efficiency %)	Anode/cathode (role played)
Gonzalez-Valls et al., 2010	Hydrothermal	0.75	Photoanode
Yengantiwara et al., 2011	Open Aqueous Solution Deposition (OASD)	0.71	Photoanode
Dwivedi and Dutta, 2012	Continuous spray pyrolysis (CoSP)	1.77	Photoanode
Wu et al., 2013	Solvothermal method	5.2	Scattering layer
Rouhi et al., 2015	Two-step approach combining electric field-assisted aqueous solution (EFAS) process and aqueous solution method	4.07	Photoanode
Krishna et al., 2019	Low-temperature hydrothermal method	1.78	1. Photoanode/electron transport layer and 2. Antireflective layer
Syrrokostas et al., 2019	Low-temperature hydrothermal method	8.2	Counter electrode (Pt decorated aligned ZnO nanowires arrays)

the ZnO NRs. The authors concluded that dye: ZnO interaction occurs in definite steps of dye diffusion, adsorption and then complex formation between dye and ZnO.

Yengantiwara et al. [18] reported a two-step approach for the deposition of ZnO nanostructures to function as photoanode. The authors used a two-step process to grow a seed layer either by electrodeposition or by spin coating technique. The authors reported device efficiency dependence on ZnO film thickness and dye adsorption on active film surface.

Dwivedi and Dutta [19] applied continuous spray pyrolysis technique by first obtaining a ZnO seed layer and then ZnO nanoparticle layer on the seeded film. Figure 2.3 shows the schematic diagram for the growth mechanism of ZnO nanorods onto the seeded layer of ZnO nanoparticles. Zn solution film annealed at elevated temperatures favors the growth of ZnO seeds [19].

The seeded layer provides preferential nucleation sites for the growth of nanorods perpendicular to the substrate. The stream of ZnO nanoparticles initially helps in the growth of ZnO nanorods, but as the stream continues in this spray pyrolysis process, all the ZnO nucleation sites become occupied and nanoparticle growth continues in the form of closed networks.

Wu et al. [20] reported hierarchical ZnO aggregates which were assembled by orderly aligned nanorods. These nanostructures were prepared by solvothermal route,

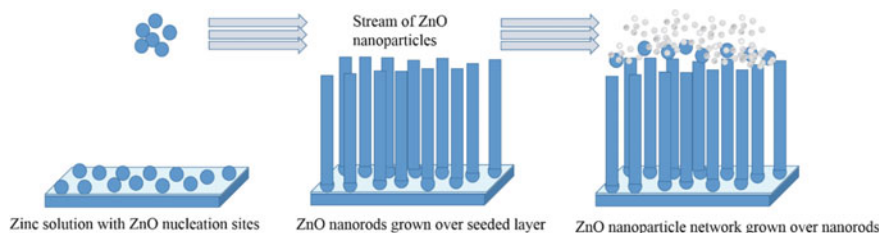


Fig. 2.3 Schematic diagram demonstrating the growth of ZnO nanorods onto the seeded layer

and it was found that the assembling process of these nanostructures was strongly influenced by the reaction medium and could be tuned by precursor zinc acetate dehydrate concentration.

Rouhi et al. [21] reported well-aligned ZnO–ZnS core–shell nanocones where ZnO nanocones serve as a template and provide sites for the growth of ZnS shell. DSSC based on these nanocones as photoanodes attained maximum efficiency of 4.07% which was attributed to the morphology of nanostructures functioning as light trapping centers as well as reduced recombination sites due to ZnS shell layer.

Krishna et al. [22] reported a simple low-temperature hydrothermal method to grow aligned ZnO nanowire arrays to function as antireflection and electron transport layer. These ZnO nanowire arrays were found to decrease reflection and increase the light scattering and thereby improve the performance of the devices. The authors used newly designed indoline moieties with different pi-spacers as sensitizers.

Syrrokostas et al. [23] have recently used well-aligned platinum decorated ZnO nanowire arrays as counter electrodes in DSSCs. The authors have used aligned ZnO nanowire arrays to provide a large surface area for platinum deposition and to transport electrons to Pt sites. This increased the active catalytic site for redox species and reduced recombination instances and provided 8.2% efficiency under AM 1.5 simulated solar illumination (1000 W/m^2). These results have been summarized in Table 2.1.

The efficiency of DSSCs based on ZnO nanostructures is comparatively less than that of devices based on Titania. ZnO being more basic than TiO_2 is more likely to be influenced by the acidic carboxyl groups of the generally used sensitizers leading to the formation of complexes of Zn^{2+} -dye molecules [24]. These agglomerates create an insulating layer which blocks the electrons coming from dye to the semiconductor oxide, that is, ZnO. The formation of Zn^{2+} -dye complex can be restricted during device fabrication by using a buffer layer at ZnO nanostructure/dye interface. Buffer layer can be made using SiO_2 , TiO_2 , Al_2O_3 or ZnO itself. Aligned one-dimensional ZnO nanostructures also restrict the formation of Zn^{2+} -dye complexes due to fast dye adsorption in the perpendicular orientation of ZnO onto conducting substrate [9]. Therefore, oriented ZnO nanostructures hold significant importance for DSSC applications as the efficiency of devices is highly dependent on the morphology of these nanostructures.

2.3 Conclusion

The optimization of aligned ZnO nanostructures in terms of size, shape and morphology is a significant area of research to use ZnO as electrode in DSSCs. The stability of these devices is an important aspect for maintaining initial performance of the devices for the practical time duration. The electrical doping of these ZnO nanostructures provides an additional way to enhance the overall efficiency of DSSCs based on liquid, solid and quasi-solid state-based electrolytes. The light scattering effect due to nanostructures at photoanode/dye interface can further enhance the performance of devices.

Acknowledgements The authors are thankful to Dr. Ashok K. Chauhan, Founder President, Amity University and Dr. V. K. Jain, Distinguished Scientist and Professor, Amity University, Noida, India, for their continuous encouragements.

References

1. C. Doroftei, L. Leontie, Nanostructured oxide semiconductor compounds with possible applications for gas sensors. *New Uses Micro Nanomater.*, Chap. 8, pp. 133–150 (2018). <https://doi.org/10.5772/intechopen.79079>
2. Y. Gyu-Chul (ed.), *Semiconductor Nanostructures for Optoelectronic Devices Processing, Characterization and Applications*. Nanoscience and Technology (Springer-Verlag, Berlin, Heidelberg, 2012). <https://doi.org/10.1007/978-3-642-22480-5>
3. J. Qiu, X. Li, W. He, S.J. Park, H.K. Kim, Y.H. Hwang, J.H. Lee, Y.D. Kim, The growth mechanism and optical properties of ultra-long ZnO nanorod arrays with a high aspect ratio by a preheating hydrothermal method. *Nanotechnology* **20**, 155603–155612 (2009)
4. G. Amin, M.H. Asif, A. Zainelabdin, S. Zaman, O. Nur, M. Willander, Influence of pH, precursor concentration, growth time, and temperature on the morphology of ZnO nanostructures grown by the hydrothermal method. *J. Nanomater.* **2011**, 1–9 (2011)
5. U. Ozgur, V. Avrutin, H. Morkoc, Zinc oxide materials and devices grown by molecular beam epitaxy, in *Molecular Beam Epitaxy*, 2nd edn. (2018)
6. D.S.Y. Jayathilake, T.A. Nirmal Peiris, Overview on transparent conducting oxides and state of the art of low-cost doped ZnO systems. *SF J. Mater. Chem. Eng.* **1**(1), 1004 (2018)
7. H. Hosono, K. Ueda, Transparent Conductive Oxides, in *Springer Handbook of Electronic and Photonic Materials*, Springer Handbooks. eds. by S. Kasap, P. Capper (Springer, Cham, 2017)
8. Y. Chen, Review of ZnO transparent conducting oxides for solar applications, in *IOP Conference Series: Materials Science and Engineering*, vol. 423, p. 012170 (2018)
9. R. Vittala, K.C. Ho, Zinc oxide based dye-sensitized solar cells: a review. *Renew. Sustain. Energy Rev.* **70**(2017), 920–935 (2017)
10. G. Jimenez-Cadena, E. Comini, M. Ferroni, A. Vomiero, G. Sberveglieri, Synthesis of different ZnO nanostructures by modified PVD process and potential use for dye-sensitized solar cells. *Mater. Chem. Phys.* **124**, 694–698 (2010)
11. S. Ma, A.H. Kitai, ZnO nanowire growth by chemical vapor deposition with spatially controlled density on Zn₂GeO₄: Mn polycrystalline substrates. *Mater. Res. Express* **4**, 065012 (2017)
12. G. Murillo, H. Lozano, J. Cases-Utrera, M. Lee, J. Esteve, Improving morphological quality and uniformity of hydrothermally grown ZnO nanowires by surface activation of catalyst layer. *Nanoscale Res. Lett.* **12**(51), 1–8 (2017)

13. M.A. Boda, B.B. Çırak, Z. Demir, Ç. Çırak, Facile synthesis of hybrid ZnO nanostructures by combined electrodeposition and chemical bath deposition for improved performance of dye-sensitized solar cell. *Mater. Lett.* **248**, 143–145 (2019)
14. Q. Zhao, T. Xie, L. Peng, Y. Lin, P. Wang, L. Peng, D. Wang, Size and orientation-dependent photovoltaic properties of ZnO nanorods. *J. Phys. Chem. C* **111**, 17136 (2007)
15. Q. Zhang, C.S. Dandeneau, X. Zhou, G. Cao, ZnO nanostructures for dye-sensitized solar cells. *Adv. Mater.* **21**, 4087–4108 (2009)
16. N. Memarian, I. Concina, A. Braga, S.M. Rozati, A. Vomiero, G. Sberveglieri, Hierarchically assembled ZnO nanocrystallites for high-efficiency dye-sensitized solar cells. *Angew. Chem. Int. Ed.* **50**, 12321–12325 (2011)
17. I. Gonzalez-Valls, M. Lira-Cantu, Dye sensitized solar cells based on vertically-aligned ZnO nanorods: effect of UV light on power conversion efficiency and lifetime. *Energy Environ. Sci.* **3**(6), 789–795 (2010)
18. A. Yengantiwara, R. Sharma, O. Game, A. Banpurkar, Growth of aligned ZnO nanorods array on ITO for dye sensitized solar cell. *Curr. Appl. Phys.* **11**, 113–116 (2011)
19. C. Dwivedi, V. Dutta, Vertically aligned ZnO nanorods via self-assembled spray pyrolyzed nanoparticles for dye-sensitized solar cells, *Adv. Nat. Sci. Nanosci. Nanotechnol.* **3**, 015011, 1–8 (2012)
20. D. Wu, Z. Gao, F. Xu, J. Chang, W. Tao, J. He, S. Gao, K. Jiang, Hierarchical ZnO aggregates assembled by orderly aligned nanorods for dye-sensitized solar cells. *Cryst. Eng. Comm.* **15**, 1210 (2013)
21. J. Rouhi, M.H. Mamat, C.R. Ooi, S. Mahmud, M.R. Mahmood, High-performance dye-sensitized solar cells based on morphology-controllable synthesis of ZnO–ZnS heterostructure nanocone photoanodes. *PLoS One.* **10**(4), e0123433 (2015). <https://doi.org/10.1371/journal.pone.0123433>
22. J.V.S. Krishna, G. Reddy, K. Devulapally, N. Islavath, L. Giribabu, Solution processed aligned ZnO nanowires as anti-reflection and electron transport layer in organic dye-sensitized solar cells. *Opt. Mater.* **5**, 109243, 1–5 (2019)
23. G. Syrokostas, K. Govatsia, G. Leftheriotis, S.N. Yannopoulos, Platinum decorated zinc oxide nanowires as an efficient counter electrode for dye sensitized solar cells. *J. Electroanal. Chem.* **835**, 86–95 (2019)
24. H. Horiuchi, R. Katoh, K. Hara, M. Yanagida, S. Murata, H. Arakawa, M. Tachiya, Electron injection efficiency from excited N₃ into nanocrystalline ZnO films: effect of (N₃–Zn²⁺) aggregate formation. *J. Phys. Chem. B* **107**(11), 2570–2574 (2003)

Chapter 3

Investigation of Heat Transfer Characteristics of Al₂O₃-Embedded Magnesium Nitrate Hexahydrate-Based Nanocomposites for Thermal Energy Storage



Neeraj Gupta, Vivek Kumar, Hrishikesh Dhasmana, Avshish Kumar, Prashant Shukla, Amit Kumar, Abhishek Verma, S. K. Dhawan and Vinod Kumar Jain

Abstract Phase change materials (PCMs) have been widely investigated as latent heat energy storage medium for effective thermal management. Presently, PCM nanocomposites have been prepared by dispersing aluminum dioxide (Al₂O₃) nanoparticles (NPs), which act as thermally conductive nanofillers, in molten magnesium nitrate hexahydrate (Mg(NO₃)₂·6H₂O), an inorganic salt hydrate. Al₂O₃ NPs with mass fractions of 0.5, 1.0 and 1.5 wt% have been dispersed in liquid PCM to obtain PCM nanocomposites, which are used to study the heat transfer properties. The morphology of the Al₂O₃ NPs, PCM and PCM nanocomposites has been studied by scanning electron microscopy (SEM). Fourier-transform infrared spectroscopy (FTIR) analysis was carried out to investigate the interaction between Al₂O₃ and PCM in PCM nanocomposite. The melting (charging) and solidification (discharging) characteristics of the PCM nanocomposites have been recorded and analyzed. The experimental results clearly showed that the rate of melting and solidification of PCM nanocomposite increases by 15% and 38%, respectively, with an increase in the mass fraction (1.5 wt%) of nanofillers as compared to the pristine PCM. The observed reduction in heat release time confirmed the effective enhancement of thermal conductivity in Al₂O₃-PCM nanocomposite samples as compared to the pristine

N. Gupta · V. Kumar · H. Dhasmana · A. Kumar · P. Shukla · A. Kumar (✉) · A. Verma · V. K. Jain

Amity Institute of Advanced Research and Studies (Materials and Devices), Amity University, Noida 201303, Uttar Pradesh, India
e-mail: kumar.amit9731@gmail.com

Present Address:

A. Kumar
School of Engineering and Technology, Central University of Haryana, Jant-Pali, Mahendergarh 123031, Haryana, India
e-mail: kumaramit@cuh.ac.in

S. K. Dhawan
Division of Materials Physics and Engineering, National Physical Laboratory, New Delhi, India

© Springer Nature Singapore Pte Ltd. 2020
V. K. Jain et al. (eds.), *Advances in Solar Power Generation and Energy Harvesting*, Springer Proceedings in Energy, https://doi.org/10.1007/978-981-15-3635-9_3

PCM. The prepared PCM nanocomposites displayed superior heat transfer capability, making it a potential candidate for thermal energy storage.

Keywords Phase change material (PCM) · Nanoparticles · Thermal energy storage · Heat transfer

3.1 Introduction

Phase change materials (PCMs) store a large amount of energy, approximately 10 times higher than sensible heat storage materials, during their phase transformation, like solid–liquid, liquid–gas or solid–solid transitions [1–4]. PCMs have been widely used in the variety of applications such as thermal management of electronic devices [5–7], aerospace engineering [8], solar water heater [9], textiles fabric [10], solar thermal energy storage [11, 12], efficient buildings [13, 14] and so on. PCMs are generally classified into two major types: inorganic and organic. The most promising class of PCMs is inorganic salt hydrates due to their extremely high storage density, high thermal conductivity, wide range of melting temperature, small volume change, nonflammable, good stability in comparison with the organic PCMs [15–17]. Nevertheless, salt hydrates exhibit some problems such as supercooling, low thermal conductivity and can be corrosive toward metals used for heat transfer which hinders their application in actual engineering [18].

To overcome these problems, a simple method can be applied, which is to increase the thermal conductivity of the base material and to lower the supercooling of (PCMs). This leads to enhancement in the heat transfer rate and also improves the energy storage efficiency. Although different techniques have been employed to increase the thermal conductivity of PCMs, such as the usage of metal fins [19], porous matrix [20] and fibrous material [21]. However, these techniques increase the weight and the final volume of the system. In addition, dispersing the highly conductive material into the PCM matrix has been proposed as a favorable method to increase the thermal conductivity, but due to the difference in their densities, it leads to the poor dispersion and poor stability of the final product [22].

The application of nanomaterial has been recently considered to enhance the performance of thermal storage system. Due to their reduced size, the thermophysical properties of PCMs such as stability, viscosity and heat transfer performance can be enhanced. Different nanomaterials such as carbon materials (CNT, graphene, expanded graphite), metallic and metal oxides nanoparticles have been proposed as a filler for dispersing in PCM media [23–26]. Metal oxides have excellent thermal conductivity and therefore can be used to enhance the thermal conductivity of PCMs [27, 28]. Among the different metal oxide nanoparticle, Al_2O_3 attracts more attention because of its different properties, high thermal conductivity and photocatalytic activity and low cost [29, 30].

Li et al. [31] showed that by dispersing the gamma- Al_2O_3 NPs in the calcium chloride hexahydrate with 0.5, 1, 1.5 and 2 wt% reduces the supercooling degree

of $\text{CaCl}_2 \cdot 6\text{H}_2\text{O}/\text{gamma-Al}_2\text{O}_3$ nanocomposite in the range of (0–2) °C. The maximum reduction in the latent heat is 5.9%, and no phase segregation was observed. Moreover, the $\text{CaCl}_2 \cdot 6\text{H}_2\text{O}/\text{gamma-Al}_2\text{O}_3$ nanocomposite with 1.0 wt% $\text{gamma-Al}_2\text{O}_3$ shows excellent thermal cycling stability. Nourani et al. [32] studied the thermal behavior of paraffin containing Al_2O_3 nanoparticles, whereas the sodium stearoyl lactylate has been used as a surfactant to increase the stability of $\text{Al}_2\text{O}_3/\text{PCM}$ nanocomposite samples. Their result showed that the thermal conductivity of composite is higher than that of pure PCM at phase change temperature of samples, while heat fusion and melting temperature of obtained composite have no significant variations. Ho and Gao [33] prepared the composite by dispersing Al_2O_3 nanoparticle with 5 and 10 wt% in n-octadecane by means of nonionic surfactant and studied the various properties such as latent heat of fusion, density, dynamic viscosity and thermal conductivity. The amount of nanoparticles and surfactant are the affecting factors on the stability of nanoparticles in the PCM. Wu et al. [34] observed the potential of $\text{Al}_2\text{O}_3\text{-H}_2\text{O}$ as a new phase change material for thermal energy storage of cooling systems. Thermal response test shows the addition of Al_2O_3 remarkably decreases the supercooling degree of water and advances the beginning freezing time and reduces the total freezing time. Nguyen et al. [35] investigated the behavior and heat transfer enhancement of an Al_2O_3 nanoparticle–water mixture for the cooling of microprocessors or other electronic components. Experimental results reveal that the inclusion of nanoparticles into fluid has produced a considerable enhancement of the cooling block convective heat transfer coefficient. Nanofluid with 6.8% particle volume concentration, heat transfer coefficient has been found to increase 40% compared to that of the base fluid. Nanofluid with 36-nm particle provides higher heat transfer coefficient than a 47-nm particle size.

Few reports are available in the literature on dispersed NPs in inorganic PCM-based nanocomposites. The present study aims to synthesis $(\text{Mg}(\text{NO}_3)_2 \cdot 6\text{H}_2\text{O})\text{-Al}_2\text{O}_3$ nanocomposites and to characterize its various properties, such as heat transfer characteristics, phase change temperature and latent heat, for its useful usage in the thermal energy storage system.

3.2 Experimental Description

3.2.1 Materials and Method

Magnesium nitrate hexahydrate ($\text{Mg}(\text{NO}_3)_2 \cdot 6\text{H}_2\text{O}$), an inorganic salt hydrate PCM, was purchased from Alfa-Aesar. Aluminum oxide nanoparticles (Al_2O_3) were procured from Sigma-Aldrich. All the materials were used directly as received without any further purification.

3.2.2 Preparation of $(\text{Mg}(\text{NO}_3)_2 \cdot 6\text{H}_2\text{O})\text{-Al}_2\text{O}_3$ Nanocomposite

The $(\text{Mg}(\text{NO}_3)_2 \cdot 6\text{H}_2\text{O})\text{-Al}_2\text{O}_3$ nanocomposite was prepared by the melt mixing technique [36]. In the formation process, nanoparticles were added to the molten PCMs, heated above its phase transition temperature and mixed thoroughly by using the magnetic stirrer with vigorous stirring around 30 min to form the uniform PCM nanocomposite. Finally, the composite was ultrasonicated for approximately 30 min to obtain a homogenous dispersion of the PCM- Al_2O_3 nanocomposite. Al_2O_3 nanoparticles with different weight fractions ranging from (0.5 to 1.5) wt% were used to prepare different PCM nanocomposites.

3.2.3 Characterization Technique

The morphology and size measurement of Al_2O_3 NPs were analyzed using a Zeiss (EVO-18) scanning electron microscope (SEM). The SEM images were used to estimate the size of Al_2O_3 nanoparticles and to observe the dispersion of the nanoparticles in the composite. The interaction between $(\text{Mg}(\text{NO}_3)_2 \cdot 6\text{H}_2\text{O})$ and Al_2O_3 in nanocomposite was determined using Fourier-transform infrared spectroscopy (FTIR). Thermogravimetric analysis (TGA) was done to analyze the thermal degradation behavior of the pristine PCM and PCM nanocomposites. Charging and discharging characteristics of the PCM nanocomposites with respect to the pristine PCM were investigated by using the conventional heating system [37].

3.3 Results and Discussion

3.3.1 SEM Analysis

Figure 3.1 shows the SEM image of pristine PCM, Al_2O_3 nanoparticles and PCM nanocomposite. It can be seen that the pristine PCM, i.e., $(\text{Mg}(\text{NO}_3)_2 \cdot 6\text{H}_2\text{O})$, is a crystalline solid which is clearly visible in the microscopic image Fig. 3.1a. Figure 3.1b reveals the SEM image of Al_2O_3 nanoparticles, which are spherical in shape. The SEM image of the PCM- Al_2O_3 nanocomposite is shown in Fig. 3.1c which shows that nanocomposite has a smooth surface, and the nanoparticles are uniformly distributed over the surface of the PCM without any agglomeration.

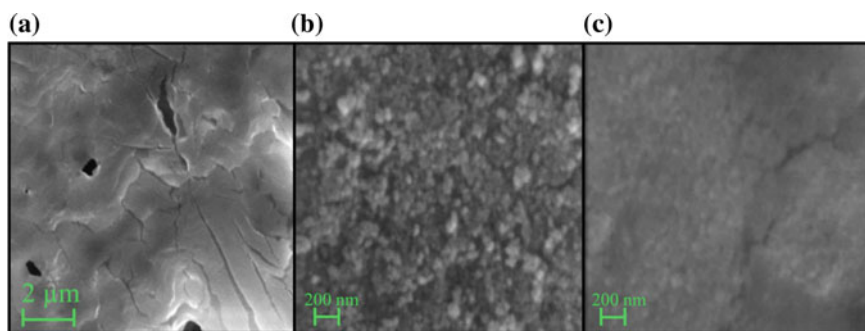


Fig. 3.1 SEM micrographs of **a** pristine PCM (magnesium nitrate hexahydrate), **b** Al_2O_3 nanoparticle and **c** PCM- Al_2O_3 nanocomposites

3.3.2 FTIR

The FTIR spectra of $(\text{Mg}(\text{NO}_3)_2 \cdot 6\text{H}_2\text{O})$ and $(\text{Mg}(\text{NO}_3)_2 \cdot 6\text{H}_2\text{O})\text{-Al}_2\text{O}_3$ nanocomposites are shown in Fig. 3.2. The FTIR spectrum of $(\text{Mg}(\text{NO}_3)_2 \cdot 6\text{H}_2\text{O})$ has characteristic peaks for O–H stretching at 3400 cm^{-1} , N=O bending at 1550 cm^{-1} , a mixture of N–O stretching and bending of N=O at 1300 cm^{-1} , plus a sharp peak at 819 cm^{-1} for NO_3^- . In the case of $(\text{Mg}(\text{NO}_3)_2 \cdot 6\text{H}_2\text{O})\text{-Al}_2\text{O}_3$ nanocomposite, no new peaks or shift is observed in comparison with pristine PCM. This clearly indicates that there is no chemical reactivity between Al_2O_3 NPs and the PCM as they are merely physically mixed together to form a stable PCM nanocomposite. Similar results were reported by other groups, where they reported the simple physical interaction between PCM and the dispersed NPs [38].

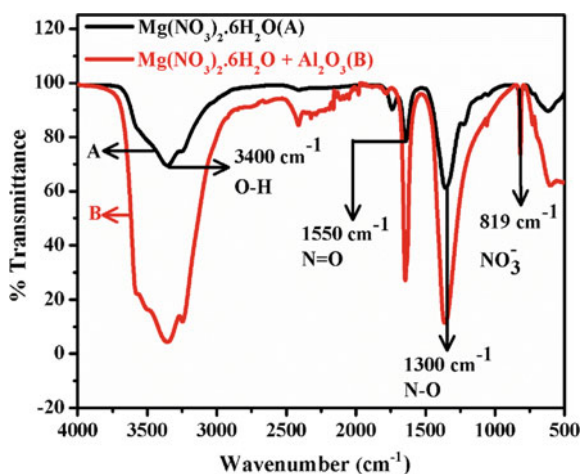


Fig. 3.2 FTIR spectra of **a** magnesium nitrate hexahydrate, **b** PCM- Al_2O_3 nanocomposite

3.3.3 Melting and Solidification Experimental Results

The thermal energy transfer characteristics of the pristine PCM and PCM nanocomposites were evaluated by comparing their melting (charging) and solidification (discharging) cycles with the help of the conventional heating method. Figure 3.3 presents the melting cycles of the pristine PCM and PCM nanocomposites with increasing concentration of Al_2O_3 from (0.5 to 1.5) wt%.

At the initial point of the melting cycle, both the pristine PCM and composites were at the ambient temperature. The temperature of pristine PCM and the composite were gradually increased by $2^\circ\text{C}/\text{min}$ until they reached their phase transition temperature. It can be seen that the pristine PCM started to melt at approximately 93 min from the starting point. As the concentration of Al_2O_3 nanoparticles was increased ranging from 0.5, 1 to 1.5 wt% in the pristine PCM, a decrease in the melting time of the PCM nanocomposites is observed. This shows the overall reduction of 15% in the melting time of the PCM nanocomposite at 1.5 wt% compared to that of pristine PCM.

The solidification cycle of pristine PCM and PCM nanocomposites was also performed, and the results are shown in Fig. 3.4. At the initial stage of the solidification process, the temperature of the pristine PCM and PCM nanocomposites was found to be 120°C . After allowing them to cool naturally, the temperature of the pristine PCM and PCM nanocomposites decreased until they reached their solidification point. The solidification curves showed similar behavior like the melting curve, i.e., the solidification time decreased as the concentration of the Al_2O_3 nanoparticles was increased ranging from (0.5–1.5) wt%. It was observed that the solidification time of the PCM nanocomposite for 1.5 wt% was reduced by 38% compared to that of pristine PCM. This reduced time is an indirect evidence of thermal conductivity enhancement of PCM- Al_2O_3 nanocomposite as compared to the Pristine PCM.

Fig. 3.3 Melting curves of pristine PCM and PCM- Al_2O_3 nanocomposite at different mass fractions (0.5–1.5) wt% of Al_2O_3

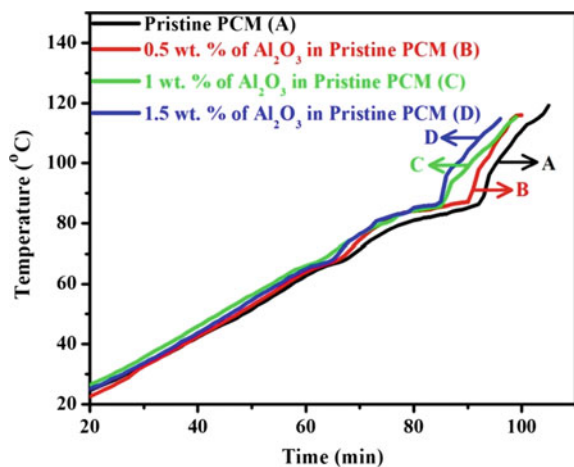
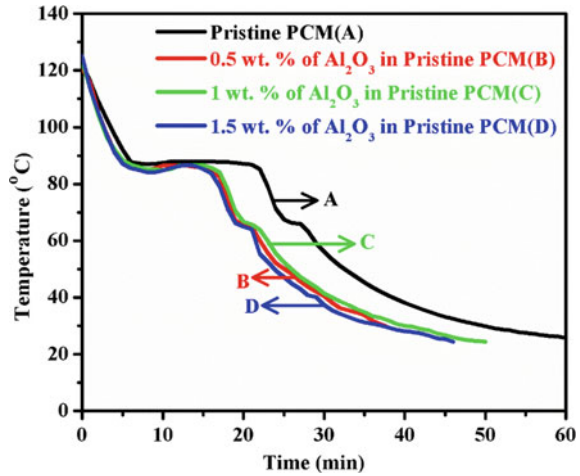


Fig. 3.4 Solidification curves of pristine PCM and PCM- Al_2O_3 nanocomposite at different mass fractions (0.5–1.5) wt% of Al_2O_3

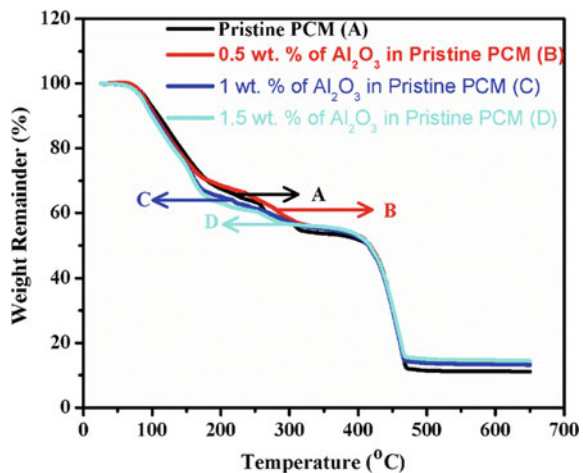


3.3.4 Thermal Analysis

Figure 3.5 compares the thermal degradation behavior of pristine PCM and PCM nanocomposites with increasing concentration of Al_2O_3 nanoparticles ranging from (0.5 to 1.5) wt%. According to TGA thermographs, $(\text{Mg}(\text{NO}_3)_2 \cdot 6\text{H}_2\text{O})$ starts to lose mass at around 70 °C and has lost 30% mass by 170 °C, which corresponds to water loss. The remaining mass was lost from 300 to 460 °C. According to the literature, $(\text{Mg}(\text{NO}_3)_2 \cdot 6\text{H}_2\text{O})$ decomposes at 330 °C. 10% mass remains after 500 °C, mainly consisting of magnesium oxide.

In PCM nanocomposites, the remaining mass was left around 15% after 500 °C. In other words, mass reduction in PCM nanocomposites was less than pristine

Fig. 3.5 TGA curve of $\text{Mg}(\text{NO}_3)_2 \cdot 6\text{H}_2\text{O}$ and $\text{Mg}(\text{NO}_3)_2 \cdot 6\text{H}_2\text{O} + \text{Al}_2\text{O}_3$ nanocomposite



PCM. This is due to the presence of Al_2O_3 nanoparticle in the composite which exhibited greater thermal stability, stabilized the PCM matrix against the thermal decomposition and also contributed to the additional heat capacity.

3.4 Conclusion

In this paper, $(\text{Mg}(\text{NO}_3)_2 \cdot 6\text{H}_2\text{O})\text{-Al}_2\text{O}_3$ nanocomposites were prepared with different compositions ranging (0.5–1.5) wt% and evaluated their phase change transfer characteristics. The prepared nanocomposite exhibited high heat transfer rate: Charging rate increased to 15% and discharging rate increased to 38% for 1.5 wt% of nanofiller as compared to the pristine PCM, suggesting an enhancement in thermal conductivity of PCM- Al_2O_3 nanocomposite samples. The characterization results of SEM revealed that the nanoparticles are uniformly distributed over the layered surface of PCM, without any agglomeration. TGA results indicated that the prepared PCM- Al_2O_3 nanocomposites had better stability. However, the PCM and Al_2O_3 are attached physically rather than chemical, which prevents the material to be degraded during the cycling process. The prepared PCM- Al_2O_3 nanocomposite displayed remarkable properties of high heat transfer which could be useful in the thermal energy storage system with enhanced thermal conductivity.

Acknowledgements We thank Dr. Ashok K. Chauhan, Founder President of Amity University, for his continuous support and also thank other members of the AIARS (M&D) Group, Amity University, Noida, for their support.

References

1. C. Rathgeber, H. Schmit, P. Hennemann, S. Hiebler, Investigation of pinacene hexahydrate as phase change material for thermal energy storage around 45 °C. *Appl. Energy* **136**, 7–13 (2014)
2. P. Felix De Castro, D.G. Shchukin, New polyurethane/docosane microcapsules as phase-change materials for thermal energy storage. *Chem. Eur. J.* **21**(31), 11174–11179 (2015)
3. D.C. Hyun, N.S. Levinson, U. Jeong, Y. Xia, Emerging applications of phase-change materials (PCMs): teaching an old dog new tricks. *Angew. Chem. Int. Ed.* **53**(15), 3780–3795 (2014)
4. P.B. Salunkhe, P.S. Shembekar, A review on effect of phase change material encapsulation on the thermal performance of a system. *Renew. Sustain. Energy Rev.* **16**(8), 5603–5616 (2012)
5. R. Kandasamy, X.-Q. Wang, A.S. Mujumdar, Application of phase change materials in thermal management of electronics. *Appl. Therm. Eng.* **27**(17–18), 2822–2832 (2007)
6. G. Setoh, F. Tan, S. Fok, Experimental studies on the use of a phase change material for cooling mobile phones. *Int. Commun. Heat Mass Transf.* **37**(9), 1403–1410 (2010)
7. R. Baby, C. Balaji, Experimental investigations on phase change material based finned heat sinks for electronic equipment cooling. *Int. J. Heat Mass Transf.* **55**(5–6), 1642–1649 (2012)
8. M.M. Farid, A.M. Khudhair, S.A.K. Razack, S. Al-Hallaj, A review on phase change energy storage: materials and applications. *Energy Convers. Manag.* **45**(9–10), 1597–1615 (2004)

9. A. Shukla, D. Buddhi, R. Sawhney, Solar water heaters with phase change material thermal energy storage medium: a review. *Renew. Sustain. Energy Rev.* **13**(8), 2119–2125 (2009)
10. B-a Ying, Y-l Kwok, Y. Li, Q-y Zhu, C-y Yeung, Assessing the performance of textiles incorporating phase change materials. *Polym. Testing* **23**(5), 541–549 (2004)
11. M.A. Fazilati, A.A. Alemrajabi, Phase change material for enhancing solar water heater, an experimental approach. *Energy Convers. Manag.* **71**, 138–145 (2013)
12. W.-D. Steinmann, D. Laing, R. Tamme, Latent heat storage systems for solar thermal power plants and process heat applications. *J. Sol. Energy Eng.* **132**(2), 021003 (2010)
13. A. Castell, I. Martorell, M. Medrano, G. Pérez, L.F. Cabeza, Experimental study of using PCM in brick constructive solutions for passive cooling. *Energy Build.* **42**(4), 534–540 (2010)
14. F. Kuznik, J. Virgone, J.-J. Roux, Energetic efficiency of room wall containing PCM wallboard: a full-scale experimental investigation. *Energy Build.* **40**(2), 148–156 (2008)
15. B. Zalba, J.M. Marin, L.F. Cabeza, H. Mehling, Review on thermal energy storage with phase change: materials, heat transfer analysis and applications. *Appl. Therm. Eng.* **23**(3), 251–283 (2003)
16. A. Abhat, Low temperature latent heat thermal energy storage: heat storage materials. *Sol. Energy* **30**(4), 313–332 (1983)
17. B. Xu, P. Li, C. Chan, Application of phase change materials for thermal energy storage in concentrated solar thermal power plants: a review to recent developments. *Appl. Energy* **160**, 286–307 (2015)
18. L.F. Cabeza, J. Illa, J. Roca, F. Badia, H. Mehling, S. Hiebler, F. Ziegler, Immersion corrosion tests on metal-salt hydrate pairs used for latent heat storage in the 32 to 36 °C temperature range. *Mater. Corr.* **52**(2), 140–146 (2001)
19. B. Kamkari, H. Shokouhmand, Experimental investigation of phase change material melting in rectangular enclosures with horizontal partial fins. *Int. J. Heat Mass Transf.* **78**, 839–851 (2014)
20. X. Py, R. Olives, S. Mauran, Paraffin/porous-graphite-matrix composite as a high and constant power thermal storage material. *Int. J. Heat Mass Transf.* **44**(14), 2727–2737 (2001)
21. J. Fukai, Y. Hamada, Y. Morozumi, O. Miyatake, Improvement of thermal characteristics of latent heat thermal energy storage units using carbon-fiber brushes: experiments and modeling. *Int. J. Heat Mass Transf.* **46**(23), 4513–4525 (2003)
22. R. Siegel, Solidification of low conductivity material containing dispersed high conductivity particles. *Int. J. Heat Mass Transf.* **20**(10), 1087–1089 (1977)
23. S. Motahar, A.A. Alemrajabi, R. Khodabandeh, Enhanced thermal conductivity of n-octadecane containing carbon-based nanomaterials. *Heat Mass Transf.* **52**(8), 1621–1631 (2016)
24. M. Li, A nano-graphite/paraffin phase change material with high thermal conductivity. *Appl. Energy* **106**, 25–30 (2013)
25. S. Motahar, N. Nikkam, A.A. Alemrajabi, R. Khodabandeh, M.S. Toprak, M. Muhammed, Experimental investigation on thermal and rheological properties of n-octadecane with dispersed TiO₂ nanoparticles. *Int. Commun. Heat Mass Transfer* **59**, 68–74 (2014)
26. A. Yadav, B. Barman, A. Kardam, S.S. Narayanan, A. Verma, V. Jain, Thermal properties of nano-graphite-embedded magnesium chloride hexahydrate phase change composites. *Energy Environ.* **28**(7), 651–660 (2017)
27. C.H. Li, G. Peterson, Experimental investigation of temperature and volume fraction variations on the effective thermal conductivity of nanoparticle suspensions (nanofluids). *J. Appl. Phys.* **99**(8), 084314 (2006)
28. H.A. Mintsu, G. Roy, C.T. Nguyen, D. Doucet, New temperature dependent thermal conductivity data for water-based nanofluids. *Int. J. Therm. Sci.* **48**(2), 363–371 (2009)
29. A.A. Altohamy, M.A. Rabbo, R. Sakr, A.A. Attia, Effect of water based Al₂O₃ nanoparticle PCM on cool storage performance. *Appl. Therm. Eng.* **84**, 331–338 (2015)
30. T.-P. Teng, Thermal conductivity and phase-change properties of aqueous alumina nanofluid. *Energy Convers. Manag.* **67**, 369–375 (2013)
31. X. Li, Y. Zhou, H. Nian, X. Zhang, O. Dong, X. Ren, J. Zeng, C. Hai, Y. Shen, Advanced nanocomposite phase change material based on calcium chloride hexahydrate with aluminum oxide nanoparticles for thermal energy storage. *Energy Fuels* **31**(6), 6560–6567 (2017)

32. M. Nourani, N. Hamdami, J. Keramat, A. Moheb, M. Shahedi, Thermal behavior of paraffin-nano- Al_2O_3 stabilized by sodium stearoyl lactylate as a stable phase change material with high thermal conductivity. *Renew. Energy* **88**, 474–482 (2016)
33. C.J. Ho, J. Gao, Preparation and thermophysical properties of nanoparticle-in-paraffin emulsion as phase change material. *Int. Commun. Heat Mass Transfer* **36**(5), 467–470 (2009)
34. S. Wu, D. Zhu, X. Li, H. Li, J. Lei, Thermal energy storage behavior of Al_2O_3 - H_2O nanofluids. *Thermochim. Acta* **483**(1–2), 73–77 (2009)
35. C. Nguyen, G. Roy, N. Galanis, S. Suiro, Heat transfer enhancement by using Al_2O_3 -water nanofluid in a liquid cooling system for microprocessors. *WSEAS Trans. Heat Mass Transf.* **1**(3), 370 (2006)
36. S.S. Narayanan, A. Kardam, V. Kumar, N. Bhardwaj, D. Madhwal, P. Shukla, A. Kumar, A. Verma, V. Jain, Development of sunlight-driven eutectic phase change material nanocomposite for applications in solar water heating. *Resour. Eff. Technol.* **3**(3), 272–279 (2017)
37. A. Kardam, S.S. Narayanan, N. Bhardwaj, D. Madhwal, P. Shukla, A. Verma, V. Jain, Ultrafast thermal charging of inorganic nano-phase change material composites for solar thermal energy storage. *RSC Adv.* **5**(70), 56541–56548 (2015)
38. S. Wu, H. Wang, S. Xiao, D. Zhu, An investigation of melting/freezing characteristics of nanoparticle-enhanced phase change materials. *J. Therm. Anal. Calorim.* **110**(3), 1127–1131 (2011)

Chapter 4

Theoretical Analysis of Temperature-Dependent Electrical Parameters of Si Solar Cell Integrated with Carbon-Based Thermal Cooling Layer



Vivek Kumar, Hrishikesh Dhasmana, Apurv Yadav, Amit Kumar,
Abhishek Verma, P. K. Bhatnagar and Vinod Kumar Jain

Abstract The heating effect in solar panels under solar irradiation is a major problem. The elevated solar cell temperature causes a decrease in its efficiency. Therefore, the research community is driven towards enhancing the working efficiency of solar panel by thermal cooling techniques. In this direction, activated carbon-based cooling layer beneath solar cell has been proposed and experimental optimization has led to enhance working efficiency by reducing the working temperature of the device from 88 to 69.5 °C. This paper presents a theoretical investigation of experimentally observed temperature-dependent solar cell parameters, such as open-circuit voltage (V_{oc}), short-circuit current density (J_{sc}), fill factor (FF) and efficiency (η), of our previous study. The reverse saturation current density (J_0) is a critical diode parameter which ultimately determines the temperature-dependent performance of the solar cell. In this work, constant factor ‘ C ’ value of 51.43 mA-cm⁻²K⁻³ is obtained for the calculation of reverse saturation current density in the temperature range from 273 to 373 K, and accordingly, solar cell output parameters are calculated.

Keywords Thermal cooling layer · Si solar cell · Open circuit voltage · Reverse saturation current density

V. Kumar · H. Dhasmana (✉) · A. Kumar · A. Verma · V. K. Jain
Amity Institute for Advanced Research and Studies (Materials & Devices), Amity University,
Noida, Uttar Pradesh 201303, India
e-mail: hrishikeshd07@gmail.com

A. Yadav
Amity Institute of Renewable and Alternative Energy, Amity University, Noida, U.P., India

P. K. Bhatnagar
Department of Electronic Science, University of Delhi, South Campus, New Delhi, Delhi, India

© Springer Nature Singapore Pte Ltd. 2020
V. K. Jain et al. (eds.), *Advances in Solar Power Generation
and Energy Harvesting*, Springer Proceedings in Energy,
https://doi.org/10.1007/978-981-15-3635-9_4

4.1 Introduction

Solar cell is amongst the most popular optoelectronic device in the field of renewable energy. It directly converts solar radiation into electrical energy [1, 2]. But it has low conversion efficiency (13–20%) due to various optical losses, such as subwavelength loss, thermalization loss, voltage loss, reflection loss, incomplete absorption, metal contact shading loss and recombination losses [3]. The solar cell is an elemental block of the solar panels. During field applications of solar panels under ambient conditions, the temperature of the panel increases with rise of ambient temperature [3, 4]. At ambient temperature of 35–40 °C, the temperature of panel rises up to 70–75 °C, and in extreme summer conditions, the panel temperature may rise beyond 80 °C [4–6]. This increased cell temperature affects output parameters of solar cell like open-circuit voltage (V_{oc}), fill factor (FF) and efficiency (η) [6–8]. The power conversion efficiency of silicon (Si) solar cell decreases by 0.45–0.5% for each degree increase in temperature above 25 °C [8, 9]. Thus, the working efficiency of the device always decreases due to rise in cell temperature. In order to address this problem, cooling of the device is always desirable for enhancing working efficiency. Many researcher groups have used various techniques, such as heat pipe [10], micro-channel [11], thermoelectric [12], PV panel cooling using phase change material (PCM) [13], hybrid PV/thermal [14] and mist water [15]. In most of the cooling systems, panels and so devices are cooled by air and water-based active and passive approaches. Active approaches make cooling system complex and bulky, which requires high maintenance and increase system cost. Therefore, passive cooling systems for solar cell are preferred over active cooling systems, which make overall cooling system simple and cost-effective. In this direction, carbon-based porous thermal cooling layer beneath solar cell is used to enhance the working efficiency by decreasing the temperature of the device from 361 to 342 K [16]. The device temperature decreases from 342 to 332 K under AM 1.5 G spectrum and so respective enhancement in V_{oc} is reported from 0.56 to 0.58 V, which contributes in enhancing working efficiency of the device from 10.7 to 11.18% and negligible changes in short-circuit current density which is observed.

This paper presents a theoretical investigation on experimental results observed for enhancing device efficiency by carbon-based nano-porous thermal cooling layer [16]. The temperature-dependent output cell parameters of silicon solar cell can be helpful in understanding degradation in the device working efficiency during field applications. Herein, we have calculated temperature-dependent solar cell parameters, like open-circuit voltage (V_{oc}), fill factor (FF) and efficiency (η) at AM 1.5 spectra in the temperature range 273–373 K. The temperature-dependent parameters, such as reverse saturation current density (J_0) and energy bandgap of Si, have been calculated and evaluated its effect on the cell parameters such as V_{oc} , FF and η . In this study, we have assumed short-circuit current density as constant value in the temperature range.

4.2 Theory of Temperature-Dependent Solar Cell Parameters

When a solar cell is illuminated, only the photons having energy higher than the bandgap energy (E_g) of the semiconductor are absorbed and create electron–hole pairs [1, 2]. The cut-off wavelength of photons of energy useful for carrier generation depends on E_g , can be calculated by Eq. (4.1),

$$\lambda_g = \frac{1240}{E_g(\text{eV})}(\text{nm}) \quad (4.1)$$

The photogeneration of electron–hole pairs in the semiconductor depends on the initial photon flux (N_{ph}) and the absorption coefficient (α_λ) of incident light in the semiconductor [1, 2]. These photogenerated charge carriers are separated by built-in electric field developed in the p–n junction.

The temperature dependence of bandgap of semiconductors is discussed in various literatures [17, 18]. The bandgap energy of semiconductors tends to fall with increasing temperature due to an increase in the amplitude of atomic vibrations. This increases interatomic spacing, and therefore, the corresponding reduction in the bandgap of semiconductor at equilibrium is observed for a particular temperature [2]. Using Varshni relation, the temperature dependence of the bandgap in semiconductors can be expressed as

$$E_g(T) = E_g(0) - \frac{\alpha T^2}{(T + \beta)} \quad (4.2)$$

where $E_g(T)$ is the bandgap of the semiconductor at some temperature T , the value of $E_g(0)$ at $T \approx 0$ K and α and β are constants. The values of $E_g(0)$, α and β for the semiconductor materials Si are 1.1557 eV, $7.021 (\text{eV K}^{-1}) \times 10^{-4}$ and 1108 K, respectively [19].

The steady state of p–n junction diode under illumination can be described by the following equation

$$J = -J_{\text{ph}} + J_o(e^{qV/nKT} - 1) \quad (4.3)$$

where J is the current density, J_{ph} is the photogenerated current density, J_o is the reverse saturation current density (the details are given below), V is the terminal voltage, n is the ideality factor and K is the Boltzmann constant.

Reverse saturation current density (J_o) measures leakage (or recombination) current of minority carriers in the p–n junction under reverse biasing. This leakage current is the result of carrier recombination in near-neutral regions on either side of the junction. Therefore, J_o primarily controls the value of V_{oc} in the solar cells. Since, minority carriers are thermally generated charge carriers, therefore J_o is highly sensitive to temperature changes. Reverse saturation current density for a p–n junction

solar cell [2] can be expressed by Eq. (4.4)

$$J_o = q \left(\frac{D_n}{L_n N_A} + \frac{D_p}{L_p N_D} \right) n_i^2 \quad (4.4)$$

where n_i^2 is the intrinsic carrier density, N_A and N_D are densities of acceptor and donor atoms, L_n and L_p are diffusion lengths, D_n and D_p are diffusion coefficients of minority carriers in n and p regions, respectively. As from Eq. (4.4), J_o is strongly determined by the proportionality to $\sim n_i^2$ and n_i can be represented as Eq. (4.5)

$$n_i^2 = N_c N_v \exp\left(-\frac{E_g}{kT}\right) = 4 \cdot \left(\frac{2\pi kT}{h^2}\right)^3 m_e^{*3/2} m_h^{*3/2} \exp\left(-\frac{E_g}{kT}\right) \quad (4.5)$$

where N_c , N_v are effective density of states in the conduction band, valance band and m_e^* , m_h^* are effective mass of electron, hole, respectively.

The expression for J_o can be rewritten in terms of temperature and bandgap energy [20] by combining Eqs. (4.4) and (4.5) as Eq. (4.6)

$$J_o = C \cdot T^3 \cdot \exp\left(-\frac{E_g}{k \cdot T}\right) \quad (4.6)$$

In above Eq. (4.6), doping and the material parameters of solar cell are combined in this constant C [20]. Thus, important solar cell parameters for the model calculations are energy bandgap and temperature. On increasing temperature, material bandgap decreases, and this enhances reverse saturation current density.

The temperature-dependent parameters of Si solar cell are discussed in detail as given below:

4.2.1 Short-Circuit Current Density

The photogenerated current density, i.e. short-circuit current density (J_{sc}), of solar cell depends on the given solar spectral irradiance and is given by Eq. (4.7)

$$J_{sc} = q \int_{h\nu=E_g}^{\infty} \frac{dN_{ph}}{dh\nu} d(h\nu) \quad (4.7)$$

where N_{ph} is the flux of incident photons of suitable energy $h\nu$. To calculate J_{sc} at each temperature, the solar spectrum is integrated into the corresponding value of E_g given by Eq. (4.2).

The photogenerated charge electron-hole pairs are separated by built-in electric field in the near p-n junction region. The minority charge carrier diffusion takes

place according to the recombination current near the junction, because of which concentration gradient profile of charge carriers is developed. The collection of the respective charge carriers at the output terminal of the device depends upon the respective diffusion length L_n and L_p of electrons and holes, respectively. The short-circuit current density expression can be given by [2]:

$$J_{sc} = qG(L_n + L_p + W) \quad (4.8)$$

where G and W are generation rate of charge carriers and depletion region of the p-n junction diode. Since, this parameter shows negligible increase in its value with device temperature, therefore a constant J_{sc} is taken into account for this study. In a practical solar cell, the value of J_{sc} may be limited by reflection losses, ohmic losses (series and shunt resistance), shadowing losses (front metal coverage) and recombination losses.

4.2.2 Open-Circuit Voltage

The maximum voltage across output terminal of a solar cell represents open-circuit voltage, which can be derived from Eq. (4.3) at $J = 0$. So,

$$V_{oc} = \frac{KT}{q} \ln\left(\frac{J_{sc}}{J_o} + 1\right) \quad (4.9)$$

where $J_{sc} \approx J_{ph}$, The equation clearly shows dependency of V_{oc} on J_{sc} and J_o . For high V_{oc} , a low J_o is absolutely necessary.

4.2.3 Fill Factor

Fill factor of solar cell depends on maximum power output (P_{max}) per unit area of respective J - V curve, open-circuit voltage and short-circuit current density and can be expressed as:

$$FF = \frac{P_{max}}{V_{oc}J_{sc}} \quad (4.10)$$

According to Green [21], the temperature-dependent FF value of solar cell with better accuracy can be given by,

$$FF = \frac{V_{oc} - \ln(V_{oc} + 0.72)}{V_{oc} + 1} \quad (4.11)$$

where $V_{oc} = \frac{V_{oc}}{V_{th}}$ is defined as normalized open-circuit voltage and $V_{th} = kT/q$.

4.2.4 Efficiency

The efficiency of a solar cell can be determined as the maximum output power point (P_{\max}) with respect to incident power and can be expressed as:

$$\eta = \frac{P_{\max}}{P_{\text{in}}} \quad (4.12)$$

Substituting the value of P_{\max} from fill factor expression Eq. 4.10

$$\eta = \frac{V_{\text{oc}} J_{\text{oc}} \cdot \text{FF}}{P_{\text{in}}} \quad (4.13)$$

where P_{in} is the intensity of the incident radiation in the unit of W/m^2 .

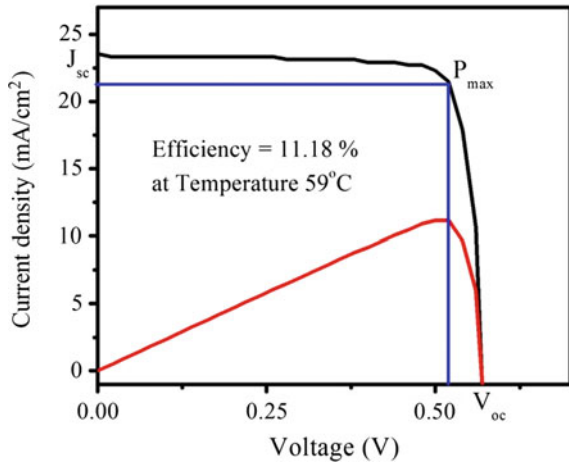
4.3 Experimental Section

The polycrystalline-Si solar cell of area 6 inch \times 6 inch was procured from IndoSolar Pvt. Ltd., India, with 17% efficiency at 25 °C temperature (under AM 1.5 G spectrum of incident irradiance of 1000 W/m^2). For the investigation purpose, this solar cell was cut into small pieces with dimensions of 3 cm \times 3.2 cm. The activated carbon disc was procured from Hindustan Unilever Limited, India, and cut into the pieces (3.2 \times 3 cm^2) for our experimental need and used as thermal cooling layer beneath Si solar cell in our experiments. We performed several experiments which included Si solar cell without cooling layer and with different thickness of cooling layer exposure to the incident radiation. We observed maximum cooling of Si solar cell with 14-mm-thick cooling layer under the incident radiation of intensity of 1000 W/m^2 . This cooling layer reduces the temperature of Si solar cell from 342 to 332 K, which is 10 °C lower as compared to without cooling layer. The J - V characteristics on both the cases (real-time conditions), i.e. Si solar cell without cooling layer and with cooling layer, were taken with the help of solar simulator and 2400-Keithley Electrometer.

4.4 Results and Discussion

The electrical evaluation of used Si solar cell under AM 1.5 G spectrum at 332 K was done by measuring J - V characteristics [16] and is shown in Fig. 4.1. The measured open-circuit voltage (V_{oc}), short-circuit current (J_{sc}) and efficiency are 0.58 V, 23.54 mA/cm^2 and 11.18%, respectively. The output cell parameters are used for evaluating temperature-sensitive reverse saturation current density. The reverse saturation current density (J_0) is calculated by using Eq. (4.9) and found to be 3.52 $\times 10^{-8}$ mA/cm^{-2} . Further, the value of constant C is calculated by using Eq. (4.6)

Fig. 4.1 $J-V$ curve of Si solar cell at temperature 332 K



and found to be $51.43 \text{ mA}\cdot\text{cm}^{-2}\text{K}^{-3}$. Based on this measured $J-V$ characteristics of solar cell device and assuming temperature insensitivity towards short-circuit density parameter, the solar cell temperature-dependent study is presented in the range of 273–373 K in this article.

The $J-V$ curve of used Si solar cell under AM 1.5 G spectrum (1000 W/m^2) at 332 and 342 K is measured [16], and output parameters are summarized in Table 4.1. The temperature-dependent behaviour of solar cell is primarily determined by reverse saturation current density. The reverse saturation current density depends exponentially on bandgap energy of solar cell material and its magnitude decrease with the increase of temperature. Herein, the temperature-dependent theoretical study is performed on the experimental results of nano-porous thermal cooling layer beneath the Si solar cell for enhancing working efficiency by decreasing the device temperature [16], in extreme summer condition. Figure 4.2 depicts bandgap and reverse saturation current density variation in temperature range of 273–372 K. The bandgap energy appears to be gradually decreasing with the temperature, while J_o shows almost constant value (1.01×10^{-7}) in the temperature range of 273–340 K. Afterwards its value exponentially shoots from 1.15×10^{-7} to 5.04×10^{-6} in the temperature range of 341–373 K. This sudden abrupt change can be attributed to J_o function-dependent

Table 4.1 Solar cell output parameters of without cooling layer and with cooling layer at 1000 W/m^2 incident irradiance

Parameters	1000 W/m ²	
	Without cooling layer	With cooling layer
Temperature (K)	342	332
V_{oc} (V)	0.56	0.58
I_{sc} (mA/cm ²)	23.33	23.54
FF (%)	81.89	82
Efficiency (%)	10.70	11.18

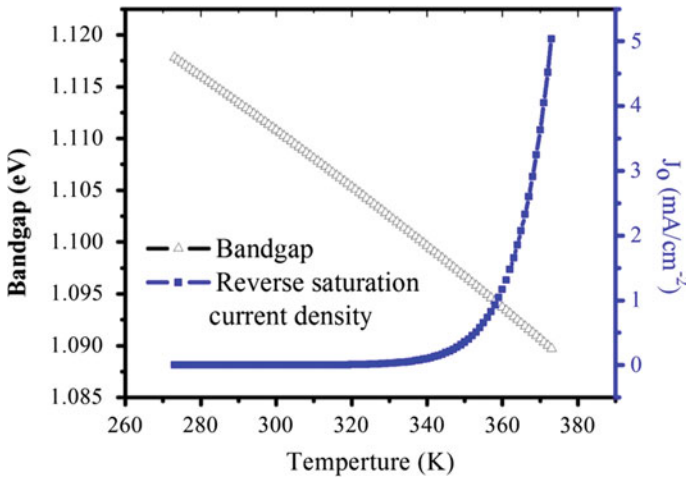


Fig. 4.2 Temperature versus bandgap and temperature versus current density of the device

behaviour on T^3 , while no significant change in J_0 is observed due to exponential factor $\exp(-E_g/KT)$.

The variation in the open-circuit voltage and fill factor of Si solar cells in temperature range of 273–373 K is shown in Fig. 4.3. The open-circuit voltage is evaluated by substituting J_{sc} and J_0 using Eq. (4.9). The V_{oc} decreases with increasing temperature and shows linear behaviour in the calculated temperature range. The fill factor decreases with increase in temperature, but it does not show linear behaviour. The J_0 value decrease with rise of temperature is slightly slower in the temperature range of

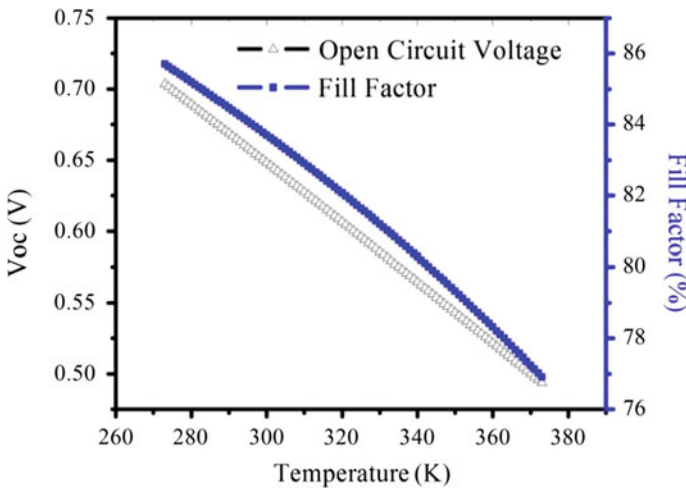
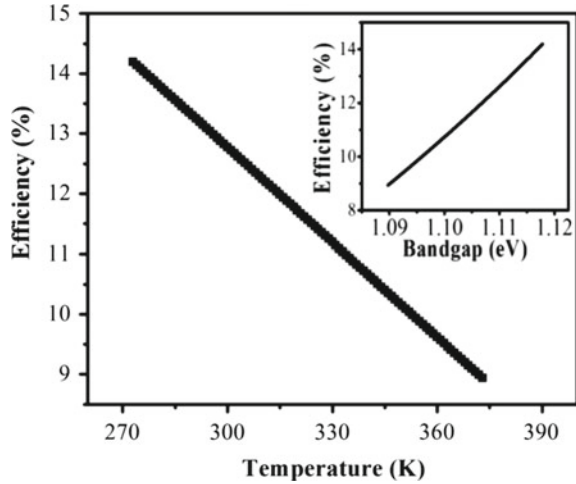


Fig. 4.3 Temperature vs open-circuit voltage and temperature versus fill factor of the device

Fig. 4.4 Temperature versus efficiency of the device and insert: bandgap versus efficiency of the device



273–342 K, and the rate of decrease in fill factor with temperature becomes slightly faster afterwards in the temperature range of 342–373 K. Thus, there exists a point of inflexion in fill factor vs temperature curve and after certain temperature (at point of inflexion) it decreases in faster manner.

The figure depicts temperature-dependent efficiency behaviour of Si solar cell based on substituting respective V_{oc} and fill factor values in the temperature range, constant J_{sc} and incident power density. Figure 4.4 clearly shows linear decrease in efficiency of solar cell with the increase in temperature. The inset figure depicts decrease in efficiency of solar cell due to decrease in bandgap energy. This bandgap energy is decreasing with the increase in temperature.

4.5 Conclusion

This work presents a theoretical study on experimental work performed for enhancing the working efficiency of Si solar cell by placing carbon-based nano-porous thermal cooling layer beneath the cell. The temperature dependent solar cell parameters such as open-circuit voltage, fill factor and so efficiency has been evaluated in the temperature range of 273–373 K. The study clearly demonstrates that the reverse saturation current density is a critical temperature-dependent parameter, which ultimately contributes in degrading the device efficiency with increase in temperature. This parameter changes significantly after 340 K with temperature and results into a faster decrease in fill factor of the device after this temperature. This study can be helpful in the optimization of Si solar cell performance during its field application.

References

1. S.M. Sze, *Physics of Semiconductor Devices* (Wiley & Sons, New York, 1981)
2. C. Hu, R.M. White, *Solar Cells* (Mc Graw-Hill, New York, 1983)
3. S. Armstrong, W.G. Hurley, A thermal model for photovoltaic panels under varying atmospheric conditions. *Appl. Therm. Eng.* **30**, 1488–1495 (2010)
4. G. Landis, R. Raffaele, D. Merritt, High temperature solar cell development, in *19th European Photovoltaic Science and Engineering Conference*, Paris, France, 7–11 June 2004
5. B.H. Khan, *Non-Conventional Energy Resources* (Tata McGraw-Hill Publishing Company Limited, New Delhi, 2004)
6. J.C.C. Fan, Theoretical temperature dependence of solar cell parameters. *Solar Cells* **17**, 309–315 (1986)
7. P. Singh, S.N. Singh, M. Lal, M. Husain, Temperature dependence of I-V characteristics and performance parameters of silicon solar cell. *Sol. Energy Mater. Sol. Cells* **92**, 1611–1616 (2008)
8. E. Skoplaki, J.A. Palyvos, On the temperature dependence of photovoltaic module electrical performance: a review of efficiency/power correlations. *Sol. Energy* **83**, 614–624 (2009)
9. M. Green, *Solar Cells: Operating Principles, Technology and System Applications*. The University of New South Wales, Sydney (1998)
10. G.H. Russell, Uniform surface temperature heat pipe and method of using the same. US Patent no. US4320246 (1982)
11. J. Barrau, A. Perona, A. Dolletb et al., Outdoor test of a hybrid jet impingement/micro-channel cooling device for densely packed concentrated photovoltaic cells. *Sol. Energy* **107**, 113–121 (2014)
12. A.N. Kane, V. Verma, Performance enhancement of building integrated photovoltaic module using thermoelectric cooling. *Int. J. Renew. Energy Res.* **3**(2), 320–324 (2013)
13. U. Stritih, Increasing the efficiency of PV panel with the use of PCM. *Renew. Energy* **97**, 671–679 (2016)
14. N. Amrizal, D. Chemisana, J.I. Rosell, Hybrid photovoltaic-thermal solar collectors dynamic modeling. *Appl. Energy* **101**, 797–807 (2013)
15. K.A. Moharram, M.S. Abd-Elhady, H.A. Kandil et al., Enhancing the performance of photovoltaic panels by water cooling. *Ain Shams Eng. J.* **4**(4), 869–877 (2013)
16. V. Kumar, A. Kumar, H. Dhasmana, A. Verma, P.K. Bhatnagar, V.K. Jain, Efficiency enhancement of silicon solar cells using highly porous thermal cooling layer. *Energy Environ.* 0958305X18781897 (2018)
17. Y.P. Varshni, Temperature dependence of the energy gap in semiconductors. *Physica* **34**, 149–154 (1967)
18. R. Passler, Parameter sets due to fittings of the temperature dependencies of fundamental band gaps in semiconductors. *Phys. Status Solidi (b)* **216**, 975–1007 (1999)
19. P. Singh, N.M. Ravindra, Temperature dependence of solar cell performance—an analysis. *Sol. Energy Mater. Sol. Cells* **101**, 36–45 (2012)
20. M.E. Nell, A.M. Barnett, The spectral p–n junction model for tandem solar-cell design. *IEEE Trans. Electron Dev.* **24**, 257–266 (1987)
21. M.A. Green, *Solar Cells* (Prentice-Hall, Englewood Cliffs, NJ, 1982)

Chapter 5

Studies of MWCNT-PEDOT:PSS Nanocomposites for Power Generation



Omita Nanda, Nidhi Gupta, Rakhi Grover and Kanchan Saxena

Abstract Poly (3, 4-ethylene dioxythiophene)-poly (styrene sulfonate) (PEDOT:PSS) is one of the most commonly explored conducting polymers for applications in numerous electronic devices. The polymer is environmentally stable and exhibits good conductivity. The evolution of carbon nanotubes (CNTs) as filler materials has contributed to the realization of CNT-polymer nanocomposites as next-generation materials. Here, we report a two-layer device based on multiwall carbon nanotubes (MWCNT) and pure PEDOT:PSS. Different devices were fabricated by varying the concentration of MWCNT to investigate the voltage generation. It was found that the voltage varied from 0.3 to 0.6 V on increasing the concentration of MWCNT from 5 to 20 wt%.

Keywords PEDOT:PSS · MWCNT · Nanocomposite · Thin Films · Power Generation

5.1 Introduction

Conductive polymers have gathered considerable attention due to their potential advantages of large-area, lightweight, low-cost and vacuum-free fabrication for different device applications [1, 2]. Among various conductive polymers, poly (3, 4-ethylene dioxythiophene)-poly (styrene sulfonate) (PEDOT:PSS) (Fig. 5.1) has been considered as a promising candidate due to its good transparency in the visible range and high thermal stability. It is extensively being used for various device applications such as solar cells, organic light-emitting diodes, electrochromic windows, thin-film transistors and sensors [3–5].

The conductivity is primarily dependent on the content of conductive PEDOT, whereas PSS acts as a doping agent and enables hydration. The conductivity of the pristine PEDOT:PSS film is approximately less than 1 Scm^{-1} . A lot of work has

O. Nanda (✉) · N. Gupta · R. Grover · K. Saxena
Amity Institute of Advanced Research and Studies (Material & Devices), Amity Institute of Renewable and Alternative Energy, Amity University, Noida, Uttar Pradesh 201303, India
e-mail: onanda@amity.edu

© Springer Nature Singapore Pte Ltd. 2020
V. K. Jain et al. (eds.), *Advances in Solar Power Generation and Energy Harvesting*, Springer Proceedings in Energy,
https://doi.org/10.1007/978-981-15-3635-9_5

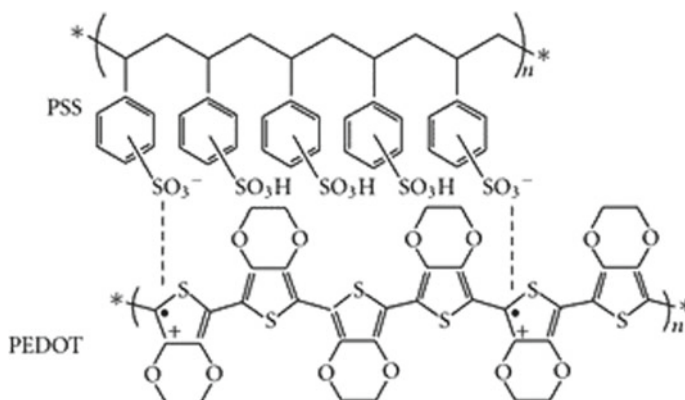


Fig. 5.1 Chemical structure of PEDOT:PSS

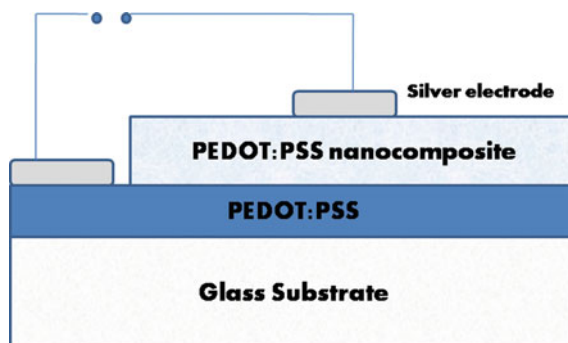
been reported to enhance the conductivity of PEDOT:PSS. Various solvents such as ethylene glycol (EG) [6], dimethyl sulfoxide (DMSO) [7] and diethylene glycol (DEG) [8] have been used for increasing the conductivity. Treating PEDOT:PSS with carboxylic inorganic acids [9] and aqueous salt solution [10] is some other reported methods for enhancing the conductivity. Besides, these methods conducting polymer nanocomposites formed by the incorporation of nanomaterials in polymer matrix possess some remarkable properties due to an interfacial third phase between nanostructure and polymer matrix. Carbon nanotubes (CNTs) are very fascinating and intensely studied nanostructures among the researchers due to their remarkable properties such as large contact area, high-dimensional aspect ratio and excellent electrical conductivity.

Previously, we had reported a bilayer device of SWCNT-PEDOT:PSS nanocomposite and PEDOT:PSS for humidity sensing and voltage generation across the two layers [11]. It was observed that the voltage increases when humidity was varied from 35% to 85%. In this paper, we report a bilayer device based on thin films of low conductivity PEDOT:PSS and its nanocomposite with multiwalled CNTs (MWCNT). Device with different concentrations of MWCNT was fabricated and investigated for voltage generation across the two layers. Surface morphology of MWCNT-PEDOT:PSS nanocomposite thin films was analyzed using scanning electron microscopy.

5.2 Experimental Details

Low conductivity grade poly(3,4-ethylene dioxythiophene)-poly(styrene sulfonate) PEDOT:PSS (2.8 wt% dispersion in water) and multiwall carbon nanotubes MWCNT were purchased from Sigma-Aldrich.

Fig. 5.2 Schematic diagram of two-layer device configuration



Functionalization of MWCNT was carried out by means of mild acid oxidation process [12]. The MWCNTs obtained after acid treatment were thoroughly washed several times with distilled water in order to remove any residual acid and were dried at 100° C in the oven for 3 h. Different nanocomposite solutions were prepared by mixing the varying wt% of MWCNT (5–20 wt%) in 1 ml of pure polymer. Glass substrates were used for sample preparation. Glass substrates were cleaned with soap solution and sonicated in distilled water. These substrates were then boiled in isopropyl alcohol and were dried in the oven. Pristine polymer was coated on the glass substrate and heated in oven for two hours. Now prepared solutions of polymer nanocomposites were coated on the polymer thin film by doctor blading method and dried in the oven for 2 h to get the bilayer device. Silver contacts were made on the surface of polymer and nanocomposite films for measurements as shown in Fig. 5.2. SEM analysis was carried to study the morphology of the nanocomposite films using Carl Zeiss EVO18 scanning electron microscope.

5.3 Results and Discussion

A two-layer device was fabricated with pristine PEDOT:PSS and its MWCNT-based nanocomposite. The concentration of MWCNT was varied between 5 and 20 wt% in low conductivity grade polymer. Figure 5.3 shows the SEM image of the 15 wt% low conductivity grade polymer nanocomposite.

The SEM micrograph clearly reveals that nanotubes are uniformly dispersed in huge quantities throughout the polymer matrix. The MWCNTs are forming a complex spider-web-like network consisting of randomly oriented nanotubes at the nanometer scale.

Polymer nanocomposite thin films with varying concentrations (0–20 wt%) of MWCNT in PEDOT:PSS were studied to determine the effect of doping level of MWCNT on electrical properties. Figure 5.4 gives the relationship between sheet resistance versus concentration of MWCNT in MWCNT-PEDOT:PSS nanocomposite. Pristine polymer thin film showed the sheet resistance of 40 K Ω . Sheet resistance

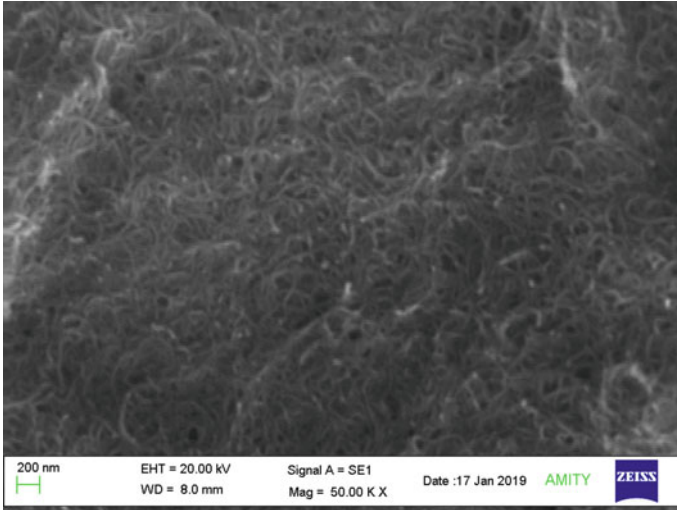


Fig. 5.3 SEM image of 15 wt% MWCNT-PEDOT:PSS

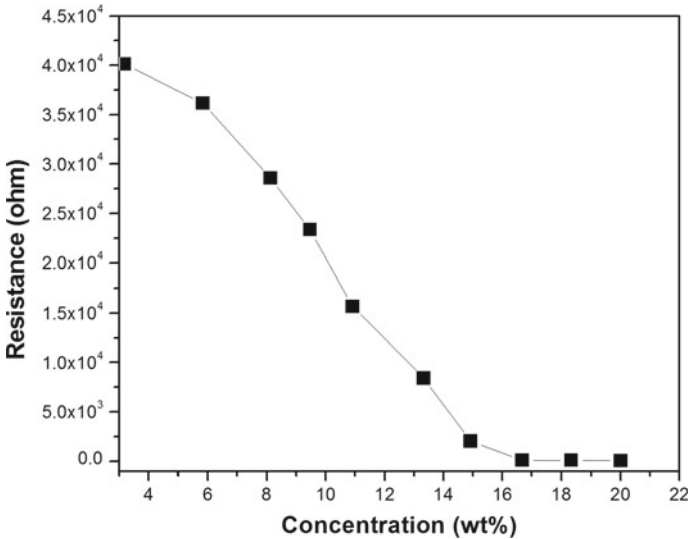


Fig. 5.4 Sheet resistance versus concentration graph for the MWCNT-PEDOT:PSS nanocomposite

of nanocomposite thin film was found to decrease from 40 KΩ to 68 Ω on increasing the concentration of MWCNT from 0 to 20 wt%. Similar trend has been reported with single-walled CNT in our previous report [11]. In both cases, a rapid decrease in sheet resistance was observed by varying the doping level of CNT from 0 to 15 wt%. Further increase in doping concentration does not affect the sheet resistance.

The enhancement in conductivity on increasing the doping concentration can be attributed to π - π interaction between MWCNT and thiophene rings in the backbone of PEDOT, which results in delocalization of electrons density from PEDOT to MWCNT and thus enhancement in conductivity [13]. However, further increase in doping concentration beyond 15 wt% does not affect the conductivity due to steric hindrance between ethylenedioxy groups of PEDOT. The MWCNT-PEDOT:PSS nanocomposite bilayer device as shown in Fig. 5.2 was also fabricated with different concentration of MWCNT. A voltage generation ranging from 0.3 to 0.6 V was measured for 5 to 20 wt% of CNT concentration. Figure 5.5 represents the voltage generated versus concentration of MWCNT in MWCNT-PEDOT:PSS nanocomposite film.

The work function of PEDOT:PSS is ~ 4.9 eV [14]. Yun et al. studied the effect of incorporation MWCNT in PEDOT:PSS. They reported that the incorporation of MWCNT in PEDOT:PSS results in decreased work function (from 4.87 to 4.66 eV) as the concentration of MWCNT (0.05–0.3 g/10 ml of PEDOT:PSS) is increased in PEDOT:PSS [14]. Therefore, the increase in voltage in device based on two layers of pure PEDOT:PSS and MWCNT-PEDOT:PSS is attributed to the difference in work function of the two electrodes. Consequently, an increasing trend was observed in voltage generation when the concentration of MWCNT was increased (up to 15 wt%) in polymer nanocomposite. A current of $0.5 \mu\text{A}$ was detected in the presence of humidity ($\sim 70\%$) between the two layers of the device. In our previous findings, we observed humidity-dependent power generation [11]. The conductivity of nanocomposite film was found to increase with humidity due to the presence of OH^- ions,

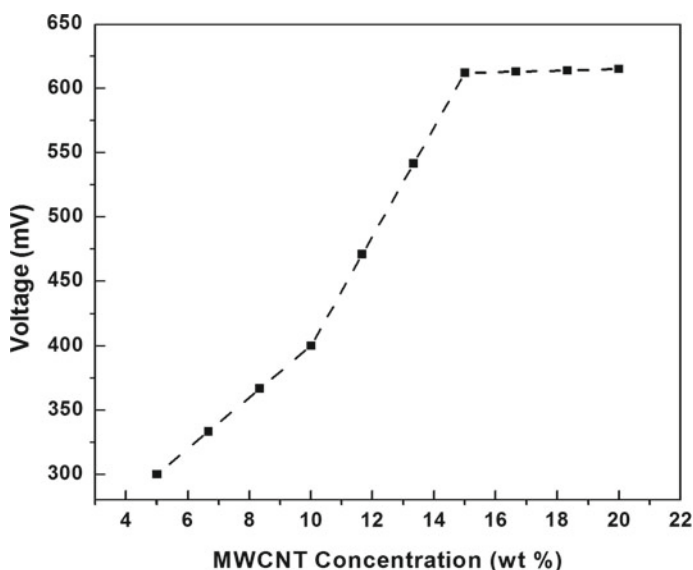


Fig. 5.5 Voltage versus MWCNT concentration in two-layer device of pristine PEDOT:PSS and MWCNT-PEDOT:PSS nanocomposite

which get attached to open bonds of CNT and thus making it depleted of holes. This creates a diode type junction between pristine PEDOT:PSS and the PEDOT:PSS nanocomposite, resulting in the generation of voltage and current across the bilayer device. In our present study, we have observed MWCNT concentration-dependent voltage generation. It was seen that a power of ~ 0.3 nWatt is generated by changing the concentration of MWCNT in the polymer nanocomposite layers.

5.4 Conclusion

MWCNT-PEDOT:PSS nanocomposite films with doping concentration (0–20 wt%) were successfully prepared. On doping of MWCNT, the conductivity of the nanocomposite films was enhanced up to 15 wt% doping. Beyond 15 wt% effect of doping of CNT reached to saturation due to increasing steric hindrance between CNTs and PEDOT. Bilayer device based on pristine polymer thin film and doped polymer nanocomposite were also fabricated and studied. A power of ~ 0.3 nWatt is generated in the bilayer device, which can be useful for humidity sensing and low power supply applications.

Acknowledgements The authors are thankful to Dr. Ashok K. Chauhan, Founder President, Amity University, and Dr. V. K. Jain, Distinguished Scientist and Professor, AIARS (M&D), Amity University, Noida, for his encouragements in carrying out this work.

References

1. M. Granström, M. Berggren, D. Pedo, O. Inganäs, M.R. Andersson, T. Hjertberg, O. Wennerstrom, Self organizing polymer films—a route to novel electronic devices based on conjugated polymers. *Supramol. Sci.* **4**, 27 (1997)
2. J. Bharathan, Y. Yang. Polymer electroluminescent devices processed by inkjet printing: I. polymer light-emitting logo. *Appl. Phys. Lett.* **72**, 2660 (1998)
3. C.J. Ko, Y.K. Lin, F.C. Chen, C.W. Chu, Modified buffer layers for polymer photovoltaic devices. *Appl. Phys. Lett.* **90**, 063509 (2007)
4. N. Gupta, R. Grover, D.S. Mehta, K. Saxena, Efficiency enhancement in blue organic light emitting diodes with a composite hole transport layer based on Poly(Ethylenedioxythiophene):Poly(Styrenesulfonate) doped with TiO_2 Nanoparticles. *Displays* **39**, 104 (2015)
5. A.A. Argun, A. Cirpan, J.R. Reynolds, The first truly all-polymer electrochromic devices. *Adv. Mater.* **15**, 1338 (2003)
6. SH Chang, CH Chiang, FS Kao, CL Tien, CG Wu, Unraveling the enhanced electrical conductivity of PEDOT: PSS thin films for ITO-free organic photovoltaics. *IEEE Photonics J.* **6**, 1 (2014)
7. T.R. Chou, S.H. Chen, Y.T. Chiang, Y.T. Lina, C.Y. Chao, Highly conductive PEDOT:PSS films by post treatment with Dimethyl Sulfoxide For ITO-free liquid crystal display. *J. Mater. Chem.* **C3**, 3760 (2015)

8. X. Crispin, F.L.E. Jakobsson, A. Crispin, P.C.M. Grim, P. Andersson, A. Volodin, C. van Haesendonck, M. Van der Auweraer, W.R. Salaneck, M. Berggren, The origin of the high conductivity of Poly (3,4-ethylenedioxythiophene) –Poly(styrenesulfonate) (PEDOT – PSS) plastic electrodes. *Chem. Mater.* 18, 4354 (2006)
9. Y. Xia, J. Ouyang, Significant conductivity enhancement of conductive 394 Poly(3,4-Ethylenedioxythiophene): Poly(Styrenesulfonate) films through a treatment with organic Carboxylic Acids and inorganic acids. *ACS Appl. Mater. Interf.* 2, 474 (2010)
10. Y. Xia, J. Ouyang, Salt-induced charge screening and significant conductivity enhancement of conducting Poly (3,4-Ethylenedioxythiophene): Poly(Styrenesulfonate). *Macromolecules* 42, 4141 (2009)
11. K. Saxena, O. Nanda, N. Gupta, A. Kumar, P. Kumar, V.K. Jain, Humidity dependent electrical response of bilayer device based on Poly (3,4-Ethylene Dioxythiophene)-Poly (Styrene Sulphonate) and Single Walled Carbon Nanotubes. *Synthetic Metals* 197, 86 (2014)
12. F. Avile's, J.V. Cauich-Rodr'iguez, L. Moo-Tah, A. May-Pat, R. Vargas-Coronado, Evaluation of Mild Acid Oxidation treatments for MWCNT functionalization. *Carbon* 47, 2970 (2009)
13. J. Li, JC Liu, C.J. Gao, On the mechanism of conductivity enhancement in PEDOT/PSS film doped with multi-walled Carbon nanotubes. *J Polym. Res.* 17, 713 (2010)
14. D.J. Yun, K. Hong, S. Kim, W. Yun, J. Jang, W. Kwon, C. Park, S. Rhee, Multiwall carbon nanotube and Poly(3,4-ethylenedioxythiophene):Polystyrene Sulfonate (PEDOT:PSS) composite films for transistor and inverter devices. *ACS Appl. Mater. Interfaces.* 3, 43 (2011)

Chapter 6

Improving Thermal Comfort in Helmet Using Phase Change Nanocomposite Material



Neeraj Gupta, Vivek Kumar, Hrishikesh Dhasmana, Abhishek Verma, Avshish Kumar, Prashant Shukla, Amit Kumar, S. K. Dhawan and Vinod Kumar Jain

Abstract During the summer season, the most common discomfort experienced by helmet wearer is heavy sweat, which occurs due to the excess heat formation, inside the helmet. During hot weather, helmet outer surface temperature can reach up to 50–60 °C. This heat is transferred from the helmet outer surface to inner surface, which cause discomfort to the wearer. In an effort to solve this problem, a novel helmet cooling system using PCM nanocomposite was designed to provide the thermal comfort. The PCM nanocomposite is prepared by dispersing carbon nanotubes (CNTs), acting as thermally conductive nanofiller in molten eicosane, an organic PCM. The PCM-CNT nanocomposite was packed into a lightweight, flexible material, i.e., aluminum foil, which also provides a thermal conducting path for better heat transfer. This novel cooling unit was placed between the wearer head and helmet which can provide the thermal comfort to the wearer head for 2 h. The heat inside the helmet is absorbed by the PCM pouch, through the process of conduction. The stored heat in the pouch had to be discharged for its reuse. The PCM helmet cooling system is simple and had the potential to be implemented as a practical solution to provide thermal comfort to helmet wearer.

Keywords Phase change material (PCM) · Nanoparticles · Thermal energy storage · Heat transfer · Thermal comfort

N. Gupta · V. Kumar · H. Dhasmana · A. Verma · A. Kumar · P. Shukla · A. Kumar (✉) · V. K. Jain

Amity Institute of Advanced Research and Studies (Materials and Devices), Amity University, Noida 201303, Uttar Pradesh, India
e-mail: kumar.amit9731@gmail.com

Present Address:

A. Kumar
School of Engineering and Technology, Central University of Haryana, Jant-Pali, Mahendergarh 123031, Haryana, India
e-mail: kumaramit@cuh.ac.in

S. K. Dhawan
Division of Materials Physics and Engineering, National Physical Laboratory, New Delhi, India

6.1 Introduction

Helmet is primary safety equipment for bike riders, workers in industrial and construction sites. The important function of the helmet is to protect the head against injuries and also to safeguard the eyes from sunlight and dust particles, fatal injuries. Generally, a helmet is composed of two principal protective components: a thin outer layer shell made of acrylonitrile butadiene styrene (ABS) plastic, fiberglass or Kevlar and a soft, thick, inner liner about one-inch thickness usually made of expanded polystyrene foam or polypropylene foam. The foam liner is very similar to that used in refrigerators as thermal insulation. The hard outer shell prevents puncture of the helmet by the sharp-pointed object and provides the framework to hold the inner liner. The inner foam liner is used to absorb the crush during an impact. The one-inch thickness of insulation liner lining the interior of the helmet restricts and virtually eliminates the heat exchange with the outside wall of the most effective part of the body. During the hot weather (sunny days) with no air stream, the helmet outer surface temperature can reach up to 50–60 °C [1]. The temperature inside the helmet increases by the heat gained from the outer environment (solar radiation) and heat generated from the head. This heat transfers by the process of conduction and temperature gradient across the helmet layer [2, 3]. This increased in temperature inside the helmet causes thermal discomfort to the wearer's head, this leads to the deadening of sense and inability to concentrate, which sometimes could also lead to hypothermia [4]. To overcome this problem, some practical solution has been implemented from time to time to provide the thermal comfort to the human body. The techniques which have already been implemented are the air-cooled system using air blower or vents [5]. Solar power-operated cooling system has also been investigated—the electricity generated from a solar cell was used to power a TE cooling module and a small fan so that cold air can be delivered into the helmet [6]. More recently, Buist and Streitwieser [7] used thermoelectric cooler (TEC), which uses a heat pump to dissipate the heat from the interior of the helmet to the surroundings. However, the TES system is unsafe to use as it has various dangling electrical wire connection from the helmet to the motorcycle battery for operation [8]. Moreover, it also requires direct current (DC) power supply for the operation of the thermoelectric cooler. The DC is provided to the system by the battery which is installed inside the helmet, which makes the system heavier, costlier and dangerous.

In the present study, a unique novel approach which eliminates the above requirement is a helmet cooling system by using PCM nanocomposite has been investigated. This PCM nanocomposite will absorb all the heat generated inside the helmet, at a relatively constant temperature and provide the thermal comfort to the wearer head, inside the helmet for 2 h.

6.2 Experimental Description

6.2.1 *Materials and Methods*

Eicosane, an inorganic salt hydrate PCM, was purchased from Alfa Aesar. Carbon nanotubes (CNT), with an average length and diameter of 1–10 μm and 20–50 nm, respectively, were procured from Reinste, Germany. All the materials were used directly as received without any further purification.

6.2.2 *Preparation PCM Nanocomposite*

The PCM nanocomposite (eicosane + CNT) was prepared by using the melt-mixing technique [9]. A typical procedure, solid pristine organic PCM (eicosane) was melted on a hot plate (IKA RCT basic). CNTs in the form of nanofillers were then added to molten PCM and mixed thoroughly, using a magnetic stirrer for 20 min to formulate a stable PCM nanocomposite [10]. Finally, the prepared PCM nanocomposite was ultrasonicated (Telesonic, Ultrasonics) for 15 min to obtain a homogeneous dispersion of the PCM nanocomposite.

6.2.3 *Selection of PCM*

The head is the most efficient and important part of the body, as it has the highest skin temperature and large constant—volume blood flow [11]. To achieve the thermal comfort of the head, it is necessary to choose the PCM which has the melting temperature close to the body temperature. Eicosane which has the melting temperature of 37 $^{\circ}\text{C}$, and thermal conductivity 0.15 W/mk is chosen. Eicosane, an organic PCM, belongs to the alkane group. It has relatively high-energy storage density, negligible supercooling degree and nonflammable. It is also relatively inexpensive and widely available in the market. However, a critical issue in this material is inherently its low thermal conductivity. To overcome the low thermal conductivity problem, a high thermal conductivity material CNT is added to the PCM matrix, as a favorable method to increase the thermal conductivity.

6.2.4 *Characterization Technique*

The morphology of CNT was observed using a Zeiss (EVO-18) scanning electron microscope (SEM). In addition, SEM images were used to examine the dispersion of nanomaterial in the PCM nanocomposite. Thin and flexible material is used for the

formation of the pouch. The thermal energy storage capability of the PCM nanocomposite was investigated by setting a conventional set up in solar irradiation. The effective thermal conductivity of solid PCM nanocomposite samples was measured using a Linseis transient hot bridge-thermal conductivity meter (THB6N43) at ambient temperature.

6.3 Result and Discussion

6.3.1 SEM Analysis

Figure 6.1 shows the SEM image of pristine PCM, CNT (nanomaterial) and PCM nanocomposite. It can be seen that the pristine PCM, i.e., eicosane, a solid material, is clearly visible in the microscopic image Fig. 6.1a. Figure 6.1b reveals the SEM image of CNT nanomaterial. The SEM image of the PCM-CNT nanocomposite is shown in Fig. 6.1c which shows that the CNT (nanomaterial) is uniformly distributed over the surface of the PCM without any agglomeration.

6.3.2 Thermal Conductivity

To study the effect of CNT in the pristine PCM for the enhancement of thermal conductivity, thermal conductivity measurements on the PCM nanocomposite was performed. The pristine PCM thermal conductivity was found to be 0.2 W/(mk). On addition of 0.2 wt% of CNT, the thermal conductivity of the PCM nanocomposite increased to 0.4 W/(mk). The enhancement in the thermal conductivity of PCM nanocomposite could be attributed to the presence of highly conductive CNT

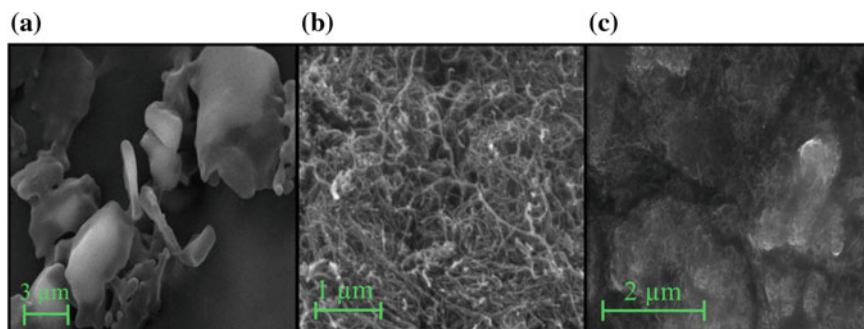


Fig. 6.1 SEM micrographs of **a** pristine PCM (eicosane), **b** CNT nanomaterial and **c** PCM-CNT nanocomposites

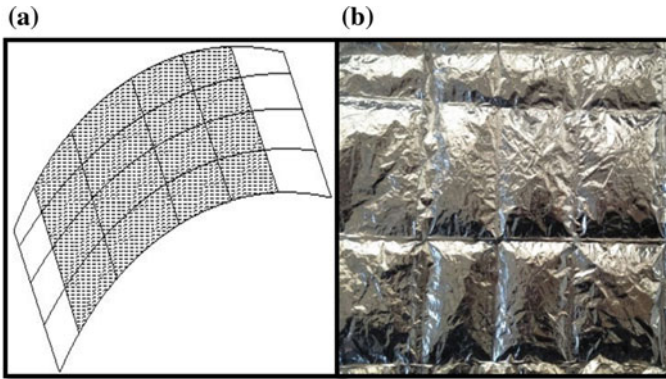


Fig. 6.2 a Formation of the grooves in the aluminum foil, b pouch containing PCM+nanomaterial

material and also its uniform dispersion in the PCM matrix. This enhancement in the thermal conductivity improves the efficiency of thermal energy storage system and also increases the effectiveness in the PCM.

6.3.3 PCM Pouch Design

A very thin, lightweight and flexible material is used for the formation of the pouch. Aluminum foil is used for this purpose as it has high thermal conductivity and also provides a good thermal path for better heat transfer. The pouch is divided into several grooves in which PCM nanocomposite is poured as shown in Fig. 6.2a. These grooves hold the PCM in the liquid state which provides the large heat transfer surface, flexibility to the pouch and also restricts the movement of the liquid inside the pouch which in turn prevents the agglomeration of PCM in the pouch. This PCM pouch as shown in Fig. 6.2b is placed between the wearer head and the helmet as shown in Fig. 6.3.

6.3.4 Experimental Setup for Studying the Heat Absorption and Storing Capability of PCM Nanocomposite-Based Helmet Under Direct Solar Irradiation

A real-time experiment was conducted to investigate the thermal energy storage capability of the modified PCM nanocomposite. The pictorial representation of this experiment is depicted in Fig. 6.4a. As shown in Fig. 6.4b, the two clamp stands, separated by a distance, were taken and used for the effective mounting of the helmet under investigation. To probe the temperatures, four different temperature sensors

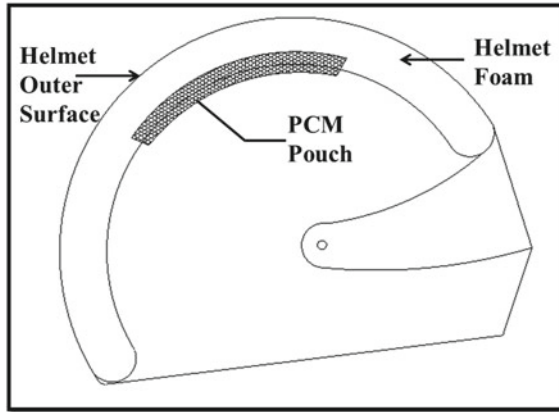


Fig. 6.3 Schematic diagram for PCM-cooled helmet

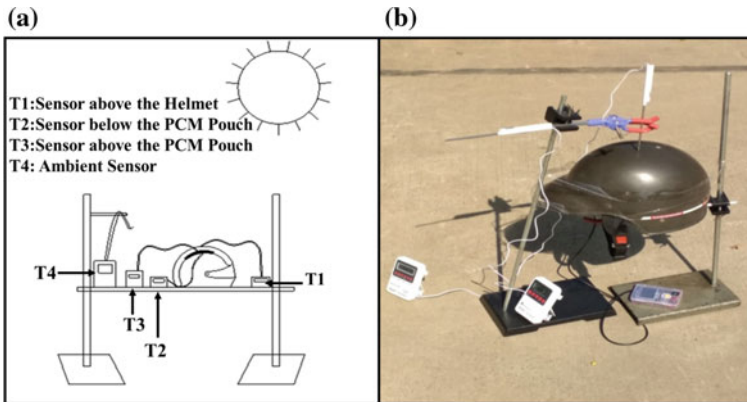


Fig. 6.4 Systematic setup of PCM-cooled helmet with real-time condition

(T1, T2, T3 and T4) were used at various places around the helmet. T1 was mounted on the top surface of the helmet to determine the temperature. T2 was placed just beneath the PCM pouch and T3 above the top layer of PCM pouch. Finally, T4 was placed well away from the helmet for sensing the ambient temperature.

6.3.5 Experimental Investigation

The experimental investigations were done in normal and PCM nanocomposite-based helmet under solar radiation. The results indicate that the temperature inside the helmet can be maintained within the thermal comfort level for a longer period

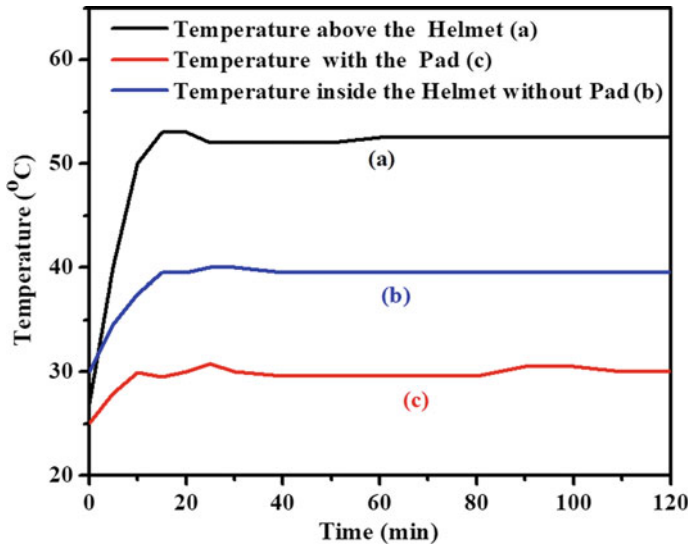


Fig. 6.5 Temperature versus time graph with and without PCM nanocomposite

of time with PCM nanocomposite. The heat is able to raise the temperature on the outer surface of the helmet from 27 to 68 °C, whereas the temperature inside the helmet contained PCM nanocomposite pouch is maintained at 38 °C and remains constant for 2 h as shown in Fig. 6.5. In comparison with the normal helmet, in which temperature inside, increased continuously and rose to 60 °C. After 2 h, the PCM will no longer stay in its natural state to store the excess heat. The temperature of the PCM will then increase continuously. The stored heat in the PCM pouch had to be discharged for its reuse.

6.4 Conclusions

In this paper, we prepared the eicosane + CNT nanocomposite. A novel helmet cooling system using PCM nanocomposite is developed to absorb and store the heat, to provide comfort, and thus, the wearer would not suffer from an uncomfortable and dangerous hot environment on the head. The results show that the pad is able to store the heat for 2 h without any external power supply. After that, the stored heat in the PCM nanocomposite needs to be discharged before it can be used again.

Acknowledgements We thank Dr. Ashok K Chauhan, Founder President of Amity University, for his continuous support and also thank another member of the AIARS (M&D) group, Amity University, Noida, for their support.

References

1. Y.-L. Hsu, C.-Y. Tai, T.-C. Chen, Improving thermal properties of industrial safety helmets. *Int. J. Ind. Ergon.* **26**(1), 109–117 (2000)
2. S.C. Fok, F.L. Tan, C.C. Sua, Experimental investigations on the cooling of a motorcycle helmet with phase change material. *Therm. Sci.* **15**(3) (2011)
3. S. Ghani, E.M.A.A. ElBialy, F. Bakochristou, S.M.A. Gamaledin, M.M. Rashwan, The effect of forced convection and PCM on helmets' thermal performance in hot and arid environments. *Appl. Therm. Eng.* **111**, 624–637 (2017)
4. S. Hachimi-Idrissi, L. Corne, G. Ebinger, Y. Michotte, L. Huyghens, Mild hypothermia induced by a helmet device: A clinical feasibility study. *Resuscitation* **51**(3), 275–281 (2001)
5. Technologies FAS, *Helmet conversions and air flow improvement*. www.fastraceproducts.com/fresh_air_systems_helmet_conversions.htm (2005)
6. C.S. Jwo, C.C. Chien, Solar power-operated cooling helmet. U.S. Patent 200701376845A1 (2007)
7. R.J. Buist, GDS the thermoelectrically cooled helmet. in *Proceedings of the seventeenth International Thermoelectric Conference*, Arlington, Texas, 6–18 (1988)
8. F. Tan, S. Fok, Cooling of helmet with phase change material. *Appl. Therm. Eng.* **26**(17–18), 2067–2072 (2006)
9. S.S. Narayanan, A. Kardam, V. Kumar, N. Bhardwaj, D. Madhwal, P. Shukla, A. Kumar, A. Verma, V. Jain, Development of sunlight-driven eutectic phase change material nanocomposite for applications in solar water heating. *Res. Eff. Technol.* **3**(3), 272–279 (2017)
10. A. Kardam, S.S. Narayanan, N. Bhardwaj, D. Madhwal, P. Shukla, A. Verma, V. Jain, Ultrafast thermal charging of inorganic nano-phase change material composites for solar thermal energy storage. *RSC Adv.* **5**(70), 56541–56548 (2015)
11. K.C. Paarsons, *Human thermal environments*. Taylor and Francis (1993)

Chapter 7

Impact of Light- and Elevated Temperature-Induced Degradation on PERC Solar Cells



Arati Joshi and Hasan Iqbal

Abstract Light-induced degradation (LID) is a major concern in solar cells as it can significantly affect the long-term stability, and this issue has been highly observed in modules of silicon substrates doped with boron during the Czochralski (Cz) process. In addition to LID, major performance degradation has been observed at elevated temperature conditions in case of Cz silicon solar cells as well as mass produced multi-crystalline PERC solar cells which use dielectrically passivated surfaces. Increasing the efficiency of solar cells has proved to be a challenging task, and hence further reduction in degradation should be controlled and mitigated for better performance of cells. This review paper helps to understand several causes behind LeTID like excess carrier concentration, temperature and its effects on PERC solar cells. Few possible mitigation techniques like fast firing and laser annealing which are practiced by Tier 1 Module manufacturers are discussed at the end.

Keywords LeTID · PERC · Light-induced degradation

7.1 Introduction

Levelized cost of electricity below 2 US dollar cents/kWh has already been achieved by Saudi Arabia [1]. This drives the pressure toward manufacturing high-efficiency solar modules with low cost. Passivated emitter and rear contact (PERC) solar cell production capacity can reach 160GW by 2022 as per “WilsonPro” an analyst firm from Taiwan. High production capacity keeps multi-crystalline (m-Si) PERC solar cells in focus [1]. According to “WilsonPro,” p-type multi-crystalline market share will diminish in 2022, PERC’s growth levels out, and it will capture nearly 70% of the total solar cell market. Thin-film, n-type PERT and HJT technologies will also

A. Joshi (✉) · H. Iqbal
Amity University Dubai, Dubai, United Arab Emirates
e-mail: aashika10@gmail.com

H. Iqbal
e-mail: hasan.iqbal1179@gmail.com

increase their market share through to 2022. Bifacial technology is predicted to grow 68 GW by 2022. PERC will play important contribution in production of bifacial solar cells.

After exposing solar cells to light if there is a loss in performance, then this is definitely not desirable. Light- and elevated temperature-induced degradation (LeTID) in solar cells and modules needs utmost attention and ways of enhancements in mass production processes to reduce its effects has gained momentum. Finding solutions in order to overcome the light- and elevated temperature-induced degradation (LeTID) is important because it can reduce solar cell efficiency by 10% or even higher [2]. On site, it can be more than a decade to stabilize and recover solar cell from LeTID, which can be even more than a 20-year warranty period of solar module [3]. The yield losses over time can be significant throughout the solar plant. The paper reviews causes behind LeTID and its effects on PERC solar cells. IEC 61215-2 is under draft version, wherein the LeTID test is proposed called as MQT23. As per survey by PVEL, 2018, the pie chart shown in Fig. 7.1 explains how significant is LeTID defect. Few mitigation techniques adopted by top module manufacturers are also discussed.

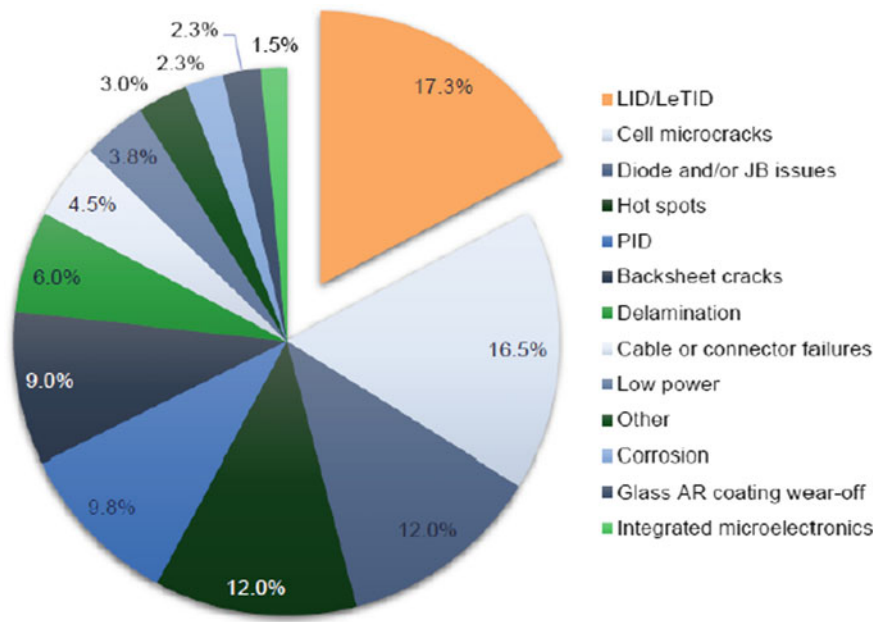


Fig. 7.1 Typical defects in solar cells Adapted from PVEL survey, 2018

7.2 Causes Behind LeTID

Two main defects in mono-Cz silicon that can lead to increased light-induced degradation (LID) are found to be boron–oxygen (BO) complex and iron–boron (FeB) pair dissociation [2]. During Cz process, quartz crucible can add oxygen impurities, 10^{18} cm^{-3} [2]. During initial exposure to sunlight, oxygen forms compound with boron and offers trap for free electrons [4]. In cast multi-crystalline silicon process, iron is introduced through crucible and coating by diffusion in crystal formation process [2]. Under illumination, iron–boron (FeB) pair dissociates and this acts as potential recombination centers degrading carrier lifetime [4].

Solar cells with dielectric rear passivation were observed for more degradation than Cz-Si than aluminum back surface field cells, especially at elevated temperatures [2]. Standard Al-BSF and mono-Si PERC cells are less affected. The cause for this degradation was not related to be the boron–oxygen complex and iron–boron pair [5]. LID when happens at elevated temperatures (above 50 °C), these can be referred to as light- and elevated temperature-induced degradation (LeTID). LID is sometimes called as carrier-induced degradation (CID) as the presence of light is not a prerequisite for LID [3], which means increase in excess carrier concentration can be through irradiation or even in dark by inducing current. LeTID cause in PERC solar cells is also linked to metallic impurities, and recently copper, nickel and cobalt contaminations are found to be related to this effect [6].

LeTID is not only responsible for degradation but also for regeneration. Different cell materials have different regeneration rates. It is possible to achieve a stabilized cell efficiency during cell or module production [3] (Table 7.1).

7.3 LeTID in PERC Solar Cells

7.3.1 *LeTID Relationship with Excess Carrier Concentration (High Injection) and Temperature*

Multi-crystalline PERC cells have shown 5% degradation at 75 °C [5]. Current injection controls minority carrier density, which is used to simulate equal excess carrier concentration for different operating conditions like short circuit, open circuit and maximum power point [5].

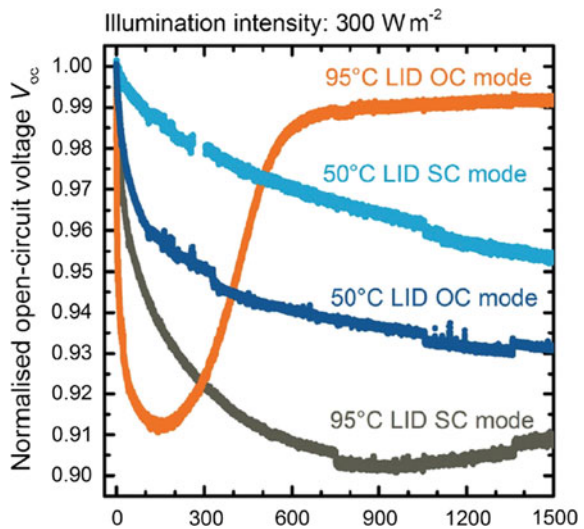
Figure 7.2 shows how PERC cells are affected by LeTID at different temperatures and operating modes.

Significant reduction in open-circuit voltage at 95 °C is seen after 150 h of light soaking (orange color curve). Open-circuit condition resembles high excess carrier concentration. The same cell in short-circuit mode degrades slowly which is lower excess carrier concentration (gray color curve). Regeneration starts after maximum degradation, and cell recovers after 1000 h of light soaking in open-circuit condition.

Table 7.1 Causes of LeTID

Cases of LeTID	Explanation
n-type and p-type multi-crystalline silicon solar cells	LeTID effect is seen [2]
Elevated temperature	LeTID effect is more pronounced [2]
Excess carrier concentration under illumination	LeTID effect is more pronounced [2]
Solar cells with dielectrically passivated rear side like PERC (hydrogen rich like silicon nitrides)	LeTID effect is seen more than aluminum back surface field (Al-BSF) [2]
High firing temperature for silver metallization contact formation at temperatures greater than 700 °C	LeTID is triggered [3]
Non-gettered samples	More sensitivity toward LeTID [7]
Wafers prone to fast firing degrades strongly than wafers at same peak temperatures following slower heating and cooling rates	Only fast firing can have strong LeTID [7]
Regions around crystal defects	LeTID effect is more pronounced [7]
	Dark annealing at high temperatures LeTID effect is more pronounced [7]
Degradation extent dependency on temperature as well as carrier injection	LeTID rate also depends upon level of carrier injection which again is dependent on operating condition modes like short circuit, open circuit and maximum power point as well as illumination intensity [7]
Performance loss in first 3 years after module installation	Around 7% [7] Metal-induced degradation LeTID effect is more pronounced [8]

Fig. 7.2 Degradation mechanisms in PERC cells. Adapted from Ref. [2]



But the degradation and regeneration time spans (more than 1000 h) are much longer [5].

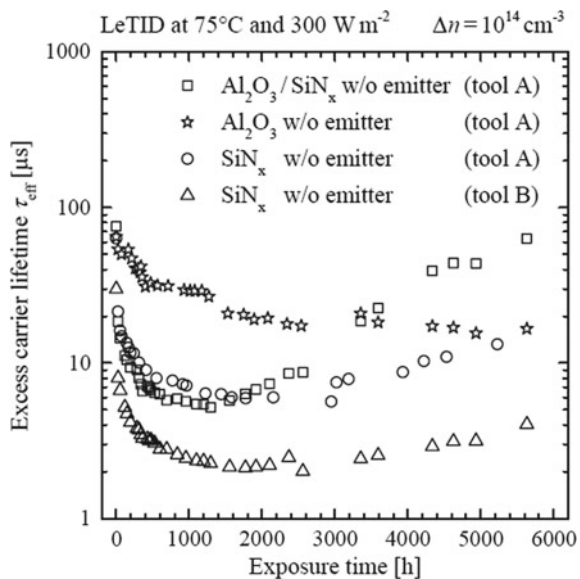
Solubility and diffusivity of impurity species can contribute to LeTID [9]. The defect rate increases with excess charge carrier concentration and temperature [2]. LeTID is suggested to be caused by defect complexes of mobile hydrogen and an intrinsic crystal defect [9]. Hydrogen can penetrate to wafer bulk and grain boundaries which are defects acting as sinks for hydrogen creating hydrogen denuded zones [9]. Cobalt a typical metal impurity acts as an interesting candidate involved in LeTID [9].

7.3.2 *LeTID Is More Severe in Dielectrically Passivated Rear Cells Than Aluminum Back Surface Field Cells [2]*

Degradation depends on passivation type but is independent of surface charge [10]. Cells are not prone to degradation if they are passivated after firing [10]. Post-light soaking bulk minority carrier lifetime degrades which indicates that LeTID has strong bulk component [11]. Degradation behavior is same for silicon nitride and aluminum oxide. Degradation is also observed in dark at elevated temperatures [10].

Figure 7.3 shows degradation and regeneration of cells with passivation layers without emitter. Block cast p-type multi-crystalline wafers are used with three types of passivation types, deposited using two different tools A (Al_2O_3 in single layer and

Fig. 7.3 Degradation and regeneration of cell with passivation layers. Adapted from Ref. [10]



$\text{Al}_2\text{O}_3/\text{SiN}_x$ multiple layers which acts as negative surface charge) and B (SiN_x acts as positive surface charge) [10].

Al_2O_3 is least degraded and even after 6000 h regeneration is not seen.

Reason for degradation can be that rear-side passivation contains hydrogen-rich dielectrics. After high peak firing process, this fraction of hydrogen is released and gets Si bulk to passivate states of defects [12]. But when light falls on cells, the weak hydrogen bonds get free leading degradation. After time passes, this free hydrogen starts to stabilize by re-bonding, passivating defects [12]. Base-passivated cells with dielectrics having surface charges and emitter which is diffused are prone to LeTID. Removing passivation layer during firing can help reduce the effect also showing LeTID's strong bulk relationship [2].

7.4 Possible LeTID Mitigation Techniques in PERC Solar Cells

7.4.1 *LeTID Peak Firing Techniques at Wafer Level*

Relationship with excess carrier concentration (high injection) and temperature

To form a better ohmic contact between front metal and silicon substrate, screen-printed solar cells undergo firing steps [3]. Open-circuit voltage degradation can be suppressed till 80% with an additional fast firing step carried out at lower temperature (650 °C rather than 900 °C) post-cell metallization [3].

But for silver front metallization, around 800 °C firing temperatures are required for proper top contact [3].

Figure 7.4 shows effects of additional fast firing step and carrier lifetime studied under work supported by Australian government through Australian Renewable Energy Agency (ARENA) [3]. Fire 1 was at standard temperature 740 °C, with belt speed = 4.5 m/min, average irradiance of 44.8 kW/m² and sample temperature of 140 °C. Second firing temperature was between 480 and 660 °C. Stability tests after light soaking at 70 °C for 380 h were carried out. Hotplate with a 938-nm fiber-coupled laser operating at 0.5 ms quasi-continuous wave mode at full width half maximum (FWHM) with frequency of 2 kHz in repetitive manner was used to perform accelerated degradation [3].

Extra firing suppressed degradation with best results at 660 °C, which is nearly 80% of open-circuit voltage loss which occurred in no extra step during firing [3]. Initial firing step still has room for optimization [3].

Firing profile changes like slower ramp rates, accelerated degradation combined with additional firing, controlling impurity distribution with aid of designing high-temperature steps and source material quality changes can be some of the strategies to deal with LeTID [13].

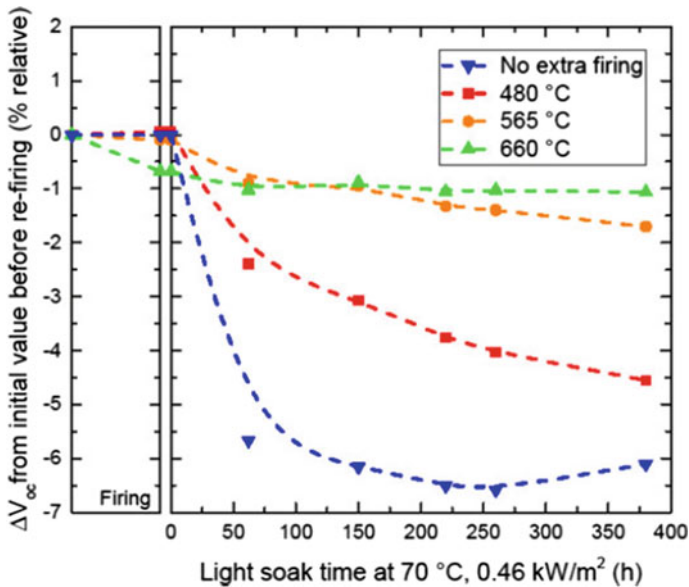


Fig. 7.4 Change in open-circuit voltage after second firing as a function of light soak. Adapted from Ref. [3]

7.4.2 *LeTID Annealing with High-Intensity Illumination to Accelerate Regeneration Process*

Carrier lifetime can be recovered by exposing cell to high-intensity illumination at elevated temperatures during annealing as it changes defect kinetics. Open-circuit voltage degradation can reduce up to 80% [3]; 30 mm × 30 mm PERC cells were taken as samples and treated for laser for a different time duration [3]. This treatment is given after metallization peak firing with standard temperatures of around 800 °C [3]. Under ARENA project with irradiance of 44.8 kW/m², at 200 °C laser stabilization was done. After 800 h of stability tests, it can be seen from Fig. 7.5 that open-circuit voltage of cell in dark for 8 min started to recover after 300 h, though this rate was very less than degradation rate [3]. Longer treated cells (15 min) showed less degradation around 80% less degradation compared to untreated cells [3]. Laser stabilized cells' maximum degradation was at 530 h of light soaking.

7.4.3 *Hanwha Q CELLS' Q.ANTUM Technology Suppresses LeTID to Less Than 1% [2]*

Hanwha Q CELLS has developed a technique called Q.ANTUM which suppresses LeTID in maximum power point (MPP) mode to as minimum as 1%. Figure 7.6

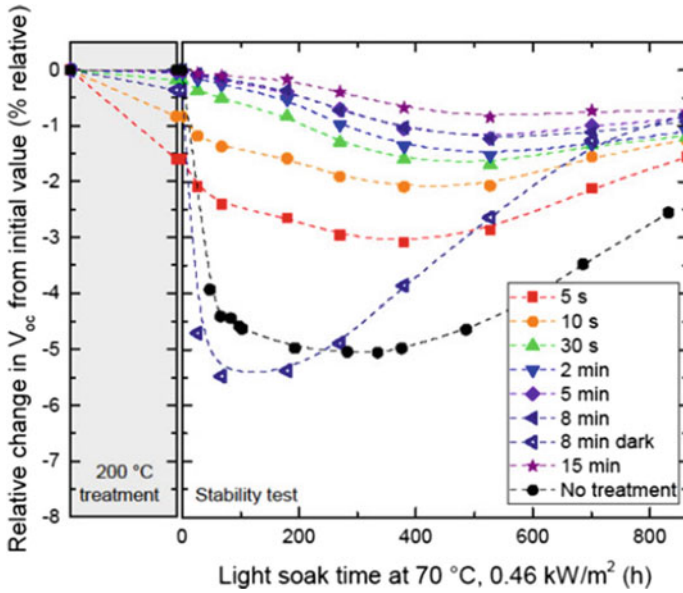


Fig. 7.5 Change in open-circuit voltage after second firing as a function of light soak. Adapted from Ref. [3]

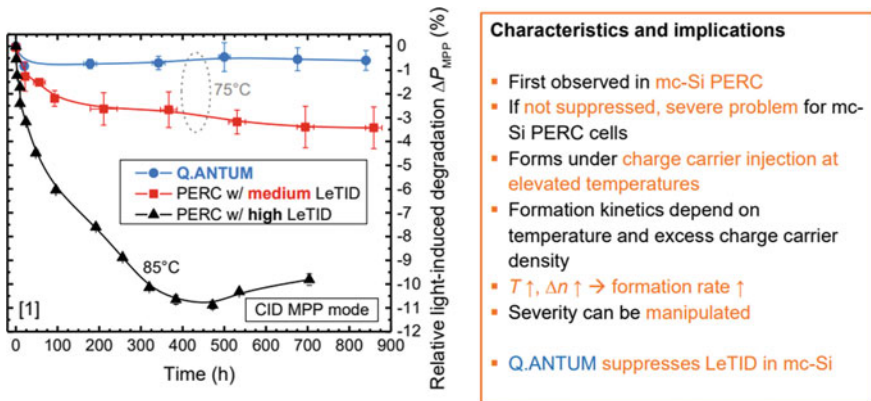


Fig. 7.6 Degradation in Q.ANTUM mc-Si is less. Adapted from Hanwa Q CELLS, Ref. [2]

shows how degradation percentage is less than 1% which is the blue line where cells are using Q.ANTUM technology.



Fig. 7.7 c.REG inline regeneration furnace. Figure adapted from reference. Figure is adapted from Ref. [13]

7.4.4 Industrially Available Inline Regeneration Tool (Centrotherm's c.REG Furnace) [14]

c.REG is an industrial-type regeneration treatment which suppresses LeTID. Finished PERC solar cell can undergo c.REG treatment to gain 6 to 15 mV of open-circuit voltage compared to untreated solar cells. This is a relative efficiency gain of up to 6.8% [14]. Regeneration takes place at intense illumination at a set temperature of 280 °C [14].

A number of runs, i.e., subsequent treatments at maximum light intensity 1 sun, are carried out with each run of approximately 40 s. The picture of commercial furnace is shown in Fig. 7.7.

7.4.5 Metal-Induced Degradation

Metal ions which gather at grain boundaries form stable defects wherein acting as recombination centers [8]. Reducing metal ion impurity from ingots is essential.

7.4.6 Summary

Table 7.2 shows how Fraunhofer CSP combines all issues and proposes solutions to mitigate LeTID.

Table 7.2 Summary of PERC degradation and possible solutions

Degradation mechanism	LID	HID	Passivation degradation
Cause	BO complex formation	High hydrogen concentration	DE passivation of dielectrics on undiffused surfaces
Reduction on cell level	Low oxygen–Si material High-resistivity Si material Stabilization process Ga doping		

7.5 Conclusion

Ways to increase the efficiency of solar cells by reduction in degradation is very important for better performance of cells. After understanding several causes behind LeTID like excess carrier concentration, temperature and its effects on PERC solar cells, possible mitigation techniques like fast firing and laser annealing which are practiced by Tier 1 Module manufacturers may be further optimized to prevent damage to contacts by over-firing. Without much hindrance in existing automated cell manufacturing line, new techniques or processes should seamlessly integrate into existing lines with minimal cost impact.

Future scope includes finding of root causes of LeTID near crystal defects as these regions are more prone to degradation and monitoring of long-term field stability under accelerated aging site conditions.

References

1. <https://www.pv-tech.org/news/acwa-power-wins-saudi-300mw-solar-project>
2. F. Fertg, F. Kersten, K. Petter, M. Bartzsch, F. Stenzel, A. Mette, B. Kloter, J.W. Muller, Light and elevated temperature induced degradation of multicrystalline silicon solar cells and modules. Hanwha Q CELLS GmbH, Bitterfeld-Wolfen, Germany
3. C.E. Chan, D.N. Payne, B.J. Hallam, M.D. Abbott, T.H. Fung, A.M. Wenham, B.S. Tjahjono, S.R. Wenham, Rapid stabilization of high-performance multicrystalline P-type Silicon PERC cells
4. <https://www.waaree.com/lid-and-letid>
5. F. Kersten, P. Engelharta, H.-C. Ploigta, A. Stekolnikova, T. Lindnera, F. Stenzela, M. Bartzscha, A. Szpetha, K. Pettera, J. Heitmannb, J.W. Mullera, A new mc-Si degradation effect called LeTID
6. <https://www.pv-tech.org/.../light-induced-degradation-newly-addressed-predicting-lon>
7. H.C. Sio, H. Wang, Q. Wang, C. Sun, W. Chen, H. jin, D. Macdonald, Light and elevated temperature induced degradation in p-type and n-type cast-grown multicrystalline and mono-like silicon, vol. 182, pp. 98–104, 1 August 2018
8. <https://www.jinkosolar.com/>

9. T. Niewelt, F. Schindler, W. Kwapil, R. Eberle, J. Schön, M.C. Schubert, Understanding the lightinduced degradation at elevated temperatures: Similarities between multicrystalline and floatzone p-type silicon. In: Progress Photovoltaics: Research Applications **26**, 533–542 (2018)
10. F. Kersten, J. Heitmannb, J.W. Müllera, Influence of Al₂O₃ and SiN_x passivation layers on LeTID
11. C. Vargas, K. Kim, G. Coletti, D. Payne, C. Chan, S. Wenham, Z. Hameiri, Carrier-induced degradation in multicrystalline silicon: dependence on the silicon nitride passivation layer and hydrogen released during firing
12. <https://www.pv-tech.org/guest-blog/is-letid-degradation-in-perc-cells-another-degradation-crisis-even-worse-th>
13. M.A. Jensen, A.E. Morishige, J. Hofstetter, D.B. Needleman, T. Buonassisi, Evolution of LeTID defects in p-Type multicrystalline silicon during degradation and regeneration
14. D. Bredemeier, D.C. Walter, T. Pernau, O. Romer, J. Schmidt, Production compatible remedy against LeTID in high-performance multicrystalline silicon solar cells

Chapter 8

Facile Fabrication of 1-D Hierarchical TiO₂ Nanomorphology and Its Application in Dye Sensitized Solar Cell



Asha Anish Madhavan

Abstract One-dimensional nanofibers fabricated by the process of electrospinning have found engaging applications in the field of dye sensitized solar cells (DSSC) due to semi-directed electron transport. Current research accounts for the development of conductive mats made from nanofibers, which is achieved through the electrospinning of TiO₂-ZnO composites and by using polyvinylpyrrolidone as a carrier solution. This fiber was annealed at 450 °C to attain a continuous network of conducting nanofibers. ZnO from the composite was selectively etched to fabricate high surface area anisotropic TiO₂ hierarchical fiber. Morphological and phase analysis conducted by scanning electron microscopy and X-ray diffraction studies confirmed the formation of anatase phase and 1-D hierarchical morphology of TiO₂. These structures were employed as photoanodes in DSSC, which had shown superior photoconversion efficiency.

Keywords TiO₂ · ZnO · Electrospinning · Hydrothermal · Photoanode · DSSC

8.1 Introduction

A wide variety of wide band gap semiconductor oxides like TiO₂, ZnO, SnO₂ and Nb₂O are used for the fabrication of working electrodes which is used in DSSC [1]. The most commonly used metal oxide is TiO₂ because of its versatile properties like thermal and chemical stability, inertness to the electrolyte, non-toxicity, cheap, abundance and many more. Light absorption and light scattering are considered as the main function of TiO₂ electrode. Also, photoanode plays a major role in charge transport and reduction in charge recombination. Based on the modification in the architectures, alteration in morphology, particle size, pore size and distribution and thickness of the thin film, maximum light harvesting can be obtained. In spite of the prospective advantages of DSSC, the net efficiencies are still lacking as compared to the conventional cells. One of the major drawbacks is the insufficient light harvesting

A. A. Madhavan (✉)

Amity University Dubai, Dubai International Academic City, Dubai, UAE
e-mail: amadhavan@amityuniversity.ae

© Springer Nature Singapore Pte Ltd. 2020

V. K. Jain et al. (eds.), *Advances in Solar Power Generation and Energy Harvesting*, Springer Proceedings in Energy, https://doi.org/10.1007/978-981-15-3635-9_8

caused by the TiO_2 [2–4]. Improved dye loading and better light scattering can also increase the performance of the DSSC. This can be achieved by replacing randomly oriented TiO_2 nanoparticle with highly organized mesoporous TiO_2 structures [5]. Mesoporous TiO_2 has a continuous network which can provide high surface area, better mass diffusion and hence can facilitate the reactions faster with higher reaction sites [6]. The mesoporous structure mainly depends on the fabrication process, and the pore size distribution can be manipulated by controlling the slurry of the TiO_2 [7, 8]. In an electrode charge, traps determine the electron transport and transfer dynamics. The primary disadvantage of the nanoparticle is the extraordinarily small diffusion coefficient. Nanoparticles with disordered arrangement can lead to lattice mismatches at the grain boundaries. It has been proved that a nanoparticulate matrix having a thickness of 10 nm had shown $\sim 10^6$ grain boundaries [10]. This will lead to an accumulation of electrons in the quasi-Fermi level, and hence, the recombination. In addition to this, another important parameter is the slow electron transport through the randomly oriented nanoparticle [11]. Many studies had been conducted to address this issue by replacing nanoparticle with one-dimensional morphologies like nanorods, nanowires, nanotubes, etc., in which the electron transport was proven to be in the direct conduction pathway [12–14]. It has also been proved that the interconnecting meso and micro prechannels in the titania film can result in the effective dye absorption, light scattering and effective percolation of the electrolyte [15]. Kislyuk et al., had proved that TiO_2 nanowires had shown almost four times larger dye absorption as compared to P-25 [16] as it act as a single crystal. However, crystalline structure depends on the fabrication process.

Many techniques have been developed to formulate one-dimensional nanostructured semiconductor oxides developed from template-based synthesis [17], template-free productions [18], by self-assembly method [19], electrospinning, [20] etc. Among these methods, electrospinning is a unique technique which offers the advantage of cost effectiveness, simple and can fabricate nanofibers with varied compositions and morphologies. Due to the semi-directed electron transport, one-dimensional nanofibers have been researched and exhibit a wide array of applications in DSSC [21]. Further, the presence of straight pores in these fibers facilitates the intercalation/de-intercalation of ions, [20, 22] etc. In spite of these appealing aspects, the electrospun TiO_2 materials have very low surface areas. It has already been proved that titanate route can be used for increasing the surface area. In this methodology, TiO_2 is chemically transformed into sodium/potassium titanate and then subsequently converted back to TiO_2 . This process is a two-step hydrothermal process which is time-consuming [23]. However, simple approaches for getting high surface area along with guided electron transport are lacking in the literature. In the present study, a two-step process of electrospinning of a bicomponent system (TiO_2 – ZnO) is followed by the selective etching of one component (ZnO) to fabricate high surface area anisotropic TiO_2 1-D hierarchical fiber. These nano-morphologies were employed as photoanodes, which had shown superior photoconversion efficiency.

8.2 Experimental

8.2.1 Chemicals and Reagents

The chemicals used in this study are acetone and methanol (Nice Chemicals), polyvinylpyrrolidone (PVP), titanium (IV) isopropoxide, glacial acetic acid, lithium iodide, iodine, acetonitrile and tertiary butyl pyridine, acetonitrile and teri-butanol (Sigma Aldrich), ruthenium (II) dye (N719) and butyl methyl imadizolium iodide, (Solaronix). The substrates used in this study were ITO conductive glass cleaned by sonicating with dilute soap solution, distilled water, acetone and then finally with methanol for 15 min each and then dried prior to use.

8.2.2 Fabrication of TiO₂-ZnO Fiber Composite

In the electrospinning process, polyvinylpyrrolidone (PVP) was used as the carrier polymer. Solution for the electrospinning process was prepared by dissolving PVP in a mixture of methanol and acetic acid. The PVP solution along with the addition of titanium isopropoxide and zinc acetate was made to completely dissolve at room temperature under constant stirring conditions. A syringe was then filled with the blend solution which was subsequently fed into an electrospinning setup (Zeonics System, India). The time and temperature for the electrospinning process were 6 h and 28 °C which was undertaken with a flow rate of 0.5 and an externally applied potential of 15 kV with a tip-to-collector space of 10 cm. The relative humidity was maintained constant of ~55%. The process of electrospinning was carried out with Al foils with dimensions 12 cm × 12 cm × 0.2 mm. After the electrospinning process, these samples were peeled off as a mat and annealed at 450 °C for 2 h to sublimate the binder PVP from the electrospun mats.

8.2.3 Fabrication of TiO₂ 1-D Hierarchical Fiber

About 300 mg of the TiO₂-ZnO (TZ), composite fibers were added to the acetic acid solution for the selective etching of ZnO. This solution was introduced into a hydrothermal setup consisting of a 100 mL Teflon-lined container followed by heating at 180 °C. After the annealing, the resultant product was filtered and washed thoroughly with deionized water and with methanol. The resultant anisotropic fibers obtained were then dried at 80 °C in an oven. Based on the components and morphology samples are designated as TiO₂-ZnO fiber (TZ) and 1-D hierarchical fiber (TH), respectively. These morphologies were used for the anode fabrication of DSSC (Fig. 8.1).

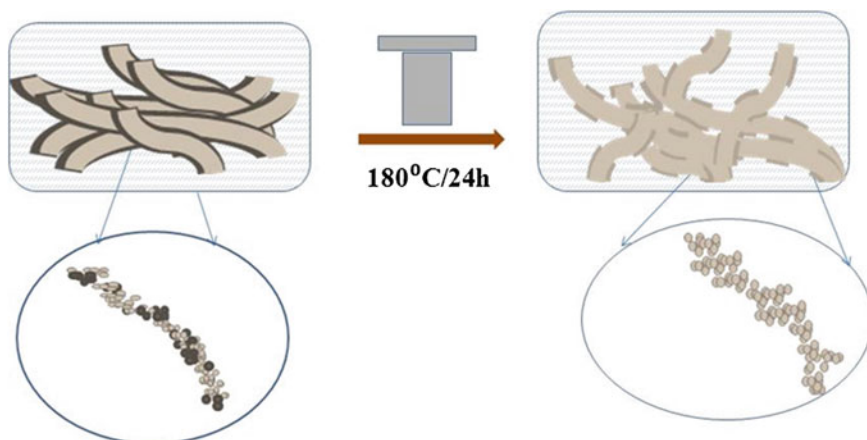


Fig. 8.1 Schematic representation of the synthesis of one-dimensional hierarchical TiO_2 fiber. Source Fig 8.1 is reproduced from author PhD thesis. Reference is https://shodhganga.inflibnet.ac.in/bitstream/10603/40981/15/15_synopsis.pdf

8.3 Results and Discussion

8.3.1 Morphological and Phase Analysis

Morphological and phase analysis of nanofibrous mats were analyzed using scanning electron microscopy (SEM) and X-ray diffraction methods. Figure 8.2a and b shows the SEM images of pre-annealed and post-annealed samples of TiO_2 -ZnO fiber (TZ), whereas Fig. 8.2c shows the image of TH fibers. It was clearly observed that the TZ fibers were smooth and continuous. The formation of hierarchical structures is induced by the acidic treatment resulting in the selective etching of ZnO by the in situ dissolution of ZnO as zinc acetate. The smooth surface of the nanofibers got distorted resulting in the formation of pits and humps when TZ is converted to TH

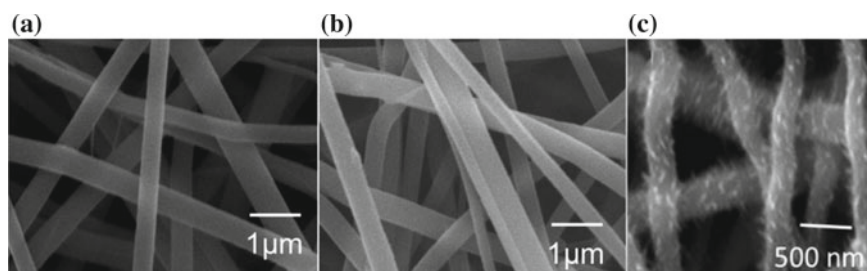
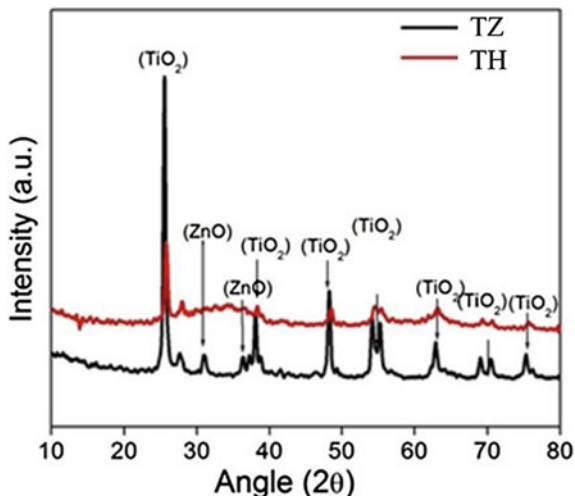


Fig. 8.2 Pre-annealed, post-annealed and 1-D hierarchical TiO_2 fibers displayed through SEM. Source Fig 8.2 is reproduced from author PhD thesis. Reference is https://shodhganga.inflibnet.ac.in/bitstream/10603/40981/15/15_synopsis.pdf

Fig. 8.3 XRD analysis of TZ and TH samples. *Source* Fig 8.3 is reproduced from author PhD thesis. Reference is https://shodhganga.inflibnet.ac.in/bitstream/10603/40981/15/15_synopsis.pdf



fiber. But it was observed that overall nanofiber morphology was maintained even after the etching process. Since the sublimation temperature of PVP is ~ 350 °C, no charring of the fibers occurred during the annealing at 450 °C.

Figure 8.3 shows the XRD pattern of the TZ fiber and TiO₂ hierarchical fiber. Distinct peaks of ZnO (wurtzite phase) and TiO₂ (anatase phase) could be seen in the spectrum (the TiO₂ and ZnO peaks are indexed in the XRD). No peaks of ZnO were observed in the hierarchical fiber which can be attributed to the complete removal of ZnO during the etching process. The surface area was calculated by the nitrogen adsorption–desorption experiments. The BET surface area of TZ fibers and TH fibers is ~ 53 and 78 m²/g, respectively. This growth in surface area can be accredited to the selective etching of ZnO from the composite. Thus, through this simple approach, the surface area of TiO₂ could be enhanced by $\sim 25\%$.

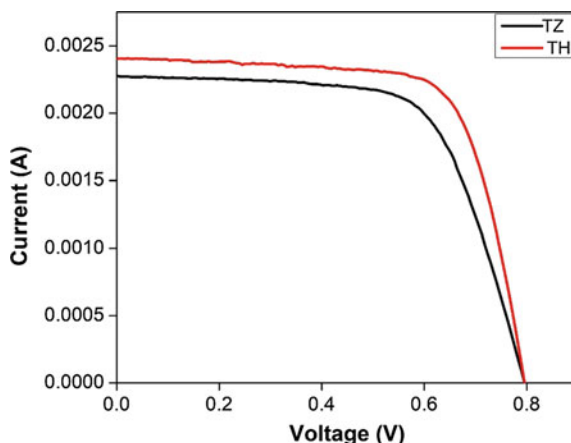
8.3.2 Photovoltaic Studies

The photocurrent (I_{sc}) and open-circuit voltage (V_{oc}) were measured using a Keithley 2400 digital source meter. The measurements were carried out under external applied potential for an exposed area of 0.2 cm². Figure 8.3 shows a typical photocurrent density–voltage (J - V) curves for TZF and TH fiber-based cells. The average performance characteristics obtained from the DSSC measurements are summarized in Table 8.1 and Fig. 8.4.

Current density of the cell depends on mainly dye loading and the efficiency of collecting the injected electrons from the metal oxide to the conducting glass substrate. From the above table, it can be observed that the performance of this TiO₂–ZnO system (TZ) was comparatively poor as compared to TiO₂ (TH) system. This

Table 8.1 Current, voltage and efficiency characteristics of DSSCs of TZ and TH samples

Samples	V_{oc} (V)	J_{sc} (mA/cm ²)	FF (%)	η (%)
TZ	0.78	11.05	67.5	5.99
TH	0.79	12.04	71.4	6.81

Fig. 8.4 Current–voltage (I–V) characteristics of DSSC using TZ and TH samples

can be attributed to the dye degradation by the formation of Zn^{+2} /dye complexes [24, 25]. This limits the charge carrier injection to the metal oxide and reduces the performance of the cells. As per the process explained in the above section, the bicomponent system is converted to the hierarchical structure by the selecting etching of one component, i.e., ZnO. Current density increases with an increase in porosity of the film, higher diffusion coefficient and higher concentration I_3^- . Recombination reactions are negative reactions which reduce the efficiency of the cell. These reactions are mainly occurring during the transport of electrons through the mesoporous TiO_2 layer. The increase in the current density of TH system could be attributed to the increased adsorption of dye due to the higher surface area. This was confirmed by the BET surface area. High surface area resulted in the binding of more dye molecules and hence better charge injection leading to high current density.

8.4 Conclusion

One-dimensional hierarchical shaped TZ fibers were fabricated from TiO_2 –ZnO composite by electrospinning followed by selective etching of ZnO using dilute acetic acid. As synthesized anisotropic TiO_2 morphology by the above mentioned method exhibited high surface areas as compared to the TiO_2 –ZnO composite. Morphological and phase analysis conducted by SEM and XRD studies conducted confirmed the anatase and hierarchical structure of one-dimensional morphology. Employing these

samples as photoanodes in DSSCs, a significant improvement in current density values was observed resulting in an efficiency of 6.8% for composites as compared with TZ with 6%.

Acknowledgements The author is grateful to Dr. Shanti Nair, Dean and Management of Amrita Center for Nano sciences, Kochi, for providing infrastructure and characterization facilities for conducting the research. Author would also like to thank Dr. A Sreekumaran Nair, MRF Limited, Chennai, for his guidance and other support for conducting the research.

References

1. R. Jose, V. Thavasi, S. Ramakrishna, Metal oxides for dye-sensitized solar cells. *J. Am. Ceram. Soc.* **92**, 289 (2009)
2. L. Schmidt-Mende, S.M. Zakeeruddin, M. Grätzel, Efficiency improvement in solid state-dye-sensitized photovoltaics with an amphiphilic Ruthenium -dye. *Appl. Phys. Lett.* **86**, 013504 (2005)
3. M.L. Schmidt, U. Bach, B.R. Humphry, T. Horiuchi, H. Miura, S. Ito, S. Uchida, M. Grätzel, Organic dye for highly efficient solid state DSSC. *Adv. Mater.* **17**, 813 (2005)
4. S. Kim, J.K. Lee, S.O. Kang, J. Ko, J.-H. Yum, S. Fantacci, F. De Angelis, D. Di Censo, M.K. Nazeeruddin, M. Grätzel, Molecular engineering of organic sensitizers for solar cell applications. *J. Am. Chem. Soc.* **128**, 16701 (2006)
5. M. Zukulová, A. Zukal, L. Kavan, M.K. Nazeeruddin, P. Liska, M. Grätzel, Organized mesoporous TiO₂ films exhibiting greatly enhanced performance in dye-sensitized solar cells. *Nano Lett.* **5**(9), 1789 (2005). <https://doi.org/10.1021/nl0514011>
6. H. Yu, S. Zhang, H. Zhao, G. Will, P. Liu, An efficient and low-cost TiO₂ compact layer for performance improvement of dye-sensitized solar cells. *Electrochim. Acta* **54**(4), 1319 (2009)
7. R.Y. Ogura, S. Nakane, M. Morooka, M. Orihashi, Y. Suzuki, K. Noda, High-performance dye-sensitized solar cell with a multiple dye system *Appl. Phys. Lett.* **94**, 073308 (2009)
8. L. Hu, S. Dai, J. Weng, S. Xiao, Y. Sui, Y. Huang, S. Chen, F. Kong, X. Pan, L. Liang, K. Wang, Microstructure design of Nanoporous TiO₂ Photoelectrodes for Dye-Sensitized solar cell modules. *J. Phys. Chem. B* **111**, 358 (2007)
9. T. Berger, T. Lana-Villarreal, D. Monllor-Satoca, R. Gomez, In situ infrared study of the adsorption and surface acid – base properties of the Anions of Dicarboxylic acids at Gold Single Crystal and thin-film electrodes. *J. Phys. Chem. C* **111**, 9936 (2007)
10. D.D. Vuong, D.T.N. Tram, P.Q. Pho, N.D. Chienin, *Phys. Eng. New Mater.* 95–102
11. Z. Miao, D. Xu, J. Ouyang, G. Guo, X. Zhao, Y. Tang, Electrochemically induced Sol – Gel preparation of single-crystalline TiO₂ nanowires. *Nano Lett.* **2**, 717 (2002)
12. J.J. Wu, C.J. Yu, *J. Phys. Chem. B* **108**, 3377 (2004)
13. Y.W. Jun, M.F. Casula, J.H. Sim, S.Y. Kim, J. Cheon, A.P. Alivisatos, Surfactant-assisted elimination of a high energy facet as a means of controlling the shapes of TiO₂ nanocrystals. *J. Am. Chem. Soc.* **125**, 15981 (2003)
14. D. Li, Y. Xia, One-dimensional nanostructures: synthesis, characterization, and applications. *Nano Lett.* **3**, 555 (2003)
15. J.B. Baxter, E.S. Aydil, Dye-sensitized solar cells based on semiconductor morphologies with ZnO nanowires *Sol. Energy Mater. Sol. Cells* **90**, 607 (2006)
16. V.V. Kislyuk, O.P. Dimitriev, Nanorods and nanotubes for solar cells. *J. Nanosci. Nanotechnol.* **8**, 131 (2008)
17. A. Kumar, R. Jose, K. Fujihara, J. Wang, S. Ramakrishna, Structural and optical properties of electrospun TiO₂ nanofibers. *Chem. Mater.* **19**, 6536 (2007)

18. A. Hagfeldt, G. Boschloo, L. Sun, L. Kloo, H. Pettersson, *Chem. Rev.* **110**, 6595 (2010)
19. G.S. Anjusree, A. Sreekumaran Nair, S.V. Nair, S. Vadukumpully, One-pot hydrothermal synthesis of TiO₂/graphene nanocomposites for enhanced visible photocatalysis and photovoltaics. *RSC Adv.* (2013)
20. K. Sujith, A.M. Asha, P. Anjali, N. Sivakumar, K.R.V. Subramanian, S.V. Nair, A. Balakrishnan, Fabrication of highly porous conducting PANI-C composite fiber mats via electrospinning. *Mater. Lett.* **67**, 376 (2012)
21. A.A. Madhavan, A. Mohandas, A. Licciulli, K.P. Sanosh, P. Praveen, R. Jayakumar, S.V. Nair, A.S. Nair, A. Balakrishnan, Electrospun continuous nanofibers based on a TiO₂-ZnO-graphene composite, *RSC Adv.* **3**, 25312 (2013)
22. M. Asha, K. Sujith, P. Anjali, N. Sivakumar, K.R.V. Subramanian, S.V. Nair, A. Balakrishnan, Effect of surface nanomorphology and interfacial galvanic coupling of PEDOT-Titanium counter electrodes on the stability of dye-sensitized solar cell. *J. Nanosci. Nanotechnol.* **12**, 1 (2012)
23. M. Chen, H. Qu, J. Zhu, Z. Luo, A. Khasanov, A.S. Kucknoor, N. Haldolaarachchige, D.P. Young, S. Wei, Z. Guo, *Polymer*, **53**, 4501 (2012)
24. S.Y. Huang, G. Schlichthorl, A.J. Nozik, M. Grätzel, A.J. Frank, Charge recombination in dye-sensitized nanocrystalline TiO₂ solar cells, *J. Phys. Chem. B*, **101**, 2576 (1997)
25. H.B. Choi, S.O.J.J. Ko, G.H. Gao, H.S. Kang, M.S. Kang, M.K. Nazeeruddin, M. Grätzel, *Angew. Chem*, **121**, 6052 (2009)

Chapter 9

Study and Analysis of Parameters Affecting Tubular Daylighting Device



Devendra Singh Bisht, Harry Garg, R. R. Shravana Kumar
and Vinod Karar

Abstract Renewable energy resources are clean and nearly everlasting in nature. These days, daylighting using renewable energy resources is of great concern. The sun is an extraordinary source of renewable energy and is an immense source of illuminance available during daytime. The available daylight can be harnessed using an appropriate daylighting device to illuminate dark spaces located at a distance from conventional fenestration. Innovative daylighting systems have the capability to deliver the desired level of illuminance in deep-plan and high-rise buildings. Tubular daylighting device (TDD), one of the passive daylighting devices, is discussed in this paper. This study reviews the effect of various parameters affecting the performance of TDD. Numerical simulation was done for 300-mm diameter transparent dome collector with two configurations of mirror light tube of a vertically projected length of 830 mm. Performance of TDD has been evaluated in the summer, equinox and the winter solstices for clear sky conditions. The results were analyzed for direct and diffuse components of sunlight separately.

Keywords Passive daylighting device · Tubular daylighting device · Collector · Mirror light pipe · Diffuser

The original version of this chapter was revised: The affiliation of the authors has been amended. The correction to this chapter is available at https://doi.org/10.1007/978-981-15-3635-9_21

D. S. Bisht · H. Garg (✉) · R. R. Shravana Kumar · V. Karar
CSIR-Central Scientific Instruments Organisation, Sector 30C, Chandigarh 160030, India

Academy of Scientific & Innovative Research (AcSIR), Ghaziabad 201002, India
e-mail: devendrab44@gmail.com

H. Garg
e-mail: harry.garg@csio.res.in

R. R. Shravana Kumar
e-mail: srr@csio.res.in

V. Karar
e-mail: vinodkarar@csio.res.in

9.1 Introduction

In recent years, daylighting using renewable energy resources is of great concern. The sun is an extraordinary source of renewable energy, and there are immense illumination levels available during daytime [1]. Sunlight can be used directly for lighting homes and other buildings. Windows and fenestrations are conventionally used for daylighting which is not so effective method considering sun's changing path across the sky. The sufficient amount of daylight for proper illumination can be harnessed using the suitable daylighting device [2, 3] to illuminate dark spaces located at a distance from conventional fenestration. Innovative daylighting systems have the capability to deliver the desired level of illumination in deep-plan and high-rise buildings where conventional fenestration fails to illuminate the target areas. Prismatic panels were introduced with the aim to redirect the incident sunlight to target areas. Use of laser cut panels [4–6] turns out to be an effective way to redirect incident sunlight for a particular range of angles. Lens systems and holographic systems have been developed for similar purposes [1]. Fresnel lens as daylight collecting device was also used [7]. But most of the systems fail to achieve the desired illuminance levels throughout the day. Many attempts have been made to tackle this problem. Some of these include the use of sun tracking systems [8, 9]. Fresnel lenses coupled to optical fiber cable were also proposed requiring a high degree of tracking precision. Some commercial systems such as the Himawari system and Parans collector work on these principles. These tracking-based daylighting devices are expensive and beyond the reach of the budget of most people [8, 9]. TDD, one of the passive daylighting devices, is discussed in the proposed work. Comprehensive analysis of the performance of the TDD with the transparent hemispherical dome as daylight collector has been evaluated for the summer solstice, equinox and the winter solstices for regional clear sky conditions.

9.2 Tubular Daylighting Device Overview

The TDD, also referred to as a light guiding device, brings daylight into interior spaces where traditional skylights and windows simply cannot reach. The performance of TDD mainly depends on the position of sun in the sky vault since the direct sunlight (or beam sunlight) entering the system mainly depends on the altitude of the sun. Figure 9.1 shows the parameters, i.e., altitude (α) and azimuth (ϕ) needed to locate the sun in the sky vault. Diffuse daylight entering the pipe also contributes to interior illumination and depends on the sky conditions which are broadly divided into 15 CIE standard sky luminance model. In general, on a broader scale we can classify the sky condition into three parts, namely clear, partly cloudy and overcast sky as shown in Fig. 9.2a–c, respectively.

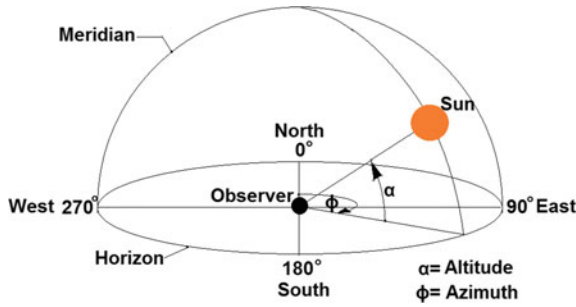


Fig. 9.1 Parameters locating the sun in the hemispherical sky vault

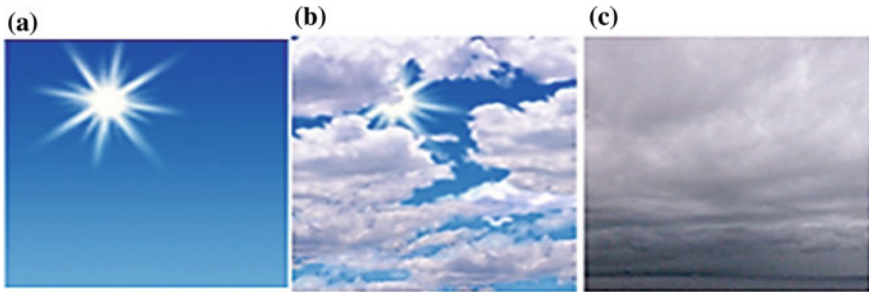


Fig. 9.2 Various sky conditions affecting the performance of TDD

Tubular light pipes have three components, viz. collector, transmitting tube and diffuser. The light collector collects sunlight from all directions and delivers light effectively throughout the day. The collector is generally made of polycarbonate, acrylic and glass. Transmitting tubes are hollow structures having a reflective lining on the internal surface. These hollowed designs with reflective sidewalls help to transmit the light deeper into spaces. Hollow light pipes are more susceptible to light losses, due to the metallic absorption on reflection. As shown in Fig. 9.3, ray 1 with high altitude does not hit the mirror light pipe surface and hence no losses are encountered. On the other hand, the ray with low altitude, i.e., ray 2, encounters multiple reflections while traveling the pipe length and therefore leads to light losses. Therefore, during the morning and evening hours when the altitude of the sun is low, light loss through pipe length rises.

For deep-plan buildings with greater depths, required level of illumination can be achieved using effective light transporting system. Some modifications in the geometry of the transmitting tube can lead to optimized light flux entry. Figure 9.4 shows the various shapes of the light transmitting tube affecting the direction and number

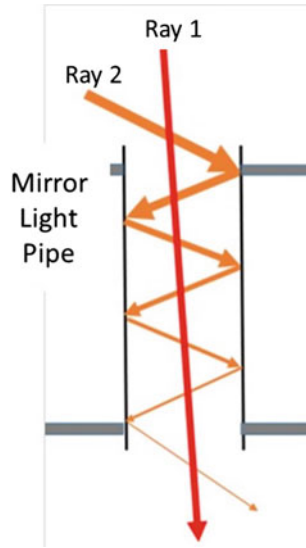


Fig. 9.3 Number of reflections in mirror light tube decreasing the luminous flux value of the incident light beam

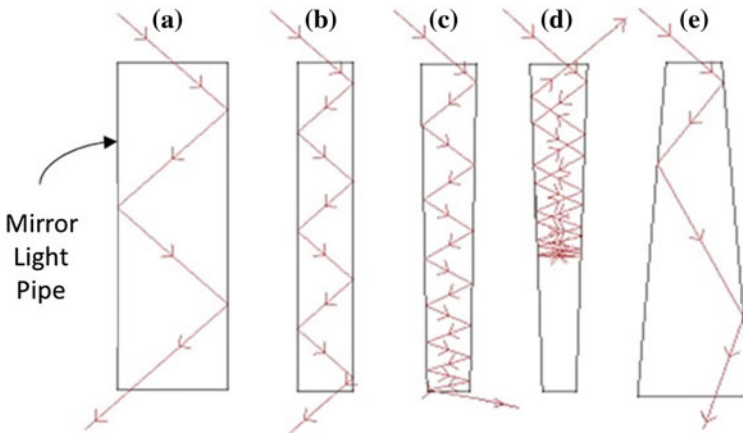


Fig. 9.4 Shape of the light transmitting tube affecting the direction and number of reflections incurred by the incident ray

of reflections incurred by the incident ray of sun at certain altitude. If we compare Fig. 9.4a, b, the reduction in diameter of the pipe leads to increased number of reflections. In Fig. 9.4c, the number of reflections further increases due to convergence of the pipe and the scenario worsens when the convergence of pipe is reached to such an extent that the light reflects back to the entering direction of incident ray as shown in Fig. 9.4d and the output section of pipe is devoid of any light flux. Figure 9.4e depicts

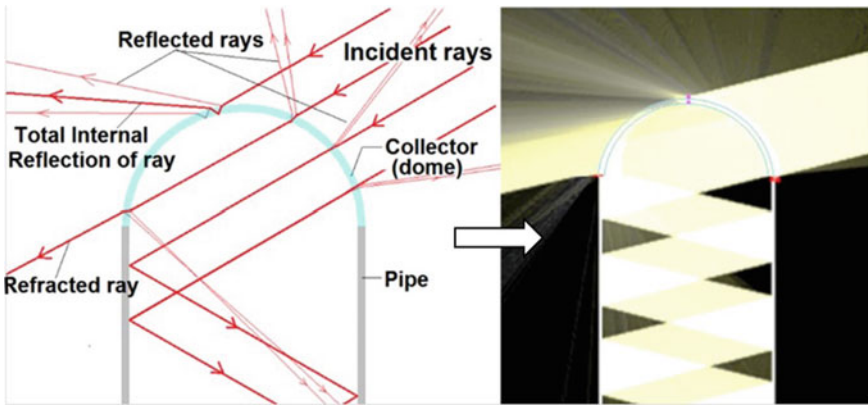


Fig. 9.5 Ray pattern in hemispherical transparent dome depicting geometrical optics light laws being followed at interfacing

the relatively optimized configuration of the mirror light pipe which is the diverging pipe length. This configuration leads to less number of reflections encountered, i.e., less light loss. The disadvantage of this configuration is that we have to have a large passage area in the ceiling of the room to be illuminated.

Figure 9.5 shows the collector, i.e., hemispherical transparent dome part of TDD. It also shows the ray pattern depicting geometrical optics light laws being followed at interfacing when exposed to beam sunlight. We can see the reflection losses (also called Fresnel losses), total internal reflection, refraction phenomenon occurring at the dome cover interfacing.

9.3 Numerical Analysis

To analyze intricate daylighting systems like light pipes, where a large number of reflections are expected, forward ray tracing method is preferred. Two cases of mirror light pipe configuration have been considered as shown in Fig. 9.6. Numerical simulation was done for the two configurations using TracePro (solar emulator utility). The results were considered for the region Chandigarh, India (30.7° N and 76.7° E), which lies in the northern hemisphere. Performance of the light pipe under both direct and diffuse sunlight has been analyzed separately. Regional clear sky conditions were assumed for all the numerical analysis. The values of the direct component of sunlight were taken as per the usual lighting levels observed in Chandigarh region. A number of illuminance values were observed using a light meter for different times of the day. The turbidity levels for the direct component of sunlight were set accordingly to match the observed values as close as possible.

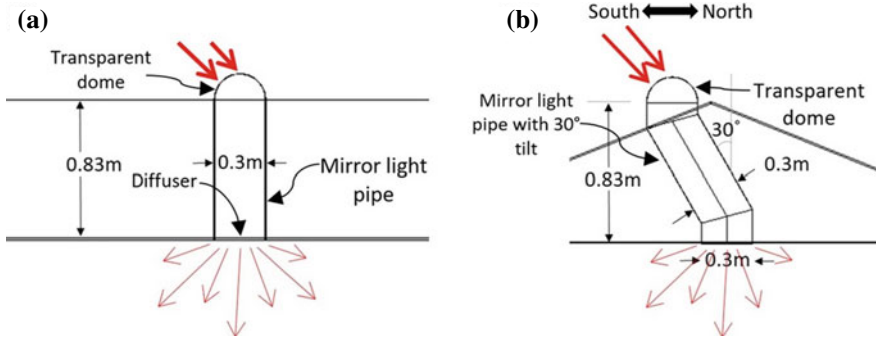


Fig. 9.6 Two configurations of the light pipe to be analyzed for daylight transmission efficiency with a transparent dome as a light collecting unit

Figure 9.7 shows the detailed diagram of the collector and room considered for numerical analysis. The vertically projected length of both the collector configurations is 0.83 m. The light pipe with slant configuration has a tilt of 30° from the vertical, lying on the plane containing north and south directions as shown in Fig. 9.7b. The value of reflectivity of different walls of room taken during the simulation is shown in the bottom left corner of Fig. 9.7. In lighting analysis of light pipe systems, reflectivity is a highly sensitive parameter. A small difference in the values leads to

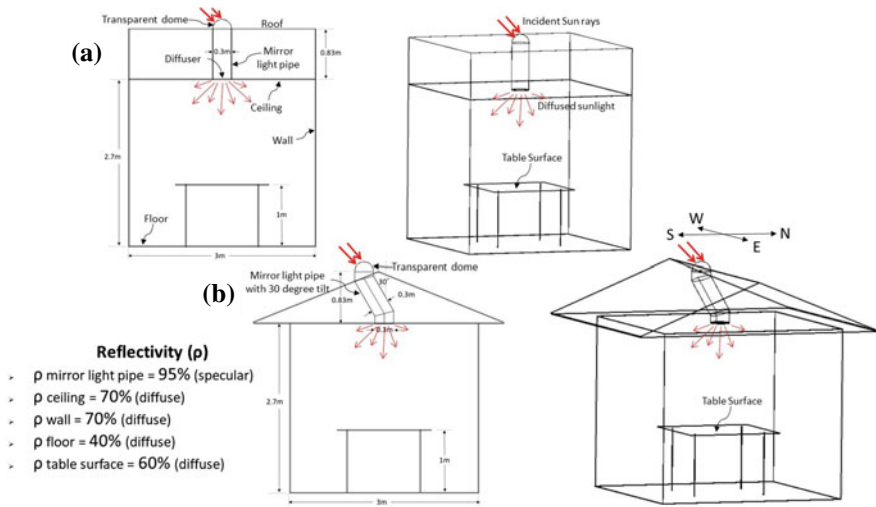


Fig. 9.7 Two configurations of light pipe installed on the roof of 3 m × 3 m × 2.7 m room with corresponding wall surface reflectivity

a large difference in the lighting values on the target plane. The surface reflectivity as 95% was considered for the mirror light pipe. After traveling light pipe length, as the light passes through the diffuser, there is a substantial loss in the lighting value of incident light. The function of the diffuser is to control and distribute the light entering the indoor spaces. The diffuser used for the analysis is Luminit (80° LSD). Figure 9.8 shows the light transmittance through diffuser for the light beam incident at 30°. Table 9.1 shows the light absorption value at a different incidence angle for the diffuser. It is always desirable to have an incidence angle as small as possible with the normal to the diffuser surface. Lesser the incidence angle, more will be the efficiency of the diffuser, i.e., lesser lighting losses.

Fig. 9.8 Light transmittance through diffuser for light beam incident at 30°

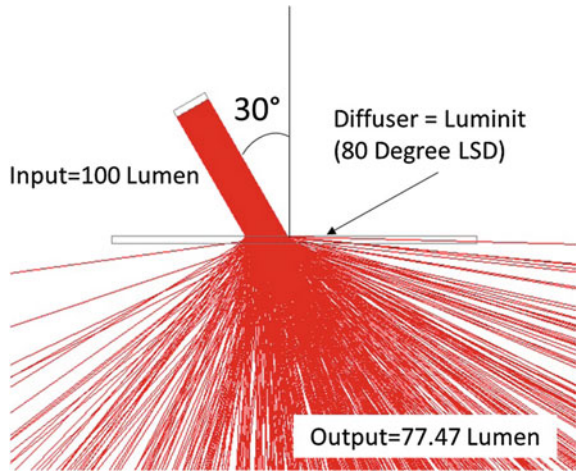


Table 9.1 Light absorption value at a different incidence angle for Luminit (80 degree LSD) diffuser

Incidence angle or zenith (°)	Absorption (%)
0	5.0767
10	6.4228
20	14.4652
30	22.5295
40	43.9477
50	52.8693
60	49.2598
70	50.2150

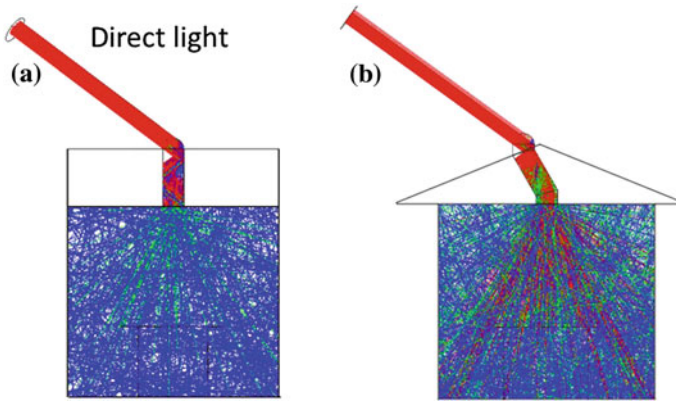


Fig. 9.9 Two configurations i.e. (a) vertical light pipe and (b) slant light pipe with 30° tilt simulated for direct light

9.3.1 Direct Light Analysis

Two configurations as shown in Fig. 9.9 were simulated for direct component of incident sunlight. Tables 9.2, 9.3 and 9.4 describe the direct light analysis at different sections of vertical mirror light pipe configuration on 21 June, 23 September and 21 December, respectively. Similarly, Tables 9.5, 9.6 and 9.7 describe the direct light analysis at different sections of tilt mirror light pipe configuration on 21 June, 23 September and 21 December, respectively. Figures 9.10 and 9.11 depict the graphical representation of lighting value obtained using numerical analysis.

From the graphical representation, it can be easily interpreted that the tilt pipe configuration imparts controlled lighting during summer solstice while giving enhanced lighting levels during the winter solstice. Performance during equinox is almost similar. Low lighting levels during morning and evening hours are a problem in both the configurations.

Figures 9.12 and 9.13 depict the comparison of Polar Iso-Candela curves of incident light at the diffuser entry section of vertical and tilt light pipe configuration, respectively, on 21 June for a different altitude (θ) of the sun. Figure 9.14 shows the ray pattern in tilt and straight light pipe configuration for a particular altitude. In the tilted pipe configuration, we can see the majority of incident direct light is making less incidence angle with the diffuser surface and simultaneously has less number of reflections too, i.e., enhanced performance during the winter sun's trajectory. In case of vertical light pipe, both the number of reflections and the incidence angle with the normal to diffuser surface are high for low-altitude sun. It is quite evident from the Polar Iso-Candela curves too which depicts the angularity (zenith angle) of the

Table 9.2 Direct light analysis at different sections of vertical mirror light pipe configuration on 21 June

Time	Altitude (°)	Azimuth (°)	Direct normal illuminance (lux)	Luminous flux incident on dome (lumen)	Luminous flux entering diffuser (lumen)	Luminous flux exiting diffuser (lumen)	Avg. illuminance on table (lux)
6 AM	6.9	66.8	5969	247	22	12	2
7 AM	19	73.4	37417	1771	521	268	34
8 AM	31.5	79.7	58765	3287	1592	814	104
9 AM	44.3	86.2	71099	4346	2695	1392	182
10 AM	57.2	93.9	78292	5198	3724	2667	387
11 AM	69.9	106	82299	5764	4486	3883	678
12 PM	80.9	141.6	84040	6031	4874	4566	803
1 PM	79.3	229.4	83872	6042	4861	4520	815
2 PM	67.6	256.8	81763	5723	4400	3681	629
3 PM	54.9	267.7	77272	5127	3607	2407	335
4 PM	42	275.1	69342	4228	2516	1251	164
5 PM	29.2	281.4	55741	3002	1337	691	88
6 PM	16.8	287.7	32229	1518	386	199	26
7 PM	4.8	294.5	2104	84	5	3	0.4

incident rays on diffuser surface. The ring pattern in Fig. 9.12 depicts the constant incidence angle (equal to zenith angle) of incident rays on the diffuser which is not varying with azimuth. While in Fig. 9.13 a substantial amount of light flux is in the central zone of the Polar Iso-Candela curves, i.e., the incident rays are making low incidence angle (zenith angle) on the diffuser surface which leads to enhanced performance of the diffuser.

Table 9.3 Direct light analysis at different sections of vertical mirror light pipe configuration on 23 September

Time	Altitude (°)	Azimuth (°)	Direct normal illuminance (lux)	Luminous flux incident on dome (lumen)	Luminous flux entering diffuser (lumen)	Luminous flux exiting diffuser (lumen)	Avg. illuminance on table (lux)
7 AM	9.7	95.7	12961	542	70	38	5
8 AM	22.3	104.1	44319	2194	769	395	50
9 AM	34.5	114.1	62267	3556	1855	928	119
10 AM	45.6	127.3	71997	4446	2804	1480	200
11 AM	54.4	146.3	77073	5059	3546	2336	333
12 PM	59	172.6	79034	5290	3845	2903	432
1 PM	57.4	201.1	78403	5215	3737	2698	396
2 PM	50.4	223.8	75015	4825	3232	1858	252
3 PM	40.3	239.6	67919	4081	2370	1144	151
4 PM	28.5	251	54747	2962	1305	674	88
5 PM	16.1	260	30451	1426	346	179	52
6 PM	3.4	267.9	605	23	1.1	0.6	0.1

9.3.2 Diffuse Light Analysis

A hemispherical sky vault as a diffuse light source was used to analyze diffuse light capturing ability of the two configurations. Figure 9.15 shows the ray pattern from the hemispherical sky vault entering into the two configurations separately. The internal side of imaginary hemispherical sky vault was given Lambertian light source, and the luminance distribution was numerically analyzed for target areas corresponding to various orientations. Figure 9.16 shows the target area and eye position considered for analyzing luminance of the source. The source was given the value such that the

Table 9.4 Direct light analysis at different sections of vertical mirror light pipe configuration on 21 December

Time	Altitude (°)	Azimuth (°)	Direct normal illuminance (lux)	Luminous flux incident on dome (lumen)	Luminous flux entering diffuser (lumen)	Luminous flux exiting diffuser (lumen)	Avg. illuminance on table (lux)
8 AM	7.4	122.9	7198	296	28	16	2
9 AM	17.6	132.3	34276	1630	438	226	29
10 AM	26.2	143.9	51248	2704	1094	563	73
11 AM	32.5	157.9	60017	3336	1641	834	107
12 PM	35.6	174.1	63536	3638	1928	957	123
1 PM	35.1	191	62920	3599	1896	945	126
2 PM	30.9	206.6	57980	3191	1501	771	98
3 PM	23.8	219.9	47114	2400	879	453	58
4 PM	14.7	230.8	26775	1218	271	141	17
5 PM	4.2	239.7	1262	50	3	2	0.2

horizontal global illuminance comes out as 10000 lx. On analyzing the diffuse light source from an observer point of view, i.e., at the origin, the luminance/brightness value came out in the range of 2800–3200 Cd/sqm. So, we can consider the source to be having fairly uniform luminance levels for all orientations as shown in Fig. 9.17.

Tables 9.8 and 9.9 show the outcome of numerical analysis for the two configurations. We can see that the luminous flux exiting the diffuser (i.e., entering the room) is marginally higher in case of vertical light pipe as compared to tilt light pipe configuration. Similarly, the average illuminance on the table surface is also slightly greater in value in case of the vertical light pipe.

Table 9.5 Direct light analysis at different sections of tilt mirror light pipe configuration on 21 June

Time	Altitude (°)	Azimuth (°)	Direct normal illuminance (lux)	Luminous flux incident on dome (lumen)	Luminous flux entering diffuser (lumen)	Luminous flux exiting diffuser (lumen)	Average illuminance on table (lux)
6 AM	6.9	66.8	5969	247	25	14	2
7 AM	19	73.4	37417	1771	526	315	44
8 AM	31.5	79.7	58765	3287	1307	844	124
9 AM	44.3	86.2	71099	4346	2380	1492	220
10 AM	57.2	93.9	78292	5198	3472	2228	337
11 AM	69.9	106	82299	5764	4231	2523	356
12 PM	80.9	141.6	84040	6031	4614	2602	366
1 PM	79.3	229.4	83872	6042	4602	2588	359
2 PM	67.6	256.8	81763	5723	4160	2538	373
3 PM	54.9	267.7	77272	5127	3292	2072	310
4 PM	42	275.1	69342	4228	2229	1416	203
5 PM	29.2	281.4	55741	3002	1115	723	105
6 PM	16.8	287.7	32229	1518	424	245	34
7 PM	4.8	294.5	2104	84	9	5	1

9.4 Significance

Table 9.10 shows the energy savings that can be achieved using the TDD in our homes. Consider 300-mm diameter of light pipe giving 2600 lumens on an average for entire year span (10 h per day). The saving will be 547 units and 102 units as compared to using incandescent and LED light source, respectively.

Table 9.6 Direct light analysis at different sections of tilt mirror light pipe configuration on 23 September

Time	Altitude (°)	Azimuth (°)	Direct normal illuminance (lux)	Luminous flux incident on dome (lumen)	Luminous flux entering diffuser (lumen)	Luminous flux exiting diffuser (lumen)	Avg. illuminance on table (lux)
7 AM	9.7	95.7	12961	542	91	51	7
8 AM	22.3	104.1	44319	2194	615	369	53
9 AM	34.5	114.1	62267	3556	1615	1003	148
10 AM	45.6	127.3	71997	4446	2744	1771	267
11 AM	54.4	146.3	77073	5059	3577	2582	406
12 PM	59	172.6	79034	5290	3920	2861	427
1 PM	57.4	201.1	78403	5215	3800	2746	413
2 PM	50.4	223.8	75015	4825	3253	2287	354
3 PM	40.3	239.6	67919	4081	2227	1321	192
4 PM	28.5	251	54747	2962	1067	689	99
5 PM	16.1	260	30451	1426	338	187	26
6 PM	3.4	267.9	605	23	2	1	0.2

9.5 Results and Future Work

Since the resulting value of illuminance in the room is the sum of direct light and diffuse light, lighting levels of 300 lx and more are easily attainable during peak daylight hours in 3 × 3 × 2.7 cubic meter room at a working height for 300-mm diameter opening at the center of the ceiling of the room.

Table 9.7 Direct light analysis at different sections of tilt mirror light pipe configuration on 21 December

Time	Altitude (°)	Azimuth (°)	Direct normal illuminance (lux)	Luminous flux incident on dome (lumen)	Luminous flux entering diffuser (lumen)	Luminous flux exiting diffuser (lumen)	Average illuminance on table (lux)
8 AM	7.4	122.9	7198	296	42	24	3
9 AM	17.6	132.3	34276	1630	352	197	28
10 AM	26.2	143.9	51248	2704	841	458	62
11 AM	32.5	157.9	60017	3336	1497	1006	148
12 PM	35.6	174.1	63536	3638	1889	1462	231
1 PM	35.1	191	62920	3599	1832	1410	228
2 PM	30.9	206.6	57980	3191	1299	780	112
3 PM	23.8	219.9	47114	2400	672	395	55
4 PM	14.7	230.8	26775	1218	247	135	17
5 PM	4.2	239.7	1262	50	5	3	1

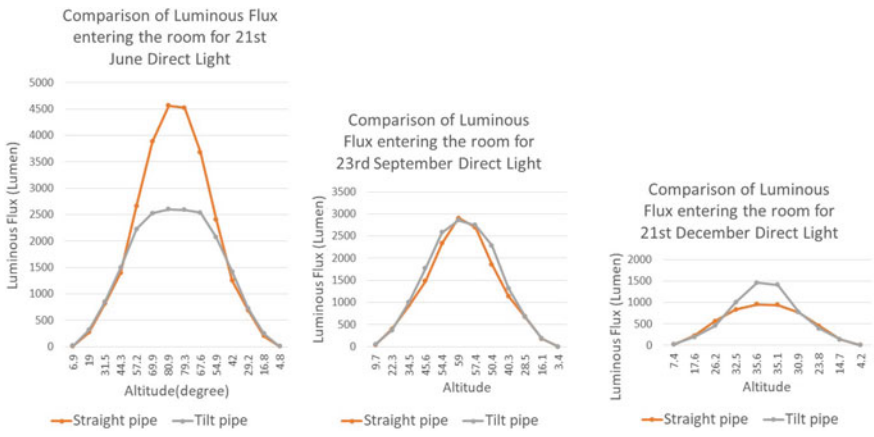


Fig. 9.10 Comparison of luminous flux due to the direct component of light entering the room (exiting the diffuser) on 21 June, 23 September and 21 December

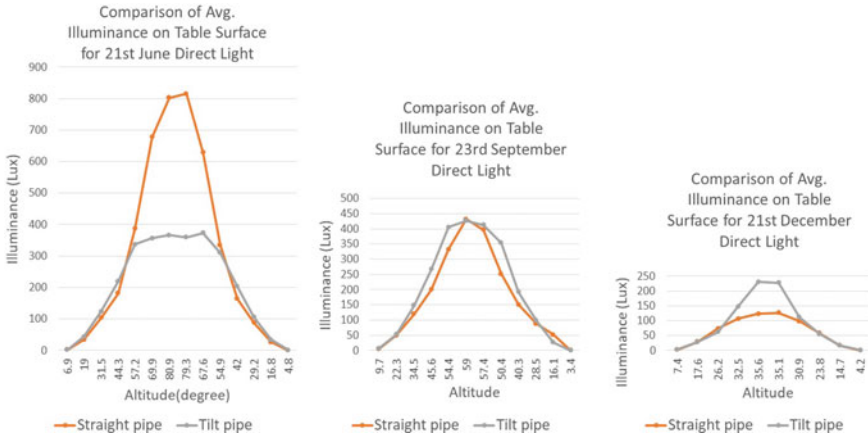


Fig. 9.11 Comparison of illuminance due to the direct component of light on the table surface on 21 June, 23 September and 21 December

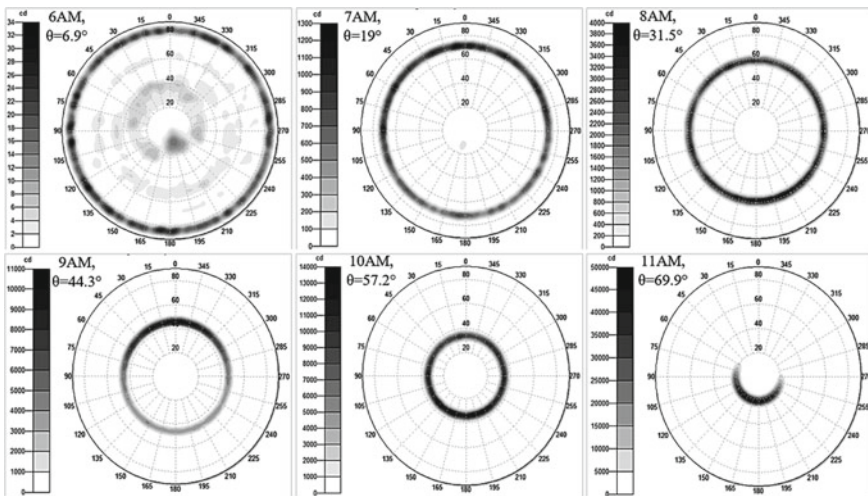


Fig. 9.12 Comparison of Polar Iso-Candela curves at the diffuser entry section of vertical light pipe configuration on 21 June for a different altitude (θ) of the sun (direct light only)

The future work aims to determine lighting levels at different locations inside the room since the homogenous lighting levels are always desirable. The numerical analysis of light collector integrated with mirror light pipe of different configurations for optimum performance of the system is highly desirable. Also, the challenge is to

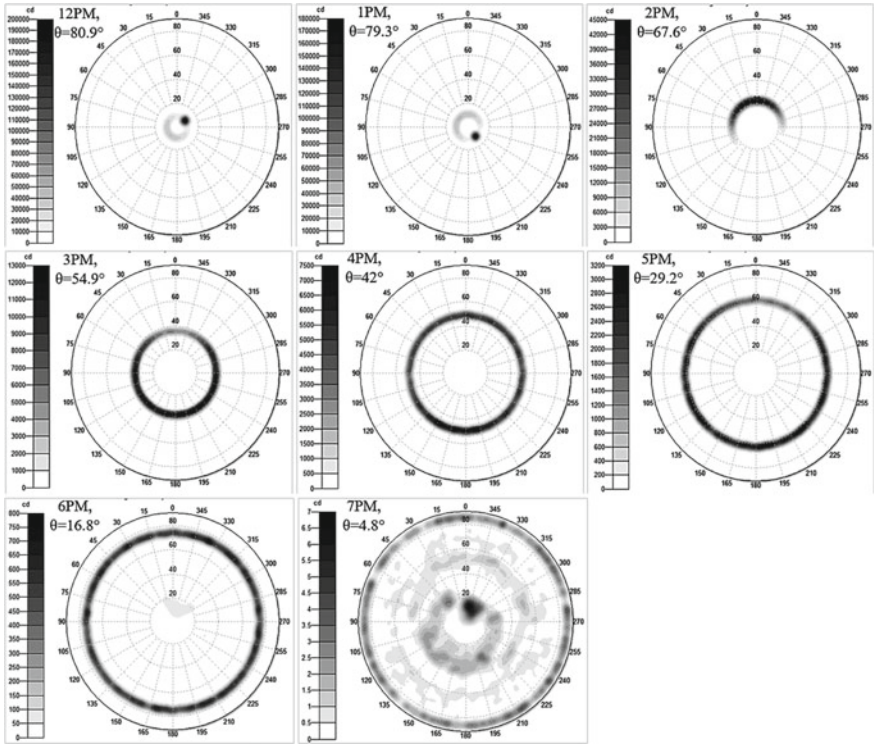


Fig. 9.12 (continued)

increase the lighting levels during morning and evening hours of the day. For this, the alteration in collector design and geometry is an important factor to be considered.

Fetching the required and homogenous lighting levels throughout the day results in reducing electrical power consumption for illuminating homes and office buildings which also leads to an eco-friendly environment.

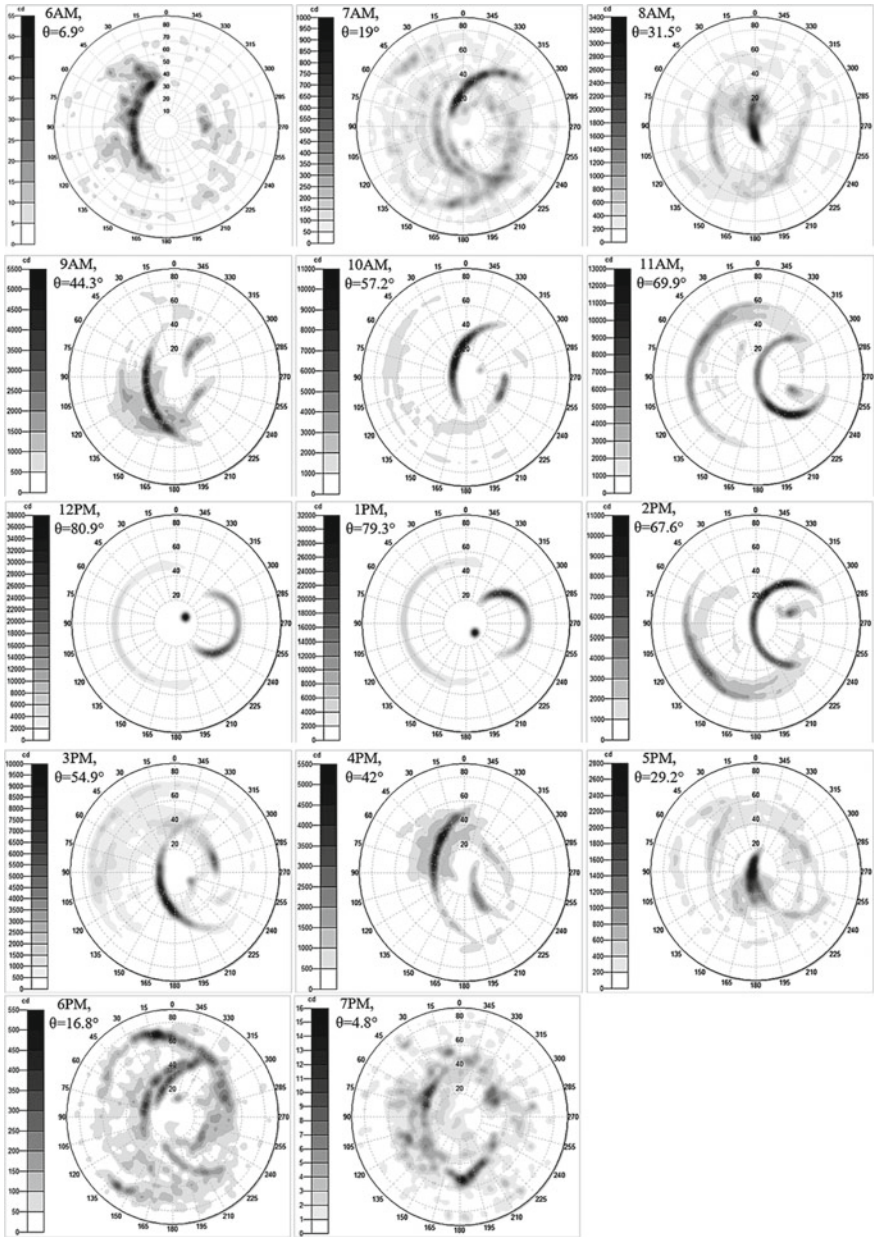


Fig. 9.13 Comparison of Polar Iso-Candela curves at the diffuser entry section of tilt light pipe configuration on 21 June for a different altitude (θ) of the sun (direct light only)

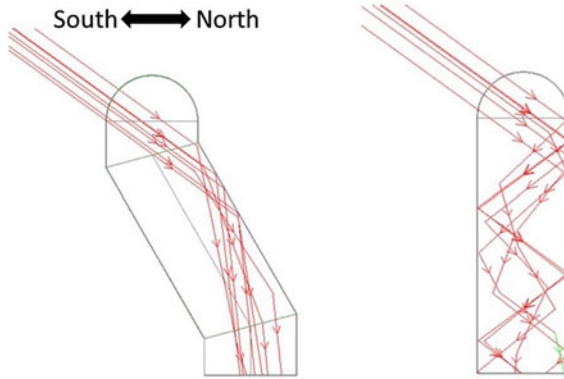


Fig. 9.14 Ray pattern in tilt and straight light pipe configuration

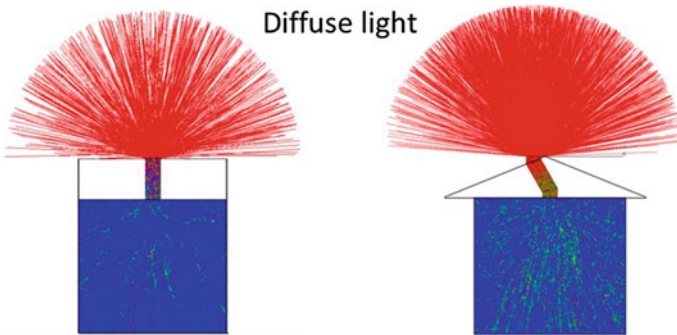


Fig. 9.15 Both the configuration simulated for a diffuse light source with uniform luminance

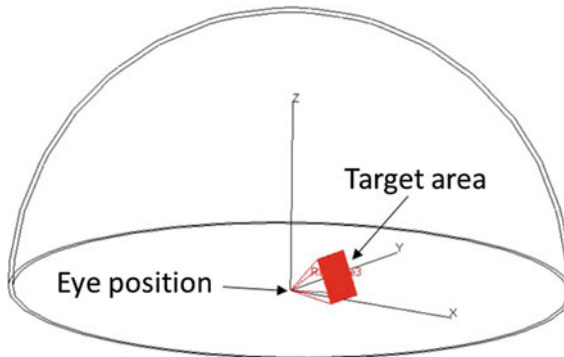


Fig. 9.16 Eye position and target area position for analyzing luminance of the source

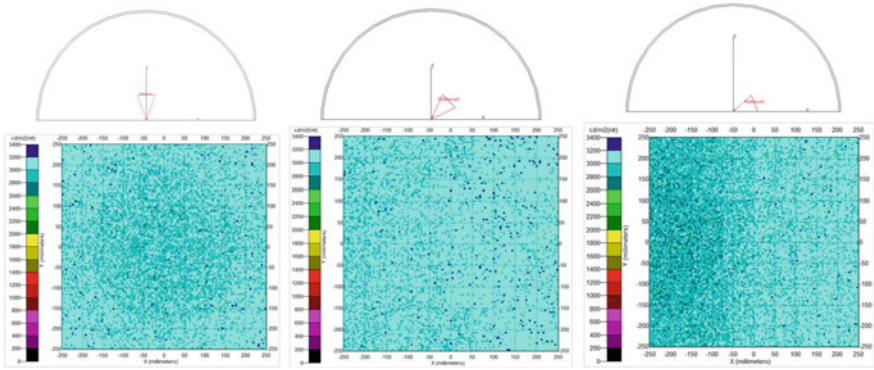


Fig. 9.17 Luminance of the hemispherical diffuse light source analyzed at eye position for target areas at different orientations

Table 9.8 Diffuse light analysis at different sections with vertical mirror light pipe configuration

Horizontal diffuse illuminance (lux)	Luminous flux incident on dome (lumen)	Luminous flux entering diffuser (lumen)	Luminous flux exiting diffuser (lumen)	Avg. illuminance on table (lux)
10000	1090	519	332	52

Table 9.9 Diffuse light analysis at different sections with tilt mirror light pipe configuration

Horizontal diffuse illuminance (lux)	Luminous flux incident on dome (lumen)	Luminous flux entering diffuser (lumen)	Luminous flux exiting diffuser (lumen)	Avg. illuminance on table (lux)
10000	1090	479	305	48

Table 9.10 Energy savings per year using TDD

Light pipe size	Avg. lumen output	Equal wattage of electrical lighting	Energy savings per year (kWh)	Target coverage
300 mm	2600 Lumens	150 W (incandescent)	547	150 Sq ft
		28 W (LED)	102	

One unit of electricity = 1 kWh, i.e., 1000 W × 1 h

Energy savings per year (considering 10 h run per day) = wattage consumption × 10-h × 365 days

References

1. P.J. Littlefair, Innovative daylighting: review of systems and evaluation methods. *Light. Res. Technol.* **22**, 1–17 (1990)
2. M. Kischkoweit-Lopin, An overview of daylighting systems. *Sol. Energy* **73**, 77–82 (2002)
3. M. Nair, K. Ramamurthy, A. Ganesan, Classification of indoor daylight enhancement systems. *Light. Res. Technol.* **46**, 245–67 (2014)
4. I. Edmonds, G. Moore, G. Smith, P. Swift, Daylighting enhancement with light pipes coupled to laser-cut light-deflecting panels. *Int. J. Light. Res. Technol.* **27**, 27–35 (1995)
5. I.R. Edmonds, Performance of laser cut light deflecting panels in daylighting applications. *Sol. Energy Mater. Sol. Cells* **29**(1), 1–26 (1993)
6. M. Nair, A. Ganesan, K. Ramamurthy, Daylight enhancement using laser cut panels integrated with a profiled Fresnel collector. *Light. Res. Technol.* **47**(8), 1017–1028 (2015)
7. M. Nair, A. Ganesan, K. Ramamurthy, Conceptual design and assessment of a profiled Fresnel lens daylight collector. *Light. Res. Technol.* **47**(5), 533–547 (2015)
8. M. Mayhoub, Innovative daylighting systems' challenges: a critical study. *Energy Build.* **80**, 394–405 (2014)
9. M. Mayhoub, D. Carter, Towards hybrid lighting systems: a review. *Light. Res. Technol.* **42**(1), 51–71 (2010)

Chapter 10

Optimization of Electron Transport Layer Based on Cadmium Sulfide for Perovskite Solar Cells



Nidhi Gupta, Shivansh Rastogi, Jampana Gayathri, Omita Nanda and Kanchan Saxena

Abstract The deposition of CdS thin film using three different methods, that is, thermal vapor deposition, electrodeposition and chemical bath deposition for the application as electron transport layer (ETL) in perovskite solar cells has been reported. Surface morphology of thin films obtained by all three methods was analyzed using SEM images. Optical properties were studied using UV-visible spectroscopy. The film deposited by thermal vapor deposition showed high uniformity, and however, adherence properties and transmittance properties are found to be poor. Thin film fabricated by chemical bath deposition showed high uniformity with very good adherence properties but poor transmittance. Thin film obtained by electrodeposition showed good surface morphology, improved adherence properties and best transmittance properties in the visible region and was found suitable to be used as ETL.

Keywords Cadmium sulfide · ETL · Electrodeposition · Thermal vapor deposition · Chemical bath deposition

10.1 Introduction

Perovskite solar cells (PSCs) are emerging technology in the field of solar photovoltaics during the last few years due to their amazing conversion efficiency, tunable band gap, long diffusion length, easy fabrication capability and low cost [1, 2].

PSCs are multilayer devices which consist of hole/electron transport layer and active layer sandwiched between two electrodes on a glass or flexible substrate [3]. In any multilayer device, each layer has a significant contribution to the efficiency of the device [4, 5]. Electron transport layer (ETL) is one of the important layers that ensure the smooth electron flow from active layer to cathode. Good transmittance in the visible range, high charge transport and stability are some important parameters

N. Gupta (✉) · S. Rastogi · J. Gayathri · O. Nanda · K. Saxena
Amity Institute of Advance Research and Studies (Material & Devices), Amity Institute of Renewable and Alternative Energy, Sector 125, Noida, Uttar Pradesh 201303, India
e-mail: nidhi.dbc@gmail.com

© Springer Nature Singapore Pte Ltd. 2020
V. K. Jain et al. (eds.), *Advances in Solar Power Generation and Energy Harvesting*, Springer Proceedings in Energy,
https://doi.org/10.1007/978-981-15-3635-9_10

of ETL [6]. Optimization of ETL is essential to achieve high-efficiency solar cell. In the initial perovskite solar cell reported by Kojima et al. [7], hybrid perovskite was used as absorber layer over mesoporous titanium dioxide (TiO_2). Other various metal oxides such as mp- Al_2O_3 zinc oxide (ZnO), tin oxide (SnO_2) and zirconium dioxide (ZrO_2) have been used as ETL in perovskite solar cells. Cadmium selenide (CdSe), cadmium sulfide (CdS), PEHT, PCBM and PEHT:PCBM, etc. have been used [6]. CdS is very promising ETL due to its properties like high stability of physicochemical properties, long diffusion length and low annealing temperature [8]. Here in this paper, CdS thin films fabricated for application as ETL in PSCs using different methods have been analyzed.

10.2 Materials and Methods

Cadmium sulfide (CdS), cadmium nitrate $\text{Cd}(\text{NO}_3)_2$ and thiourea were purchased from Thermo Fisher Scientific. Ammonia and ethanol were provided by Qualigens Fine Chemicals Pvt. Ltd. All the chemicals and solvents were used without any further purification.

10.2.1 Thermal Vapor Deposition

CdS thin film was coated over a pre-cleaned glass substrate of size 1 in. \times 1 in. using thermal vapor deposition. High vacuum of 10^{-5} Torr was sustained throughout the deposition process. A 300 Å thick film was deposited with the rate of deposition maintained between 0.2 and 0.5 Å s^{-1} during the process.

10.2.2 Chemical Bath Deposition

Another method used for the fabrication of CdS thin film was chemical bath deposition. It was a two-step deposition method which includes the deposition of seed layer followed by the deposition of CdS film. In the first step, the precursor solution was prepared by mixing the alcoholic solutions of $\text{Cd}(\text{NO}_3)_2$ (0.015 M) and thiourea (0.15 M) in a ratio of 1:1 (v/v) followed by heating 60 °C for one hr. Prepared precursor solution was then spin coated over the pre-cleaned glass substrates at 2000 rpm using APEX spin coater (Model: APEX Spin NXG-M1). Finally, the seed layer was produced by thermal annealing of the coated substrates at 450 °C. This seed layer acted as a nucleation site when coated substrates were dipped in a concentrated precursor solution in the second step. The concentrated precursor solution was prepared using equimolar solutions of aqueous cadmium nitrate (0.15 M) and aqueous thiourea

(0.15 M) and 2.5 ml ammonia. Seeded plates were held vertical in a chemical bath, and the temperature was maintained at 60 °C for 8 h.

10.2.3 Electrodeposition

CdS thin films were also deposited using electrodeposition technique using ITO-coated glass plate and graphite as cathode and anode, respectively. For the precursor solution, 0.2 M $\text{CdCl}_2 \cdot \text{H}_2\text{O}$ was mixed with 0.3 M of thiourea. A voltage of 0.7 was applied using Keithley SourceMeter (Model 2400). Temperature was maintained at 85 °C with continuous stirring during the deposition of CdS. Electrodes were kept at a distance of 1 cm.

10.3 Result and Discussion

Surface morphologies of CdS films deposited by all three methods were analyzed using scanning electron microscope Carl Zeiss (Model no. MA EVO-18). Figure 10.1a–c shows the SEM images of the CdS film deposited by thermal vapor deposition, chemical bath deposition and electrodeposition, respectively. In case of thermal vapor deposition, the film was found to be uniform and pinhole-free (Fig. 10.1a). However, it did not sustain itself when the next layer was deposited over it by solution processing. CdS layer deposited by chemical bath deposition is much more stable as compared to the previous method. This may be due to the reason that seed layer acts as a link between the deposited layer and the glass substrate. SEM images of CdS film deposited by chemical bath deposition were found to uniform as well. It is shown in Fig. 10.1b that film was uniform consisting of particles around 50–150 nm merged together to form a continuous film. This film is suitable for using as ETL in solar cells as the next layer can be deposited by solution processing easily. Surface morphology of CdS deposited by electrodeposition (Fig. 10.1c) was found to be rough in comparison to CdS films deposited by thermal vapor deposition and chemical bath deposition. This may result in the increased interfacial area which can further improve the charge transfer from ETL to active layer and consequently improved device performance. Further, thickness of the layer can be controlled by changing the time and voltage applied for electrodeposition. Electrodeposited CdS thin film was also stable with other solvents such as propanol and toluene which make it suitable to be used as ETL in PSCs.

Transparency in the visible region is another important factor that ETL of solar cell must possess so that it does not hinder the path of light rays to the absorber layer. To study the optical transparency of ETL, UV-visible spectrum was recorded using spectrophotometer (Shimadzu, UV-2600) for CdS thin films fabricated by all three methods as depicted in Fig. 10.2. Electrodeposited layer showed the highest transmittance due to nanostructured surface morphology as compared to uniform CdS

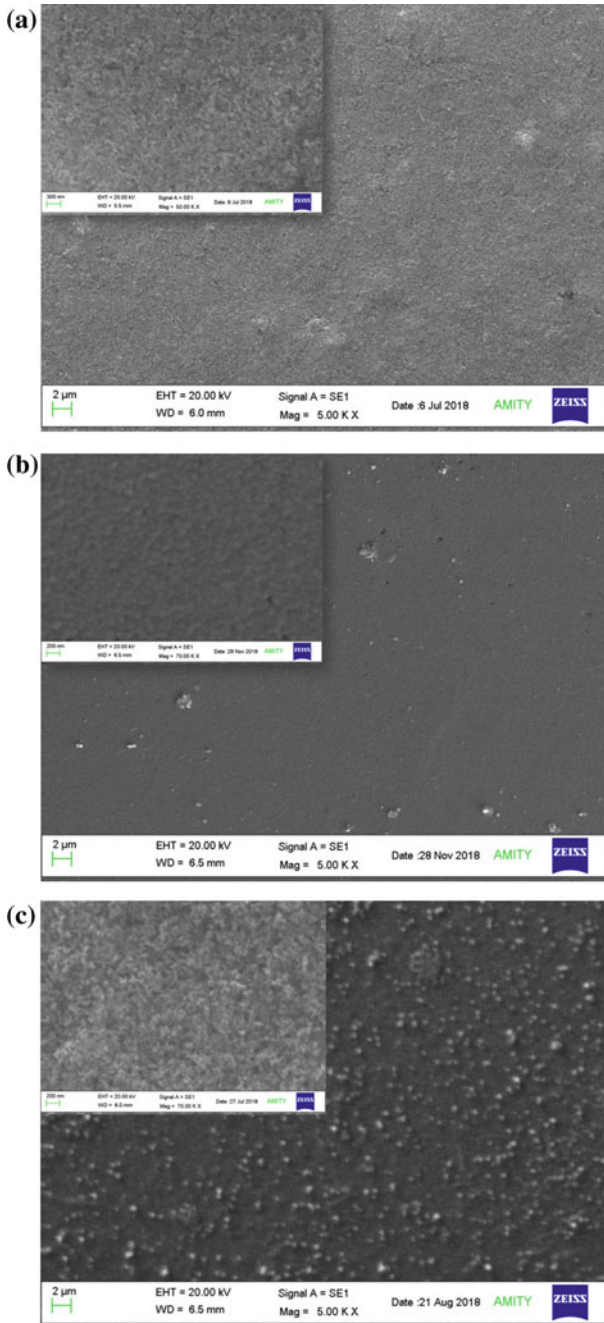
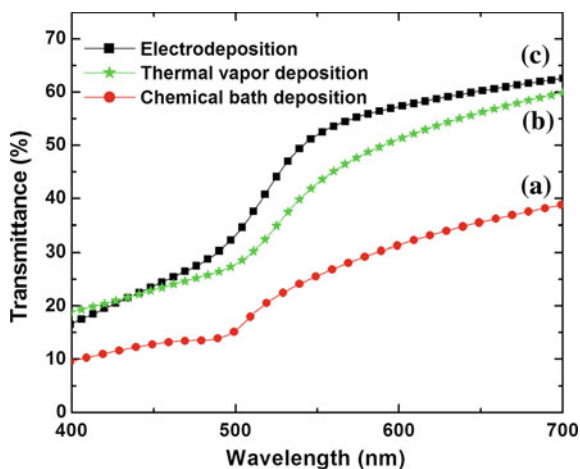


Fig. 10.1 SEM images of CdS thin film deposited using **a** thermal vapor deposition [at higher magnification (inset of 10.1a)], **b** chemical bath technique [at higher magnification (inset of 10.1b)] and **c** electrodeposition [at higher magnification (inset of 10.1c)]

Fig. 10.2 UV-visible spectra of **a** chemical bath deposition, **b** thermal vapor deposition and **c** electrodeposition



film in case of other two methods. Reduced transmittance of uniform films found in case of thermal vapor deposition and chemical bath deposition. Transmittance of approximately 60% in wavelength range of 500 nm to 700 nm was recorded, whereas up to 500 nm, transmittance was only 20–30%. CdS thin film deposited by thermal vapor deposition showed the same trend as an electrodeposited film. The relatively low transmittance may be due to poor crystallinity and large amorphous component [9]. High thickness leads to dense structure and hence higher absorption or reduced transmittance in case of the film deposited using thermal vapor deposition and chemical bath deposition.

10.4 Conclusions

CdS thin films were deposited by three different methods, that is, thermal vapor deposition, chemical bath deposition and electrodeposition. CdS film deposited by thermal vapor deposition was smooth but cannot withstand the solvent treatment. CdS film deposited by chemical bath deposition is also uniform and stable as well, and however, it showed poor transmittance in visible region. Electrodeposited film is rough in comparison with uniform films obtained in case of thermal vapor deposition and chemical bath deposition. Further, this film was stable and transparent as well which makes it suitable to be used as ETL in PSCs which are under progress.

Acknowledgements Authors are thankful to SERB, Government of India, for funding the project (Project No.: EMR/2017/004615. The authors are grateful to Dr. Ashok K. Chauhan, Founder President, Amity University Uttar Pradesh, Noida, India, for their continuous encouragements.

References

1. D. Zhao, C. Wang, Z. Song, Y. Yu, C. Chen, X. Zhong Zhao, K. Zhu, and Y. Yan, Four-terminal all-perovskite tandem solar cells achieving power conversion efficiencies exceeding 23%, *ACS Energy Lett.* **2**, 305–306 (2018)
2. S.A. Kulkarni, A.T. Baikie, P.P. Boix, N. Yantara, N. Mathews, S. Mhaisalkarab, Band-gap tuning of lead halide perovskites using a sequential deposition process. *J. Mater. Chem. A* **2** 9221–9225 (2014)
3. I. Hussain, H. Phong Tran, J. Jaksik, J. Moore, N. Islam, M. Jasim Uddin, Functional materials, device architecture, and flexibility of perovskite solar cell. *Emergent Mater.* **1**, 133–154 (2018)
4. N.E. Courtier, J.M. Cave, J.M. Foster, A.B. Walkerb, G. Richardson, How transport layer properties affect perovskite solar cell performance: insights from a coupled charge transport/ion migration model. *Energy Environ. Sci.* **12**, 396–409 (2019)
5. P. Morvillo, E. Bobeico, S. Esposito, R. Diana, Effect of the active layer thickness on the device performance of polymer solar cells having [60] PCBM and [70] PCBM as electron acceptor. *Energy Procedia* **31**, 69–73 (2012)
6. K. Mahmood, S. Sarwarb, M.T. Mehranb, Current status of electron transport layers in perovskite solar cells: materials and properties. *RSC Adv.* **7**, 17044–17062 (2017)
7. A. Kojima, K. Teshima, Y. Shirai, T. Miyasaka, Organometal halide perovskites as visible-light sensitizers for photovoltaic cell. *Am. Chem. Soc.* **131**, 6050–6051 (2009)
8. J. Jia, J. Wu, J. Dong, L. Fan, M. Huang, J. Lin, Z. Lan, Cadmium sulfide as an efficient electron transport material for inverted planar perovskite solar cells. *Chem. Commun.* **54**, 3170–3173 (2018)
9. S. Kumar, S. Kumar, P. Sharma, V. Sharma, S.C. Kalyal, CdS nanofilms: effect of film thickness on morphology and optical band gap. *J. Appl. Phys.* **112**, 123512-1–123512-8 (2012)

Chapter 11

Intelligent Energy Information and Management System for Academic Institutes



Maneesha, Praveen Kant Pandey and Sachin Kumar

Abstract Requirement of energy for human sustenance and growth has increased exponentially during the last century. The rate of rise in demand for energy has reached unprecedented levels leading to widening of gap between demand and supply of electric energy due to the scarcity of resources. The harmful effects of excessive usage of energy on the environment pose a great danger to the sustainability of our ecosystem. In this scenario, it becomes pertinent to design a strategy for increased efficiency of electricity utilization with an aim to minimize air pollution and carbon footprint. Hence, energy management systems are the need of the hour to identify the potential for improvements in energy efficiency. However, the implementation of Energy Information and Management System (EIMS) in academic institutes is extremely limited due to lack of awareness and relevant green policies. The current work presents a blueprint of Energy Information and Management System for an academic institute leading to multi-measure energy efficiency through multiple strategies including equipment operational improvements and upgrades, and occupant behavioural changes. The design of Intelligent EIMS enables energy savings relative to a baseline model, which predicts energy consumption from key parameters such as occupancy levels mapped with the timetable and operational schedule. The need for policies to be adopted by educational institutes for optimum utilization of electrical energy has been discussed and presented in the paper. In the present work, the different sub-domains/facilities of the college were primarily divided into three categories, namely facilities mapped with college timetable (like classrooms, laboratories, etc.), facilities mapped with fixed or regular schedule (like hostel mess, corridors, etc.) and facilities independent of college timetable or fixed schedule (like canteen, staffroom, common room, etc.). The two basic categories were further subdivided on the basis of scheduled usage and ad hoc usage of these facilities. Based on these categorizations, policies for energy usage were framed for these facilities, and prototype EIMS was designed and implemented at Maharaja Agrasen College,

Maneesha · P. K. Pandey (✉) · S. Kumar
Maharaja Agrasen College, University of Delhi, Delhi, India
e-mail: pkpandey.du@gmail.com

Maneesha
e-mail: maneesha.du@gmail.com

© Springer Nature Singapore Pte Ltd. 2020
V. K. Jain et al. (eds.), *Advances in Solar Power Generation and Energy Harvesting*, Springer Proceedings in Energy,
https://doi.org/10.1007/978-981-15-3635-9_11

University of Delhi. 4.8% saving in the power consumption was observed post-EIMS implementation.

Keywords Energy information system · Energy management · RS-485 network · Baselineing · Benchmarking · Green policy for academic institutes · Energy efficiency · EIMS in academic institutes

11.1 Introduction

Energy is at the forefront of the global agenda and is central to the issues of development, security and environmental protection. Due to continuous depletion of conventional resources, acute energy shortage and environmental concern, it is crucial to continuously monitor the use of electrical energy and employ intelligent and innovative methods to control and reduce wastage of energy. The harmful effects of excessive usage of energy on the environment pose a great danger to the sustainability of our ecosystem. Under these circumstances, it becomes pertinent to design a strategy for increased efficiency of electricity utilization with an aim to minimize air pollution and carbon footprint. In today's scenario, the challenge is (a) to use the energy efficiently to attain energy security as each bit of energy saved is equivalent to energy generated, thereby reducing our negative impact on environment; (b) to sensitize government bodies, industrial sector and the academic institutes to respond to this challenge of converging the difference between the demand and supply of the energy system; and (c) devise new strategies to address this crisis and undertake innovative measures in energy-saving technology and policies.

Hence, energy management systems are the need of the hour to identify the potential for improvements in energy efficiency. Energy Information and Management Systems (EIMS) address these issues and improve the energy efficiency of the system by providing energy usage information and further, controlling electric supply continuously. EIMS is broadly defined as performance monitoring and data acquisition hardware and software with communication systems to store, analyse and display energy information [1]. The role of EIMS in measuring and monitoring energy consumption data along with energy information feedback plays a vital role in benchmarking and improving building efficiency [1]. Data from the EIMS comprising of energy meters, electronic sensors, etc. is logged into a server on a regular interval. The electric data so collected can be further analysed for load profiling, baselining and benchmarking. The significant gap between post-occupancy measurement of energy consumption and the desired energy performance of the building in accordance with the design was identified by New Buildings Institute [2]. Piette et al. [3], Brown et al. [4], Mills et al. [5] and Mills and Mathew [6] stressed upon the importance of permanent metering for monitoring-based and continuous commissioning. The effect of energy monitoring has led to positive behavioural impact when energy consumption patterns were made visible to the occupants of the building [7, 8].

Today more and more industries are adopting Energy Information and Management Systems to manage their power requirement with policies designed to reduce the losses in the system and thereby reduce the cost of operations. However, the implementation of EIMS in academic institutes is extremely limited due to lack of awareness and relevant green policies.

The need analysis for EIMS was performed by studying the existing norms regarding the usage of electrical energy in various sub-domains of three colleges affiliated with the University of Delhi. It was found that the normal practice is that the electrical supply to all the college facilities is switched on in the morning and remains on till the working hours of the college in the evening. Although there are some exceptions to this practice, for example, the conference room is powered as and when required; corridor lights are turned on in the evening till the morning. It was observed that in this model, the electrical appliances such as lights, fans and air conditioners remain on even when they were not in use leading to wastage of energy and college finances. Supply to laboratory equipments is another area for optimization. Unchecked usage of energy in the college hostel, including rooms, mess and common area also contributes to excessive and wasteful usage of energy. To address some of these issues, the college launched energy conservation drives to sensitize students, teachers and staff to save this wastage of energy. The message was spread through various awareness drives such as posters, signboards and special talks. Although these efforts produced results in many domains of the college, all such measures proved to be short-lived and usually could not sustain beyond a couple of weeks.

The focus of this research is the design of Energy Information and Management Systems in an academic institute to improve energy performance. The proposed EIMS facilitates energy efficiency in an academic institute using a baseline model with a focus on occupancy levels mapped with the timetable and operational schedule. The essentials of a smart EIMS are shown in Fig. 11.1.

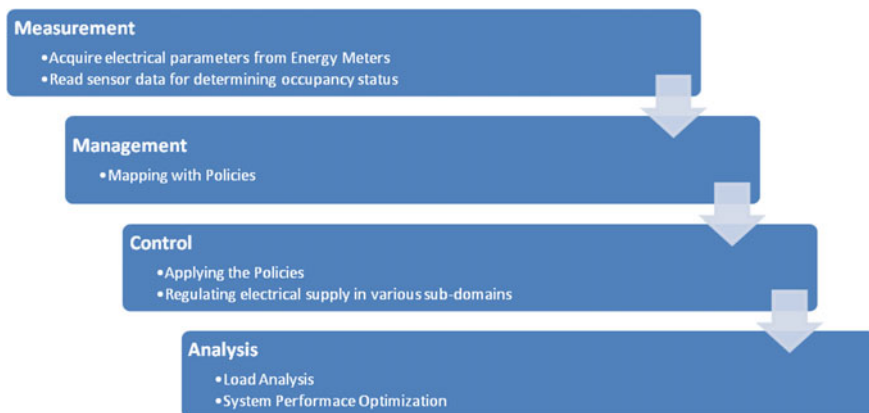


Fig. 11.1 Essential features of Energy Information and Management System

The current work presents a blueprint of the Energy Information and Management System for an academic institute. A general methodology to evaluate baseline model performance was developed to predict load based on occupancy levels of facilities mapped with timetable and operational schedule. The need for policies to be adopted by educational institutes for optimum utilization of electrical energy was identified. Accordingly, the following policies for energy usage were framed for the college.

- Implement EIMS in institute keeping in mind the needs of an academic institute
- Implement systems for authentication of energy utilized in the institute
- Promotion of the use of certified energy-efficient appliances
- Increase the use of renewable energy
- Build green buildings for all future infrastructure projects
- Conduct an annual energy audit of the institute.

11.2 Design of Energy Information and Management System (EIMS)

The different sub-domains/facilities of the college were primarily divided into three categories, namely (a) facilities mapped with college timetable (like classrooms, laboratories, etc.), (b) facilities mapped with fixed or regular schedule (like hostel mess, corridors, etc.) and (c) facilities independent of college timetable and fixed schedule (like canteen, staffroom, common room, etc.).

These categories were further subdivided on the basis of scheduled usage and ad hoc usage of these facilities. Based on these categorizations, the policies for energy usage were framed.

A prototype EIMS incorporating the proposed energy management policies and strategies was designed and deployed at Maharaja Agrasen College (Fig. 11.2). EIMS was implemented at Maharaja Agrasen College in two stages. In the first part, energy information system (EIS) was designed and implemented in the college, under which a network of energy meters (Make: Crystal, Model: CCM-603P) was installed in various units of the college to monitor and analyse the energy consumption pattern in different sub-domains of the college [9]. The technical specifications of the CCM-603P energy meter are given in Table 11.1.

The data for real-time instantaneous electrical parameters such as phase voltage, frequency, line current, active and reactive power along with cumulative parameters like apparent and active energy was logged in through the various electricity meters into the server [9]. The CCM-603P energy meters were connected to the server through USB to RS-232/422/485 converter module (Make: ICP CON, Model: I-7561). I-7561 module contains Self-Tuner ASIC which automatically tunes to the baud rate and data format for the RS-485 network [9]. This eliminates the need for

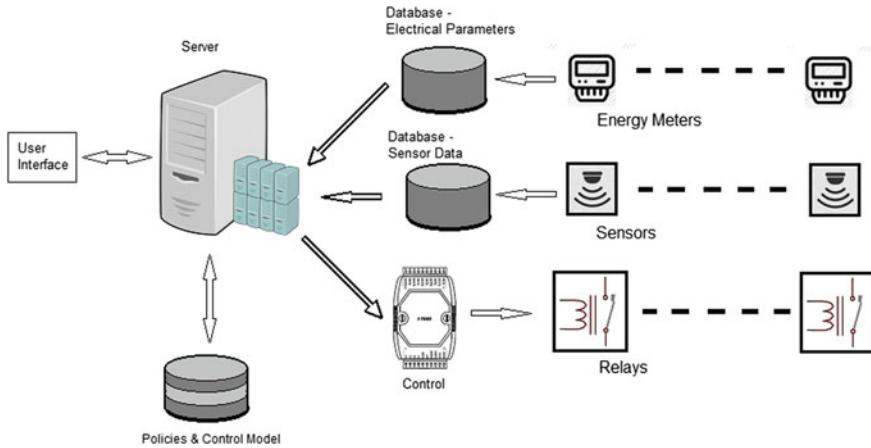


Fig. 11.2 EIMS block diagram

Table 11.1 Technical specifications of CCM-603P energy meter

<i>Electrical parameters</i>	
Power system	3-phase, 4-wire
Voltage	90–300 VAC per phase
Maximum current	120 A
<i>Accuracy parameters</i>	
Accuracy class	1.0 as per IS: 13779-99
Voltage	$\pm 1.0\%$ of full scale ± 1 V
Current	$\pm 1.0\%$ of full scale ± 0.1 A
Active power	$\pm 1\%$ of full scale
Reactive power	$\pm 1\%$ of full scale
Apparent power	$\pm 1\%$ of full scale
Power factor	$\pm 0.2^\circ$
Energy	Class 1.0
Frequency	± 0.04 Hz (47–53 Hz)
<i>Communication module parameters</i>	
Type	RS-485
Protocol	Modbus RTU
Baud rate	9600
Stop bit	1
Parity	None
Isolation	2.5 kV rms at 50 Hz for 1 min

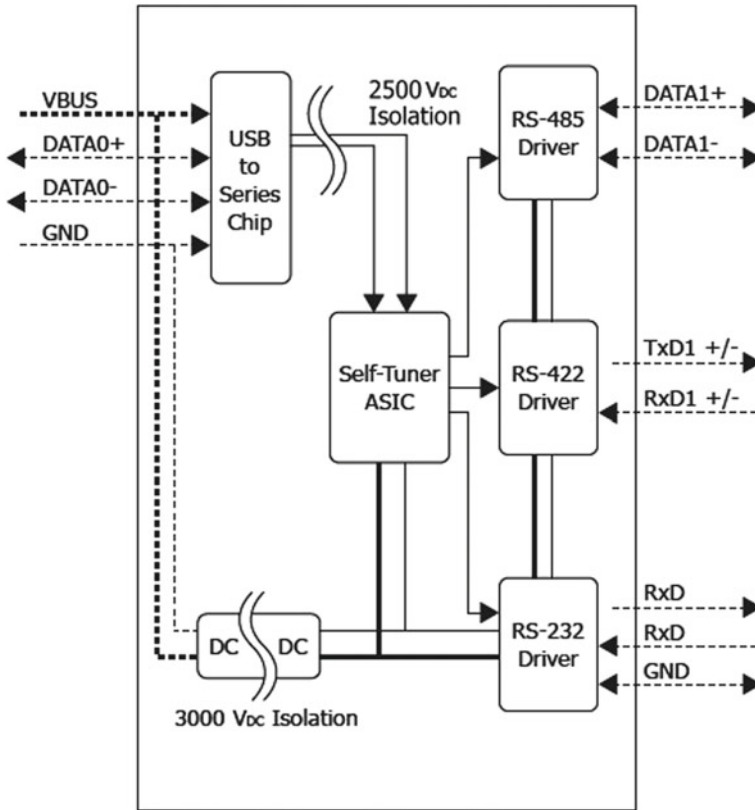


Fig. 11.3 ICP I-7561 module block diagram

direction pin for half-duplex data transmission. Block diagram of ICPI-7561 is given in Fig. 11.3.

A schematic of the RS-485 network implemented for EIS is shown in Fig. 11.4 [10].

A customized PC software for data logging and user interface was designed. The software was monitored and logged instantaneous and cumulative parameters in database server every 10 min.

The baseline model for energy consumption was developed taking into account the occupancy level of the sub-domains. For the facilities which were usually used in accordance with the timetable (like classrooms, laboratories, etc.), the occupancy was decided by mapping with the respective timetable of the sub-domain. In addition to the scheduled usage of facilities, the ad hoc usage of these facilities was also taken into account while preparing the model. The occupancy level of sub-domains/facilities which have a fixed or regular schedule was mapped to their specific schedule in

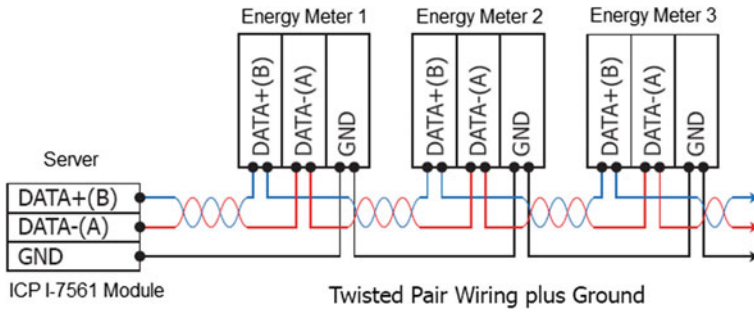


Fig. 11.4 RS-485 network diagram

Table 11.2 ICP I-7065 module technical specifications

Module	I-7065
Output channels	5
Relay type	Form A
Contact rating	5 A@250 VAC/5 A@30 VDC
Surge strength	400 V
Operate time	6 ms Max
Release time	3 ms Max
Minimum life	100,000 operations
Input channels	4
Isolation voltage	3750 V rms
Supply voltage	+10 to 30 VDC
Power	1.3 W

the academic institute. Occupancy level of the third category of sub-domains was obtained using the sensor data.

In the second stage of EIMS implementation, the data collected from the servers was analysed, and the energy consumption pattern was evaluated. Power supply to various electrical appliances in a sub-domain was controlled using ICP I-7065 relay module for energy management. Each ICP I-7065 module has five Form A, NO type, 250 VAC/5 A rated relay contacts and operates on RS-485 bus. For operating appliances of higher power rating, a contactor of suitable capacity was connected after the relay module. The specification of the module is given in Table 11.2.

Figure 11.5 shows the ICP I-7065 relay module block diagram.

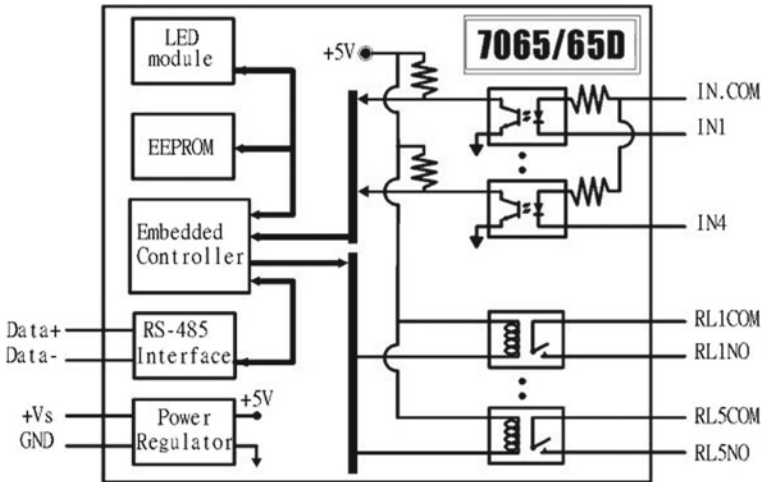


Fig. 11.5 ICP I-7065 module block diagram

11.3 Result

The data collected from the energy meters was analysed, and the energy consumption pattern for each sub-domain was evaluated. The baseline model for energy consumption was developed taking into account the occupancy level of the sub-domains. A snapshot of the database file with raw data is shown in Fig. 11.6.

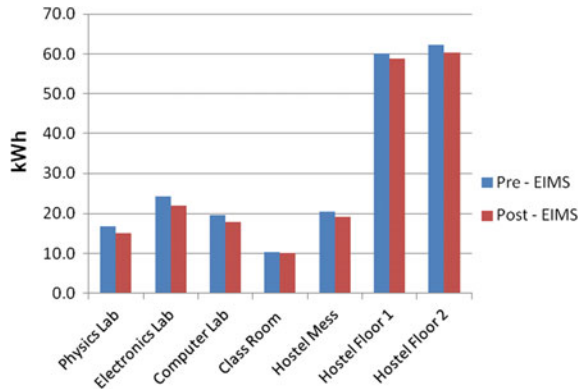
The pattern of actual energy usage was compared with the baseline energy model developed on the basis of occupancy data. The electrical energy is controlled in these facilities in accordance with the policies to reduce its wastage and thereby increase the energy efficiency.

Figure 11.7 shows the comparison of energy consumed in a day in various sub-domains of the college. Both pre-EIMS and post-EIMS results are plotted in the graph. It was observed that the prototype EIMS designed and deployed in the college resulted in about 4.8% average saving in the power utilization.

DateTime	MeterAddr	Voltage	Current	PF	Frequency	KW	KVA	KVAR
19-01-2017 12:10:05	7	237	0.2	0.94	50.09	0.06	0.07	0.02
19-01-2017 12:10:04	6	237	0.2	0.76	50.11	0.05	0.06	0.04
19-01-2017 12:10:04	5	237	0.5	0.73	50.1	0.09	0.12	0.08
19-01-2017 12:10:03	4	233	4.7	1	50.11	1.28	1.28	0
19-01-2017 12:10:03	3	238	0.5	0.74	50.07	0.1	0.14	0.09
19-01-2017 12:10:01	2	234	4.6	1	50.09	1.23	1.23	0
19-01-2017 12:10:01	1	237	0.3	0.79	50.1	0.07	0.09	0.05

Fig. 11.6 Snapshot of electrical data captured by EIMS

Fig. 11.7 Electrical energy consumed in various sub-domains of college in a day for both pre-EIMS and post-EIMS installation period



11.4 Conclusion

The research paper emphasizes the importance and advantages of EIMS in an academic institute in terms of energy savings as part of best practice energy management programs. The EIMS implemented at Maharaja Agrasen College, University of Delhi, monitored real-time energy utilization by acquiring energy parameters from energy meters. The system analysed the data taking into account the expected occupancy level in different sub-domains of the college in accordance with the occupancy model developed for the institute. The energy supply to the facilities was thus managed to improve the energy efficiency of the college.

The use of EIMS prototype facilitated the necessary information to the decision-makers of the institute to make an informed choice in framing relevant policies and further undertake pro-active measures for better utilization of energy in academic institutes, resulting in the efficient management of energy and further reduction of their carbon footprints.

Acknowledgements Design of energy information system (EIS) has been financed by University of Delhi, Innovation Project MAC101: “Measuring Environmental Footprint of University of Delhi and Transforming it into a Zero-Impact University”. The authors would like to thank the Principal Investigators Dr. A. Pundir, Dr. V. Pundir and Dr. P. Rai for their contribution during the course of work.

References

1. J. Granderson, M.A. Piette, G. Ghatikar, P.N. Price, Building Energy Information Systems: State of the Technology and User Case Studies (Lawrence Berkeley National Laboratory, LBNL—2899E, November 2009)
2. New Buildings Institute, Energy performance of LEED for new construction buildings. Prepared for the US Green Building Council (2008). http://www.newbuildings.org/sites/default/files/Energy_Performance_of_LEEDNC_Buildings-Final_3-4-08b.pdf

3. N. Motegi, M.A. Piette, Web-based energy information systems for large commercial buildings. Lawrence Berkeley National Laboratory. Paper LBNL-49977 (2003). <http://repositories.cdlib.org/lbnl/LBNL-49977>
4. K. Brown, M. Anderson, J. Harris, How monitoring-based commissioning contributes to energy efficiency for commercial buildings. Am. Counc. Energy Efficient Econ. Summer Study Proc. **3**, 27–40 (2006)
5. E. Mills, N. Bourassa, M.A. Piette, H. Friedman, T. Haasl, T. Powell et al., The cost-effectiveness of commissioning new and existing commercial buildings: lessons from 224 buildings, in *Proceedings of the National Conference on Building Commissioning*. Lawrence Berkeley National Laboratory Report No. 56637 (2005). http://eetd.lbl.gov/emills/PUBS/PDF/NCBC_Mills_6Apr05.pdf
6. E. Mills, P. Mathew, Monitoring-based commissioning: Benchmarking analysis of 24 UC/CSU/IOU projects. Report Prepared for: California Energy Commission Public Interest Energy Research (PIER) Technology Demonstration Program. Lawrence Berkeley National Laboratory. Paper LBNL-1972E (2009)
7. S. Darby, *The Effectiveness of Feedback on Energy Consumption: A Review for DEFRA of the Literature on Metering, Billing, and Direct Displays* (Environmental Change Institute, University of Oxford, 2006). <http://www.eci.ox.ac.uk/research/energy/downloads/smart-meteringreport.pdf>
8. J. Petersen, V. Shunturov, K. Janda, G. Platt, K. Weinberger, Dormitory residents reduce electricity consumption when exposed to real-time visual feedback and incentives. *Int. J. Sustain. High. Educ.* **8**(1), 16–33 (2007)
9. P.K. Pandey, Maneesha, Designing and developing energy information system for Academic Institutes. *J. Eng. Appl. Sci.* **12** (special issue 7), 7990–7994 (2017). ISSN: 1816- 949X
10. Modbus Application Protocol V1.1b3, Modbus, Modbus Organization Inc

Chapter 12

Thermal Performance Enhancement of Flat-Plate Solar Collector Using CeO₂–Water Nanofluid



Shubham Sharma, Sandeep Tiwari, Arun Kumar Tiwari, Gopal Nandan and Ravi Prakash

Abstract In the present study, the effects on the thermal performance of nanofluid in flat-plate solar collector are studied experimentally. The thermophysical properties (thermal conductivity, viscosity, density, and specific heat) of CeO₂–water nanofluid measured with a wide range of volume concentrations (0.25–2.0%) using 30 nm particle size. Maximum enhancement in thermal conductivity is observed up to 41.7% at 1.5% volume fraction of nanofluid at an 80 °C temperature in comparison with the base fluid. Viscosity decreases with increasing the temperature but increases with a particle volume concentration of nanofluid at a particular temperature. The experimental setup fabricated for the study of heat collection using a flat plate. The mass flow rate of nanofluids was adjusted (at a given volume concentration) for experimentation. The collector temperatures, ambient, and tap water temperatures, radiation, and wind speed were measured. Experimental results exhibit that the maximum collector efficiency is obtained up to 57.1% at an optimum concentration with a mass flow rate of 0.03 kg/s. The results show that the CeO₂–water nanofluid as working fluid improves the collector efficiency in comparison with water as a working fluid. This also has been observed that the thermal efficiency of collector increases with a decrease in the temperature reduced parameter.

Keywords Solar radiation · Nanofluids · Thermal efficiency · Thermal collector

S. Sharma (✉)

Mechanical Engineering Department, ASET, Amity University, Noida, Uttar Pradesh, India
e-mail: shubhamsharma1986@gmail.com; ssharma32@amity.edu

S. Tiwari

Krishna Engineering College, Ghaziabad, India

A. K. Tiwari

Mechanical Engineering Department, IET, Lucknow, Uttar Pradesh, India

G. Nandan

Mechanical Engineering Department, Amity University Uttar Pradesh, Noida, India
e-mail: gopalnandan@gmail.com

R. Prakash

AIT, Amity University Uttar Pradesh, Noida, Uttar Pradesh, India

12.1 Introduction

Solar collectors are the kind of green energy devices which are most preferred to utilize this free energy source in domestic and industrial applications. These collectors are very efficient to absorb the solar radiation by the absorber plate and convert it into the heat and then transfer this heat into conventional fluids like water. Flat-plate collectors are the most primitive and most common type of collectors, but these collectors are suffered from relatively low efficiency with the use of conventional fluids. To overcome this critical problem, an innovative type of fluid was invented by Choi [1] (1995) which is called “nanofluid.” Nowadays, most of the scientists and engineers are focusing on new nanotechnology and most efficient devices to harness solar energy. The mixture of nanoparticles (1–100 nm) and base fluids is known as nanofluids which have superior thermal properties to enhance the performance of the collectors.

Noghrehabadi et al. [2] have elucidated the collector efficiency of square flat-plate type with SiO_2 /water nanofluid without a surface-active agent and 1% particle volume concentration of nanofluid and mass flux rates from 0.35 to 2.8 l/min. Bazdidi-Tehrani et al. [3] examined that the enhancement in ribbed duct efficiency was approximately 10% more than the efficiency of the plain duct, so the collector efficiency was increased more with the selection of ribbed duct in flat-plate collector as compared to the plain duct at a different volume fraction of nanofluids. Said et al. [4] studied that the maximum efficiency of energy and exergy was enhanced up to 95.12% and 26.25% in comparison with water as a base fluid which was observed up to 42.07 and 8.77% of flat-plate solar collectors, respectively.

Nasrin et al. [5] have taken four different types of nanofluid like Al_2O_3 –water nanofluid, Ag–water nanofluid, CuO–water nanofluid, and Cu–water nanofluid. Faisal et al. [6] analyzed the four different nanofluids like SiO_2 , Al_2O_3 , TiO_2 , and CuO at different particle concentrations. Meibodi et al. [7] have been conducted an experiment about the thermal performance of FPSC using SiO_2 /EG–water nanofluids experimentally. Samples were prepared for 0.018, 0.032, and 0.045 kg/s mass flow rates including 0, 0.50, 0.75, and 1.0% particle volume concentration. Sarkar et al. [8] reviewed the recent research work, development, and applications of hybrid nanofluids. In this review, the author has summarized the thermophysical properties, synthesis, pressure drop, heat transfer characteristics, applications, and challenges of a hybrid type of nanofluids. The review examined that the hybrid nanofluids have excellent properties to enhance the thermal performance, but still more research work is required in this field. Nasrin et al. [9] examined the numerical values of irradiation (200, 215, 230, and 250 W/m^2) and inner diameter (0.01, 0.012, 0.013, and 0.015 m) of collector at 2% particle volume concentration of Cu–water nanofluid for calculating the mean bulk temperature, collector efficiency, outlet temperature of DM water and Cu–water nanofluid of flat-plate collector. Mirzaei et al. [10] had studied the optimal solution of FPC using Al_2O_3 –water nanofluid experimentally. Muhammad et al. [11] reviewed the usage of different types of nanofluids in the flat-plate and

evacuated tube collectors. Said et al. [12] has been analyzed about the entropy generation theoretically and also determined the exergy efficiency and pumping power of FPSC with the use of SWCNTs–water nanofluid. Results illustrated that the reduction in entropy generation was observed about 4.34% and the enhancement of the heat transfer coefficient was around 15.33%. A penalty of pumping power had obtained around 1.20% more than the conventional fluids like water. Keyvani et al. [13] had focused on the variation in thermal conductivity using CeO₂-EG. Results revealed that the enhancement in thermal conductivity was observed about 22% at 2.5% particle concentration and 50 °C temperature. Colangelo et al. [14] had investigated the new approach for reduction in sedimentation with dispersing the nanoparticles in the base fluid. Alim et al. [15] had used different nanoparticles like CuO, Al₂O₃, TiO₂, and SiO₂, respectively, with water as a base fluid and analyzed the entropy generation and pressure drop in FPSC. Results revealed that the maximum reduction in entropy generation was found around 4.34% and maximum enhancement in heat transfer coefficient was observed about 22.15%, respectively, in comparison with conventional fluid, and also, a penalty had considered in pumping power around 1.58%.

Said et al. [16] had investigated the thermophysical properties of Al₂O₃–water/EG nanofluid at the particle concentration of 0.05 and 0.1% at 25–80 °C temperature range. Hawwash et al. [17] have been illustrated about the performance of collector with the use of alumina particle dispersed in double distilled water as base fluid at a wide range of concentrations from 0.1 to 3%. Vincely et al. [18] investigated the FPC performance with the graphene oxide nanofluid. Results exhibited that the maximum collector efficiency was observed about 7.3% at 0.02% particle concentration and 0.0167 kg/s mass flow rate of graphene oxide nanofluid as compared to demineralized water used as a base fluid and maximum enhancement in heat transfer coefficient was measured about 11.5% at same volume concentration. Ziyadanogullari et al. [19] illustrated the thermophysical properties and collector efficiency at the particle concentration of 0.2%, 0.4%, and 0.8% for three different nanofluids as AhCb–water, CuO–water, and TiCh–water, respectively. Various researchers [20–31] investigated the performance with the various nanofluids.

The objectives of the present work is to evaluate the performance of flat-plate collector using CeO₂/water nanofluid and to find optimum vol. concentration of CeO₂/water nanofluid for which the thermal performance is maximum along with the exergetic performance evaluation using CeO₂/water nanofluid.

12.2 Preparation and Characterization of Nanofluids

Synthesis of CeO₂/water nanofluid is done by mixing of nanofluid in a beaker filled with double distilled water. The two-step method is the most effective method for the preparation of nanofluid and samples have been prepared for experimentation of flat-plate collector and characterization of nanofluid. In this method, CeO₂–water nanoparticles with 30 nm particle size are dispersed into the base fluid. To attain

proper stability of nanoparticles in base fluid, the repetition of mechanical mixing and ultrasonic sonification is done at the time of performing a test of each sample. Volume concentration (%) is calculated using the following formula:

$$\varphi \times 100 = \frac{\left[\frac{W_{\text{particle}}}{\rho_{\text{particle}}} \right]}{\left[\frac{W_{\text{particle}}}{\rho_{\text{particle}}} \right] + \left[\frac{W_{\text{water}}}{\rho_{\text{water}}} \right]}$$

The thermophysical properties of the nanofluid are measured systematically before performing the experiment. Thermal conductivity, viscosity, density, and specific heat are the essential thermophysical properties of the nanofluid and measured experimentally for accurate and reliable measurement. Characterization of nanofluid is done at 0.25%, 0.50%, 0.75%, 1.0%, 1.25%, and 1.50% volume concentration and 55 °C, 60 °C, 65 °C, 70 °C, 75 °C, and 80 °C temperatures, respectively. Samples are prepared for characterization of CeO₂/water nanofluid at varying temperature (55, 60, 65, 70, 75, and 80 °C) and volume fraction (0.25, 0.50, 0.75, 1.0, 1.25, and 1.50%) for measuring thermophysical properties (thermal conductivity, viscosity, density, and specific heat) experimentally.

The values of the thermal conductivity of nanofluid are measured using a hot wire transient technique (KD-2 Pro thermal properties analyzer, Decagon company, Inc., USA). A microprocessor and a thermoresistor are used to control and measure the heat conduction in the needle-like probe with a 1.3 mm diameter and 60 mm length. Before measurement, the calibration of the sensor probe is carried out at room temperature of 25 °C by the measurement of thermal conductivity of DM water 0.600 W/m K, which is favorable for accurate measurement. A KD-2 Pro thermal properties analyzer has indicated the repeatability and the accuracy which is specified by the manufacturer, i.e., ±5.0% and ±4.0%, respectively. The viscosity of the used nanofluid is measured using the LVDV-II + Pro Brookfield Viscometer. Specific heat is an important thermophysical property of the nanofluids which is essential for absorbing and transporting the quality of heat energy to enhance the performance of the nanofluid. The superiority of nanofluid over conventional fluids is obtained from lesser specific heat capacity. Specific heat is inversely proportional to the increase in particle volume concentration which is favorable to enhance heat transport capacity and absorbing medium of the nanofluids.

12.3 Results and Discussions

Characterization of nanofluid is done at a wide range of volume concentration (0.25–1.50% vol. conc. at an interval of 0.25%) and temperature (55–80 °C at an interval of 5 °C). Samples are prepared for characterization of CeO₂/water nanofluid at varying temperatures and volume fraction (0.25–1.50% Vol. conc. at an interval of 0.25%) for measuring thermophysical properties (thermal conductivity, viscosity, density, and

specific heat) experimentally. Experimental results indicate that observed thermal conductivity is maximum at 1.50% volume concentration with 80 °C as compared to water. The thermal conductivity ratio is determined at varying temperature and at a different volume concentration of nanofluid. The ratio of thermal conductivity is 23.18%, 23.19%, 24.10%, 24.53%, 24.80%, and 25.18% for 0.25%, 0.50%, 0.75%, 1.0%, 1.25%, and 1.50% volume concentration at 55 °C, respectively. Similarly, at 60 °C, the ratio of thermal conductivity is 26.02%, 26.33%, 26.74%, 26.85%, 27.25%, and 27.76% at same volume concentration; for 65 °C, the ratio of thermal conductivity is 27.91%, 28.68%, 29.08%, 29.47%, 29.86%, and 30.65% at same volume fraction; for 70 °C, the ratio of thermal conductivity is 31.54%, 31.66%, 31.88%, 32.09%, 32.46%, and 33.99% at same volume concentration; for 75 °C, the ratio of thermal conductivity is 33.91%, 34.95%, 34.99%, 35.49%, 35.83%, and 37.93% at same volume fraction; and for 80 °C, the ratio of thermal conductivity is 36.43%, 38.40%, 38.72%, 39.04%, 39.35%, and 41.72%, respectively, at same volume concentration. The graph between thermal conductivity ratio and the temperature is shown in Fig. 12.1. Results exhibit that the maximum ratio of thermal conductivity of nanofluid and DM water is observed 41.72% at an 80 °C temperature with 1.50% volume concentration and a minimum ratio of thermal conductivity is observed 23.18% at 55 °C with 0.25% volume concentration.

Experimental results exhibit that the viscosity increases linearly with an increase in particle volume fraction and a decrease in temperature limits. Results exhibit that the maximum viscosity is observed 1.587 mPa.s for 1.5% volume concentration of nanofluid and 0.480 mPa.s for water and minimum viscosity is observed 0.788 mPa.s for 0.25% volume fraction of nanofluid and 0.310 mPa.s for water at 80 °C temperature. From the observation of experimental data, it is concluded that the viscosity increases linearly with particle volume fraction due to cohesive forces among like and unlike molecules which increase at higher particle volume concentration as shown in Fig. 12.2 for CeO₂/water-based nanofluid, respectively. Further, viscosity decreases with an increase in temperature because of fall in cohesive forces predominantly,

Fig. 12.1 Relative thermal conductivity versus volume concentration

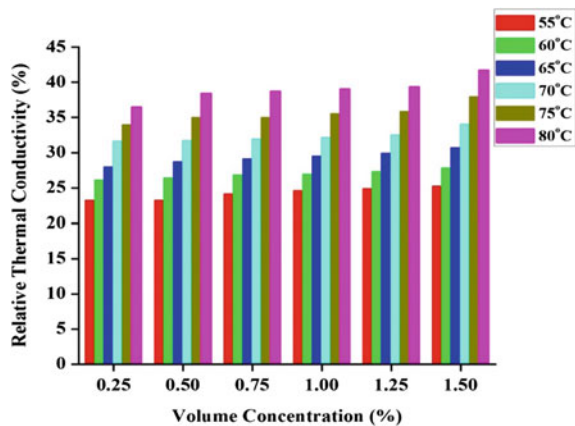
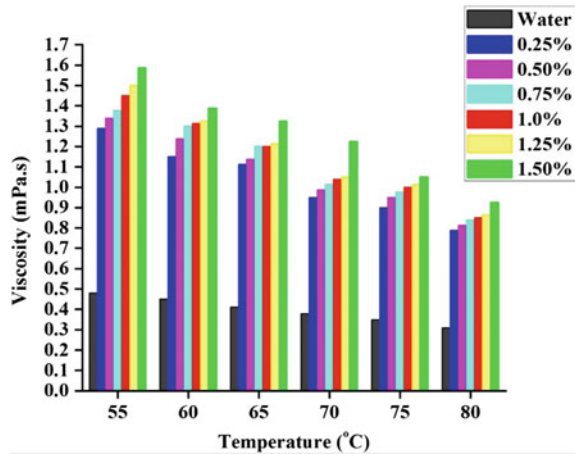


Fig. 12.2 Viscosity versus temperature graph at varying concentrations

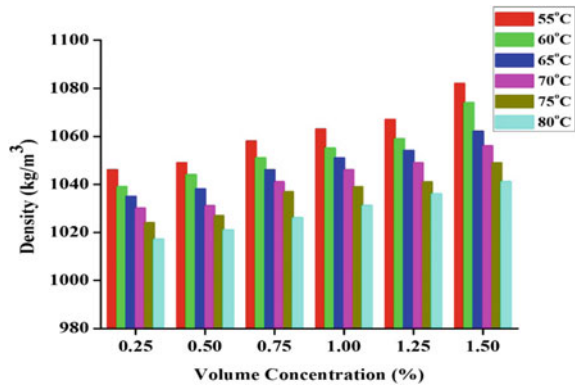


and across the adjacent layers, the viscosity increases marginally due to enhanced momentum transfer. Viscosity is more expressive in liquids due to cohesive forces than due to momentum transfer across the adjacent layers of the fluids.

The density of nanofluid is the thermophysical property which increases linearly with an increase in particle volume concentration. The high density of nanofluid has a negative impact on the efficiency of heat energy devices based on nanofluids. High density increases the entropy generation of nanofluid and also enhances the pressure drop which is the negative impact on heat transfer characteristics. So, experimental observation is necessary for precise measurement of nanofluid for performance analysis. Experimental results exhibit that the maximum density of the nanofluid is measured 1082 kg/m^3 at 55°C temperature with 1.50% particle volume concentration and a minimum density of nanofluid is measured 1017 kg/m^3 at 80°C temperature with 0.25% volume fraction. The effect of temperature and particle volume concentration on density is investigated experimentally. In this study, density and viscosity of nanofluids are the two important properties which affect the pumping power and pressure drop characteristics. Mixing rule is preferred for measuring the density of nanofluid experimentally. Results reveal from experimental data that the density is increased with particle volume concentration and decreased with an increase in temperature. The graphs between density versus temperature and density versus particle volume concentration are shown in Fig. 12.3.

Specific heat is an important thermophysical property of the nanofluids which is essential for absorbing and transporting the quality of heat energy to enhance the performance of the nanofluid. The superiority of nanofluid over conventional fluids is obtained from lesser specific heat capacity. Specific heat is inversely proportional to the increase in particle volume concentration which is favorable to enhance heat transport capacity and absorbing medium of the nanofluids. Maximum specific heat capacity is measured 3988 J/kg K at 80°C temperature with 0.25% particle volume concentration, and minimum specific heat capacity is measured 3532 J/kg K at

Fig. 12.3 Density versus volume concentration



55 °C with 1.50% volume concentration. Specific heat capacity increases with temperature and decreases with particle volume concentration as shown in Fig. 12.4 for CeO₂/water nanofluid, respectively. Effective thermal conductivity increases with particle volume concentration because of the specific heat of nanofluid which increases marginally with temperature than the decrease in volume concentration.

Experimental observation of flat-plate collector is administrated to find out variation in collector efficiency at varying mass flow rates (0.01, 0.02, 0.03, 0.04, and 0.05 kg/s) and at different particle volume concentrations (0.25, 0.50, 0.75, 1.0, 1.25, 1.50, and 2.0%). Figure 12.5 shows the relation between collector efficiency and particle concentration at varying mass flow rates. In this graph, collector efficiency increases for each mass flow rate of nanofluid with volume concentration up to a certain point of volume concentration (1%) and decreases the collector efficiency with particle concentration after this valuable point of concentration. Experimental results exhibit that the maximum efficiency of the flat-plate collector is observed 57.1% at optimum particle concentration (vol 1%) with 0.03 kg/s mass flow rate, respectively.

Fig. 12.4 Specific heat capacity versus volume concentration

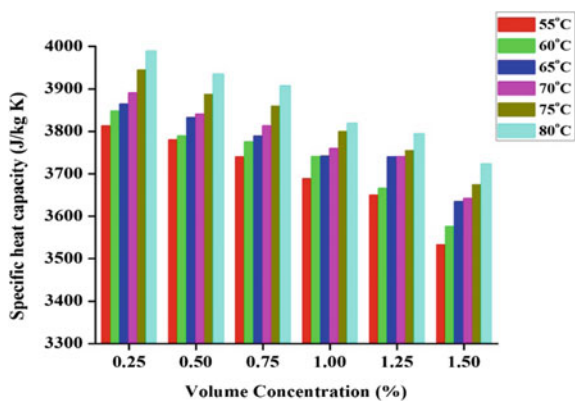


Fig. 12.5 Collector efficiency versus mass flow rate

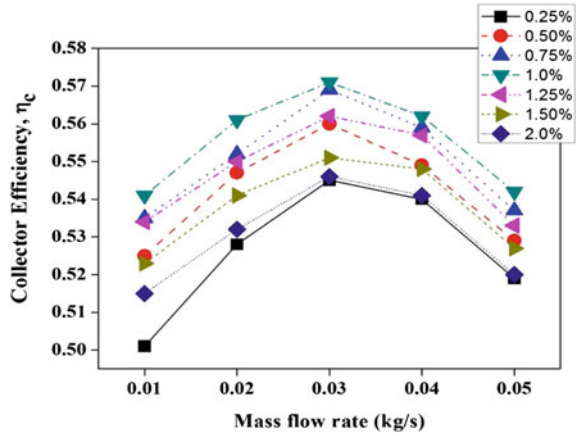
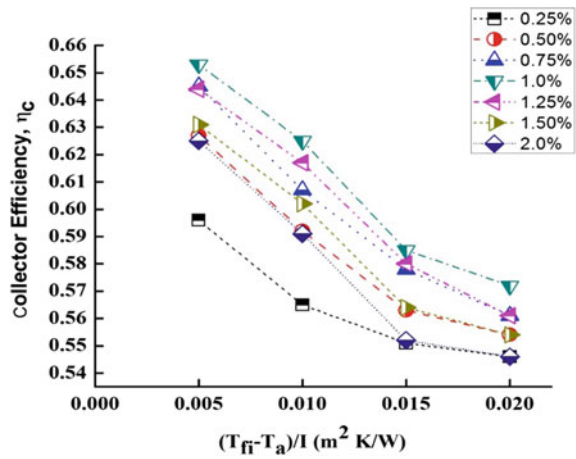


Figure 12.6 illustrates the collector efficiency and reduced temperature difference parameter at the volume concentration of 0.25–2%. From the observed data, the efficiency of the flat-plate collector is inversely proportional to temperature reduced parameter at different particle concentrations. It means collector efficiency increases with decreasing the temperature reduced parameter. Experimental results show that the maximum efficiency is observed 65.3% at optimum particle concentration (vol 1%) with temperature reduced parameter of 0.005 m² K/W and minimum collector efficiency is measured 54.6% at temperature reduced parameter of 0.02 m² K/W with the particle volume fraction of 2%, respectively. So, the temperature reduced parameter should be minimum for enhancement in the efficiency of flat-plate collector.

Fig. 12.6 Collector efficiency versus reduced temperature difference parameter



12.4 Conclusion

The present work focuses on improvement in thermal performance of flat-plate collector using CeO₂–water nanofluid at varying mass flow rates (0.01, 0.02, 0.03, 0.04, and 0.05 kg/s) and different particle volume concentrations (0.25%–1.5%), respectively. Thermophysical properties of nanofluid are investigated experimentally at different particle volume concentrations and at different temperatures (55–80 °C) and observe that the maximum enhancement in thermal conductivity is obtained 41.7% at 80 °C temperature with 1.5% volume concentration. On the basis of various experiments, it has been found that 1.0% volume concentration is optimum for different operating conditions. At optimum particle volume concentration and 0.03 kg/s mass flow rate, maximum collector efficiency has been calculated at 57.1%. At 0.005 m² K/W temperature reduced parameter and optimum volume fraction, efficiency is observed 65.3%, and for 700 W/m² intensity of radiation, maximum instantaneous efficiency is found 58.1% at an optimum concentration.

References

1. S.U.S. Choi, J.A. Eastman, Enhancing Thermal Conductivity of Fluids with Nanoparticles (ASME International Mechanical Engineering Congress & Exposition, San Francisco, CA, vol. 66. pp. 99–105, 1995)
2. A. Noghrehabadi, E. Hajidavalloo, M. Moravej, Experimental investigation of the efficiency of the square flat-plate solar collector using SiO₂/water nanofluid. *Case Stud. Therm. Eng.* **8**, 378–386 (2016)
3. F. Bazdidi-Tehrani, A. Khabazipur, S.I. Vasefi, Flow and heat transfer analysis of TiO₂/water nanofluid in a ribbed flat-plate solar collector. *Renew. Energy* **122**, 406–418 (2018)
4. Z. Said et al., Thermophysical properties of single-wall carbon nanotubes and its effect on exergy efficiency of a flat plate solar collector. *Sol. Energy* **115**, 757–769 (2015)
5. R. Nasrin, S. Parvin, M.A. Alim, Heat transfer by nanofluids through a flat plate solar collector. *Procedia Eng.* **90**, 364–370 (2014)
6. M. Faizal et al., Energy, economic and environmental analysis of metal oxides nanofluid for a flat-plate solar collector. *Energy Convers. Manag.* **76**, 162–168 (2013)
7. S. Salavati Meibodi et al., Experimental investigation on the thermal efficiency and performance characteristics of a flat plate solar collector using SiO₂/EG–water nanofluids. *Int. Commun. Heat Mass Transfer* **65**, 71–75 (2015)
8. J. Sarkar, P. Ghosh, A. Adil, A review on hybrid nanofluids: recent research, development, and applications. *Renew. Sustain. Energy Rev.* **43**, 164–177 (2015)
9. R. Nasrin, M. Alim, Thermal performance of nanofluid filled solar flat plate collector. *Int. J. Heat Technol.* **33**(2), 17–24 (2015)
10. M. Mirzaei, S.M.S. Hosseini, A.M.M. Kashkooli, Assessment of Al₂O₃ nanoparticles for the optimal operation of the flat plate solar collector. *Appl. Therm. Eng.* **134**, 68–77 (2018)
11. M.J. Muhammad, I.A. Muhammad, N.A.C. Sidik, M.N.A.W.N. Yazid, Thermal performance enhancement of flat-plate and evacuated tube solar collectors using nanofluid: a review. *Int. Commun. Heat Mass Transfer* **76**, 6–15 (2016)
12. Z. Said, R. Saidura, N.A. Rahim, M.A. Alim, Analyses of exergy efficiency and pumping power for a conventional flat plate solar collector using SWCNTs based nanofluid. *Energy Build.* **78**, 1–9 (2014)

13. M. Keyvani, M. Afrand, D. Toghraie, M. Reiszadeh, An experimental study on the thermal conductivity of cerium oxide/ethylene glycol nanofluid: developing a new correlation. *J. Mol. Liq.* (2018)
14. G. Colangelo, E. Favale, A. De Risi, D. Laforgia, A new solution for reduced sedimentation flat panel solar thermal collector using nanofluids. *Appl. Energy* **111**, 80–93 (2013)
15. M.A. Alim, Z. Abidin, R. Saidur, A. Hepbasli, M.A. Khairul, N.A. Rahim, Analyses of entropy generation and pressure drop for a conventional flat plate solar collector using different types of metal oxide nanofluids. *Energy Build.* (2013)
16. Z. Said, M.H. Sajid, M.A. Alim, R. Saidur, N.A. Rahim, Experimental investigation of the thermophysical properties of Al_2O_3 -nanofluid and its effect on a flat plate solar collector. *Int. Commun. Heat Mass Transfer* (2013)
17. A.A. Hawwash, A.K.A. Rahman, S.A. Nada, S. Ookawara, Numerical investigation and experimental verification of performance enhancement of flat plate solar collector using nanofluids. *Appl. Therm. Eng.* (2017)
18. D.A. Vincely, E. Natarajan, Experimental investigation of the solar FPC performance using graphene oxide nanofluid under forced circulation. *Energy Conv. Manag.* **117**, 1–11 (2016)
19. N.B. Ziyadanogullari, H.L. Yucel, C. Yildiz, Thermal performance enhancement of flat-plate solar collectors by means of three different nanofluids. *Therm. Sci. Eng. Prog.* (2018)
20. S.K. Verma, A.K. Tiwari, D.S. Chauhan, Experimental evaluation of flat plate solar collector using nanofluids. *Energy Conv. Manag.* **134**, 103–115 (2017)
21. S.K. Verma, A.K. Tiwari, Application of nanoparticles in solar collectors: a review. *Mater. Today Proc.* **2**(4–5), 3638–3647 (2015)
22. S.K. Verma, A.K. Tiwari, Characterization of nanofluids as an advanced heat transporting medium for energy systems. *Mater. Today Proc.* **4**(2), 4095–4103 (2017)
23. A.K. Tiwari, P. Ghosh, J. Sarkar, A.K. Tiwari, Solar water heating using nanofluids—a comprehensive overview and environmental impact analysis. *IJETAE* **3**(3), 221–224 (2013)
24. S. Sharma, A.K. Tiwari, S. Tiwari, R. Prakash, Viscosity of hybrid nanofluids: measurement and comparison. *J. Mech. Eng. Sci.* **12**(2), 3614–3623 (2018)
25. T.V.R. Sekhar, R. Prakash, G. Nandan, M. Muthuraman, Performance enhancement of a renewable thermal energy collector using metallic oxide nanofluids. *Micro Nano Lett.* **13**(2), 248–251 (2018)
26. T. Sekhar, G. Nandan, R. Prakash, M. Muthuraman, Investigations on viscosity and thermal conductivity of cobalt oxide- water nano fluid. *Mater. Today: Proc.* **5**(2), 6176–6182 (2018)
27. R.S. Rathour, V. Chauhan, K. Agarwal, S. Sharma, G. Nandan, Cooling of solar photovoltaic cell: using novel technique, in *Lecture Notes in Mechanical Engineering* (Springer, Singapore, 2019), pp. 521–529
28. S. Sharma, A.K. Tiwari, S. Tiwari, R. Prakash, Particle optimization of CeO_2 /water nanofluids in flat plate solar collector. *Int. J. Eng. Adv. Technol.* **9**(2), 1467–1474 (2019)
29. A.K. Suresh, S. Khurana, G. Nandan, G. Dwivedi, S. Kumar, Role on nanofluids in cooling solar photovoltaic cell to enhance overall efficiency. *Mater. Today: Proc.* **5**(9), 20614–20620 (2018)
30. T.V.R. Sekhar, R. Prakash, G. Nandan, M. Muthuraman, Pressure drop characteristics and efficiency enhancement by using TiO_2 - H_2O nanofluid in a sustainable solar thermal energy collector. *Int. J. Environ. Sustain. Dev.* **17**(2/3), 273 (2018)
31. T.V.R. Sekhar, R. Prakash, G. Nandan, M. Muthuraman, Preparation of Co_3O_4 - H_2O nanofluid and application to CR-60 concentrating solar collector. *Prog. Ind. Ecol. Int. J.* **11**(3), 227 (2017)

Chapter 13

Study of Hybrid Photovoltaic–Thermoelectric System for Efficiency Enhancement of Solar Cells



Sahitya Singh, Akshaj Arora, Vivek Kumar, Abhishek Verma, Hrishikesh Dhasmana, Amit Kumar and V. K. Jain

Abstract In the development of next-generation solar panels, high-energy conversion efficiency has been the focal point of global research in energy. More than 80% of the efficiency of solar panels is wasted. In order to materialize this wasted energy, there has been an emerging interest in innovating hybrid solar–thermoelectric systems. In this chapter, we propose a novel hybrid photovoltaic–thermoelectric system and its expansive experimental analysis. This modified system consists of a solar wafer, thermoelectric generator (TEG), and a heat sink, which is placed beneath the solar cell of the same size to dissipate heat. A series of experiments have been performed under certain laboratory conditions, which remain constant for all sets of experiments. The heat sink beneath the solar cell reduces the working temperature of the cell from 72 °C (without heat sink) to 52 °C (with heat sink and TEG), which leads to approximately 10% increment in the relative efficiency of the solar cell. Finally, a thermoelectric generator (TEG) is inserted between the solar cell and heat sink. The TEG adds an extra power of 1.2 mW to the total output of the system.

Keywords Photovoltaic · Hybrid system · Thermoelectric generator · Heat sink

13.1 Introduction

In this modern age, there is an ever-increasing focus on the growth of renewable energy technologies because of the worldwide awareness about the climate change, air pollution, oil spills and other hazardous effects of fossil fuels [1]. As a result of which, research in harnessing alternate energy such as solar, wind, geothermal, biomass, and others has expanded over the last few decades [2–4]. Based on the availability of raw material, cost of production and efficiency, solar energy harvesting is one of the most prominent ones [5, 6]. Monocrystalline silicon (Si) cells offer a conversion efficiency greater than 20%, which makes them the most efficient Si

S. Singh · A. Arora · V. Kumar · A. Verma (✉) · H. Dhasmana · A. Kumar · V. K. Jain
Amity Institute for Advanced Research and Studies (Materials & Devices), Amity University,
Noida, Uttar Pradesh 201303, India
e-mail: abhiverma10@gmail.com

© Springer Nature Singapore Pte Ltd. 2020
V. K. Jain et al. (eds.), *Advances in Solar Power Generation and Energy Harvesting*, Springer Proceedings in Energy,
https://doi.org/10.1007/978-981-15-3635-9_13

cells. Furthermore, the classification includes polycrystalline solar cells, which have an efficiency from 14% to 16% and amorphous solar cells, which have the lowest efficiency (6–9%), [2]. Some latest amorphous solar panels, which are equipped with shade-resistant technology, perform better than the conventional amorphous solar panels [7]. Although the cost of solar panels has decreased over the years, for solar technology to cause a worldwide energy revolution, the price of commercially available solar panels needs to be decremented such that the trade-off between efficiency and cost leads to a win-win situation. One way of doing this is to harness the energy wasted from solar panels. Approximately, more than 50% of the efficiency of the solar panels is wasted due to rise in temperature. The relation between temperature and output characteristics of the solar cell is expressed in (13.1) [8].

$$J = -J_{\text{ph}} + J_0(e^{qV/nkT} - 1) \quad (13.1)$$

where J_{ph} represents the photo-generated current density, V is the terminal voltage, k is the Boltzmann constant, and η is the ideality factor.

In the current era, efforts are made in two directions: creating new materials and modeling the physical aspects of the solar panel to avoid energy loss, one way of doing this is to make advantageous use of thermoelectric generators (TEGs) [9–13]. Thermoelectric generator is a solid-state device which works on the principle of Seebeck effect; that is, it converts the temperature gradient into electricity. Several studies have been performed on the manufacturing of TEG module for higher efficiency [14, 15]. Basically, TEGs are of two types: p-type and n-type, and they made up of different materials such as Bi_2Te_3 , PbTe , CoSb_3 , Sb_2Te_3 . The performance of a TEG depends on various factors such as the temperature on hot and cold sides of the TEG, thermal and electrical conductivity, and Seebeck coefficient.

In general, the performance of a TEG module is determined by its figure of merit, which represents the conversion efficiency of heat energy to electrical energy. Studies have shown that TEG made up of organic materials has high efficiency, but they are highly expensive too. Out of all the materials used for developing TEGs, Bi_2Te_3 is one of the few materials which have better performance at room temperature. It offers a figure of merit (ZT) between 0.8 and 1.0, which is independent of the temperature. TEGs are widely used in a variety of applications, such as harvesting energy from stove heat [16], scavenging energy from heat emitted out of automobiles [17–19], and aerospace industry [20]. Furthermore, there is an emerging focus on innovating hybrid photovoltaic–thermoelectric systems to augment the overall efficiency of a solar panel [21, 22]. Various models have been developed to optimize the performance of such systems [23, 24]. The principle of hybrid thermoelectric systems is even investigated for dye-synthesized solar cells [25], where the performance of dye-synthesized solar cell is significantly enhanced by developing carbon nanotubes of thermoelectric materials such as bismuth telluride (Bi_2Te_3) or directly employing thermoelectric generators. While energy loss minimization aspects are explored in Si-based solar panels, new materials are explored in non-Si-based photovoltaic technology.

In this chapter, we present a novel hybrid photovoltaic–thermoelectric system in which performing a series of experiments is proven to be more efficient than a standard solar system.

13.2 Experimental Setup and Preliminary Studies

The hybrid photovoltaic–thermoelectric system consists of a Si wafer, TEG, and heat sink. Leakproof property of a standard solar panel is incorporated by using a glass plate and adequate insulating materials to create the greenhouse effect inside the system.

The idea of inserting TEG in-between wafer and sink is fostered by performing few preliminary studies. All the laboratory experiments are performed under a sun lamp, which has a constant radiation intensity of 880 W/m^2 . The radiation intensity of the sun lamp is measured by a Pyranometer. Initially, only Si wafer is placed inside the system to examine its temperature variation. Then, heat sink is added to the system, and as expected, the steady-state temperature of wafer decreases. This decrement in wafer's temperature increases the overall efficiency of the system. In another experiment, only Si wafer and TEG are used in the system such that a significant portion of the TEG is exposed to the ambient. Power generated by the TEG is directly proportional to the temperature difference (ΔT) between hot and cold junctions. In order to increase the temperature difference (ΔT), a heat sink is placed underneath the cold end of the TEG. The difference in temperature is measured using a thermocouple as shown in Fig. 13.2. The purposed system and the experimental setup are illustrated in Figs. 13.1 and 13.2, respectively.

In order to understand the behavior of this system at regions with sub-zero temperatures, ice is placed underneath the heat sink, which further reduces its temperature.

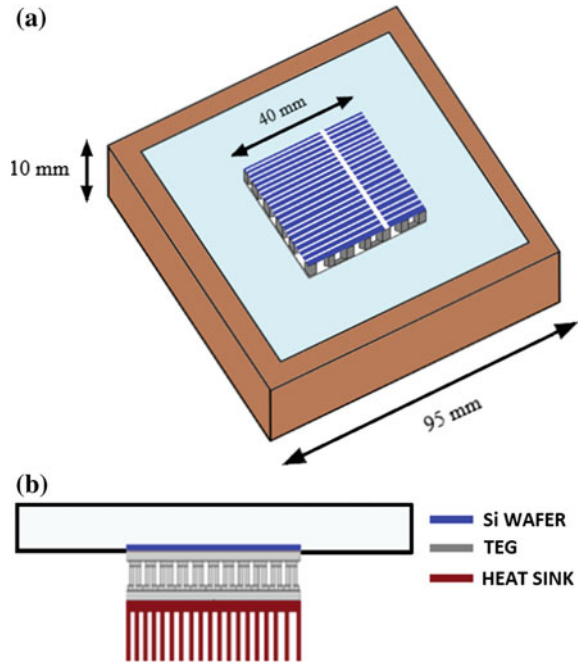
13.3 Results and Discussion

The hybrid system is appropriately scrutinized by performing all the experiments mentioned in the preliminary study, i.e., wafer, wafer + sink, wafer +TEG, wafer + TEG + sink, and wafer + TEG + sink + ice. Each experiment is performed for 2 h, and the temperature of wafer reached saturation around 20 min. The temperatures are given in Fig. 13.3.

A summary of the optimized experiments, wafer + TEG + sink, and wafer + TEG + sink + ice is given in Table 13.1 where various characteristics such as steady-state temperature of the wafer (T_w), the temperature of the cold side of the TEG (T_c), ΔT and power (P) generated from the TEG are obtained.

At steady-state condition, measured ΔT for both cases is 15 and 36 °C, respectively, and the corresponding output power generated by the TEG is 1.2 and 2.4 mW.

Fig. 13.1 **a** Hybrid photovoltaic–thermoelectric system and **b** side view of the system



It is also important to note that the saturation temperature of the wafer in the proposed system is significantly lower as compared to a standard solar panel. This drop in the saturation temperature increases the overall efficiency of the proposed system. However, if the temperature of the wafer further increases, ΔT will also increase and this will eventually result in more output power.

13.4 Conclusion

The proposed hybrid photovoltaic–thermoelectric system consists of a Si wafer, TEG, and a heat sink. All the experiments in the preliminary studies have been performed under a lamp with a constant radiation intensity of 880 W/m^2 . The temperature of wafer is reached to $52 \text{ }^\circ\text{C}$ in the proposed system, and the output power generated by the TEG adds an extra 1.2 mW to the total output of the system. Moreover, the hybrid solar cell is also examined at higher altitudes conditions, where the saturation temperature of wafer is further reduced to $44 \text{ }^\circ\text{C}$, which significantly increases the efficiency of the wafer. Alongside higher solar conversion efficiency, the output power generated by the TEG doubled to 2.4 mW . Moreover, the proposed system produces an extra power of 1.2 mW per $40 \times 40 \text{ mm}^2$ of the wafer area. Therefore, the designed system has a promising potential to be implemented on a large scale.

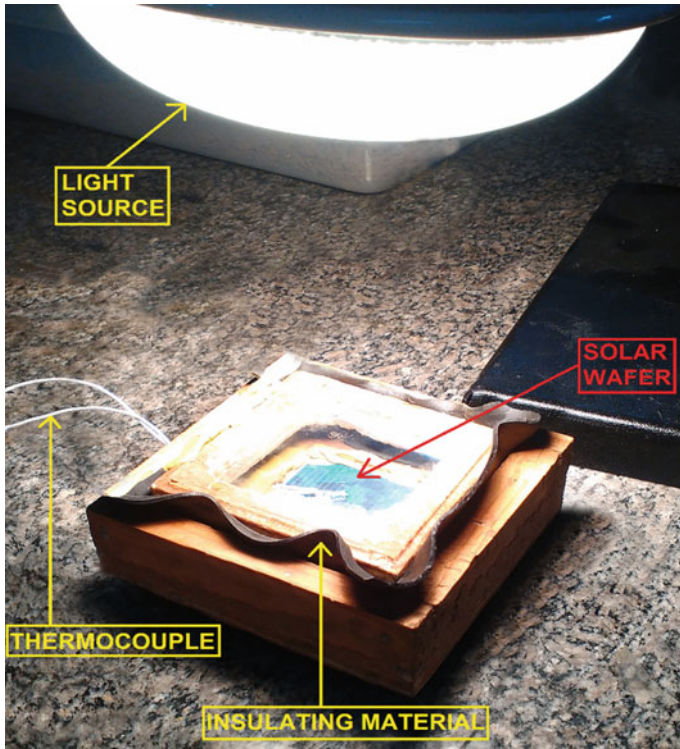


Fig. 13.2 Experimental setup for the hybrid photovoltaic–thermoelectric system

Fig. 13.3 Measured steady-state temperatures for each experiment

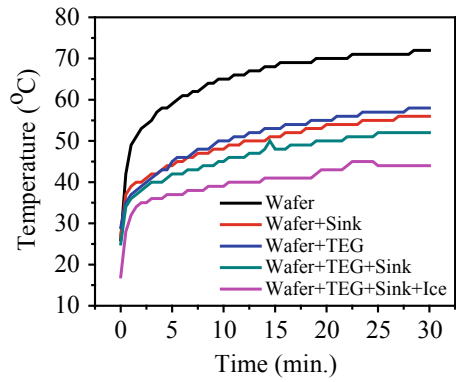


Table 13.1 Measured characteristics

Characteristics	Wafer + TEG + Sink	Wafer + TEG + Sink + Ice
T_w (°C)	52	44
T_c (°C)	37	8
ΔT (°C)	15	36
V (mV)	30	40
I (mA)	40	60
P (mW)	1.2	2.4

Acknowledgements The authors would like to thank Mr. Manas Nyati, RF/Wireless Engineer II at Shure incorporated for his help in photography.

References

1. I. Yahyaoui (ed.), *Advances in Renewable Energies and Power Technologies*, vol 1. Solar and Wind Energies (Elsevier, 2018)
2. V.V. Tyagi, N.A.A. Rahim, N. Abd Rahim, A. Jeyraj, L. Selvaraj, Progress in solar PV technology: research and achievement. *Renew. Sustain. Energy Rev.* **20**, 443–461 (2013)
3. E. Ghiani, G. Pisano, Impact of renewable energy sources and energy storage technologies on the operation and planning of smart distribution networks, in *Operation of Distributed Energy Resources in Smart Distribution Networks* (Academic Press, 2018), pp. 25–48
4. O. Ellabban, H. Abu-Rub, F. Blaabjerg, Renewable energy resources: current status, future prospects and their enabling technology. *Renew. Sustain. Energy Rev.* **39**, 748–764 (2014)
5. N.S. Lewis, Toward cost-effective solar energy use. *Science* **315**(5813), 798–801 (2007)
6. N.S. Lewis, Research opportunities to advance solar energy utilization. *Science* **351**(6271), aad1920 (2016)
7. F. Attivissimo, A. Di Nisio, A.M.L. Lanzolla, M. Paul, Feasibility of a photovoltaic–thermoelectric generator: performance analysis and simulation results. *IEEE Trans. Instrum. Measure.* **64**(5), 1158–1169 (2015)
8. P. Singh, N.M. Ravindra, Temperature dependence of solar cell performance—an analysis. *Solar Energy Mater Solar Cells* **101**, 36–45 (2012)
9. K.A. Moharram, M.S. Abd-Elhady, H.A. Kandil, H. El-Sherif, Enhancing the performance of photovoltaic panels by water cooling. *Ain Shams Eng. J.* **4**(4), 869–877 (2013)
10. V. Kumar, A. Kumar, H. Dhasmana, A. Verma, P.K. Bhatnagar, V.K. Jain, Efficiency enhancement of silicon solar cells using highly porous thermal cooling layer. *Energy Environ.* **29**(8), 1495–1511 (2018)
11. V. Kumar, A. Kumar, H. Dhasmana, A. Verma, A. Kumar, P.K. Bhatnagar, V.K. Jain, Enhanced working efficiency of Si solar cell by water induced nano-porous thermal cooling layer. *Mater. Res. Express* **6**(9), 095053 (2019)
12. N. Amrizal, D. Chemisana, J.I. Rosell, Hybrid photovoltaic–thermal solar collectors dynamic modeling. *Appl. Energy* **101**, 797–807 (2013)
13. D. Champier, Thermoelectric generators: a review of applications. *Energy Convers. Manage.* **140**, 167–181 (2017)
14. C. Ofoegbu, S. Mazumder, Computational modeling of a solar thermoelectric generator. *J. Thermal Sci. Eng. Appl.* **7**(4), 041004 (2015)

15. E. Toberer, Solar thermoelectric generators: pushing the efficiency up. *Nat. Energy* **1**(11), 16172 (2016)
16. I. Osmani, M. Haque, A. Hossain, M. Haque, H.K. Bhuiyan, Fabrication of a biomass stove and conversion of electricity from waste heat using TEG, in *AIP Conference Proceedings*, vol 1919, no. 1 (AIP Publishing, 2017), p. 020050
17. D. Baek, C. Ding, S. Lin, D. Shin, J. Kim, X. Lin, Y. Wang, N. Chang, Reconfigurable thermoelectric generators for vehicle radiators energy harvesting, in *2017 IEEE/ACM International Symposium on Low Power Electronics and Design (ISLPED)* (IEEE, 2017), pp. 1–6
18. B. Orr, A. Akbarzadeh, M. Mochizuki, R. Singh, A review of car waste heat recovery systems utilising thermoelectric generators and heat pipes. *Appl. Thermal Eng.* **101**, 490–495 (2016)
19. K.T. Zorbas, E. Hatzikraniotis, K.M. Paraskevopoulos, Power and efficiency calculation in commercial TEG and application in wasted heat recovery in automobile, in *Proceedings of 5th European Conference on Thermoelectrics*, vol 8, p. 2007
20. A. Elefsiniotis, N. Kokorakis, T. Becker, U. Schmid, A novel high-temperature aircraft-specific energy harvester using PCMs and state of the art TEGs, in *Materials Today: Proceedings*, vol 2, no. 2 (2015), pp. 814–822
21. T.-C. Cheng, C.-H. Cheng, Z.-Z. Huang, G.-C. Liao, Development of an energy-saving module via combination of solar cells and thermoelectric coolers for green building applications. *Energy* **36**(1), 133–140 (2011)
22. P. Huen, W.A. Daoud, Advances in hybrid photovoltaic and thermoelectric generators. *Renew. Sustain. Energy Rev.* **72**, 1295–1302 (2017)
23. M.R. Ariffin, S. Shafie, W.Z.W. Hassan, N. Azis, M.E. Ya’acob, Conceptual design of hybrid photovoltaic-thermoelectric generator (PV/TEG) for automated greenhouse system, in *2017 IEEE 15th Student Conference on Research and Development (SCoReD)* (IEEE, 2017), pp. 309–314
24. R. Kiflemaryam, M. Almas, C. Lin, Modeling integrated Thermoelectric Generator-Photovoltaic Thermal (TEG-PVT) system, in *Proceedings of 2014 COMSOL Conference* (2014), pp. 1–5
25. H. Chang, Z.-R. Yu, Integration of dye-sensitized solar cells, thermoelectric modules and electrical storage loop system to constitute a novel photothermoelectric generator. *J. Nanosci. Nanotechnol.* **12**(8), 6811–6816 (2012)

Chapter 14

Periodical Imaging of Microstructure During Temperature Regulated Electrical Conductivity Measurements of Supercritically Synthesized Polypyrrole



Anjali Bisht, Rekha Sati, Kavita Singhal, Sameena Mehtab
and M. G. H. Zaidi

Abstract Electrochemically active conducting polymers are an important class of materials for applications in energy storage devices. Herein, we report the synthesis of an electrically conducting polypyrrole (PPY) through ferric chloride initiated chemical oxidative polymerization of pyrrole in presence of supercritical carbon dioxide at 70 and 80 °C. The formation of PPY was ascertained through various analytical methods. Polypyrrole graphite electrodes (PGEs) were fabricated through dispersion of PPY synthesized at 70 and 80 °C into graphite in presence of sulfonated polysulfone binder and named as PGE1 and PGE2, respectively. PGE2 demonstrated better DC conductivity over that of PGE1 with morphology retention up to 35 K. Electrochemical studies reveal superior capacitive performance of PGE2 in KOH electrolyte (97.74 F/g) and reduction in corrosion rate of steel electrode @0.16 mm/y.

14.1 Introduction

Electrochemically active conducting polymers are an important class of materials for applications in electronics and energy storage devices [1]. The major technical challenge in the performance of CPs-based electronic and energy storage systems is the loss in material integrity under prolonged exposure of temperature and electrolyte media [2–4]. The morphology of polymer and related composite materials is altered due to segmental movement of macromolecules under exposure of temperature and electrolyte media with time that imparts reduction in their conductivity and charges storage performance. Polyaniline, polypyrrole, polyindole are the common CPs employed for semiconducting and charge storage applications [5]. Among them,

A. Bisht (✉) · R. Sati · K. Singhal · S. Mehtab · M. G. H. Zaidi
Department of Chemistry, College of Basic Sciences and Humanities, G.B. Pant University of
Agriculture and Technology, Pantnagar, Uttarakhand 263145, India
e-mail: anjalibisht564@gmail.com

© Springer Nature Singapore Pte Ltd. 2020
V. K. Jain et al. (eds.), *Advances in Solar Power Generation
and Energy Harvesting*, Springer Proceedings in Energy,
https://doi.org/10.1007/978-981-15-3635-9_14

polypyrrole (PPY) has received increasing attention as electrode material owing to ease of preparation, environmental stability, electrical conductivity and charge storage [6]. In the present investigation, PPY was synthesized at various temperatures under supercritical conditions, and PPY/graphite electrodes (PGEs) were prepared in presence of sulfonated polysulfone (SPS). PPY-based electrodes with higher DC conductivity were selected and further investigated for morphological changes with temperature, capacitive behavior and corrosion stability.

14.2 Experimental

14.2.1 Materials

PPY was synthesized in a PID controlled high-pressure reactor (100 mL) procured from Ms PPI USA. The reactor was charged with pyrrole (0.25 g) and FeCl_3 (0.17 g). The cell was initially pressurized with carbon dioxide (99.98%) at 2200 psi at 70 and 80 °C for 8 h. The crude products in each of the cases were purified through successive washing with deionized water and named as P1 and P2, respectively [7].

14.2.2 Preparation of Electrodes

Polypyrrole graphite electrodes (PGEs) were fabricated through dispersion of PPY synthesized at 70 and 80 °C into graphite in presence of sulfonated polysulfone binder and named as PGE1 and PGE2, respectively.

14.3 Characterization

Fourier transform infrared (FTIR) spectra of samples were recorded on Thermo Nicolet in KBr from 4000 to 500 cm^{-1} on transmission mode. XRD spectra of powdered samples were recorded at room temperature over Rigaku-Geigerflex X-ray diffractometer using $\text{Cu-K}\alpha$ radiation ($\lambda = 0.154$ nm) in the range of 10°–70° at 30 kV and 15 mA with step size 0.05 and step time of 19.2 s. Thermo-oxidative stability of samples was investigated through simultaneous thermogravimetric-differential thermogravimetry-differential thermal analysis (TG-DTG-DTA) over EXSTAR TG/DTA 6300 instrument in static air in the temperature ranging from 30 to 700 °C. SEM was recorded on JEOL, JSM 6610 LV using a primary beam voltage of 20 kV. Electrical conductivities (σ_{DC}) of PGEs were evaluated over Keithley four-point probe conductivity meter. The effect of temperature on electrical conductivity of PGEs was investigated. Electrochemical measurements were performed

over IVIUM potentiostat–galvanostat at 1 mA with reference to Ag/AgCl electrode and Pt sheet as counter electrode in KOH (1 M). C_s was calculated from CV curves by using formula: $C_s = I/m (dV/dt)$ [8].

14.4 Results and Discussion

14.4.1 Spectral and Thermal Studies

Figure 14.1 demonstrates FTIR spectra of P2. Peak at 1546 and 1461 cm^{-1} corresponds to C–N and C–C stretching vibration is due to formation of 2, 5-substituted PPY [9]. Figure 14.2 represents XRD spectra of P2, where broad peak at 24.47° ($d = 36.3$ nm) reveals amorphous nature of PPY [10].

Fig. 14.1 FT-IR spectra of PPY

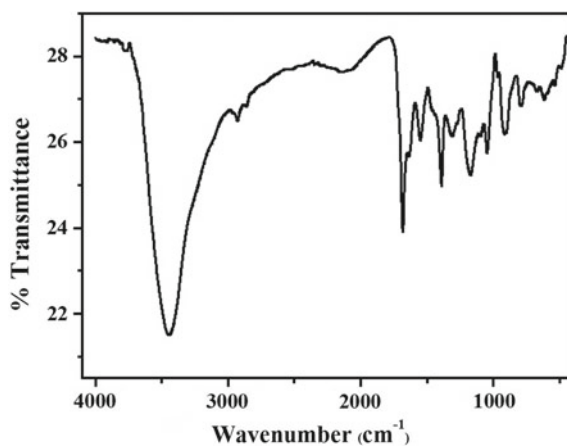
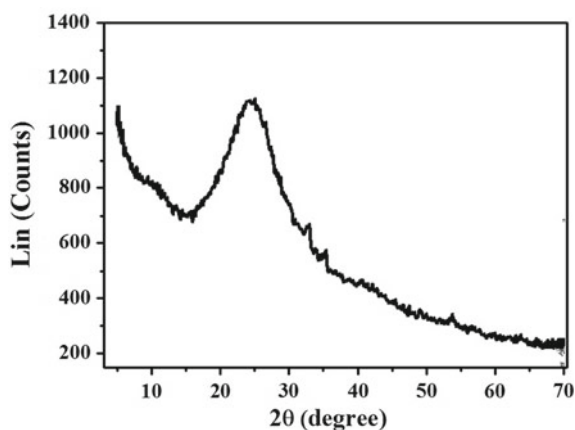


Fig. 14.2 XRD spectra of PPY



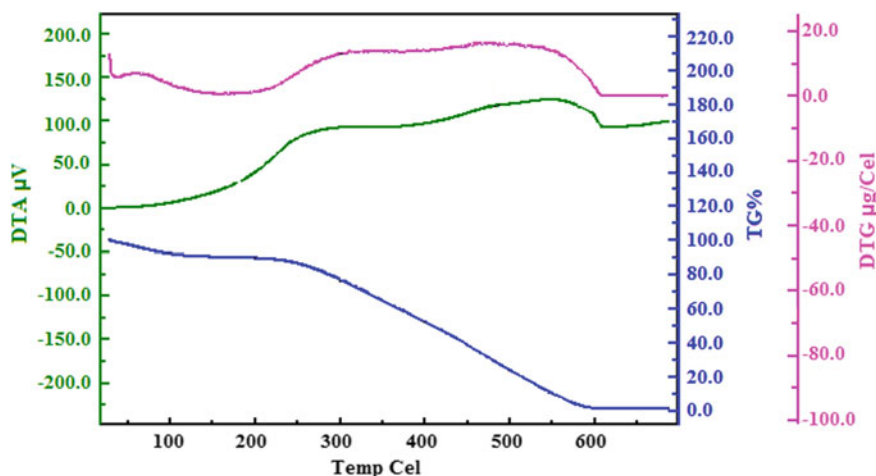


Fig. 14.3 Thermogram of PPY

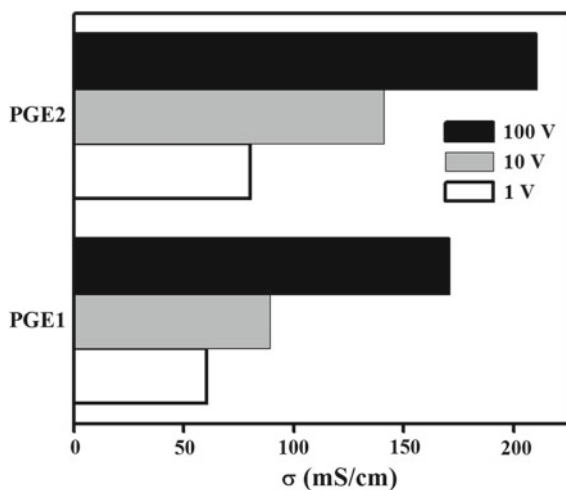
The thermal characteristics of P2 have been investigated through simultaneous TG-DTA-DTG (Fig. 14.3). P2 shows single step decomposition with temperature ranging from 200 to 600 °C. The corresponding weight residue (W_r , %) at onset and endset temperature were 89.74 and 2.0. Moisture may be responsible for the weight loss (W_L , %) of 10.26 before the onset temperature. Decomposition of P2 has been supported with broad DTA signal ranging from 89.1 to $-117.1 \mu\text{V}$ with peak temperature in the range of 278–482 °C. DTG reveals the rate of decomposition of P2 ranging from 13.06 to $16.14 \mu\text{g}/^\circ\text{C}$ with peak temperature ranging from 304 to 482 °C.

14.4.2 DC Conductivity

PGEs were further investigated for their electrical behavior. Measurement of σ_{DC} was conducted in the range of 1–100 V and 323–403 K. At 323 K, σ_{DC} of PGE1 and PGE2 was increased from 60.4 to 170.4 and 80.1 to 210.3, respectively, with voltage up to 100 V (Fig. 14.4).

This increase in σ_{DC} with voltage is due to the localized motion of trapped charges in PPY that induce the formation of polarons and bipolarons [11].

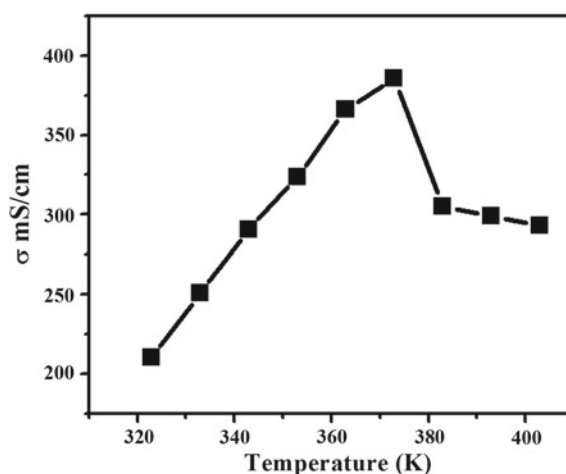
Fig. 14.4 Effect of voltage on DC conductivity of PPY



14.4.3 Effect of Temperature on Conductivity and Periodical Imaging of Microstructure

PGE with maximum electrical conductivity (σ_{DC} , mS/cm) was identified and microscopically imaged during temperature-dependent electrical conductivity (σ_{DC} , mS/cm) measurements. At variable voltage, PGE2 shows higher electrical conductivity than that of PGE1. PGE2 was, therefore, selected for onward investigation of electrical and electrochemical studies. Increase in temperature up to 373 K has raised the σ_{DC} to 385.5. Increase in temperature to 403 K has declined σ_{DC} of PGE2 to 292.9 (Fig. 14.5). The dependence of σ_{DC} on temperature can be attributed

Fig. 14.5 Variation in σ_{DC} (mS/cm) of PGE2 at various values of T (K) ranging from 323 to 403



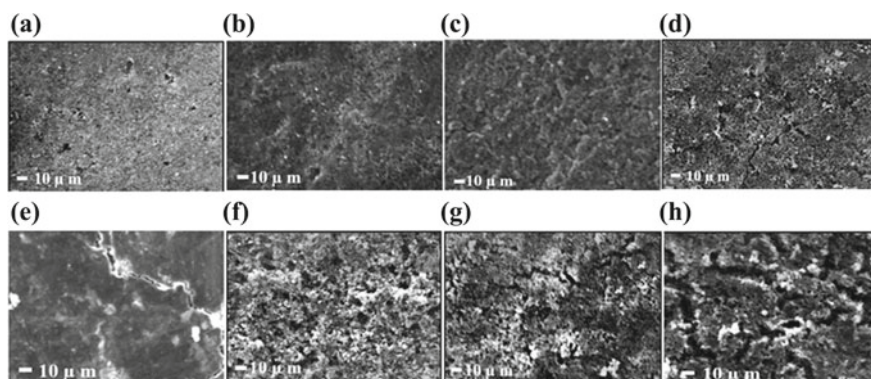


Fig. 14.6 SEM images of PPY at variable temperature (K) ranging from 323 to 403

to increased thermal energy at high temperatures, wherein electrons are excited from the valence band to conduction bands [12].

The morphological examination reveals the workability of electrodes for semiconductor applications 323–363 K. SEM images indicate retention in surface and bulk morphology of PGE2 up to 353 K with σ_{DC} of 323.5. Increase in temperature up to 383 K has declined the σ_{DC} to 305.1 with destruction in morphology of PGE2 (Fig. 14.6). Onward increase in temperature from 363 to 373 K further imparts a marginal increase in σ_{DC} ranging from 365.9 to 385.5 mS/cm with a distinct morphological disorder in electrode (Fig. 14.6e–f). Further, increase in temperature to 403 K has declined the σ_{DC} with complete destruction in the coating of material over electrode (Fig. 14.6g–h).

14.4.4 Electrochemical Behavior

The CV of PGE2 was recorded in a three-electrode assembly in various electrolytes (LiCl, NaOH and KOH) at identical concentration of 1.0 M. C_s values are strictly connected with the nature and surface of the electrode/electrolyte interface. The better the accessibility of the ions to the electrochemically active surface, the higher values of C_s are observed. The experiment was performed at common scan rate of 0.2–0.01 V/s, with limit on the positive and negative end potentials at 0.6 and -0.1 V. In LiCl, the C_s (F/g) ranges from 62.27 to 10.15, in presence of NaOH, C_s (F/g) ranges from 76.73 to 12.39, and in KOH, C_s (F/g) ranges from 97.74 to 13.31 (Table 14.1). The difference in the current and capacitive response is attributed to hydrated cationic radius, cationic mobility and conductivity and their effect on ion/charge diffusion and exchange. The hydrated cations follow $K^+ - H_2O < Na^+ - H_2O < Li^+ - H_2O$ order of radius, and the ionic mobility decreases with increase in cationic hydrated radius [13, 14]. Thus, due to high ionic mobility, conductivity and small hydrated ions, the

Table 14.1 Effect of electrolyte on scan rate functional electrochemical performance of PGE2 in selected electrolyte media (1.0 M) at $25 \pm 1^\circ\text{C}$

Scan rate (mV/s)	LiCl	NaOH	KOH
200	10.15	12.39	13.31
150	11.52	14.09	15.48
100	13.98	16.23	23.70
50	18.88	19.00	27.87
10	62.27	76.73	97.74

electrode showed largest C_s of 97.74 F/g in KOH electrolyte, followed by NaOH (F/g) and LiCl (F/g). Figure 14.7 represents CV of PGE2 in presence of KOH electrolyte.

Figure 14.8 represents the corrosion resistance of PGE2 with reference to steel through the Tafel plot under potentiodynamic conditions from -1.5 V to 1.5 V @ 0.1

Fig. 14.7 CV of PPY versus Ag/Ag^+ at various scan rate in KOH solution

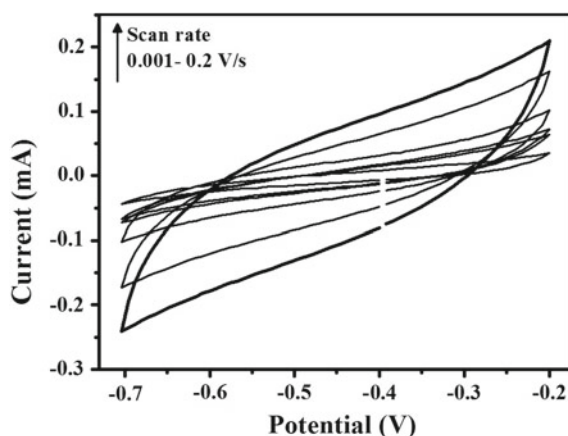
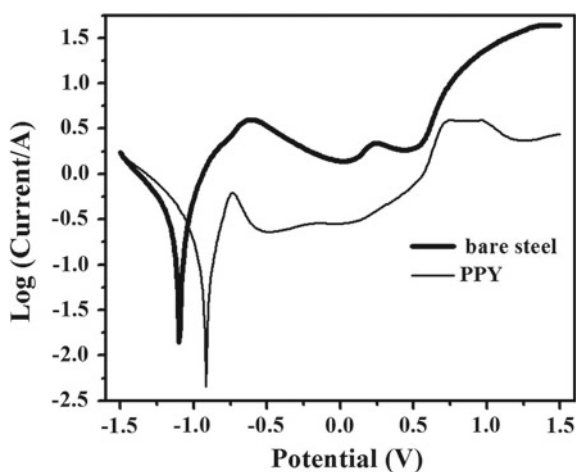


Fig. 14.8 DC polarization of PPY (a) and bare steel (b)



V/s in KOH (1.0 M) at 25 ± 1 °C. Electrochemical data are presented through E_{corr} (V), I_{corr} (A/cm²) and corrosion rate (mm/year). Charge transfer controlled reactions induce corrosion in electrodes that intensify with negative values of E_{corr} and positive values of I_{corr} . Tafel plots reveal that steel electrode shows corrosion at the rate of 0.74 mm/y with negative E_{corr} (−1.03) and positive I_{corr} (2.25×10^{-4}). Coating of PGE2 has reduced the corrosion rate of steel electrode by 0.16 mm/y with less negative E_{corr} −0.48 and positive I_{corr} 4.82×10^{-5} [15].

14.5 Conclusion

PPY was synthesized under supercritical conditions at different temperatures. Electroactive PGEs with higher electrical conductivity were detected and investigated for morphological variations during temperature regulated σ DC measurements. With voltage and temperature ranging from 1 to 100 V and 323 to 403 K, a regular increase in σ DC of PGEs was observed. SPS displays dual behavior with polysulfone as binder and sulfonic acid functionality as dopant for PPY. Simultaneous imaging of electrodes through SEM during temperature-dependent conductivity measurements reveals the stability of PGE2 up to 353 K. Complete destruction in morphology of PGE2 was noticed at 403 K at 100 V with decline in σ DC to 292.9 mS/cm. The electroactive nature of PGE2 was confirmed through cyclic voltammetry in KOH (1.0 M) with electrochemical supercapacitance of 97.74 F/g. Tafel plot reveals corrosion protection behavior of PGE2. The present investigation delivers fabrication of electrodes with semiconducting, capacitive and corrosion protection behavior that make it suitable for electronic and electrochemical energy storage applications.

References

1. Q. Meng, K. Cai, Y. Chen, L. Chen, *Nano Energy* **36**, 268–285 (2017)
2. D. Kopecký, M. Varga, J. Prokeš, M. Vřnata, M. Trchová, J. Kopecká, M. Václavík, *Synth. Met.* **230**, 89–96 (2017)
3. M.T.F. Rodrigues, F.N. Sayed, H. Gullapalli, P.M. Ajayan, *J. Power Sources* **381**, 107–115 (2018)
4. R.M. Agrawal, T.S. Wasnik, K.B. Raulkar, G.T. Lamdhade, *Int. J. Sci. Res. Sci. Eng. Technol.* **4**, 1249–1253 (2018)
5. K. Gurunathan, A.V. Murugan, R. Marimuthu, U.P. Mulik, D.P. Amalnerkar, *Mater. Chem. Phys.* **61**, 173–191 (1999)
6. A. Kassim, Z.B. Basar, H.E. Mahmud, *J. Chem. Sci.* **114**, 155–162 (2002)
7. H. Mudila, S. Rana, M.G.H. Zaidi, *Adv. Mater. Lett.* **8**, 269–275 (2017)
8. H. Mudila, S. Rana, M.G. Zaidi, *J. Anal. Sci. Technol.* **7**, 1–11 (2016)
9. Y. Zhao, L. Zhan, J. Tian, S. Nie, Z. Ning, *Electrochim. Acta* **56**, 1967–1972 (2011)
10. G. Ma, H. Peng, J. Mu, H. Huang, X. Zhou, Z. Lei, *J. Power Sources* **229**, 72–78 (2013)
11. M.R. Bengoechea, F.M. Aliev, N.J. Pinto, *J. Phys. Condens. Matter* **14**, 11769 (2002)
12. C. Basavaraja, Y.M. Choi, H.T. Park, D.S. Huh, J.W. Lee, M. Revanasiddappa, S.C. Raghavendra, S. Khasim, T.K. Vishnuvardhan, *Bull. Korean Chem. Soc.* **28**, 1104–1108 (2007)

13. F. Barzegar, D.Y. Momodu, O.O. Fashedemi, A. Bello, J.K. Dangbegnon, N. Manyala, *RSC Adv.* **5**, 107482–107487 (2015)
14. J. Zhu, Y. Xu, J. Wang, J. Lin, X. Sun, S. Mao, *Phys. Chem. Chem. Phys.* **17**, 28666–28673 (2015)
15. J. Mondal, M. Marandi, J. Kozlova, M. Merisalu, A. Niilisk, V. Sammelselg, *J. Chem. Chem. Eng.* **8**, 786–793 (2014)

Chapter 15

Thermal Efficiency Enhancement of Solar Parabolic Trough Collector Using Nanofluids: A Recent Review



Gopal Nandan

Abstract Recent studies on the potential of the nanofluids on the performance enhancement of the parabolic trough collectors seem to be pointing toward development of the next generation of the solar collectors having great potential to be used for co-generation with integrated solar thermal systems. To achieve it, most researchers are investigating the superior performance of non-conventional heat transfer fluids, such as the nanofluids. The present paper is an effort to review recent research efforts on the performance of parabolic trough collectors using nanofluids. Studies on the various properties of nanofluids seem to be suggesting the positive impact of these fluids in increasing the heat transfer characteristics. The concurrent studies carried out to use nanofluids in coupled solar thermal systems are likely to enhance the process of heat energy collection from the sun in a highly concentrating trough type collector. The objective of the current study is to report recent progress on thermal efficiency enhancement in the parabolic solar trough collector using nanofluids. Experimental and numerical simulation results have been covered by referring to recent research papers. This work will act as a valuable tool to future researchers.

Keywords Nanofluids · Parabolic trough collector · Thermal efficiency

15.1 Introduction

Depletion of fossil fuels and greenhouse effect forced the researcher worldwide for proper alternative environmental benign, sustainable and inexhaustible energy sources. In solar thermal power generation systems, three types of collectors: parabolic trough, central receiver and parabolic dish are used. The technology of the parabolic trough collector (PTC) is the most proven and cost-effective today. The incident solar radiation is reflected by the concentrator to heat collector element (HCE) which is a metallic tube placed in the focal line of the concentrator. The HCE first captures the solar irradiation and then absorbs by spectral selective coating on

G. Nandan (✉)

Mechanical Engineering Department, Amity University Uttar Pradesh, Noida, Uttar Pradesh, India
e-mail: gopalnandan@gmail.com

© Springer Nature Singapore Pte Ltd. 2020
V. K. Jain et al. (eds.), *Advances in Solar Power Generation and Energy Harvesting*, Springer Proceedings in Energy,
https://doi.org/10.1007/978-981-15-3635-9_15

137

its wall (tube/plate) and converts into heat. The heat transfer fluids (HTFs) circulate through the HCE where the heat is indirectly transferred to it [1]. To minimize the heat losses, the HCE is enveloped by a glass tube. The annular space between HCE and the glass tube is maintained at vacuum pressure [2]. The PTC is the best choice for medium temperature (150–400 °C) heat requirements [3]. The HTF for medium temperature ranges 100–400 °C, which is suitable for Rankine thermal cycles, must be highly absorptive [4]. The most common type of working heat transfer fluids is synthetic oil, molten salt or water/steam. Nowadays, several researchers experimented the use of nanofluids and shown appreciable advantages in thermal efficiency. The nanofluids are a mixture of very nanosized engineered particles and the conventional liquids used as HTF. Common base liquids in solar collectors are water, synthetic heat transfer oil or molten salts which is based on operating temperatures. The optical efficiency depends on the reflectivity of trough collector and its optical parameter, the transmittance of glass envelope and absorptivity of the receiver tube. It is the ratio of the absorbed energy to the incidence of solar energy. In this paper, the effect of nanoparticles on the thermal aspects of PTC has been revealed. The present work focuses on the performance of PTC when nanofluids are used as HTC. Due to nanofluids, the pressure drop in the channel, heat transfer, thermal efficiency based on the experimental and analytical solution has been covered. Inserts used HCE which contributed to the increase of thermal performance [5]. Still, there is a need for commercial nanofluid solar collectors due to its higher thermal performance as compared to traditional HTF.

15.2 Heat Transfer

The motion of molecules of fluid accounts for the transfer of heat to the fluids. The mechanisms involved are conduction of heat, convection of heat and radiation of heat. When a fluid passes through an enclosed boundary and encounters a heated solid boundary like a pipe wall, heat energy gets conducted in the boundary and the outer layer of the fluid which is directly in contact with the metal surface gets the heat energy by conduction. However, the mechanism of convection occurs inside the flowing fluid in the inner zones of the tube. When the outermost layer gets heated, the density in this layer reduces and the nearby layers fill up this zone; thereby, a continuous fluid circulation takes place inside the tube. This circulation of fluid aids in the transfer of energy to the farther layers of the fluid lying away from the pipe wall. The circulating fluid transfers heat energy to the innermost layers of the flowing nanofluids over some time. This circulation of fluid occurring due to natural buoyancy effects is called natural circulation and this process is slow. To speed up the process, an external pump is used. In assisted circulation mode, the fluid is circulated using an external pump and thus the convection can be imagined to be forcefully executed using an external device. This kind of convection is rapid than the natural convection mode. Heat transfer rate also depends on the material properties, fluid flow rate, temperature gradient and the geometry of the surface transferring the heat.

Ajay and Lal [6] used CuO/water nanofluids for experimentation and validated the experimental observation numerically. Choudhri et al. [7] used Al_2O_3 /water nanofluids of 40 nm size and found improvement in heat transfer concerning water. Jafar and Sivaraman conducted experiments with Al_2O_3 /water nanofluid which maintains volumetric fraction at 0.1% and 0.3. In the tube, a twisted tube with nails was used to further enhance heat transfer in laminar flow range having Re from 710 to 2130. The heat transfer rate further improved [8]. The heat transfer further improved in silica water nanofluid after providing transverse vibration on the heat transfer surface. The heat transfer coefficient enhanced up to 182% as compared to base fluids water [9]. This improvement is due to thermal diffusion effects due to the Brownian motion of nanoparticles and the thermophoresis effect. Bellos et al. [10] reported energy and exergy analysis in the temperature range 300 K to 1300 K for water, Therminol VP-1, molten salt, sodium liquid, air, CO_2 and helium. For high temperature, CO_2 and helium are the most suitable working fluids [10].

15.3 Experimental Study of PTC

The actual energy absorbed by the collector is represented by the rise of temperature of the circulating fluid in PTC using nanofluid which results in the increase of the useful energy collected. This improves the thermal efficiency of the collector. Kasaiean et al. [11] investigated thermal and optical performance of steel mirror and then compared with four different HCEs: (a) black painted vacuumed steel tube, (b) copper tube with black chrome coating, (c) copper tube with black chrome coating enveloped in glass (non-evacuated) and (d) copper tube with black chrome coating vacuumed. The black chrome has the highest absorptivity (0.98). The thermal efficiency of vacuumed HCE has averagely 11% higher efficiency than bare HCE, due to convection losses. The thermal performance of the copper tube with black chrome coating vacuumed found to be best between them. They used 0.2 and 0.3% (in weight fraction) MWCNT/mineral oil-based nanofluid and found global efficiency improved about 4–5% and 6–7% as compared to instead of pure oil.

Therminol VP-1 base fluid was dispersed with alumina nanoparticles [12], and 10% improvement in the efficiency of the thermal collection device fitted with transparent receiver tubes was observed during the experimentation. The optical efficiency of the collector was dependent on the diameter of the receiver tube and the nanoparticle concentration. Numerical dependence is also computed with alumina nanoparticles in different base fluids like ethylene glycol, propylene glycol and Therminol VP-1 in this study. The summary of efficiency enhancements reported is presented in Table 15.1.

Table 15.1 Experimental findings of PTC using nanofluids

Researcher	Nanofluid	Fraction of nanoparticles	Findings
Chaudhari et al. [7]	Al ₂ O ₃ /water	• 1% weight fraction	<ul style="list-style-type: none"> • Heat transfer coefficient enhanced by 32% • Nail twisted tapes inserts
Ajay and Lal [6]	CuO/H ₂ O	• 0.01% volume fraction	<ul style="list-style-type: none"> • Thermal efficiency improved by 7.4% • Good agreement with experimental
Ajay and Lal [13]	Al ₂ O ₃ /water	Volume concentration of 0.05, 0.75, 0.1 and 0.125%	<ul style="list-style-type: none"> • Overall efficiency improvement by 13.98% at 0.125% volumetric fraction at 80 L/h
Kasaeian et al. [11]	MWCNT/oil	0.2 and 0.3%	<ul style="list-style-type: none"> • Efficiency improved by 3–5% at 0.2% concentration • Efficiency improved by 5–7% at 0.3% concentration • Vacuumed HCE has 11% more efficiency
Khullar et al. [12]	Al ₂ O ₃ /Therminol VP-1	0.05%	5–10% enhancement in efficiency
Kaloudis et al. [14]	Al ₂ O ₃ /Syltherm 800	4% concentration ration	<ul style="list-style-type: none"> • Collector efficiency improved by 10% • Modeling is based on two-phase approach
Mwesigye et al. [15]	CuO/Therminol VP-1	Up to 6% volumetric fraction	Increase in efficiency by 12.5%
Jafar and Sivaraman [8]	Al ₂ O ₃ /water	0.1% and 0.3% volume concentration	<ul style="list-style-type: none"> • Heat transfer rate improved further due to improve in turbulence • Nail twisted tapes inserts
Chaudhari et al. [7]	Al ₂ O ₃ /H ₂ O	Weight fraction 0.1%	Thermal efficiency enhanced by 32%

15.4 Simulation of Parabolic Trough Collectors

The use of nanofluids as working fluids in the PTC has been simulated by several researchers to study thermal and hydraulic behaviors. The simulation study reported in the literature more than 65% in these areas. It is perhaps accounted due to relatively cheaper than experimentation cost for both system setup and material purchase. For

modeling purpose, ANSYS Fluent, ANSYS CFX, Engineering Equation Solver and users own code has been used by most of them. Exergy efficiency and entropy generation rate were investigated by some researchers [15–18]. Simulations were carried out by several authors using nanofluids as the working fluid by solving mass, momentum and energy conservation equations. These equations are

$$\text{Continuity equation: } \frac{\partial \rho}{\partial t} + \frac{\partial(\rho u_j)}{\partial x_j} = 0$$

$$\text{Momentum equation: } \frac{\partial(\rho u_i)}{\partial t} + \frac{\partial(\rho u_i \rho u_j)}{\partial x_j} = \frac{\partial}{\partial x_j} \left[\rho \delta_{ij} + \mu \left(\frac{\partial u_i}{\partial x_j} + \frac{\partial u_j}{\partial x_i} \right) \right] + \rho g_i$$

$$\text{Energy equation: } \frac{\partial(\rho C_p T)}{\partial t} + \frac{\partial(\rho u_i C_p T)}{\partial x_i} - \frac{\partial \left[\lambda \frac{\partial T}{\partial x_j} \right]}{\partial x_j} = S_T$$

$$\text{Turbulence kinetic energy equation: } \frac{\partial(\rho k)}{\partial t} + \frac{\partial(\rho k u_i)}{\partial x_i} = \frac{\partial y \left[\Gamma_k \frac{\partial k}{\partial x_j} \right]}{\partial x_j} + G_k + Y_k + S_k$$

15.4.1 Constant Heat Flux Over HCE

Several simulations work considered constant heat flux over HCE [2, 19–21]. For a low concentration ratio (<5%) of Al₂O₃/synthetic oil nanofluid convection heat transfer coefficients directly depend on the volume fraction of the nanofluid. This was numerically studied considering constant heat flux over PTC [22]. Padilla et al. [2] performed one-dimensional numerical heat transfer analysis and compared experimental data of Sandia National Laboratories.

15.4.2 Heterogeneous Heat Flux Over HCE

A three-dimensional model was solved for fully developed turbulent heat transfer by Sokhansefat et al. [23]. The influences of the non-uniform distribution of the solar energy flux on the thermal, fluid and structural characteristics of the HCEs have been reported by Wang et al. [24]. The incident solar energy on the HCE considered as constant heat flux on the upper side and non-uniform heat flux in the lower side in the circumferential direction. However, along its length, it is constant at any circumferential position on the tube. Along the tube circumference, heat flux is extremely non-uniform which results in very complicated heat transfer mechanism inside the tube. Non-uniform heat flux is due to the reflection of incident solar radian over the trough reflector, which is modeled using solar ray tracing method and finite element method. This complex condition is then coupled with HTF. Due to non-uniform heat flux, circumferential temperature difference (CTD) is developed in the HCE which decreases with increase in inlet velocity and the temperature of the HTF. Authors considered inlet velocity in a range of 1–4 m/s and the inlet temperature in the range of 373–673 K and observed the thermal stress as well as CTD in the HCE which is in the range of 22–94 K. Further Wang et al. [25] extended his result and presented the effect of Al₂O₃/synthetic oil nanofluids. He et al. [26] wrote codes for

MCRT implementation and validated with the experimental data. The heterogeneous heat flux distribution on HCE divided into four parts: (i) shadow effect area, (ii) heat flux increasing area, (iii) heat flux reducing area and (iv) direct radiation area. The effect of concentration ratio and rim angle is also presented. In 2014, Islam et al. [27] used commercial code *Zemax* simulation for Monte Carlo Ray Tracing (MCRT) and provided solar irradiance in terms of the angular position overall four locations. Turbulence modeling has been used [13, 24, 28, 29]. This model gave good agreement with the experimental data. For numerical analysis single-phase model, two-phase model, volume of fluids model and mixture models were used in ANSYS Fluent and their comparative performance has been reported [28]. The pressure-based solver was used for the calculations and Semi-Implicit Method for Pressure Linked Equations (SIMPLE) algorithm was chosen for the pressure velocity coupling. They used five different volume fractions of nanofluid from 0.0625% to 1% of MgO nanofluid. Results from the simulation study show that Nu increases with the volume fraction of the nanofluid. Two-phase models give more accurate than the others for heat transfer prediction particularly in the higher volume fractions of nanoparticle with a deviation of about 2%, whereas in the single-phase model, it is about 11%.

It was tested with Al₂O₃ nanofluid and improved heat transfer results [14] were established. A base fluid synthetic in nature like Syltherm 800 was selected, and alumina nanoparticle volume concentration of 4% was maintained, which led to an improvement of the thermal collector efficiency, which is comparably higher by 10% to the thermal efficiency obtained with water as the working fluid.

The thermal performance improves with increasing the nanoparticles volumetric fraction. The entropy generation decreases and the thermal efficiency increase by 12.5% when the volume fraction Cu-Therminol VP-1 of 6%. Using MCRT and FVM, inlet fluids temperatures were maintained in the range of 350–650 K and flow rates in the range 1.22–135 m³/h. The concentration ratio and a rim angle were maintained of 113° and 80°, respectively. Using MATLAB, programming has been done for a theoretical formulation which is based on the finite-difference technique [12]. Heat transfer using the forced mode of convection by using aluminum oxide and cuprous oxide water nanofluid was simulated using k-ε model [30]. At a volume concentration of 3%, heat transfer increased by 28% and 35%, respectively.

Ajay and Lal [6, 13] did simulation studies using ANSYS *Fluent* and compared with the experimental observation with CuO/water nanofluids at a flow rate of 20 L per hour. In the simulation, the use of solar load model also has been reported. At 0.01% volumetric concentration of nanofluids, outlet temperature of experimental and simulation had good agreement throughout. The thermal efficiency at the low flow rate (low Re) was improved by 7.4% as compared to the base fluids. The difference of 8% in the results of experimental and simulation results was obtained for Al₂O₃ nanofluids at a very low volumetric fraction of 0.125%.

Further, Kumar et al. [31] considered CuO/water nanofluids as a single phase in the modeling thermal efficiency improved by 6% at the same volumetric fraction 0.01%. Modeling has been done using VB.NET considering solar aspects and heat transfer aspect of PTC [32]. Effect of several collating, efficiency and outlet temperature of heat transfer fluid was discussed.

Huang et al. [33] studied optical performance with vacuum tube receiver analytically and suggested a modified integration algorithm for optical efficiency of each point at the reflector. The numerical integration provides overall optical cosine factor, receiver efficiency, heat loss and efficiency of conversion of solar energy into net heat energy at any time considering optical error and tracking error.

Zadeh et al. [34] used a genetic algorithm and sequential quadratic programming for thermal analysis of the collector using MATLAB and Fluent software. They considered non-uniform heat flux on the absorber tube and flow of heat transfer tube as fully developed mixed convection. The HTF was Al_2O_3 nanofluids having synthetic oil as a base fluid. It was concluded that heat transfer enhancement directly depends on the nanoparticle concentration ratio. As the operational temperature increases, it gives a negative effect on heat collection efficiency.

Overall efficiency and exergy efficiency were studied using Engineering Equation Solver (EES) by Abid et al. [35]. They considered PTC for solar irradiation from 400 to 1000 W/m^2 and water-based nanofluids (Al_2O_3 and Fe_2O_3) as well as molten salts (LiCl-RbCl and $\text{NaNO}_3\text{-KNO}_3$). The overall efficiency, exergy efficiency and outlet temperature of HTF are maximum for $\text{Fe}_2\text{O}_3/\text{H}_2\text{O}$ nanofluids.

Wani and Nandan [36] further extended their work and used MCRT to model non-uniform in the circumferential direction but uniform in the axial direction. Three-dimensional models were solved using Fluent. The operational temperature was maintained at 300, 400 and 500 °C. The error in the simulated and experimental data for the outlet temperature of HCE was less than 3.8 °C. Due to unsymmetrical heat flux over PTC, circumferential temperature gradient in observed in the tube [36]. Ghasemi and Ahangar [37] developed code in FORTRAN and studied thermal and optical performance for Cu-water nanofluid in PTC.

Mwesigye et al. used [15, 17, 38] copper, silver and alumina with Therminol VP-1 as base fluid. Based on numerical analysis, comparative analysis has been presented. The thermal performance of the receiver tube is calculated and found that silver-Therminol VP-1 nanofluid exhibited maximum enhancement of thermal efficiency of 14% at volume fraction varying from 0 to 6%. Later on, Basbous et al. used nanofluid $\text{Al}_2\text{O}_3\text{-Syltherm 800}$ for numerical analysis [39].

Bellos et al. [40] modeled PTC in SolidWorks and used flow simulation studio for its simulation. They used experimental results for its validation and compared the results of Al_2O_3 nanoparticles in two different base fluids separately. In thermal oil, the mean efficiency increased by 4.25% and enhancement of 6.34% was observed at high-pressure water in PTC.

Other investigators [40] used base fluids like thermal oil and used thermal oil with nanoparticle dispersion along with pressurized water. The study was conducted in a high temperature-based PTC. Geometrical modifications in addition to the use of nanofluid were performed to improve the thermal efficiency of the collector by around 9%. A few researchers employed a combination of collectors to good effect. The geometry of the tube was also modified to study thermal efficiency. Using thermal oil, wavy geometry gave better efficiency as compared to a cylindrical tube. Numerical simulation results are shown in Table 15.2.

Table 15.2 Summary of simulation studies of nanofluids in PTC

Researcher	Nanofluids used	Findings
Sokhansefat et al. [23]	Al ₂ O ₃ /synthetic oil	<ul style="list-style-type: none"> • MCRT used and solved using Fluent software • Volumetric concentration considered up to 5% • At high operational temperature, heat transfer enhancement is reduced
Ajay and Kundan [13]	Al ₂ O ₃ -H ₂ O	<ul style="list-style-type: none"> • With 0.125% volumetric fraction, thermal efficiency is 24.3% and instantaneous efficiency is 68.5% • About 8% discrepancy with experimental data
Mwesigye et al. [38]	CuO/Therminol VP-1, AgO/Therminol VP-1 Al ₂ O ₃ /Therminol VP-1	<ul style="list-style-type: none"> • Comparison of thermal efficiency presented in volume fraction increases from 0 to 6% using SolTrace • Concentration ratio is 113 and rim angle was 80° • Thermal efficiency enhanced by about 12.5, 13.9 and 7.2% for the copper-Therminol@VP-1, silver-Therminol@VP-1 and Al₂O₃-Therminol@VP-1 nanofluids
Mwesigye and Meyer [41]	SWCNTs-Therminol VP-1	<ul style="list-style-type: none"> • Volume fraction maintained in the range 0–2.5% • Heat transfer coefficient improved by 64% • Entropy generation rate decreased by increasing volume fraction and remained constant for higher value of Reynolds number
Bellos and Tzivanidis [42]	Al ₂ O ₃ /Syltherm 800 CuO/Syltherm 800	<ul style="list-style-type: none"> • Model developed in EES • Using Al₂O₃ heat transfer coefficient enhancement is 34.7% • Using CuO heat transfer coefficient enhancement is 40.9%
Ghasemi and Ranjbar [30]	Al ₂ O ₃ /H ₂ O, CuO/H ₂ O	<ul style="list-style-type: none"> • With Al₂O₃/H₂O heat transfer enhanced by 28% • With CuO/H₂O heat transfer enhanced by 35% • 3% Volumetric fraction maintained in both cases
Antonio et al. [32]	Water	VB.Net programming is used for mathematical model to study flow and heat transfer in a PTC

(continued)

Table 15.2 (continued)

Researcher	Nanofluids used	Findings
Huang et al. [33]	Water	Numerical integration algorithm is used to evaluate the optical efficiency of PTC
Kumar et al. [31]	CuO/H ₂ O	<ul style="list-style-type: none"> • Marginal difference in results of experimentation and simulation for outlet temperature • Thermal efficiency improved by 6% at 0.01% volumetric fraction
Abid et al. [35]	<ul style="list-style-type: none"> • Al₂O₃/H₂O • Fe₂O₃/H₂O • LiCl-RbCl/H₂O • NaNO₃-KNO₃/H₂O 	<ul style="list-style-type: none"> • Comparative study of four fluids having water as base fluids • Salts were in molten state • Overall efficiency and exergy efficiency of Fe₂O₃ in PTC • Outlet temperature in PTC was maximum for Fe₂O₃/water • Results were also compared with parabolic dish collector
Bellos et al. [40]	Al ₂ O ₃ /thermal oil Al ₂ O ₃ /pressurized water	<ul style="list-style-type: none"> • Thermal efficiency enhancement by 4.25% • Surface modified to wavy surface provided increase in efficiency by 4.55% • SolidWorks used for modeling
Mwesigye et al. [43]	Al ₂ O ₃ /Syltherm 800	<ul style="list-style-type: none"> • Collector thermal efficiency increases by 7.6% • Local entropy generation calculated • Volumetric fraction of nanoparticles used 0–8% • 3560 < Re < 1,151,000
Basbous et al. [39]	Al ₂ O ₃ /Syltherm 800	<ul style="list-style-type: none"> • Dispersion on nanoparticles increased the convection heat transfer coefficient about 18% and heat loss decreased by 10% • Convection heat transfer coefficient increases at high temperatures
Sokhansefat et al. [23]	Al ₂ O ₃ /synthetic oil	<ul style="list-style-type: none"> • Up to 5% volumetric fraction for temperatures of 300, 400 and 500 K • Asymmetric temperature distribution in circumferential direction considered • Difference in experimental and simulation result shows less than 3.8 °C in the exit temperature

(continued)

Table 15.2 (continued)

Researcher	Nanofluids used	Findings
Islam et al. [27]	–	<ul style="list-style-type: none"> • Zemax simulation for MCRT simulation used • Solar irradiance at HCE in terms of angular position presented

15.5 Conclusion

To harness solar energy and to achieve improved efficiencies of solar collectors, the researchers have focused engineered fluids as heat transport fluids which exhibit higher heat absorption and better heat transfer properties as compared to the conventional fluids. In this paper recent development in the thermal performance, the thermodynamic performance of a solar parabolic trough collector is discussed. Most of the research papers available are based on numerical analysis of the system starting from a one-dimensional approach to three-dimensional approach. Focus is on the application of nanofluids in the collector. The use of nanoparticles of CuO, Al₂O₃, Fe₂O₃, AgO, SWCNT, SiO₂, LiCl-RbCl and NaNO₃-KNO₃ has been experimented using water, mineral oil, Therminol VP-1 and Syltherm 800 as working fluids. In some of the research papers used, performance of molten salt, sodium liquid, air, CO₂ and helium also has been reported. Numerical solution considering constant heat flux along the circumferential direction is also available. The solar ray simulation using Monte Carlo Ray Technique has been used to model heterogeneous heat flux along the circumferential direction on the collector. For the implementation of MCRT technique, researchers used their codes in VB.net, Engineering Equation Solver, Zemax simulation and SolTrace solved using ANSYS Fluent. The validation of codes has been done using the standard data of Sandia National Laboratories. The performance is found to be satisfactory.

References

1. G. Xu, W. Chen, S. Deng, X. Zhang, S. Zhao, Performance evaluation of a nanofluid-based direct absorption solar collector with parabolic trough concentrator. *Nanomaterials* **5**, 2131–2147 (2015)
2. R.V. Padilla, G. Demirkaya, D.Y. Goswami, E. Stefanakos, M.M. Rahman, Heat transfer analysis of parabolic trough solar receiver. *Appl. Energy* **88**, 5097–5110 (2011)
3. G. Kumaresan, P. Sudhakar, R. Santosh, R. Velraj, Experimental and numerical studies of thermal performance enhancement in the receiver part of solar parabolic trough collectors. *Renew. Sustain. Energy Rev.* **77**, 1363–1374 (2017)
4. R.A. Taylor, P.E. Phelan, T.P. Otanicar, C.A. Walker, M. Nguyen, S. Trimble, R. Prasher, Applicability of nanofluids in high flux solar collectors. *J. Renew. Sustain. Energy* **3**, 023104 (2011)
5. M. Natarajana, R. T. Karuppa Raj, Y. R. Sekhar, T. Srinivas, P. Gupta, Numerical simulation of heat transfer characteristics in the absorber tube of parabolic trough collector with internal

- flow obstructions. *ARPN J. Eng. Appl. Sci.* **9**, 674–681 (2014)
6. K. Ajay, K. Lal, An experimental and cfd analysis of cuo-h₂o (di) nanofluid based parabolic solar collector. *IOSR J. Mech.Civ. Eng.* 78–82 (2015)
 7. K. Chaudhari, P. Walke, U. Wankhede, R. Shelke, An experimental investigation of a nanofluid (AL₂O₃/H₂O) based parabolic trough solar collectors. *Br. J. Appl. Sci. Technol.* **9**, 551–557 (2015)
 8. K.S. Jafar, B. Sivaraman, Thermal performance of solar parabolic trough collector using nanofluids and the absorber with nail twisted tapes inserts. *Int. Energy J.* **14**, 189–198 (2014)
 9. L. Zhang, J. Lv, M. Bai, D. Guo, Effect of vibration on forced convection heat transfer for SiO₂ water nanofluids. *Heat Transfer Eng.* **36**, 452–461 (2014)
 10. E. Bellos, C. Tzivanidis, K.A. Antonopoulos, A detailed working fluid investigation for solar parabolic trough collectors. *Appl. Therm. Eng.* **114**, 374–386 (2017)
 11. A. Kasaeian, S. Daviran, R.D. Azarian, A. Rashidi, Performance evaluation and nanofluid using capability study of a solar parabolic trough collector. *Energy Convers. Manag.* **89**, 368–375 (2015)
 12. V. Khullar, H. Tyagi, P.E. Phelan, T.P. Otanicar, H. Singh, R.A. Taylor, Solar energy harvesting using nanofluids-based concentrating solar collector. *J. Nanotechnol. Eng. Med.* **3**, 031003 (2013)
 13. K. Ajay, L. Kundan, Experimental and cfd investigation on the efficiency of parabolic solar collector involving AL₂O₃/H₂O (di) nanofluid as a working fluid. *Int. J. Renew. Energy Res.* **6**(2), 392–401 (2016)
 14. E. Kaloudis, E. Papanicolaou, V. Belessiotis, Numerical simulations of a parabolic trough solar collector with nanofluid using a two-phase model. *Renew. Energy* **97**, 218–229 (2016)
 15. A. Mwesigye, Z. Huan, J.P. Meyer, Thermal performance and entropy generation analysis of a high concentration ratio parabolic trough solar collector with cu-therminolVP-1 nanofluid. *Energy Convers. Manag.* **120**, 449–465 (2016)
 16. A. Mwesigye, I.H. Ylmaz, J.P. Meyer, Numerical analysis of the thermal and thermodynamic performance of a parabolic trough solar collector using SWCNTs-therminol VP-1 nanofluid. *Renew. Energy* **119**, 844–862 (2018)
 17. A. Mwesigye, J.P. Meyer, Optimal thermal and thermodynamic performance of a solar parabolic trough receiver with different nanofluids and at different concentration ratios. *Appl. Energy* **193**, 393–413 (2017)
 18. R.V. Padilla, A. Fontalvo, G. Demirkaya, A. Martinez, A.G. Quiroga, Exergy analysis of parabolic trough solar receiver. *Appl. Therm. Eng.* **67**, 579–586 (2014)
 19. S. Odeh, G. Morrison, M. Behnia, Modelling of parabolic trough direct steam generation solar collectors. *Solar Energy* **62**, 395–406 (1998)
 20. O. Garcá-Valladares, N. Velázquez, Numerical simulation of parabolic trough solar collector: Improvement using counter flow concentric circular heat exchangers. *Int. J. Heat Mass Transf.* **52**, 597–609 (2009)
 21. P. Daniel, Y. Joshi, A.K. Das, Numerical investigation of parabolic trough receiver performance with outer vacuum shell. *Solar Energy* **85**, 1910–1914 (2011)
 22. M. Chandrasekar, S. Suresh, T. Senthilkumar, Mechanisms proposed through experimental investigations on thermophysical properties and forced convective heat transfer characteristics of various nanofluids a review. *Renew. Sustain. Energy Rev.* **16**, 3917–3938 (2012)
 23. T. Sokhansefat, A. Kasaeian, F. Kowsary, Heat transfer enhancement in parabolic trough collector tube using Al₂O₃/synthetic oil nanofluid. *Renew. Sustain. Energy Rev.* **33**, 636–644 (2014)
 24. Y. Wang, Q. Liu, J. Lei, H. Jin, Performance analysis of a parabolic trough solar collector with non-uniform solar flux conditions. *Int. J. Heat Mass Transf.* **82**, 236–249 (2015)
 25. Y. Wang, J. Xu, Q. Liu, Y. Chen, H. Liu, Performance analysis of a parabolic trough solar collector using Al₂O₃/synthetic oil nanofluid. *Appl. Therm. Eng.* **107**, 469–478 (2016)
 26. Y.L. He, J. Xiao, Z.-D. Cheng, Y.-B. Tao, A MCRT and FVM coupled simulation method for energy conversion process in parabolic trough solar collector. *Renew. Energy* **36**, 976–985 (2011)

27. M. Islam, M.A. Karim, S.C. Saha, S. Miller, P.K.D.V. Yarlagadda, Development of empirical equations for irradiance profile of a standard parabolic trough collector using monte carlo ray tracing technique. *Adv. Mater. Res.* **860–863**, 180–190 (2013)
28. R. Davarnejad, M. Jamshidzadeh, CFD modeling of heat transfer performance of MgO-water nanofluid under turbulent flow. *Eng. Sci. Technol. Int. J.* **18**, 536–542 (2015)
29. T. Sokhansefat, A. Kasaeian, M.J. Abbaspour, M. Sokhansefat, Numerical study of heat transfer enhancement by using Al₂O₃/synthetic oil nanofluid in a parabolic trough collector tube. *World Acad. Sci. Eng. Technol.* **69**, 1154–1159 (2012)
30. S.E. Ghasemi, A.A. Ranjbar, Thermal performance analysis of solar parabolic trough collector using nanofluid as working fluid: a CFD modelling study. *J. Mol. Liq.* **222**, 159–166 (2016)
31. M. Kumar, D. Patel, V. Sehrawat, T. Gupta, Experimental and cfd analysis of Cuo-H₂O (di) nano fluid based parabolic solar trough collector. *Int. J. Innovative Res. Sci. Eng. Technol.* **5** (2016)
32. A.M. de Oliveira Siqueira, P.E.N. Gomes, L. Torrezani, E.O. Lucas, G.M. da Cruz Pereira, Heat transfer analysis and modeling of a parabolic trough solar collector: an analysis. *Energy Procedia* **57**, 401–410 (2014)
33. W. Huang, P. Hu, Z. Chen, Performance simulation of a parabolic trough solar collector. *Sol. Energy* **86**, 746–755 (2012)
34. P.M. Zadeh, T. Sokhansefat, A. Kasaeian, F. Kowsary, A. Akbarzadeh, Hybrid optimization algorithm for thermal analysis in a solar parabolic trough collector based on nanofluid. *Energy* **82**, 857–864 (2015)
35. M. Abid, T.A.H. Ratlamwala, U. Atikol, Performance assessment of parabolic dish and parabolic trough solar thermal power plant using nanofluids and molten salts. *Int. J. Energy Res.* **40**, 550–563 (2015)
36. Wani, N.A., Nandan, G.: Modelling of solar parabolic trough collector considering unsymmetrical heat flux. In: 3rd International Conference on Recent Developments in Control, Automation & Power Engineering (RDCAPE). No. 526–530, IEEE (2019)
37. S.E. Ghasemi, G.R.M. Ahangar, Numerical analysis of performance of solar parabolic trough collector with cu-water nanofluid. *Int. J. Nano Dimension* **5**(3), 233–240 (2014)
38. A. Mwesigye, Z. Huan, Comparative thermal performance of a parabolic trough receiver with Cu-therminol@vp-1, Ag-therminol@vp-1 and Al₂O₃—therminol@vp-1 nanofluids, in *Proceedings of the ASME 2016 International Mechanical Engineering Congress and Exposition IMECE2016* (ASME, ed.), (2016, Phoenix, Arizona, USA, November 2016)
39. N. Basbous, M. Taqi, N. Belouaggadia, Numerical study of a parabolic trough collector using a nanofluid. *Asian J. Curr. Eng. Maths* **4**, 40–44 (2015)
40. E. Bellos, C. Tzivanidis, K. Antonopoulos, G. Gkinis, Thermal enhancement of solar parabolic trough collectors by using nanofluids and converging-diverging absorber tube. *Renew. Energy* **94**, 213–222 (2016)
41. A. Mwesigye, J.P. Meyer, Heat transfer performance of a parabolic trough receiver using SWCNTs-therminolVP-1 nanofluids, in *Volume 8: Heat Transfer and Thermal Engineering* (ASME, 2017)
42. E. Bellos, C. Tzivanidis, Parametric investigation of nanofluids utilization in parabolic trough collectors. *Therm. Sci. Eng. Prog.* **2**, 71–79 (2017)
43. A. Mwesigye, Z. Huan, J.P. Meyer, Thermodynamic optimisation of the performance of a parabolic trough receiver using synthetic oilal 2 o 3 nanofluid. *Appl. Energy* **156**, 398–412 (2015)

Chapter 16

Structural Transformations in Fullerene C₇₀ Thin Film by 65 MeV Ni Ion Beam Irradiation



Ritu Vishnoi, Vaishali Singh and Rahul Singhal

Abstract Under swift heavy ion irradiation at different fluences, the structural transformations of fullerene C₇₀ thin film prepared by thermal evaporation are investigated. Fullerene C₇₀ thin films are irradiated with 65 MeV Ni ions beam at different fluences from 1×10^{12} to 1×10^{14} ions/cm². The impact of energetic ions on the fullerene molecule leads to the extinction of C₇₀ molecule. In order to study the stability of fullerene C₇₀ under ion irradiation, damage cross section and ion track radius of damaged cylindrical zones are determined using fullerene C₇₀ vibration modes and their change at different fluences as recorded by Raman spectroscopy. Damage cross section is found to be 1.01×10^{-13} cm², and ion track radius of damaged cylindrical zone is found to 1.8 nm. Fullerene C₇₀ is completely converted from crystalline structure to amorphous carbon at a fluence of 1×10^{14} ions/cm².

Keywords Swift heavy ion · Fullerene · Ion track · Raman spectroscopy

16.1 Introduction

In 1985, Richard Smalley, Robert Curl, and Harold Kroto discovered Fullerene, an allotrope of carbon [1] at the University of Sussex and Rice University. Fullerene molecules are in the form of a hollow ellipsoid, sphere, or other shapes and made of entirely carbon atoms. These molecules are also called buckyballs. Due to noticeable optical, structural, and electrical properties, fullerenes have always been of keen interest to researchers [2, 3]. Fullerene C₆₀ is a highly symmetrical molecule similar to the shape of a football, whereas the shape of fullerene C₇₀ is like a rugby ball. The fullerene C₇₀ molecule is little bit more complex than fullerene C₆₀ molecule. The C₇₀ molecule has an ellipsoid structure consisting of 12 pentagons and 25 hexagons [4]. The diameter of the equator of the relaxed molecule and overall height is ~ 6.94 Å and ~ 7.80 Å, respectively [5]. It has been reported that fullerene C₇₀ will have

R. Vishnoi · V. Singh · R. Singhal (✉)

Department of Physics, Malaviya National Institute of Technology Jaipur, JLN Marg, Jaipur, Rajasthan 302017, India

e-mail: rsinghal.phy@mmit.ac.in

prepared by the solution route; it has hcp structure at room temperature; but if it is prepared by sublimation route, it has fcc structure at room temperature [6, 7]. C_{70} has poor crystallinity and orientational disorder at room temperature, and therefore, Raman spectroscopy is a better tool to investigate the structural transformation of fullerene C_{70} than the other conventional crystallographic techniques. Fullerene C_{70} has 53 Raman active vibrational modes as per the symmetry selection rules [8]. For tailoring the optical, structural, and electrical properties of fullerenes, swift heavy ion irradiation technique can be [9–13] utilized. The interaction of ion beam with fullerene is of interest for the generation of new properties as well as to the general field of ion beam processing of carbonaceous materials. When material is irradiated with energetic ions, they will lose their energy to the material, which results in upgradation of material properties. Ions lose their energy in two processes; these are elastic collisions with lattice atoms called nuclear energy loss (S_n) and in electronic ionizations and excitations called electronic energy loss (S_e). The S_n predominates at low energies (~ 1 keV/amu), whereas S_e dominates at high energies (~ 1 MeV/amu) of incoming ions. The variation of nuclear and electronic energy losses for high mass ion with the energy of the ion in carbon matrix is shown in Fig. 16.1. From figure, it is seen that there are mainly three regions according to the different energy of the incoming ion. (i) The region where S_n dominates over S_e is low energy region (~ 1 keV/amu). The ions corresponding to this range of energy lose their energy via collisions with the nucleus of target atoms and transfer momentum and energy to the recoil atoms, (ii) mid-energy region, where S_e increases with energy and reaches to a maximum value, after which it decreases with energy (region III). The most

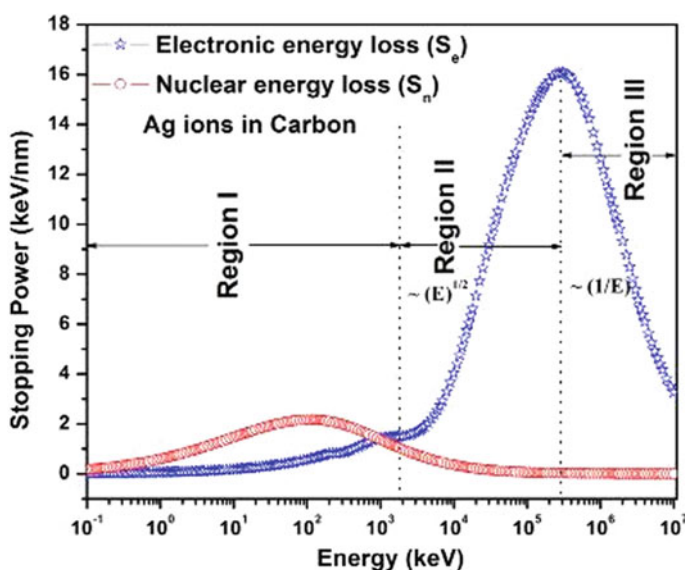


Fig. 16.1 Stopping powers (in keV/nm) for Ag ions in carbon as calculated by SRIM program

important primary radiation effects responsible for the modifications of different materials are (i) collective electronic excitations, (ii) breakage of bonds, cross-linking or scissoring, (iii) formation of phonons, leading to localized heating of the target, (iv) sputtering of atoms from the surface, (v) displacement of atoms in the bulk of the target, (vi) generation of ion track by high energy ions (~1 MeV/amu), (vii) defect annealing and defect creation, etc. Ion beam effect on the materials depends on the ion fluence, energy, and ion species.

In the case of a swift heavy ion, the inelastic collision is the dominant mechanism for the transfer of energy into the material and the passage of ion generally produces ion tracks above a threshold value of electronic energy loss. The transfer of energy from the incoming ion to the atoms of target materials is through excitation and ionization. These ion tracks which are produced due to the passage of incoming ion consist of material having properties that are drastically different from the surrounding which is not being irradiated. It is therefore clear that a desired modification of materials can be obtained by the appropriate selection of the ion and its energy. Also, since the energy deposition is much localized and the process is far from equilibrium, the selective modifications can be performed without affecting the surrounding region.

The modifications induced in the fullerene C₆₀ by ion irradiation have been reported by many groups for a large range of masses and ion energies. Kastner et al. [14] irradiated the thin films of fullerene C₆₀, with 160–300 keV H, He, C, and Ar ions with dose ranging from 1×10^{12} to 5×10^{16} ions/cm². At high doses, a structural conversion of fullerene C₆₀ from crystalline form to non-crystalline form of carbon was observed. Praver et al. [15] studied the energetic ion impact on fullerene C₆₀ molecule using 620 keV Xe ions. They concluded that when hit by an energetic ion, each C₆₀ molecule was entirely broken down. For the obstruction, the cross section was about $\sim 6 \times 10^{-13}$ cm². Bajwa et al. [16] studied the upgradation that has been generated by irradiation of 110 MeV Ni ions at different fluences in thin-film samples of C₆₀ on quartz and Si substrates. They concluded that at low fluences swift heavy ion irradiation results in agglomeration formation involving multiple molecular units such as polymers or dimmers. Although many reports are available for the modifications of fullerene C₆₀ by energetic ion irradiation, the upgradation produced by swift heavy ion beam in fullerene C₇₀ thin films has not yet been studied in detail. Our group has reported few reports [17–19] for the modifications of fullerene C₇₀ using high energy ion irradiation.

In the present work, modifications produced by 65 MeV Ni ion beams in fullerene C₇₀ have been investigated using Raman spectroscopy and ion track radius is determined.

16.2 Experimental Section

Pure fullerene films can be deposited by the sublimation of respective material using resistive heating due to very small binding energy among carbon atoms in these

molecules. Other popular physical vapor deposition techniques such as evaporation by e-gun or sputtering cannot be used to deposit thin films of fullerenes due to higher energy (\sim keV) of the incoming species to the target material, compared to the binding energy among carbon atoms in fullerene molecule, which leads the damages to the fullerene molecules. The sublimation temperature of fullerene C_{60} and C_{70} is in the range of 400–600 °C. So, the energy required for the sublimation of these molecules is less than 1 eV which can be imparted to these molecules by resistive heating technique.

On quartz substrates, a thickness of \sim 200 nm C_{70} fullerenes thin film was deposited by resistive heating. By applying a weight of 5 Ton in a dye of 10 mm diameter and using C_{70} powder (Alfa Aesar, 99% pure), the pellets of C_{70} were made. Before the evaporation, the base pressure in the chamber was of the order of 10^{-7} torr. To determine the thickness of the film during deposition, a quartz crystal oscillator was used. These films were irradiated with 65 MeV Ni ion beam using pelletron accelerator at Inter University Accelerator Centre, New Delhi, in Materials Science beamline. Irradiation was done at different fluences ranging from 1×10^{12} to 1×10^{14} ions/cm². In the case of 65 MeV Ni ions, the electronic (S_e) energy loss is $\sim 6.75 \times 10^2$ eV/Å and nuclear energy is (S_n) is ~ 1.50 eV/Å in C_{70} and the range of Ni ions is ~ 15.3 μ m as determined by the Stopping and Range of Ions in Matter 2003 (SRIM) program. The Raman spectroscopy was used to characterize the pristine and irradiated thin films of fullerene C_{70} to determine the structural transformation in thin film under ion impact on 65 MeV Ni ion beam.

16.3 Results and Discussion

16.3.1 Raman Spectroscopy

Fullerene C_{70} molecule is having D_{5h} point group symmetry. For pure C_{70} at room temperature, from group theory and various first principle theories, 53 Raman active modes are predicted ($12 A_1' + 22 E_2' + 19 E_1''$) [20]. Figure 16.2 shows the typical Raman spectrum of a pure C_{70} thin film on quartz substrate.

Figure 16.3 shows the Raman spectra of pristine and irradiated fullerene films at various fluences. It can be seen that there is decrease in intensity of all Raman modes after ion irradiation. With increasing ion fluence, there is decrease in intensity of the C_{70} Raman peaks which shows that ion impact leads to the cleavage of C_{70} molecules. At fluences equal and above to 1×10^{14} ions/cm², the C_{70} characteristic modes are almost disappeared. The broad peaks observed at 1487 and 1573 cm⁻¹ at this fluence are identified as *D* and *G* peaks, which are characteristics of amorphous carbon [21]. The appearance of *D* and *G* peaks in the spectrum confirms the conversion of fullerene C_{70} into amorphous carbon at this fluence.

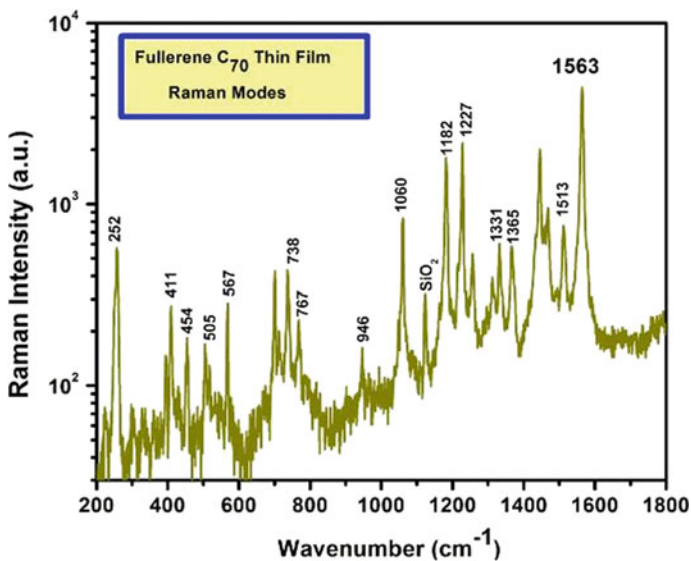


Fig. 16.2 Raman spectrum of pristine C₇₀ thin film. Raman peaks are also marked by their wavenumber

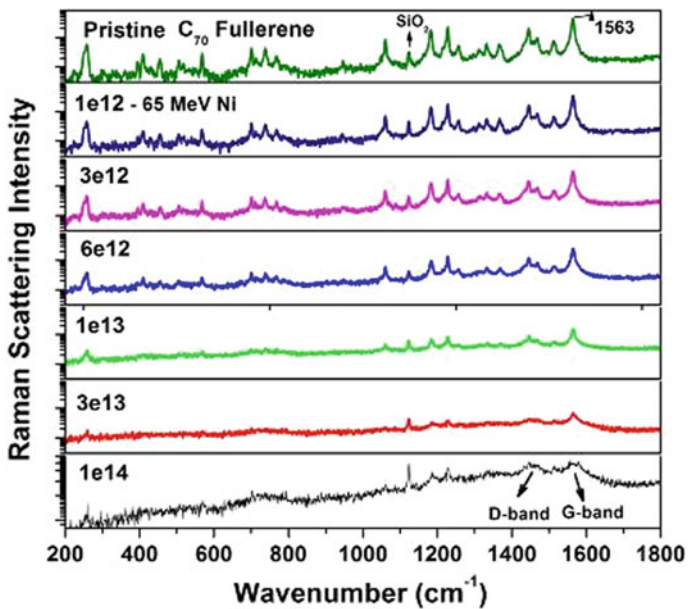


Fig. 16.3 Raman spectra of un-irradiated as well as 65 MeV Ni ions irradiated C₇₀ samples at different fluences

16.3.2 Ion Track Radius Calculations

The peak of the highest intensity (1563 cm^{-1}) of Raman spectrum of C_{70} was selected for the calculation to determine the damage cross section and ion track radius. With increasing fluence, the effect of ion irradiation on this peak is shown in Fig. 16.4. By assuming the single ion impact, the cross section σ for the destruction of the C_{70} molecules was estimated and given by the relation [22]:

$$N(\phi) = N_0 \exp(-\sigma\phi)$$

where N_0 is the areal density of pristine C_{70} , σ is the damage cross section of fullerene, and $N(\phi)$ is the areal density of the fullerene molecules remaining after irradiation at fluence ϕ . The above relation can be further simplified as follows:

$$\frac{N(\phi)}{N_0} = \exp(-\sigma\phi)$$

$$\ln\left(\frac{N(\phi)}{N_0}\right) = -\sigma\phi$$

By plotting the natural logarithm of integrated intensity $N(\phi)$ of the Raman band at 1563 cm^{-1} , normalized to the intensity of this peak for the un-irradiated film N_0 , as a function of the fluence, almost a straight line is obtained up to the fluence of $3 \times 10^{13} \text{ ions/cm}^2$ and slope is changing after this fluence (Fig. 16.5). The reason for the change in slope after $3 \times 10^{13} \text{ ions/cm}^2$ is that ion tracks start overlapping with each other after this fluence. By analyzing Raman data, a damage cross section $\sigma = 1.01 \times 10^{-13} \text{ cm}^2$ was obtained. The ion track radius r is calculated to be 1.8 nm. At

Fig. 16.4 Variations of most intense Raman peak (1563 cm^{-1}) of pristine sample with different fluences for 65 MeV Ni ion beam irradiation

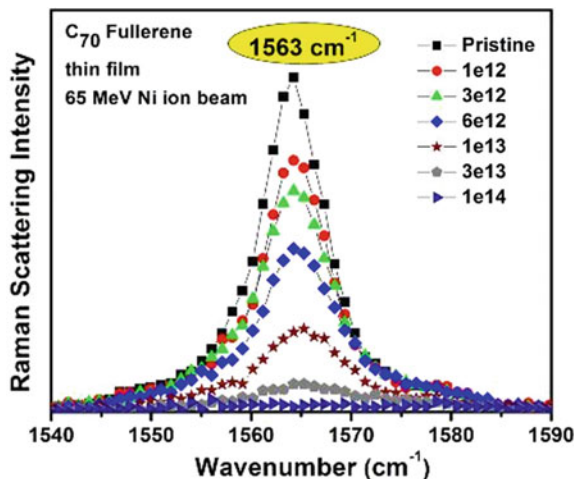
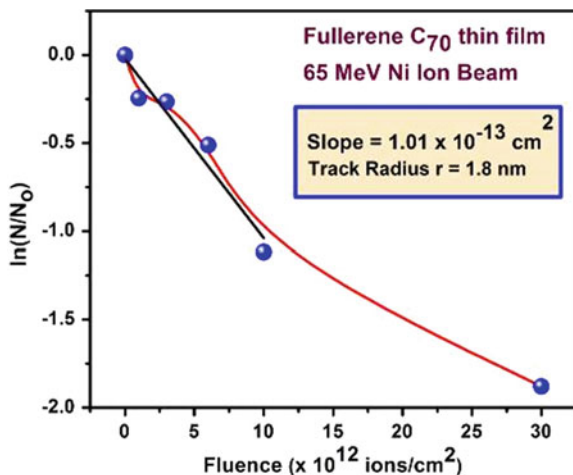


Fig. 16.5 Plot showing the decrease of the logarithm of the Raman peak intensity when normalized to the intensity of the un-irradiated sample

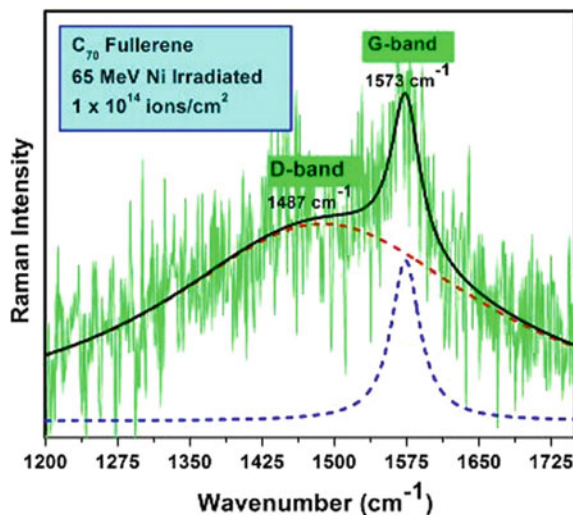


a fluence of 1×10^{14} ions/cm², when fullerene C₇₀ thin film is irradiated, the fitting of *D* and *G* bands of amorphous carbon is obtained, as shown in Fig. 16.6.

By the superposition of the two bands which are *D*-band (*D* as disorder) and comparatively sharp *G*-band (*G* for graphite), a very broadband is formed which is shown by the spectrum of amorphous carbon. These two bands are the characteristic of amorphous carbon structure with a significant degree of sp² hybridization [22].

The ion track formation can be described using thermal spike model. The incoming ion loses its energy to the electron gas of the target material, and then energy is transferred to the lattice via electron-phonon coupling during the time 10^{-13} s. The interaction between electrons and phonons comes from the local polarization.

Fig. 16.6 Fitting of *D* and *G* bands of amorphous carbon when fullerene C₇₀ film is irradiated at 1×10^{14} ions/cm²



When the temperature of the cylindrical zone exceeds the melting point of the target material, a molten state is formed in a localized cylindrical zone with a diameter of few nanometers. This high-temperature molten zone is rapidly quenched which results in an amorphous ion track along the ion path in a time ($t \geq 10^{-11}$ s) and known as ion track.

16.4 Conclusion

With 65 MeV Ni ions, the transformations of fullerene C₇₀ to amorphous thin films following ion beam irradiation have been investigated. Due to this energetic ion, the C₇₀ molecules are being destructed. Due to ionization and electronic excitation produced by 65 MeV Ni ions, the cross section for the destruction of C₇₀ molecules is found to be $\sigma = 1.01 \times 10^{-13}$ cm². The radius r of damaged cylindrical zone (ion track) is about 1.8 nm. The film irradiated at the fluence of 1×10^{14} ions/cm², and the appearance of *D* and *G* bands are ascribed to the conversion of C₇₀ into amorphous carbon.

Acknowledgements This work is financially supported by the Department of Science and Technology (DST) under INSPIRE Faculty Project with scheme (IFA-11PH-01). One of the authors (R. Vishnoi) acknowledges the financial support from DST New Delhi for the DST Women Scientist (WOS-A) Project (SR/WOS-A/PM-47/2019). The financial support from IUAC New Delhi under the UFP scheme (UFR No. 60301) is also highly acknowledged. The help of Mr. Himanshu Dixit is acknowledged here.

References

1. H. Kroto, J.R. Heath, S.C. O'Brien, R.F. Curl, R.E. Smalley, *Nature* **318**, 162 (1985)
2. R. Singhal, A. Kumar, Y.K. Mishra, S. Mohapatra, J.C. Pivin, D.K. Avasthi, *Nucl. Instr. Meth. Phys. Res. B*, **266**, 3257 (2008)
3. R. Singhal, F. Singh, A. Tripathi, D.K. Avasthi, *Radiat. Eff. Defects Solids* **164**, 38 (2009)
4. G.E. Scuseria, *Chem. Phys. Lett.* **180**, 451 (1991)
5. D.R. McKenzie, C.A. Davis, D.J.H. Cockayne, D.A. Muller, A.M. Vassallo, *Nature* **355**, 622 (1992)
6. G.B.H. Vaughan, *Science* **254**, 350 (1991)
7. M.C. Valsakumar, *Phys. Rev. B* **48**, 9080 (1993)
8. M.S. Dresselhaus, G. Dresselhaus, R. Satio, *Phys. Rev. B* **45**, 6234 (1992)
9. A. Gupta, R. Singhal, J. Narayan, D.K. Avasthi, *J. Mater. Res.* **26**, 2901 (2011)
10. D.K. Avasthi, Y.K. Mishra, R. Singhal, D. Kabiraj, S. Mohapatra, B. Mohanta, *J. Nanosci. Nanotechnol.* **10**, 2705 (2010)
11. R. Singhal, J.C. Pivin, R. Chandra, D.K. Avasthi, *Surf. Coat. Technol.* **229**, 50 (2013)
12. R. Singhal, D. Kabiraj, P.K. Kulriya, J.C. Pivin, R. Chandra, D.K. Avasthi, *Plasmonics* **8**, 295 (2013)
13. R. Singhal, J.C. Pivin, D.K. Avasthi, *J. Nanopart. Res.* **15**, 1641 (2013)
14. J. Kastner, H. Kuzmany, L. Palmethofer, *Appl. Phys. Lett.* **65**, 543 (1994)

15. S. Praver, K.W. Nugent, S. Biggs, D.G. McCulloch, W.H. Leong, A. Hoffman, R. Kalish, *Phys. Rev. B* **52**, 841 (1995)
16. N. Bajwa, K. Dharamvir, V.K. Jindal, A. Ingale, D.K. Avasthi, R. Kumar, A. Tripathi, *J. Appl. Phys.* **94**, 326 (2003)
17. P. Sharma, R. Singhal, R. Vishnoi, R. Kaushik, M.K. Banerjee, D.K. Avasthi, V. Ganesan, *Vacuum* **123**, 35 (2016)
18. P. Sharma, R. Singhal, R. Vishnoi, M.K. Banerjee, R. Kaushik, K.V. Kamma, G.B.V.S. Lakshmi, A. Tripathi, D.K. Avasthi, *Surf. Eng.* (2016). <https://doi.org/10.1080/02670844.2016.1185838>
19. P. Sharma, R. Singhal, M.K. Banerjee, R. Vishnoi, R. Kaushik, F. Singh, *Nucl. Instr. Meth. Phys. Res. B.* **379**, 188 (2016)
20. R.A. Jishi, R.M. Mirie, M.S. Dresselhaus, G. Dresselhaus, P.C. Eklund, *Phys. Rev. B* **48**, 5634 (1993)
21. A.C. Ferrai, J. Robertson, *Phys. Rev. B.* **61**, 14095 (2000)
22. P. Sharma, R. Singhal, R. Vishnoi, M.K. Banerjee, Ion track in fullerene C₇₀ thin film: dependence of electronic energy loss. in *AIP Conference Proceedings*, vol. 1832 (AIP Publishing), p. 050158

Chapter 17

Enhancement of Incident Solar Energy on Panels and Indoor Load Leveling Due to Seasonal Adjustment of Rooftop Solar PV Arrays



Prakhar Duggal, R. K. Tomar and N. D. Kaushika

Abstract The energy generating modular array network is the costliest unit of solar photovoltaic systems. The amount of energy that is transformed into electricity by the solar photovoltaic panels depends on its tilt angle with the horizontal plane as well as the orientation of the module. The optimum tilt angle of these panels is decided on the basis of annual solar energy incident on the panels, and this angle is kept fixed during the year-round cycle. In this paper, we have investigated the optimum tilt angles determined on the basis of the amount of energy incident on the panels at yearly and seasonal basis. In this investigation, we have also investigated the shading effect of these panels on the rooftop at Delhi (latitude 28.7° N). In accordance with the latitude of Delhi, the solar radiation data has been classified into three seasons, i.e., summer (May, June, July, August), winter (November, December, January, February) and equinoxes (March, April, September, October). It is found that the panels placed facing due south and seasonally adjusted at their optimum tilt angles will produce more electrical energy, 6.52% in summer, 5.94% in winter and 5–7% more electrical energy on annual basis and a larger shadow in summer and smaller shadow in winter in comparison with the panels at annually fixed tilt angle, and this in turn will decrease the indoor solar heat flux in summer and enhance the indoor solar heat flux in winter and hence will favorably affect the indoor solar heat flux as well as load leveling.

Keywords Solar photovoltaics systems · Solar radiation · Tilt angles · Irradiance · Shadow length · Heat flux and load leveling in buildings

P. Duggal (✉) · R. K. Tomar
Department of Civil Engineering, Amity University Uttar Pradesh, Noida 201313, India
e-mail: pduggal@amity.edu

N. D. Kaushika
Centre for Energy Studies, Indian Institute of Technology, Hauz Khas, New Delhi 110016, India

Present Address:
Innovation research network, H-40 Masjid moth, New Delhi (GK-2) 110048, India

17.1 Introduction

Building integrated photovoltaic system has received steadily increasing attention in the last two decades owing to the viability and reliability of solar photovoltaic conversion in electricity. It does not involve any prime mover. In India, rooftop solar photovoltaic systems are being promulgated by the government in urban areas. The buildings of hospitals, schools and other community centers are being widely used.

Reliability and viability of Building Solar Photovoltaic (BIPV) in past few decades have made it quite popular and demand for it is steadily increasing and now it stands as an important tool to harness electric energy. The government's persistent efforts have also lead to BIPV being steadily promulgated into both urban and rural areas, though urban areas are benefitting more owing to the information and ready availability. Rooftop solar photovoltaic modules are now widely used in buildings like educational institutions, hospitals, offices, etc. This practice also helps us in reducing the emission of harmful gases responsible for climatic changes into the atmosphere. The researchers from all over the world are investigating the efficacy of BIPV.

Yadav et al. [1] examined the influence of shadow through a mathematical model on BIPV module from adjacent buildings situated in four directions. The model highlights the adverse shadow effect in achieving efficacy for a BIPV thermal system. Bahrami et al. [2] examined the performance of different solar tracker at varying latitudes across Europe and Africa. The solar potential around various locations in Europe and Africa was analyzed, and energy gain was found using Perez anisotropic model. Despotovic and Nedic [3] examined the optimum tilt angle for the city of Belgrade. He found out the optimum tilt angle for flat plate collectors at yearly, seasonally and monthly basis and compared the amount of solar energy on surface of rooftop PV panel by varying tilt angle at yearly, seasonally and monthly basis. Okoye et al. [4] examined and analyzed the solar energy potentials of various strategically located cities of Nigeria highlighting the energy situation and unreliable grid connection. Through hourly analysis of metrological data in a typical metrological year format, the study was conducted to study the viability of use of rooftop solar photovoltaic for residential applications. Ahmad and Tiwari [5] examined the variation in collected energy by varying tilt angle for flat plate collector at ten locations around the world and analyzed the optimum annual tilt angle by collecting monthly mean daily global solar radiation data and monthly average clearness index on a horizontal surface. Yakup and Malik [6] determined the solar collector's optimum tilt angle and orientation for Brunei Darussalam by estimating the total solar radiation on a tilted surface through a mathematical model. The determination was made at a daily basis as well as for a specific period.

In this paper, we have investigated the optimum tilt angles determined on the basis of the amount of energy incident on the panels at yearly and seasonal basis along with the shading effect of these panels on the rooftop at Delhi (latitude 28.7° N). The solar radiation data has been categorized into three seasons, namely summer (May, June, July, August), winter (November, December, January, February) and

equinox (March, April, September, October). In this approach, we have analyzed the total solar irradiance on the south-facing surface, which is to favorably affect the air-conditioning load leveling in underneath building.

17.2 Mathematical Formulations

Total radiation incident on the tilted surface may be expressed as

$$S_t = S_{bh}R_b + S_{dh}R_d + S_{gh}\rho R_r \quad (17.1)$$

where S_t is the total radiation on the tilted surface, ρ is the ground reflectivity. S_{bh} , S_{dh} and S_{gh} are beam radiation, diffused radiation and global radiation on a horizontal surface, respectively. R_b , R_r and R_d are the beam, grounds reflected and diffuse radiation tilt factors (tilt factor is the ratio of the radiation on a sloping surface to that on a horizontal surface, or the conversion factor used to multiply radiation on a horizontal surface to give that on a sloping surface), which can be expressed as follows:

$$R_b = \cos \theta / \cos \theta_z \quad (17.2)$$

where θ , the incident angle for the beam radiation on tilted surface.

17.3 Solar Radiation on Tilted SPV Panels

The routine measurements of solar global and diffuse radiation are usually on the horizontal surface. Seldom, if ever, the solar radiation data on tilted surfaces is available. Solar radiation on tilted surfaces has been investigated by various authors [7–11]. Total solar radiation incident on tilted surface consists of three components: the beam radiation, diffuse radiation and ground reflected radiation. The diffuse radiation estimation involves a debatable assumption of the sky as an isotropic/anisotropic source. Some authors have used the simplifying assumption of an isotropic distribution of diffuse radiation, and others have considered the sky as the anisotropic source. In this paper, following Kaushika et al. [12], we have carried out an explicit evaluation of an isotropic model to estimate global radiation on inclined surfaces and also study total global radiation on variously tilted surfaces in Indian region to investigate optimal collector tilt for various solar energy applications.

17.4 Computational Results and Discussion

Solar PV modules are characterized by their wattage and their tilt with respect to horizontal. It is this aspect which has been investigated. Panel under consideration is of 33 W at Standard Temperature and Pressure (STP). The solar radiation incident on panel is proportional to electricity generation. The following table shows the seasonal variation of solar radiation incident on panels. It also indicates that the 6.52% more solar energy is incident in summer, 5.94% in winter as compared to the fixed tilt arrays (Table 17.1).

Monthly comparison of variation of solar radiation incident on solar panels at fixed and optimum tilt is indicated in Table 17.2. The effect of the adjustment of the arrays on the shadow of modules on rooftop is also investigated. Table 17.3 gives the shadow length of modules for the mean solar tilt angle of PV array for different season. Wherein, Table 17.4 gives shadow length of modules for the fixed tilt angle across year.

The amount of solar radiation incident on rooftop is responsible for the solar heat flux reaching the indoor environment of building, so to see the requirement of the air-conditioning load, shadow length pattern is also studied. The investigation also helps us in deciding adequate spacing of arrays (Table 17.5).

The variation of shadow length of panels placed on seasonally optimum angle with respect to fixed tilt array of shadow length in winter and summer months is shown in Fig. 17.1a, b, respectively.

We also investigated the variation in shadow length for a fixed tilt angle across year and seasonally adjusted PV array (Fig. 17.2).

Table 17.1 Seasonal variation of solar radiation incident on panels

Season of year	Mean declination angle (°)	Total solar radiation on South-facing surface (Wh/m ²)		Increment in solar irradiance (Wh/m ²)	Angle of incidence (°)
		Seasonally adjusted	Fixed tilt (@ 28.68°)		
Summer (May, June, July, August)	19.13	5859 (@9.57°)	5500	359 (6.52%)	9.57
Winter (November, December, January, February)	-18.96	6331 (@47.66°)	5976	355 (5.94%)	47.66
Equinox (March, April, September, October)	-0.1	6519.44 (@28.8°)	6519.58	0	28.8

Table 17.2 Monthly variation of solar radiation incident on panels

Month of the year	Declination angle	Total solar radiation on south-facing surface (Wh/m ²)		Variation (%)
		Fixed tilt (28.7°)	Optimum tilt	
January	-20.92	5565.06	5937	6.68
February	-12.95	6356.54	6520	2.57
March	-2.42	6793.44	6795	0.02
April	9.41	6711.22	6867	2.32
May	18.79	6211.86	6647	7.01
June	23.09	5505.6	6011	9.18
July	21.18	5095	5503	8.01
August	13.45	5184.52	5412	4.38
September	2.22	6038.06	6061	0.38
October	-9.6	6534.78	6638	1.58
November	-18.91	6278.74	6720	7.03
December	-23.05	5703.66	6240	9.40

Table 17.3 Shadow length for mean solar tilt angle of PV array

Weather	Months	Mean solar tilt angle of PV array (°)	Angle of incidence (°)	Shadow length (m)
Summer	May–August	3.75	May = 9.79	1.0093
			June = 5.49	1.0043
			July = 7.4	1.0065
			August = 15.13	1.0157
Winter	November–February	50	November = 47.49	1.479
			December = 51.63	1.61
			January = 49.50	1.54
			February = 41.53	1.321
Equinox	March–April, September–October	27.5	March = 31	1.164
			April = 19.17	1.047
			September = 26.36	1.15
			October = 38.18	1.25

Table 17.4 Shadow length at fixed tilt angle of PV array

Weather	Months	Solar tilt Angle of PV array (°)	Angle of incidence (°)	Shadow length (m)
Summer	May–August	27.5	May = 9.79	0.966
			June = 5.49	0.931
			July = 7.4	0.947
			August = 15.13	1.012
Winter	November–February	27.5	November = 47.49	1.39
			December = 51.63	1.469
			January = 49.50	1.427
			February = 41.53	1.407
Equinox	March–April, September–October	27.5	March = 31	1.164
			April = 19.17	1.047
			September = 26.36	1.15
			Oct = 38.18	1.25

Table 17.5 Variation in shadow length of rooftop PV array

Season of year	Shadow length (m)		Variation	Variation (%)
	At fixed tilt angle (28.68°)	Seasonally adjusted		
Summer (May, June, July, August)	0.958	1.014 (9.57°)	0.056	5.52
Winter (November, December, January, February)	1.404	1.485 (47.66°)	0.081	5.45
Equinox (March, April, September, October)	1.137	1.14 (28.8°)	0.003	0.26

17.5 Conclusion

It is found that the panels placed facing due south and seasonally adjusted at their optimum tilt angles will produce more electrical energy, 6.52% in summer, 5.94% in winter and 5–7% more electrical energy on annual basis and a larger shadow in summer and smaller shadow in winter in comparison with the panels at annually fixed tilt angle, and this in turn will decrease the indoor solar heat flux in summer and enhance the indoor solar heat flux in winter and hence will favorably affect the incident solar heat flux as well as load leveling.

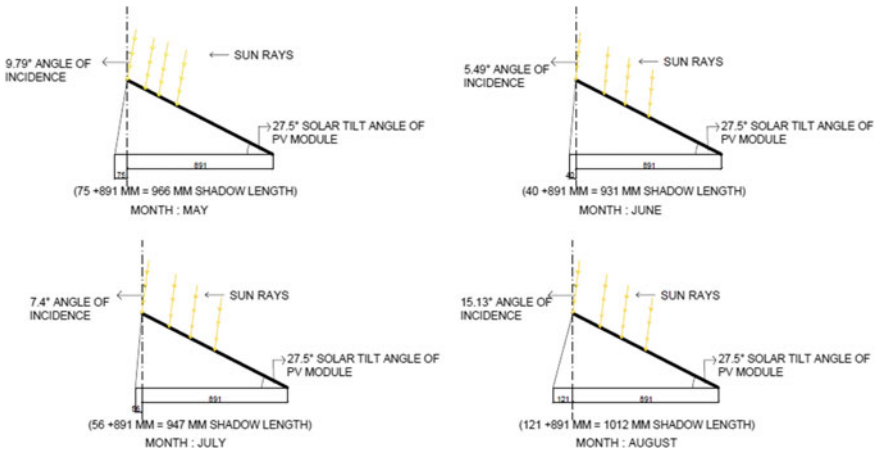


Fig. 17.1 Shadow length of solar PV array at fixed solar tilt angle for summer

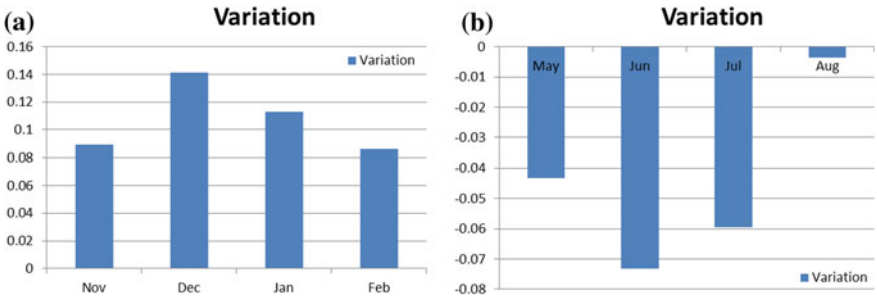


Fig. 17.2 a Variation in shadow length for winter b Variation in shadow length for summer

References

1. S. Yadav, S.K. Panda, M. Tripathy, Performance of building integrated photovoltaic thermal system with PV module. *Renew. Energy* **127**, 11–23 (2018)
2. A. Bahrami, C.O. Okoye, U. Atikol, The effect of latitude on the performance of different solar trackers in Europe and Africa. *Appl. Energy* **177**, 896–906 (2016)
3. M. Despotovic, V. Nedic, Comparison of optimum tilt angles of solar collectors determined at yearly, seasonal and monthly levels. *Energy Convers. Manag.* **97**, 121–131 (2015)
4. C.O. Okoye, O. Taylan, D.K. Baker, Solar energy potentials in strategically located cities in Nigeria: review, resource assessment and PV system design. *Renew. Sustain. Energy Rev.* **55**, 550–566 (2016)
5. M.J. Ahmad, G.N. Tiwari, Optimum tilt angle for solar collectors used in India. *Int. J. Ambient Energy* **30**(2), 73–78 (2009)
6. M.A. Yakup, A.Q. Malik, Optimum tilt angle and orientation for solar collector in Brunei Darussalam. *Renew. Energy* **24**(2), 223–234 (2001)
7. B. Liu, R. Jordan, Daily insolation on surfaces tilted towards equator. *ASHRAE J.* **10** (1961) (United States)

8. T.M. Klucher, Evaluation of models to predict insolation on tilted surfaces. *Solar Energy*, **23**, 111–114 (1979)
9. K.K. Gopinathan, Solar radiation on variously oriented sloping surfaces. *Solar Energy*, **47**(3), 173–179 (1991)
10. A.A. Sebaei, F.S. Al-Hazmi, A. Al-Ghamdi, S.J. Yaghmour, Global, direct and diffuse solar radiation on horizontal and tilted surfaces in Jeddah, Saudi Arabia, **87**(2), 568–576 (2009)
11. G. Notton, C. Paoli, S. Diaf, Estimation of tilted solar irradiation using artificial neural networks. *Energy Procedia*, **42**, 33–42 (2013)
12. N.D. Kaushika, R.K. Tomar, S.C. Kaushik, Artificial neural network model based on inter-relationship of direct, diffuse and global solar radiations. *Solar Energy* **103**, 327–342 (2014)
13. H. Yang, L. Lin, The optimum tilt angles and orientations of PV claddings for Building-Integrated Photovoltaic (BIPV) applications. *J. Solar energy Eng. Ver.* **129**, 253–255 (2007)

Chapter 18

Overview of Heat Transfer Augmentation Techniques for Parabolic Solar Concentrator Receiver



Milind S. Patil and Sanjay Pratapsingh Shekhawat

Abstract Solar energy is an alternative to conventional resources of energy. Among the many applications, solar parabolic trough collector is an application that receives heat from the radiation of the sun. Such energy is an alternative way for many rural applications: solar cooker, water pumping, water heating, solar driers, etc. Parabolic trough collector consists of the collector of a paraboloid shape and mounted with the mirrors to reflect and concentrate the solar radiation and focus the same over the receiver/absorber. This heat energy is absorbed by the heat transfer fluid inside the receiver. Such energy also converts water into steam and usually used to drive conventional electrical generators. Receiver heat loss by the mode of convection and radiation is the major cause of lower thermal efficiency. This is why it is essential to study the methods for enhancement of the heat transfer in the parabolic trough receiver. This study focused on the review and feasibility of various heat transfer augmentation techniques for parabolic trough collector receiver/absorber. Study from various publications considers various techniques that are being used by many researchers; this includes use of evacuated receivers, inserts, porous disk, fins, nanofluids, various types of inserts, etc. It is observed that with the use of insert heat transfer augmentation was reported as the highest; however, few of the insert types are yet not used.

Keywords Solar energy · Collector · Receiver · Heat loss

18.1 Introduction

Increase in the continuous demand for energy and depletion of the resources has increased the challenges to explore the more and more new resources. The use of non-conventional energy is an alternative to cater the needs. Presently, there are many

M. S. Patil (✉) · S. P. Shekhawat
Research Centre, KBC North Maharashtra University, SSBT's College of Engineering and
Technology, Jalgaon, Maharashtra 424005, India
e-mail: mspiso2012@yahoo.com

© Springer Nature Singapore Pte Ltd. 2020
V. K. Jain et al. (eds.), *Advances in Solar Power Generation
and Energy Harvesting*, Springer Proceedings in Energy,
https://doi.org/10.1007/978-981-15-3635-9_18

more solar appliances that satisfy the need for energy especially in solar thermal applications. All such applications use the technology of concentrating the solar radiation due to its availability at low density on the earth's surface. In such applications, heat energy is generated with wide range of temperatures and use of various types of heat transfer fluid. For high-temperature applications, concentrating solar collectors is selected. In an application of parabolic trough collectors, incoming solar radiation is concentrated with parabolic reflector on the focal axis where receiver is located. Heat transfer fluid is circulated through the receiver that absorbs the heat energy from solar radiation. All such receivers produce a temperature of approximately 400 °C [1]. The receivers or the absorbers are coated with the selective coating. Selective coatings increase the surface emissivity, and hence, with an increase in temperature the radiation heat loss also increases. Thus, it is important to absorb the maximum amount of heat by the heat transfer fluid circulating through the receiver. Also, the heating of the receiver results in excessive thermal stress, and glass envelop may get damage that causes loss of vacuum maintained inside envelop. Thus, it is important to study the various ways to improve the heat absorption by the receiver heat transfer fluid and improve its optical and thermal efficiency. Hence, heat transfer enhancement in PTC is of major concern.

18.2 Parabolic Trough Collector Applications

Incoming solar radiation is concentrated by the parabolic collector and heats the heat transfer fluid. There are many applications reported by researchers like low enthalpy processes [1, 2], power generation [3–5], water desalination [6], use of Rankine cycle [7, 8], cooking [9], and refrigeration [10–13]. Summary of all such applications is represented in Table 18.1.

It is observed from the reported literature that many analyses were done with the use of mathematical modeling or numerical based. Studies are performed with parameters like inclination angle, mass flow rate of heat transfer fluid, and fluid inlet

Table 18.1 Applications of solar parabolic systems

Authors	Year	Parabolic trough system applications	Reference(s)
Jaramillo et al.	2013	Low enthalpy processes	[2]
Siqueira et al.	2014	Power generation	[3, 4]
Mussard and Nydal	2014	Cooking	[9]
Balghouthi et al.	2014	Solar cooling	[13]
Larcher et al.	2014	Solar heat to industrial processes	[14]
Bigoni et al.	2014	Water pasteurization	[15]
Col et al.	2014	CPVT	[16]
Wang et al.	2015	Heat pump	[17]

temperature. Various methods were used by many researchers. All such studies were reported using finite volume method [11, 16–23], finite element method [24–29], CFD [30], Monte Carlo method of ray tracing [30–32], finite difference [33–35], and many others [10, 11, 18, 20, 21, 23, 27, 28, 36–42]. Analysis was reported using many of the engineering computer programs. The main software programs are used such as Solar Advisor Model (SAM) [43], MATLAB [44], TRNSYS [45, 46], MCRT [47], ANSYS CFX 15.0 [48], EES [49], LabVIEW [50], Thermoflex [51], and Visual C++ programming language [52]. Table 18.2 represents the summary of various literature findings of parabolic trough system.

18.3 Parabolic Trough Collector Receiver Analysis

Schematic of a solar parabolic trough collector is described in Fig. 18.1. The receiver of the system is located at the focus line of parabolic trough. The receiver is made of outer and inner tubes. The outer tube is a glass tube, and the vacuum is present in the annular space between outer and inner tubes. The inner tube is provided with a selective coating of a low emissivity to reduce radiation losses [74]. Thermal resistance network is presented in Fig. 18.2. Heat transfer study was performed by Siqueira et al. [31] by developing a mathematical model. With model, studies were reported for thermal and optical efficiency.

One-dimensional analysis for heat transfer surfaces is presented in Fig. 18.3. This is used for an energy balance and thermal analysis between the heat transfer fluid and the atmosphere [76]. Conductive, convective, and radiation heat loss were analyzed using the thermal network and the energy balance. Heat transfer analysis with the use of twisted tape was reported by Jaramillo et al. [1], as represented in Fig. 18.4. It is observed that heat transfer in the receiver/absorber tube was improved. With the use of spiral tape inside the receiver tube, the flow rotates in an axial direction, and hence, the turbulence is increased that causes a rise in Reynolds and the Nusselt numbers. Hence, there is an improvement in the convective heat transfer coefficient; this enhances the heat transfer, and larger amount of solar energy is being absorbed by the heat transfer fluid inside the receiver tube.

Bellos et al. [77] reported the studies performed with the use of three different nanoparticles. They used SOLIDWORKS Flow Simulation studio for this study. The performance was analyzed for three working fluids: thermal oil, thermal oil with nanoparticles, and pressurized water. Heat transfer efficiency was examined for each of these fluids.

Another design studied by Bellos et al. [77] is as shown in Fig. 18.5. He tested new geometry of the absorber tube with the wavy internal surface. Nanoparticle of the Al_2O_3 was used in the study and reported improved mean efficiency by 4.25%. Use of wavy internal surface provides a converging and diverging path, and this creates more turbulence and vortex flow conditions and resulted in 4.55% improvements in the mean efficiency. It was also observed that the rise in efficiency is higher for the higher fluid temperatures.

Table 18.2 Recent studies on solar parabolic trough systems

Authors	Year	Research	Theoretical (Th)/experimental (Ex)	Reference(s)
Al-Sulaiman et al.	2012	CCHP was studied with various modes of solar and solar storage operation	Th.	[53]
Kalogirou	2012	PTC receiver thermal analysis was studied with validation, and satisfactory results were obtained	Th.	[49]
Reddy and Kumar	2012	Performance optimization was reported for thermal analysis for the Indian parabolic trough collectors	Th.	[54]
Kumaresan et al.	2012	PTC instantaneous efficiency and overall system efficiency were studied with energy storage	Ex.	[55]
Calise et al.	2012	CPVT simulation study was reported	Th.	[56]
He et al.	2012	Organic Rankine cycle study was reported using TRNSYS simulation. Heat loss characterization was reported for solar collector	Th.	[45]
Al-Sulaiman	2013	Comparative study was reported for the binary vapor cycle, and Rankine cycle was reported PTC	Th.	[57]
Yilmaz et al.	2014	Mathematical model was studied for thermal performance of PTC	Th.	[58]
Peterseim et al.	2014	Reported the use of biomass fuel as a source for backup and cost-saving	Ex.	[59]

(continued)

Table 18.2 (continued)

Authors	Year	Research	Theoretical (Th)/experimental (Ex)	Reference(s)
Vogel et al.	2014	Hybridization with natural gas was studied for PTC power plant	Th.	[60]
Alguacil et al.	2014	PTC application for direct steam generation was reported	Th. Ex.	[61]
Ramos et al.	2014	PTC was studied for the shedding light effects	Th.	[62]
Lobón and Valenzuela	2014	PTC was studied for thermal and hydraulic behavior	Th.	[63]
Boukelia et al.	2015	Reported PTC power plant studies with and without thermal storage and backup system	Th.	[64]
Qu and Wang	2015	Experimental analysis for thermal efficiency of the PTC system was reported	Ex.	[65]
Luo et al.	2015	PTC system simulation with pumps and oil–water heat exchanger was reported	Th.	[66]
Almasabi et al.	2015	Reported transient performance of PTC	Th. Ex.	[67]
Bouvier et al.	2015	Reported experimental analysis for micro-cogeneration system using PTC for direct steam generation	Ex.	[68]
Mwesigye et al.	2016	Reported the effect of intercept factor and heat flux distribution	Th.	[69]

(continued)

Table 18.2 (continued)

Authors	Year	Research	Theoretical (Th)/experimental (Ex)	Reference(s)
Caron and Röger	2016	Reported receiver thermal performance and heat loss measurements	Ex.	[70]
Martín and Valenzuela	2016	Reported the studies on flow measurements for a PTC	Ex.	[71]
Chafie et al.	2016	Thermal performance analysis was reported for a PTC system with incidence angle, intercept factor, and thermal efficiency	Ex.	[72]
Al-Maliki et al.	2016	Simulation study was reported for a PTC based 50 MWe solar thermal power plant	Th.	[73]

Fig. 18.1 Solar parabolic trough collector. *Source* De Risi et al. [74]

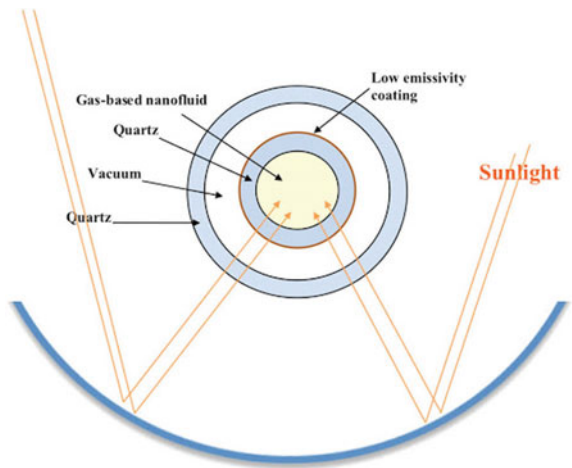
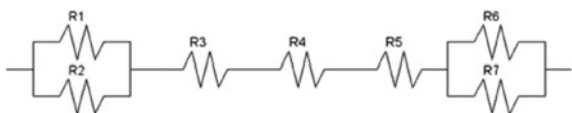


Fig. 18.2 Heat transfer thermal resistance network



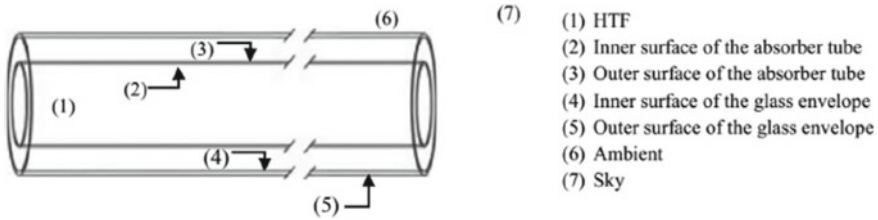


Fig. 18.3 Schematic diagram for energy balance. *Source* Antônio Marcos et al. [75]

Fig. 18.4 Diagram indicating the use of twisted tape inside the receiver tube. *Source* Jaramillo et al. [1]

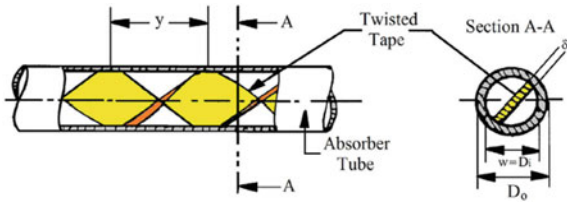
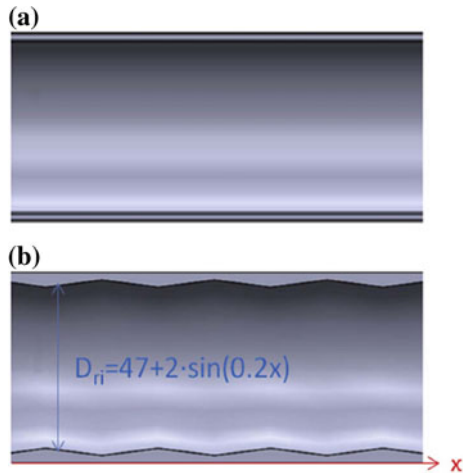


Fig. 18.5 Regular and converging–diverging receiver tube. *Source* Bellos et al. [77]



Bimetallic absorber tube application was reported by Khanna et al. [76]. Study was conducted for the effects of thicknesses and material used on the temperature gradient. Two different layers were used to reduce the temperature gradient across the circumference of the absorber tube as shown in Fig. 18.6. Thickness and thermal conductivity of the two different layers of the receiver tube were varied. It was reported that the material with higher thermal conductivity should form the outer layer for the reduction in non-uniformity of the temperature. Also, it is found that the increase in rim angle decreases the maximum circumferential temperature of the receiver tube (Fig. 18.7).

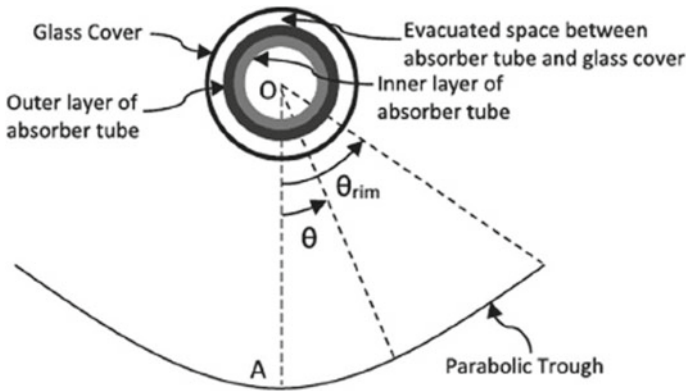


Fig. 18.6 Sectional view of a PTC system receiver with two different layers of the absorber tube. *Source* Khanna et al. [76]

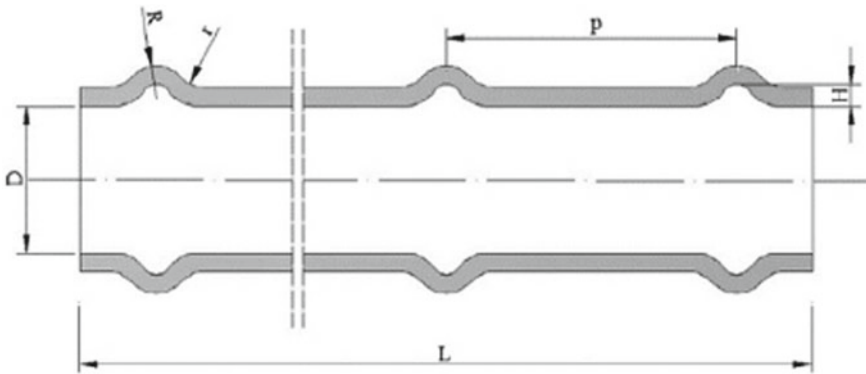


Fig. 18.7 Corrugated tube-type receiver. *Source* Fuqiang et al. [78]

Fuqiang et al. [78] reported the use of corrugated tube-type receiver for the PTC system. Improvement in heat transfer and decreases in thermal strain analysis were observed. The shape of the receiver tube was convex corrugated type; this shape increases the turbulence and hence enhances the heat transfer performance (Fig. 18.8).

Receivers with dimples, protrusions, and helical were studied by Huang et al. [79]. It was reported that heat transfer rate was enhancement with the use of all such types of geometries inside the tube. Increase in surface area is the cause of heat transfer enhancement. It was reported that the dimple tube design was better than the other two types of receiver tube. More in numbers of dimples with deeper dimples and closely spaced dimples have a better performance.

Reddy et al. [56] used a porous disk into the receiver with different configurations as shown in Fig. 18.9. It was observed that thermal gradient was smaller between the

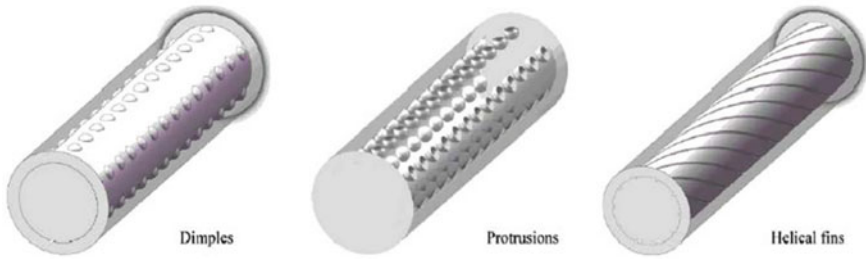


Fig. 18.8 PTC receiver with dimples, protrusions, and helical fin-type surface. *Source* Huang et al. [79]

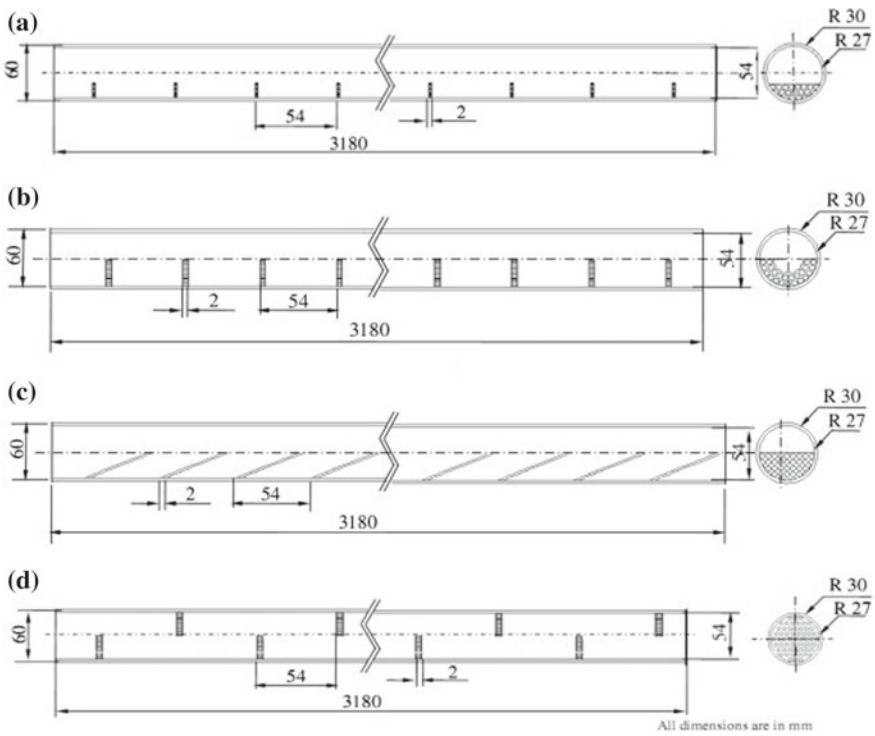


Fig. 18.9 PTC receiver with various porous configurations. *Source* Ravi Kumar [56]

wall surface of the receiver and the heat transfer fluid, and therefore, the heat transfer enhanced in such type of receiver compared with the conventional receiver.

Studies on perforated plate type of inserts were reported by Mwesigye et al. [80]. Thermodynamic optimization of a parabolic trough receiver was investigated with such inserts as shown in Fig. 18.10. Studies were conducted for three different designs

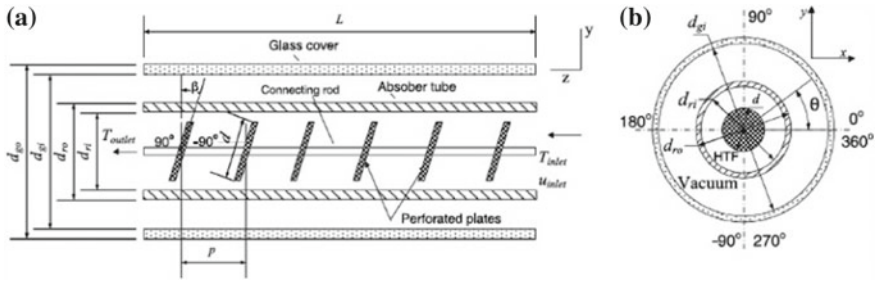


Fig. 18.10 PTC receiver with perforated tape. *Source* Mwesigye et al. [80]

like the spacing between two sequential perforated plates (P), the angle of orientation (β), and the diameter of perforated plate (d) [80].

Zhang et al. [81] reported the studies on U-type heat pipe solar receiver as shown in Fig. 18.11. The receiver that used was vacuum type with outer surface coated with black coating. The performance of a steam generating system and overall heat losses was analyzed. Thermal efficiency was reported as 0.791 and 0.47 in calm and windy days. Table 18.2 summarizes the various literature findings on thermal analysis parabolic trough system receiver. Table 18.3 summarizes the various types of inserts that are used with parabolic trough receiver (Table 18.4).

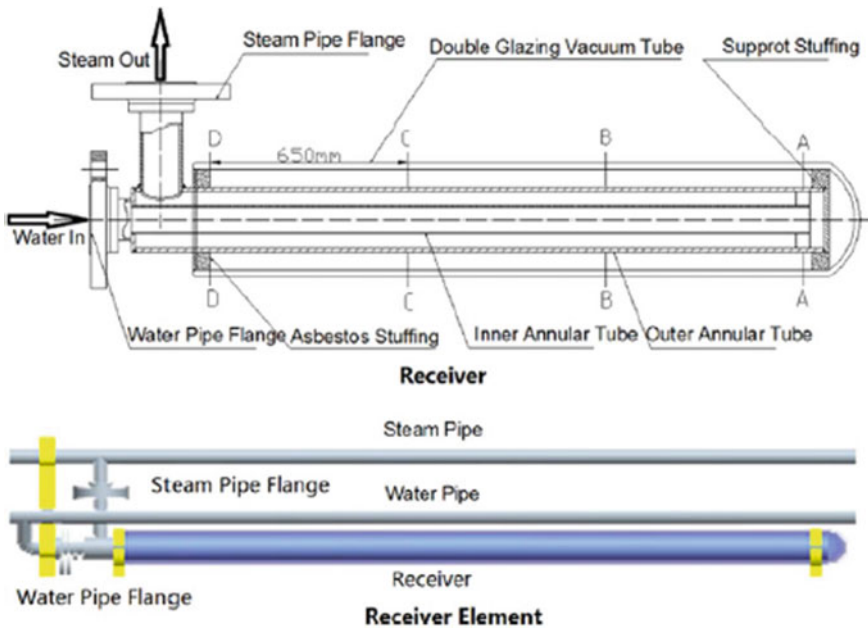


Fig. 18.11 PTC receiver with U-type heat pipe. *Source* Zhang et al. [81]

Table 18.3 Literature findings on heat transfer analysis of solar parabolic trough collector systems

Authors	Year	Receiver analysis	Theoretical (Th)/experimental (Ex)	Reference(s)
Li et al.	2012	Reported studies on reliability of the vacuum parabolic trough receivers	Ex.	[82]
Hong et al.	2012	Studies on development of solar receiver/reactor PTC system to produce hydrogen	Ex.	[83]
Zhang et al.	2013	Reported studies on heat losses of a double-glazing vacuum U-type solar receiver	Th. Ex.	[84]
Lei et al.	2013	Reported total heat loss, end loss, and coating thermal emittance for a new design of a receiver	Th. Ex.	[85]
Mwesigye et al.	2014	Investigated thermal performance of a PTC receiver with perforated plate inserts	Th.	[86]
Song et al.	2014	Reported numerical studies on the effect on the flux distribution for transverse and longitudinal angle	Th.	[87]
Xiao et al.	2014	Reported investigations on optical activity and heat transfer process of a heat transfer fluid through V-cavity absorber	Th.	[88]
Wu et al.	2014	Reported structural reliability study about stainless steel tube	Th. Ex.	[89]
Padilla et al.	2014	Reported energy analysis for a PTC's receiver and collector energy efficiency	Th.	[90]
Waghole et al.	2014	Reported the effect of using silver nanofluid in the receiver tube of PTC system	Th.	[91]

(continued)

Table 18.3 (continued)

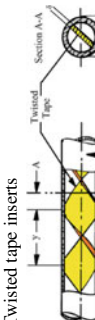

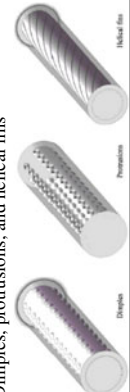
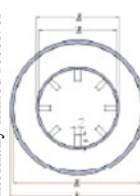
Authors	Year	Receiver analysis	Theoretical (Th)/experimental (Ex)	Reference(s)
Valdés et al.	2014	Studies were reported on effect of temperature distribution along the receiver tube	Th.	[92]
Canavarro et al.	2014	Reported on new optical designs for PTC	Th.	[93]
Zavattoni et al.	2014	Reported reliability studies and effectiveness of receiver design	Th.	[94]
Habib et al.	2015	Reported numerical analysis for the use of long receiver	Th.	[95]
Mwesigye et al.	2015	Reported the analysis of the PTC receiver with the use of perforated plate	Th.	[80]
Chen et al.	2015	Reported thermal analysis design of cavity receiver	Th. Ex.	[96]
Jaramillo et al.	2016	Reported thermal analysis with the use of twisted tape inserts	Th. Ex.	[1]
Bellos et al.	2016	Studies were performed for a dimpled receiver tube with sine geometry	Th.	[77]
Hermoso et al.	2016	Studies were reported for the receiver with different manufacturers and diameters	Ex.	[97]

(continued)

Table 18.3 (continued)


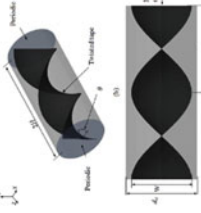
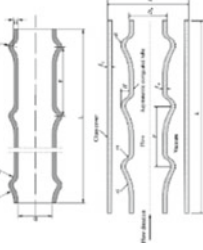
Authors	Year	Receiver analysis	Theoretical (Th)/experimental (Ex)	Reference(s)
Khanna et al.	2016	Studies were reported on the use of bimetallic receiver tube	Ex.	[76]
Guo et al.	2016	Reported studies on receiver thermal efficiency. Effect of parameters like mass flow rate of the working fluid, the inlet, and ambient temperatures, and the diameter of the absorber and the cover glass, the wind speed, and the incident angle were studied	Th.	[98]
Fuqiang et al.	2016	Reported the studies on the use of symmetric outward convex corrugated receiver tube	Th.	[78]

Table 18.4 Literature findings various types of inserts used inside the receiver tube of a solar parabolic trough collector systems

Authors	Year	Technology used for analysis of PTC	Type of study	Findings	Reference(s)
Jaramillo et al.	2016	 <p>Twisted tape inserts</p>	Numerical	Improvement in efficiency by 4.5%	[1]
Bellos et al.	2016	 <p>Wavy absorber tube—2016</p>	Numerical	Improvement in efficiency by 6–8%	[77]
Bellos et al.	2016	 <p>Dimples, protrusions, and helical fins</p>	Numerical	$Re = 1 \times 10^4$ to 2×10^4 Nu increases 44–64%, Friction factor increases 56–77%	[79]
Bellos et al.	2017	 <p>Internally finned receiver</p>	Numerical	Re = 2300 flow is assumed to be turbulent Thermal efficiency 69.11%, friction factor increases by 12%	[99]

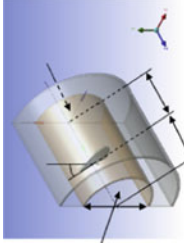
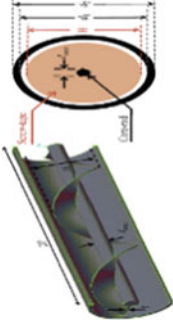
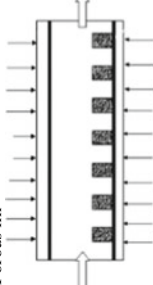
(continued)

Table 18.4 (continued)

Authors	Year	Technology used for analysis of PTC	Type of study	Findings	Reference(s)
Xiangtao et al.	2017	Pin fin 	Numerical	Re = 7063.2 Nu increased up to 9.0% Overall heat transfer performance factor increased up to 12%	[100]
Mwesigye et al.	2016	Wall-detached twisted tape 	Numerical	Re = 150,300 Heat transfer performance of about 69% Friction factor increases range 1.6–14.5 Entropy generation reduced up to 58.8%	[101]
Fuqiang et al.	2016	Symmetric outward convex corrugated 	Numerical	Re = 52,518 Overall heat transfer performance factor is 148%	[78]

(continued)

Table 18.4 (continued)

Authors	Year	Technology used for analysis of PTC	Type of study	Findings	Reference(s)
Mwesigye et al.	2015	Perforated plate 	Numerical	$Re = 1 \times 10^4$ to 2×10^4 Heat transfer performance increases between 1.02 and 2.34 times Entropy generation reduced up to 53%	[80]
Song et al.	2014	Showed numerically that the transversal angle affects the flux distribution more greatly than longitudinal angle	Numerical	Increase receiver temperature. But with a decreasing effect with the increase of Re. At the range of studied Re, certain helical screw-tape inserts reduce Q_{loss} , T_{max} , and ΔT	[87]
Song et al.	2014	Helical screw-tape insert 	Numerical	Heat loss 6 times decreased Friction factor 23 times increased	[87]
Reddy et al.	2014	Porous fin 	Numerical	1.7 kPa of pressure penalty Enhanced the heat transfer 13.8%	[102]

(continued)

Table 18.4 (continued)

Authors	Year	Technology used for analysis of PTC	Type of study	Findings	Reference(s)
Kaspersk a et al	2013	Internal multiple fin array 	Numerical	14% improvement of the efficiency	[103]

18.4 Conclusions

Review presented here has an objective to study the methods for enhancement of heat transfer adopted by the various researchers. Inserts can be effective in the laminar zone. With the use of various types of inserts, heat transfer rate was increased but at the cost of pressure drops inside the receiver tube. Findings of this comprehensive review can be summarized as below:

- In direct steam generation, since there is a change of phase, it is not possible to use nanofluids.
- PTC receiver with evacuated tube has higher thermal efficiency (65–70%) because of the elimination of convection and radiation losses.
- The performance of use of inserts with nanofluids was observed to be better in both laminar and turbulent regions.
- The base fluids with insert were found to augment heat transfer in the range of 10–200% in turbulent region compared to its flow in plane receiver.
- It is evident from the review that research carried out till date is focused more on aqueous nanofluids than oil-based nanofluids.
- Coiled tube with larger pitches has higher heat transfer enhancement than smaller pitches.
- Use of longer twisted tape increases the pressure drop as compared with plain receiver tube. Thus, experimental analysis for use of short-length twisted tape can be conducted. Also, receivers with diverging/converging section for the full length and with the use of inserts can be analyzed for PTC receiver performance.
- The other several passive techniques to enhance the heat transfer in a flow, such as ribs, conical nozzle, are generally more efficient in the turbulent flow than in the laminar flow.
- Receiver of the PTC shall be analyzed for the various heat losses. For such characterization, laboratory simulation can be performed experimentally. Results of such simulation can be then used for the development of various correlations which can be used for the prediction of heat loss.

There are many numerical studies but there is a need for experimental study; also for analyzing, performance of heat transfer augmentation technique using turbulators used with receivers of the solar parabolic trough collector. Also, reported investigations so far are observed with constant cross-sectional area of flow, and any investigations are reported for receiver with converging–diverging cross-sectional area.

Studies reported so far does not consider the heat loss analysis from the receiver surface due to convection as a result of wind flow that occurs near the surface of the receiver. The development of laboratory experimental simulation setup will be useful for heat loss characterization as a result of wind flow conditions that are occurred in practical application. Data obtained from such an experimental analysis will be then used to develop a prediction model using adaptive neuro-fuzzy inference system (ANFIS) which has better prediction ability than the conventional heat transfer methods and analysis.

References

1. O.A. Jaramillo, M. Borunda, K.M. Velazquez-Lucho, M. Robles, Parabolic trough solar collector for low enthalpy processes: an analysis of the efficiency enhancement by using twisted tape inserts. *Renew Energy* **93**, 125–141 (2016). <https://doi.org/10.1016/j.renene.2016.02.046>
2. O.A. Jaramillo, E. Venegas-Reyes, J.O. Aguilar, R. Castrejón-García, F. Sosa-Montemayor, Parabolic trough concentrators for low enthalpy processes. *Renew Energy* **60**, 529–539 (2013). <https://doi.org/10.1016/j.renene.2013.04.019>
3. J. Macedo-Valencia, J. Ramírez-Ávila, R. Acosta, O.A. Jaramillo, J.O. Aguilar, Design, construction and evaluation of parabolic trough collector as demonstrative prototype. *Energy Procedia* **57**, 989–998 (2014). <http://dx.doi.org/10.1016/j.egypro.2014.10.082>
4. V.C.P. Filho, A.B. De Sá, J.C. Passos, S. Colle, Experimental and numerical analysis of thermal losses of a parabolic trough solar collector. *Energy Procedia* **57**, 381–390 (2014). <https://doi.org/10.1016/j.egypro.2014.10.191>
5. T. Richert, K. Riffelmann, P. Nava, The influence of solar field inlet and outlet temperature on the cost of electricity in a molten salt parabolic trough power plant. *Energy Procedia* **69**, 1143–1151 (2015). <https://doi.org/10.1016/j.egypro.2015.03.184>
6. H. Jafari Mosleh, S.J. Mamouri, M.B. Shafii, Sima A. Hakim, A new desalination system using a combination of heat pipe, evacuated tube and parabolic through collector. *Energy Convers. Manag.* **99**, 141–150 (2015). <https://doi.org/10.1016/j.enconman.2015.04.028>
7. J.L. Bouvier, G. Michaux, P. Salagnac, T. Kientz, D. Rochier, Experimental study of a micro combined heat and power system with a solar parabolic trough collector coupled to a steam Rankine cycle expander. *Sol. Energy* **134**, 180–192 (2016). <https://doi.org/10.1016/j.solener.2016.04.028>
8. S. Toghyani, E. Baniasadi, E. Afshari, Thermodynamic analysis and optimization of an integrated Rankine power cycle and nano-fluid based parabolic trough solar collector. *Energy Convers. Manag.* **121**, 93–104 (2016). <https://doi.org/10.1016/j.enconman.2016.05.029>
9. M. Mussard, O.J. Nydal, Influence of solar tracking inaccuracy and sun rays modeling on the efficiency of a small-scale parabolic trough. *Energy Procedia* **57**, 1508–1515 (2014). <https://doi.org/10.1016/j.egypro.2014.10.143>
10. F. Wang, H. Feng, J. Zhao, W. Li, F. Zhang, R. Liu, Performance assessment of solar assisted absorption heat pump system with parabolic trough collectors. *Energy Procedia* **70**, 529–536 (2015). <https://doi.org/10.1016/j.egypro.2015.02.157>
11. Z.D. Cheng, Y.L. He, F.Q. Cui, R.J. Xu, Y.B. Tao, Numerical simulation of a parabolic trough solar collector with nonuniform solar flux conditions by coupling FVM and MCRT method. *Sol. Energy* **86**, 1770–1784 (2012). <https://doi.org/10.1016/j.solener.2012.02.039>
12. M. Balghouthi, A.B.H. Ali, S.E. Trabelsi, A. Guizani, Optical and thermal evaluations of a medium temperature parabolic trough solar collector used in a cooling installation. *Energy Convers Manag.* **86**, 1134–1146 (2014). <http://dx.doi.org/10.1016/j.enconman.2014.06.095>
13. O. Kizilkan, A. Kabul, I. Dincer, Development and performance assessment of a parabolic trough solar collector-based integrated system for an ice-cream factory. *Energy* **100**, 167–176 (2016). <https://doi.org/10.1016/j.energy.2016.01.098>
14. M. Larcher, M. Rommel, A. Bohren, E. Frank, S. Minder, Characterization of a parabolic trough collector for process heat applications. *Energy Procedia* **57**, 2804–2811 (2014). <https://doi.org/10.1016/j.egypro.2014.10.313>
15. R. Bigoni, S. Kötzsch, S. Sorlini, T. Egli, Solar water disinfection by a parabolic trough concentrator (PTC): flow-cytometric analysis of bacterial inactivation. *J. Clean. Prod.* **67**, 62–71 (2014). <https://doi.org/10.1016/j.jclepro.2013.12.014>
16. D. Del Col, M. Bortolato, A. Padovan, M. Quaggia, Experimental and numerical study of a parabolic trough linear CPVT system. *Energy Procedia* **57**, 255–1164 (2014). <http://dx.doi.org/10.1016/j.egypro.2014.10.030>
17. F. Calise, A. Palombo, L. Vanoli, A finite-volume model of a parabolic trough photo-voltaic/thermal collector: energetic and exergetic analyses. *Energy* **46**, 283–294 (2012). <https://doi.org/10.1016/j.energy.2012.08.021>

18. S.M. Akbarimosavi, M. Yaghoubi, 3D thermal-structural analysis of an absorber tube of a parabolic trough collector and the effect of tube deflection on optical efficiency. *Energy Procedia* **49**, 2433–2443 (2013). <https://doi.org/10.1016/j.egypro.2014.03.258>
19. Z.Y. Li, Z. Huang, W.Q. Tao, Three-dimensional numerical study on turbulent mixed convection in parabolic trough solar receiver tube. *Energy Procedia* **75**, 462–466 (2015). <https://doi.org/10.1016/j.egypro.2015.07.422>
20. Z.-D. Cheng, Y.-L. He, K. Wang, B.-C. Du, F.Q. Cui, A detailed parameter study on the comprehensive characteristics and performance of a parabolic trough solar collector system. *Appl. Therm. Eng.* **63**, 278–289 (2014). <https://doi.org/10.1016/j.applthermaleng.2013.11.011>
21. Z.D. Cheng, Y.L. He, F.Q. Cui, Numerical study of heat transfer enhancement by unilateral longitudinal vortex generators inside parabolic trough solar receivers. *Int. J. Heat Mass Transf.* **55**, 5631–5641 (2012). <https://doi.org/10.1016/j.ijheatmasstransfer.2012.05.057>
22. H. Al-Ansary, O. Zeitoun, Numerical study of conduction and convection heat losses from a half-insulated air-filled annulus of the receiver of a parabolic trough collector. *Sol. Energy* **85**, 3036–3045 (2011). <https://doi.org/10.1016/j.solener.2011.09.002>
23. Y.-L. He, J. Xiao, Z.-D. Cheng, Y.-B. Tao, A MCRT and FVM coupled simulation method for energy conversion process in parabolic trough solar collector. *Renew Energy* **36**, 976–985 (2011). <https://doi.org/10.1016/j.renene.2010.07.017>
24. Y. Wang, Q. Liu, J. Lei, H. Jin, A three-dimensional simulation of a parabolic trough solar collector system using molten salt as heat transfer fluid. *Appl. Therm. Eng.* **70**, 462–476 (2014). <https://doi.org/10.1016/j.applthermaleng.2014.05.051>
25. Y. Wang, J. Xu, Q. Liu, Y. Chen, H. Liu, Performance analysis of a parabolic trough solar collector using Al₂O₃/synthetic oil nanofluid. *Appl. Therm. Eng.* **107**, 469–478 (2016). <https://doi.org/10.1016/j.applthermaleng.2016.06.170>
26. S. Meiser, S. Schneider, E. Lüpfert, B. Schiricke, R. Pitz-Paal, Evaluation and assessment of gravity load on mirror shape and focusing quality of parabolic trough solar mirrors using finite-element analysis. *Appl. Energy* (2015). <https://doi.org/10.1016/j.apenergy.2016.04.045>
27. M. Andre, M. Mier-Torrecilla, R. Wüchner, Numerical simulation of wind loads on a parabolic trough solar collector using lattice Boltzmann and finite element methods. *J. Wind Eng. Ind. Aerodyn.* **146**, 185–194 (2015). <https://doi.org/10.1016/j.jweia.2015.08.010>
28. Y. Wang, Q. Liu, J. Lei, H. Jin, Performance analysis of a parabolic trough solar collector with non-uniform solar flux conditions. *Int. J. Heat Mass Transf.* **82**, 236–249 (2015). <https://doi.org/10.1016/j.ijheatmasstransfer.2014.11.055>
29. S. Meiser, E. Lüpfert, B. Schiricke, R. Pitz-Paal, Conversion of parabolic trough mirror shape results measured in different laboratory setups. *Sol. Energy* (2015). <https://doi.org/10.1016/j.solener.2014.09.021>
30. E. Kaloudis, E. Papanicolaou, V. Belessiotis, Numerical simulations of a parabolic trough solar collector with nanofluid using a two-phase model. *Renew Energy* **97**, 218–229 (2016). <https://doi.org/10.1016/j.renene.2016.05.046>
31. A.M. de Oliveira Siqueira, P.E.N. Gomes, L. Torrezani, E.O. Lucas, G.M. da Cruz Pereira, Heat transfer analysis and modeling of a parabolic trough solar collector: an analysis. *Energy Procedia* **57**, 401–410 (2014). <http://dx.doi.org/10.1016/j.egypro.2014.10.193>
32. H. Liang, S. You, H. Zhang, Comparison of three optical models and analysis of geometric parameters for parabolic trough solar collectors. *Energy* **96**, 37–47 (2016). <https://doi.org/10.1016/j.energy.2015.12.050>
33. Z.D. Cheng, Y.L. He, F.Q. Cui, B.C. Du, Z.J. Zheng, Y. Xu, Comparative and sensitive analysis for parabolic trough solar collectors with a detailed Monte Carlo ray-tracing optical model. *Appl. Energy* **115**, 559–572 (2014). <https://doi.org/10.1016/j.apenergy.2013.11.001>
34. Y. Marif, H. Benmoussa, H. Bouguettaia, M.M. Belhadj, M. Zerrouki, Numerical simulation of solar parabolic trough collector performance in the Algeria Saharan region. *Energy Convers. Manag.* **85**, 521–529 (2014). <https://doi.org/10.1016/j.enconman.2014.06.002>
35. A.M.I. Mohamed, N.A. El-Minshawy, Theoretical investigation of solar humidification dehumidification desalination system using parabolic trough concentrators. *Energy Convers. Manag.* **52**, 3112–3119 (2011). <https://doi.org/10.1016/j.enconman.2011.04.026>

36. L. Zhang, M.C. Yang, Y.Z. Zhu, H.J. Chen, Numerical study and optimization of mirror gap effect on wind load on parabolic trough solar collectors. *Energy Procedia* **69**, 233–241 (2015). <https://doi.org/10.1016/j.egypro.2015.03.027>
37. Z.-D. Cheng, Y.-L. He, B.-C. Du, K. Wang, Q. Liang, Geometric optimization on optical performance of parabolic trough solar collector systems using particle swarm optimization algorithm. *Appl. Energy* **148**, 282–293 (2015). <https://doi.org/10.1016/j.apenergy.2015.03.079>
38. S. Caron, M. Röger, Modelling simulation and identification of heat loss mechanisms for parabolic trough receivers installed in concentrated solar power plants. *IFAC Proc* **48**, 372–377 (2015). <http://dx.doi.org/10.1016/j.ifacol.2015.05.058>
39. R. Silva, M. Pérez, M. Berenguel, L. Valenzuela, E. Zarza, Uncertainty and global sensitivity analysis in the design of parabolic-trough direct steam generation plants for process heat applications. *Appl. Energy* **121**, 233–244 (2014). <https://doi.org/10.1016/j.apenergy.2014.01.095>
40. Q. Liu, M. Yang, J. Lei, H. Jin, Z. Gao, Y. Wang, Modeling and optimizing parabolic trough solar collector systems using the least squares support vector machine method. *Sol. Energy* **86**, 1973–1980 (2012). <https://doi.org/10.1016/j.solener.2012.01.026>
41. Y.B. Tao, Y.L. He, Numerical study on coupled fluid flow and heat transfer process in parabolic trough solar collector tube. *Sol. Energy* **84**, 1863–1872 (2010). <https://doi.org/10.1016/j.solener.2010.07.012>
42. M. Biencinto, L. González, E. Zarza, L.E. Díez, J. Muñoz-Antón, Performance model and annual yield comparison of parabolic-trough solar thermal power plants with either nitrogen or synthetic oil as heat transfer fluid. *Energy Convers. Manag.* **87**, 238–249 (2014). <https://doi.org/10.1016/j.enconman.2014.07.017>
43. T.E. Boukelia, O. Arslan, M.S. Mecibah, ANN-based optimization of a parabolic trough solar thermal power plant. *Appl. Therm. Eng.* **107**, 1210–1218 (2016). <https://doi.org/10.1016/j.applthermaleng.2016.07.084>
44. M. Ashouri, A.M. Khoshkar Vandani, M. Mehrpooya, M.H. Ahmadi, A. Abdollahpour, Techno-economic assessment of a Kalina cycle driven by a parabolic Trough solar collector. *Energy Convers. Manag.* **105**, 1328–1339 (2015). <https://doi.org/10.1016/j.enconman.2015.09.015>
45. Y.-L. He, D.-H. Mei, W.-Q. Tao, W.-W. Yang, H.-L. Liu, Simulation of the parabolic trough solar energy generation system with Organic Rankine Cycle. *Appl. Energy* **97**, 630–641 (2012). <https://doi.org/10.1016/j.apenergy.2012.02.047>
46. M. Borunda, O.A. Jaramillo, R. Dorantes, A. Reyes, Organic rankine cycle coupling with a parabolic trough solar power plant for cogeneration and industrial processes. *Renew Energy* **86**, 651–663 (2016). <https://doi.org/10.1016/j.renene.2015.08.041>
47. Z.D. Cheng, Y.L. He, J. Xiao, Y.B. Tao, R.J. Xu, Three-dimensional numerical study of heat transfer characteristics in the receiver tube of parabolic trough solar collector. *Int Commun Heat Mass Transf* **37**, 782–787 (2010). <https://doi.org/10.1016/j.icheatmasstransfer.2010.05.002>
48. J. Paetzold, S. Cochar, A. Vassallo, D.F. Fletcher, Wind engineering analysis of parabolic trough solar collectors: the effects of varying the trough depth. *J. Wind Eng. Ind. Aerodyn.* **135**, 118–128 (2014). <https://doi.org/10.1016/j.jweia.2014.10.017>
49. S.A. Kalogirou, A detailed thermal model of a parabolic trough collector receiver. *Energy* **48**, 298–306 (2012). <https://doi.org/10.1016/j.energy.2012.06.023>
50. A. Maccari, M. Montecchi, An optical profilometer for the characterisation of parabolic trough solar concentrators. *Sol. Energy* **81**, 185–194 (2007). <https://doi.org/10.1016/j.solener.2006.04.004>
51. A. Trad, M.A. Ait Ali, Determination of the optimum design through different funding scenarios for future parabolic trough solar power plant in Algeria. *Energy Convers. Manag.* **91**, 267–279 (2015). <https://doi.org/10.1016/j.enconman.2014.12.013>
52. G.C. Bakos, Design and construction of a two-axis Sun tracking system for parabolic trough collector (PTC) efficiency improvement. *Renew. Energy* **31**, 2411–2421 (2006). <https://doi.org/10.1016/j.renene.2005.11.008>

53. F.A. Al-Sulaiman, F. Hamdullahpur, I. Dincer, Performance assessment of a novel system using parabolic trough solar collectors for combined cooling, heating, and power production. *Renew. Energy* **48**, 161–172 (2012). <https://doi.org/10.1016/j.renene.2012.04.034>
54. K.S. Reddy, K.R. Kumar, Solar collector field design and viability analysis of standalone parabolic trough power plants for Indian conditions. *Energy. Sustain. Dev.* **16**, 456–470 (2012). <https://doi.org/10.1016/j.esd.2012.09.003>
55. G. Kumaresan, R. Sridhar, R. Velraj, Performance studies of a solar parabolic trough collector with a thermal energy storage system. *Energy* **47**, 395–402 (2012). <https://doi.org/10.1016/j.energy.2012.09.036>
56. K.S. Reddy, K. Ravi Kumar, C.S. Ajay, Experimental investigation of porous disc enhanced receiver for solar parabolic trough collector. *Renew. Energy* **77**, 308–319 (2015). <https://doi.org/10.1016/j.renene.2014.12.016>
57. F.A. Al-Sulaiman, Energy and sizing analyses of parabolic trough solar collector integrated with steam and binary vapor cycles. *Energy* **58**, 561–570 (2013). <https://doi.org/10.1016/j.energy.2013.05.020>
58. I.H. Yilmaz, M.S. Söylemez, Thermo-mathematical modeling of parabolic trough collector. *Energy Convers. Manag.* **88**, 768–784 (2014). <https://doi.org/10.1016/j.enconman.2014.09.031>
59. J.H. Peterseim, A. Tadros, U. Hellwig, S. White, Increasing the efficiency of parabolic trough plants using thermal oil through external superheating with biomass. *Energy Convers. Manag.* **77**, 784–793 (2014). <https://doi.org/10.1016/j.enconman.2013.10.022>
60. T. Vogel, G. Oeljeklaus, K. Gorner, J. Dersch, T. Polklas, Hybridization of parabolic trough power plants with natural gas. *Energy Procedia* **49**, 1238–1247 (2013). <https://doi.org/10.1016/j.egypro.2014.03.133>
61. M. Alguacil, C. Prieto, A. Rodriguez, J. Lohr, Direct steam generation in parabolic trough collectors. *Energy Procedia* **49**, 21–29 (2013). <https://doi.org/10.1016/j.egypro.2014.03.003>
62. C. Ramos, J. Beltran, R. Ramirez, Advances on the development of the parabolic trough technology in Mexico. *Energy Procedia* **57**, 2090–2097 (2014). <https://doi.org/10.1016/j.egypro.2014.10.174>
63. D.H. Lobón, L. Valenzuela, Impact of pressure losses in small-sized parabolic-trough collectors for direct steam generation. *Energy* **61**, 502–512 (2013). <https://doi.org/10.1016/j.energy.2013.08.049>
64. T.E. Boukelia, M.S. Mecibah, B.N. Kumar, K.S. Reddy, Investigation of solar parabolic trough power plants with and without integrated TES (thermal energy storage) and FBS (fuel backup system) using thermic oil and solar salt. *Energy* **88**, 292–303 (2015). <https://doi.org/10.1016/j.energy.2015.05.038>
65. H. Qu, M. Wang, Experimental study of a parabolic trough medium temperature solar thermal system. *Energy Procedia* **70**, 504–509 (2015). <https://doi.org/10.1016/j.egypro.2015.02.154>
66. N. Luo, G. Yu, H. Hou, Y. Yang, Dynamic modeling and simulation of parabolic trough solar system. *Energy Procedia* **69**, 1344–1348 (2015). <https://doi.org/10.1016/j.egypro.2015.03.137>
67. A. Almasabi, A. Alobaidli, T.J. Zhang, Transient characterization of multiple parabolic trough collector loops in a 100 MW CSP plant for solar energy harvesting. *Energy Procedia* **69**, 24–33 (2015). <https://doi.org/10.1016/j.egypro.2015.03.004>
68. J.L. Bouvier, G. Michaux, P. Salagnac, F. Nepveu, D. Rochier, T. Kientz, Experimental characterisation of a solar parabolic trough collector used in a micro-CHP (microcogeneration) system with direct steam generation. *Energy* **83**, 474–485 (2015). <https://doi.org/10.1016/j.energy.2015.02.050>
69. A. Mwesigye, Z. Huan, T. Bello-Ochende, J.P. Meyer, Influence of optical errors on the thermal and thermodynamic performance of a solar parabolic trough receiver. *Sol. Energy* **135**, 703–718 (2016). <https://doi.org/10.1016/j.solener.2016.06.045>
70. S. Caron, M. Röger, In-situ heat loss measurements of parabolic trough receivers based on transient infrared thermography. *Sol. Energy* **135**, 111–121 (2016). <https://doi.org/10.1016/j.solener.2016.05.033>

71. R. López-Martín, L. Valenzuela, On-site comparison of flowmeters installed in a parabolic-trough solar collector test facility. *Meas. J. Int. Meas. Confed.* **92**, 271–278 (2016). <https://doi.org/10.1016/j.measurement.2016.06.033>
72. M. Chafie, M.F. Ben Aissa, S. Bouadila, M. Balghouthi, A. Farhat, A. Guizani, Experimental investigation of parabolic trough collector system under Tunisian climate: design, manufacturing and performance assessment. *Appl. Therm. Eng.* **101**, 273–283 (2016). <https://doi.org/10.1016/j.applthermaleng.2016.02.073>
73. W.A.K. Al-Maliki, F. Alobaid, V. Kez, B. Epple, Modelling and dynamic simulation of a parabolic trough power plant. *J. Process Control* **39**, 123–138 (2016). <https://doi.org/10.1016/j.jprocont.2016.01.002>
74. A. De Risi, M. Milanese, D. Laforgia, Modelling and optimization of transparent parabolic trough collector based on gas-phase nanofluids. *Renew. Energy* **58**, 134–139 (2013). <https://doi.org/10.1016/j.renene.2013.03.014>
75. A. Marcos et al., Heat transfer analysis and modeling of a parabolic trough solar collector: an analysis. *Energy Procedia* **57**, 401–410 (2014)
76. S. Khanna, V. Sharma, S. Singh, S.B. Kedare, Explicit expression for temperature distribution of receiver of parabolic trough concentrator considering bimetallic absorber tube. *Appl. Therm. Eng.* **103**, 323–332 (2016). <https://doi.org/10.1016/j.applthermaleng.2016.04.110>
77. E. Bellos, C. Tzivanidis, K.A. Antonopoulos, G. Gkinis, Thermal enhancement of solar parabolic trough collectors by using nanofluids and converging-diverging absorber tube. *Renew. Energy* **94**, 213–222 (2016). <https://doi.org/10.1016/j.renene.2016.03.062>
78. W. Fuqiang, T. Zhexiang, G. Xiangtao, T. Jianyu, H. Huaizhi, L. Bingxi, Heat transfer performance enhancement and thermal strain restrain of tube receiver for parabolic trough solar collector by using asymmetric outward convex corrugated tube. *Energy* **114**, 275–92 (2016). <https://dx.doi.org/10.1016/j.energy.2016.08.013>
79. Z. Huang, G.L. Yu, Z.Y. Li, W.Q. Tao, Numerical study on heat transfer enhancement in a receiver tube of parabolic trough solar collector with dimples, protrusions and helical fins. *Energy Procedia* **69**, 1306–1316 (2015). <https://doi.org/10.1016/j.egypro.2015.03.149>
80. A. Mwesigye, T. Bello-Ochende, J.P. Meyer, Multi-objective and thermodynamic optimisation of a parabolic trough receiver with perforated plate inserts. *Appl. Therm. Eng.* **77**, 42–56 (2015). <https://doi.org/10.1016/j.applthermaleng.2014.12.018>
81. L. Zhang, Z. Yu, L. Fan, W. Wang, H. Chen, Y. Hu et al., An experimental investigation of the heat losses of a U-type solar heat pipe receiver of a parabolic trough collector-based natural circulation steam generation system. *Renew. Energy* **57**, 262–268 (2013). <https://doi.org/10.1016/j.renene.2013.01.029>
82. J. Li, Z. Wang, J. Li, D. Lei, Vacuum reliability analysis of parabolic trough receiver. *Sol. Energy Mater. Sol. Cells* **105**, 302–308 (2012). <https://doi.org/10.1016/j.solmat.2012.06.034>
83. H. Hong, Q. Liu, H. Jin, Operational performance of the development of a 15 kW parabolic trough mid-temperature solar receiver/reactor for hydrogen production. *Appl. Energy* **90**, 137–141 (2012). <https://doi.org/10.1016/j.apenergy.2011.04.050>
84. S. Peng, H. Hong, H. Jin, Z. Zhang, A new rotatable-axis tracking solar parabolic trough collector for solar-hybrid coal-fired power plants. *Sol. Energy* **98**, 492–502 (2013). <https://doi.org/10.1016/j.solener.2013.09.039>
85. D. Lei, Q. Li, Z. Wang, J. Li, J. Li, An experimental study of thermal characterization of parabolic trough receivers. *Energy Convers. Manag.* **69**, 107–115 (2013). <https://doi.org/10.1016/j.enconman.2013.02.002>
86. A. Mwesigye, T. Bello-Ochende, J.P. Meyer, Heat transfer and thermodynamic performance of a parabolic trough receiver with centrally placed perforated plate inserts. *Appl. Energy* **136**, 989–1003 (2014). <https://doi.org/10.1016/j.apenergy.2014.03.037>
87. X. Song, G. Dong, F. Gao, X. Diao, L. Zheng, F. Zhou, A numerical study of parabolic trough receiver with nonuniform heat flux and helical screw-tape inserts. *Energy* **77**, 771–782 (2014). <https://doi.org/10.1016/j.energy.2014.09.049>
88. X. Xiao, P. Zhang, D.D. Shao, M. Li, Experimental and numerical heat transfer analysis of a V-cavity absorber for linear parabolic trough solar collector. *Energy Convers. Manag.* **86**, 49–59 (2014). <https://doi.org/10.1016/j.enconman.2014.05.001>

89. Z. Wu, D. Lei, G. Yuan, J. Shao, Y. Zhang, Z. Wang, Structural reliability analysis of parabolic trough receivers. *Appl. Energy* **123**, 232–241 (2014). <https://doi.org/10.1016/j.apenergy.2014.02.068>
90. R.V. Padilla, A. Fontalvo, G. Demirkaya, A. Martinez, A.G. Quiroga, Exergy analysis of parabolic trough solar receiver. *Appl. Therm. Eng.* **67**, 579–586 (2014). <https://doi.org/10.1016/j.applthermaleng.2014.03.053>
91. D.R. Waghole, R.M. Warkhedkar, V.S. Kulkarni, R.K. Shrivastva, Experimental investigations on heat transfer and friction factor of silver nanofluid in absorber/receiver of parabolic trough collector with twisted tape inserts. *Energy Procedia* **45**, 558–567 (2014). <https://doi.org/10.1016/j.egypro.2014.01.060>
92. A. Valdés, R. Almanza, A. Soria, Determining the deflection magnitude of a steel receiver from a DSG parabolic trough concentrator under stratified flow conditions. *Energy Procedia* **57**, 341–350 (2014). <https://doi.org/10.1016/j.egypro.2014.10.039>
93. D. Canavaro, J. Chaves, M. Collares-Pereira, New optical designs for large parabolic troughs. *Energy Procedia* **49**, 1279–1287 (2013). <https://doi.org/10.1016/j.egypro.2014.03.137>
94. S.A. Zavattoni, A. Gaetano, M.C. Barbato, G. Ambrosetti, P. Good, F. Malnati et al., CFD analysis of a receiving cavity suitable for a novel CSP parabolic trough receiver. *Energy Procedia* **49**, 579–588 (2013). <https://doi.org/10.1016/j.egypro.2014.03.062>
95. L. Habib, M.I. Hassan, Y. Shatilla, A realistic numerical model of lengthy solar thermal receivers used in parabolic trough CSP plants. *Energy Procedia* **75**, 473–478 (2015). <https://doi.org/10.1016/j.egypro.2015.07.427>
96. F. Chen, M. Li, P. Zhang, X. Luo, Thermal performance of a novel linear cavity absorber for parabolic trough solar concentrator. *Energy Convers. Manag.* **90**, 292–299 (2015). <https://doi.org/10.1016/j.enconman.2014.11.034>
97. J.L. Navarro-Hermoso, G. Espinosa-Rueda, C. Heras, I. Salinas, N. Martinez, M. Gallas, Parabolic trough solar receivers characterization using specific test bench for transmittance, absorptance and heat loss simultaneous measurement. *Sol. Energy* **136**, 268–277 (2016). <https://doi.org/10.1016/j.solener.2016.07.012>
98. J. Guo, X. Huai, Z. Liu, Performance investigation of parabolic trough solar receiver. *Appl. Therm. Eng.* **95**, 357–364 (2016). <https://doi.org/10.1016/j.applthermaleng.2015.11.035>
99. E. Bellos, C. Tzivanidis, D. Tsimpoukis, Thermal enhancement of parabolic trough collector with internally 2 finned absorbers. *Solar energy*, **32** (2017). <https://doi.org/10.1016/j.solener.2017.08.067>
100. F. Wang, Z. Tang, X. Gong, J. Tan, H. Han, B. Li, Heat transfer performance enhancement and thermal strain restraint of tube receiver for parabolic trough solar collector by using asymmetric outward convex corrugated tube. *Energy* **114**, 275–292 (2016)
101. A. Mwesigye, T. Bello-Ochende, J.P. Meyer, Heat transfer and entropy generation in a parabolic trough receiver with wall-detached twisted tape inserts. *Int. J. Therm. Sci.* **99**, 238–257 (2016)
102. K.S. Reddy, G.V. Satyanarayana, Numerical study of porous finned receiver for solar parabolic trough concentrator. *Eng. Appl. Comput. Fluid. Mech.* **2**(2), 172–184 (2008)
103. K. Jacek, N. Magdalena, Investigation of thermo-hydraulic performance of concentrated solar air-heater with internal multiple-fin array. *Appl. Therm. Eng.* **58**(1–2), 411–419 (2013)

Chapter 19

Synthesis of ZnO Nanostructures Using RTCVD, Suitable for Various Applications



Ravi Keshwar Kumar, Avshish Kumar, Samina Husain, M. Husain and M. Zulfequar

Abstract Zinc oxide (ZnO) nanostructures have been successfully synthesized using rapid thermal chemical vapor deposition (RTCVD) technique under ambient oxygen environment. During the growth of ZnO nanostructure, the gas pressure of oxygen was maintained at 5 Torr, and the low pressure inside the growth chamber was kept of the order of 10^{-6} Torr in order to increase the vapor pressure during sublimation. The morphological and application aspects of the grown ZnO nanostructures were studied at room temperature and at LN₂ temperature. Different characterization techniques such as X-ray diffraction (XRD), field emission scanning electron microscopy (FESEM), energy-dispersive X-ray spectroscopy (EDAX) and UV–Vis spectroscopy have been performed for elemental analysis, crystalline nature, shape, size and band gap calculation of as-grown ZnO nanostructure. The results exhibited that grown ZnO nanostructures have various applications including solar cells and supercapacitor for energy storage devices.

Keywords Zinc oxide · Morphological variations · Structural properties · RTCVD

19.1 Introduction

Various synthesis techniques have been used for the preparation of zinc oxide (ZnO) nanostructures for variety of device applications such as sensing device (gas, chemical and biosensor), transparent conductors in solar cell, opto-electronic devices and LED as well as in high power electronics [1–11]. Instead of these, ZnO nanostructures have also been used in hydrogen storage, piezo transducer, photo-detectors and

R. Keshwar Kumar · M. Husain · M. Zulfequar (✉)
Department of Physics, Jamia Millia Islamia, New Delhi, India
e-mail: mzulfe@rediffmail.com

A. Kumar
Amity Institute for Advanced Research and Studies (Materials & Devices), Amity University,
Noida, Uttar Pradesh, India

S. Husain
Centre for Nanoscience and Nanotechnology, Jamia Millia Islamia, New Delhi, India

© Springer Nature Singapore Pte Ltd. 2020
V. K. Jain et al. (eds.), *Advances in Solar Power Generation and Energy Harvesting*, Springer Proceedings in Energy,
https://doi.org/10.1007/978-981-15-3635-9_19

spintronic devices due to electrical and optical properties of nanostructures [12–18]. Most ZnO application is based on its semiconducting, catalytic and piezoelectric properties [19]. ZnO nanostructures with desirable morphology have been synthesized using various interesting techniques. Depending on the mode of synthesis, ZnO nanostructures synthesis is classified into two main categories, dry and wet chemical synthesis. Both the methods have their advantages and disadvantages [20]. Out of these synthesis methods, ZnO nanostructures can be synthesized by various physical methods like thermal oxidation, sputtering and hydrothermal method with focus on studying the properties of as-grown material or on the application in different forms [21–34]. Amongst these, aligned one dimensional (1D) ZnO nanowires/nanorods and snowflake shape nanostructure are demonstrating superior device properties with high carrier mobility compared to that of nonaligned ZnO nanostructures [7, 35]. Due to the quantum size effect, increasing band gap energy of 1D ZnO and nanoparticles can be proved by its photoluminescence property. Therefore, study of the properties of individual ZnO nanostructures is fundamentally essential to future innovative design of functional nanoscale devices.

ZnO has a key feature of large excitonic binding energy (~ 60 meV) and high optical gain of 300 cm^{-1} at room temperature; results in an efficient and extreme stable excitonic emission at room temperature (RT) are promising to various applications [2, 4]. However, in spite of practical importance, knowledge of vibrational phonon properties and dependency on morphology of ZnO nanostructures is yet to be explored, which enhance the understanding of solar cell and hydrogen storage application of the specific nanostructure [10–15]. In spite of these promising applications, few doped ZnO nanostructure has promising applications in ultraviolet photo-sensor and medical applications also [36, 37]. Therefore, we chose to study the morphological variation and structural properties of ZnO deposited by RTCVD at room temperature and at liquid nitrogen temperature, for various solar cell, supercapacitor and energy storage applications.

19.2 Experimental Details

Rapid thermal chemical vapor deposition (RTCVD) was used to prepare various nanostructures of ZnO. Pure Zn (99.9%) was evaporated in oxygen ambient. Thermal evaporation system was modified to RTCVD by constructing a small subevaporation chamber using quartz tube (25 mm diameter and 120 mm length). An arrangement was made in this quartz tube for gas inlet, opening for evaporation source, sample holder and gas outlet, as shown in Fig. 19.1. With the quartz tube, we were able to confine the evaporated material and maintain the uniform oxygen pressure in the vicinity of the evaporation source. Mo-boat was used as an evaporation source. After loading the substrates and source material, chamber was evacuated to 10^{-5} Torr, then 5 Torr oxygen was injected into the subchamber, and this oxygen pressure was maintained throughout the evaporation. The as-prepared samples were analyzed for elemental and structural properties.

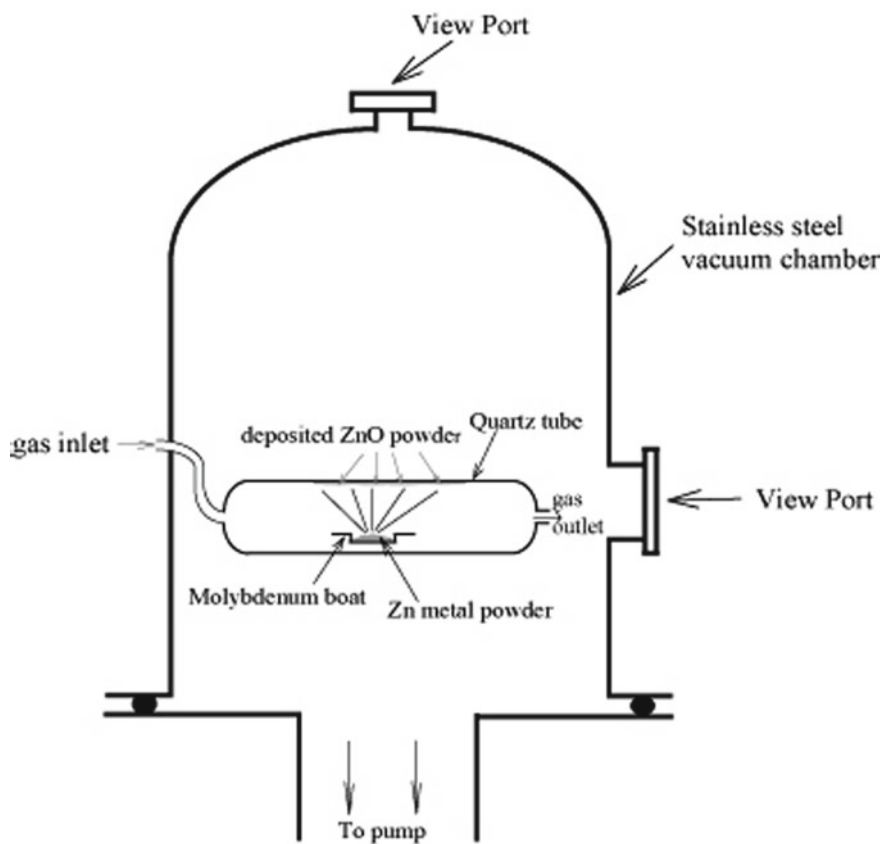


Fig. 19.1 Experimental setup of RTCVD system used for the growth of ZnO nanostructures

X-ray diffraction measurements were performed using Rigaku advanced diffractometer with $\text{CuK}\alpha$ radiation ($\lambda = 1.542 \text{ \AA}$) for the Bragg angle ranging from 20° to 80° . Raman scattering spectra were obtained using LabRam HR800 JY with HeNe source ($\lambda = 632.8 \text{ nm}$) and beam diameter of $1.2 \mu\text{m}$ operating at fixed laser power of 2 mW and scanning range of $200\text{--}650 \text{ cm}^{-1}$. Scanning electron microscopic (SEM) images were obtained using JEOL (JSM-6380) electron microscope.

19.3 Results and Discussion

Figure 19.2 depicts the X-ray diffraction patterns of ZnO nanostructures grown at room temperature (RT) and liquid nitrogen (LN_2) temperature. The variation in peak intensities with liquid nitrogen temperature is observed. The observed peaks matched well with the standard peaks related to the JCPDS files (36–1451, 21–1486, 01–1136),

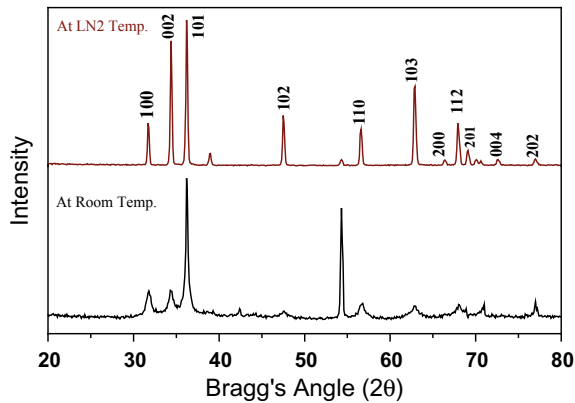


Fig. 19.2 X-ray diffraction patterns of ZnO nanostructures grown at RT and LN₂ show peaks related to various phases indicating wurtzite crystal structure

which are of wurtzite hexagonal phase. The presence of intense peaks reflects good crystallinity of grown ZnO nanocrystal. The peak intensity related to (002) plane increased with the sample grown at LN₂ temperature, whereas the intensity of other peaks related to (100), (002), (101), (102), (110), (103), (112) (201) (004) and (202) has changed. A peak related to (101) exhibits maximum intensity with a peak of unknown phase of ZnO having maximum intensity. The peak related to (110), (102), (200), (201), (202) and (004) exhibits low intensity, whereas peaks related to (100), (002), (101), (103) phases exhibit maximum intensity compared to peaks related to other phases which suggest the growth of wurtzite structure ZnO. The high peak intensity reflects the good crystallinity. Besides hexagonal wurtzite structure, as-grown samples at LN₂ having nanocrystal like structures (Fig. 19.3), a peak related to (110) and (004) ZnO phase with remarkable intensity is present which can be correlated to radial orientation of nanocrystal. Slight intensity variation of peaks related to various ZnO phases suggests different order of crystallinity. It is noticed that peaks related to metallic Zn were not present indicating the proper oxide growth during the investigated process.

Figure 19.3 shows the scanning electron micrographs of samples deposited at room temperatures and at LN₂ temperature, which clearly depicts the change in morphology from sea urchin-like structure (at RT) to nanocrystal (at LN₂). The size of the synthesized structure has also varied greatly from 300 nm to 1 μm with the length of 2–5 μm at normal conditions, whereas at liquid nitrogen, temperature size of the nanocrystal varied from 100 nm to 1 μm. Deposition at room temperature resulted in the sea urchin-like structure forming porous microscopic bunches of about 5–10 μm as shown in Fig. 19.3. At some places, these structures are apparently fused together forming bunches of sea urchin-like structures. Although various reports available to grow similar ZnO nanostructures like nanopins and nanoneedles using thermal evaporation techniques, under oxygen atmosphere, our experiments were confined

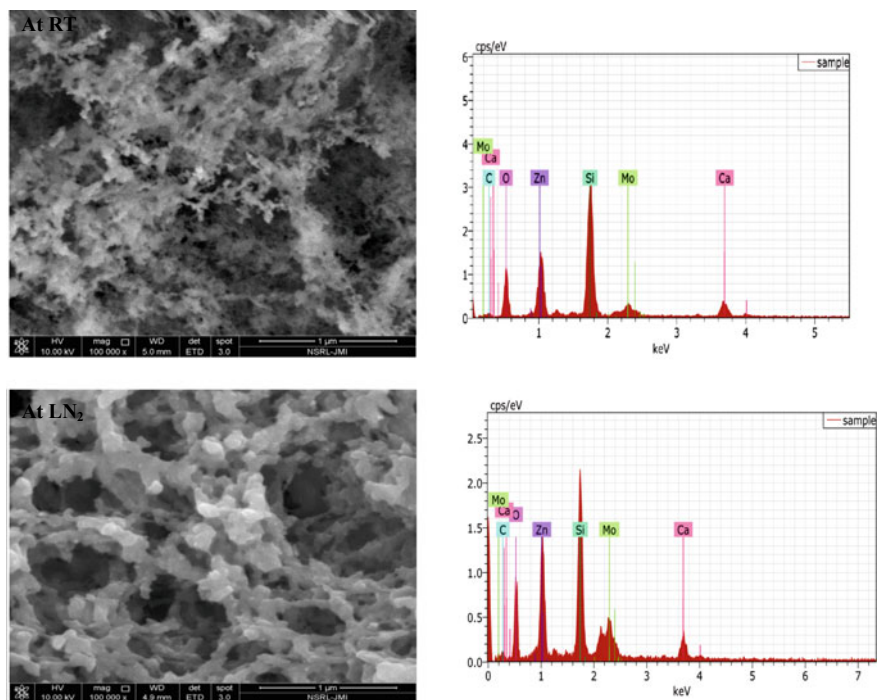


Fig. 19.3 FESEM micrographs with EDS spectrum of ZnO nanostructures grown at RT and at LN₂ temperature

to a controlled oxygen pressure of 5 Torr and chamber base pressure of 10^{-5} Torr aiming to good quality ZnO nanostructures.

EDS confirms that no other contents present in the as-prepared sample of ZnO nanostructures at room temperature and at LN₂ temperature.

Raman spectroscopy study was carried out as it is sensitive to the morphology and size of the nanostructures, and spectra of the samples are shown in Fig. 19.4. The spectra show three different peaks around 330, 434 and 578 cm^{-1} suggest the presence of wurtzite ZnO phase. There are three types of peaks observed, (i) a suppressed and broad peak around 326.5–330 cm^{-1} is of lower E_2 and related to the multiple photon scattering processes, (ii) a most dominant phonon peak for both the samples is about 433–435.1 cm^{-1} is the E_2 high peaks associated with oxygen atoms and (iii) a comparatively symmetric peak about 572.5–578 cm^{-1} of $E_1(\text{LO})$ modes. Presence of $E_1(\text{LO})$ peak reflects the impurities, oxygen-deficient sites and Zn interstitial sites exists in the grown nanostructures. The suppressed lower E_2 peak and a significant E_2 high peak suggest the good crystalline nature of the grown ZnO nanostructures. The Raman observed peaks are describing lower E_2 , E_2 high and $E_1(\text{LO})$ modes are in well agreement to that of reported vibrational modes of ZnO nanostructures as well as in Raman spectra of bulk ZnO.

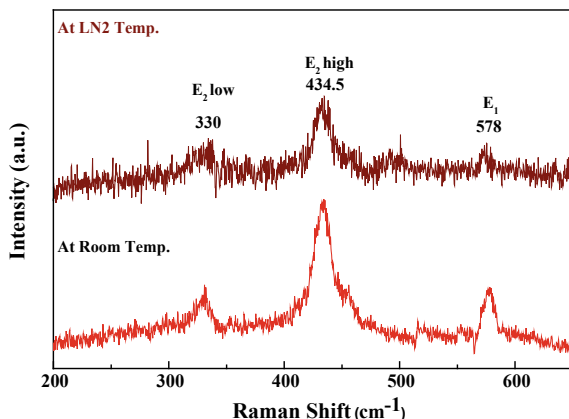


Fig. 19.4 Raman spectra of ZnO nanostructures obtained at RT as well as at LN₂ temperature

UV–Vis spectroscopy has been done for the calculation of band gap for the as-grown ZnO nanostructures at various substrate temperatures. The experimental data for the present sample of ZnO gives a best fit with $n = 1/2$, which suggests that the absorption in this ZnO film is due to direct transition. Therefore, the experimental data is re-plotted as $(\alpha h\nu)^2$ versus photon energy ($h\nu$) for direct transition. Figure 19.5 shows the variation of $(\alpha h\nu)^2$ with photon energy ($h\nu$) for as-grown ZnO at room temperature and at LN₂ temperature. The value of direct optical band gap (E_g) is calculated by taking the intercept on the X-axis. The calculated value of E_g for the ZnO film is found to be 3.32 eV at RT, whereas at LN₂ temperature, the band gap slightly increased to 3.75 eV. So, it is clear that variation in band gap can be seen at various substrate temperatures.

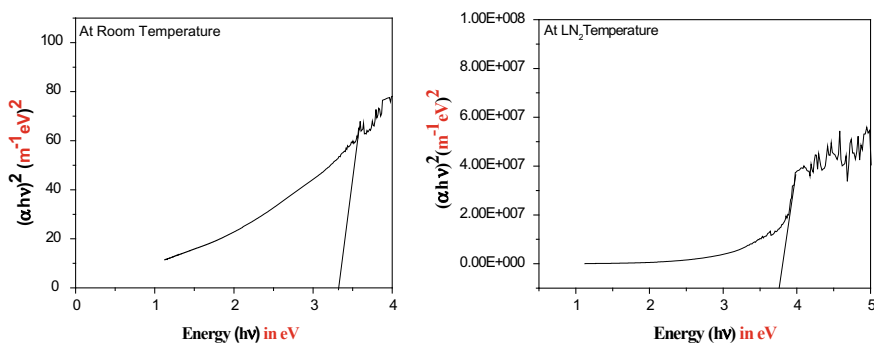


Fig. 19.5 Variation of $(\alpha h\nu)^2$ versus photon energy ($h\nu$) for ZnO grown at RT and LN₂ temperature

19.4 Conclusion

In summary, we have successfully grown ZnO nanostructures like sea urchin nanostructure and nanocrystal, at 5 Torr constant oxygen pressure in the chamber during rapid thermal evaporation. XRD, SEM and Raman were used to characterize the grown nanostructures. XRD analysis reveals the single crystalline hexagonal wurtzite ZnO phase. E_2 high peak in Raman spectra suggests the growth of hexagonal wurtzite structure, and the presence of lower E_2 peak indicates the presence of Zn interstitial sites and oxygen deficiency in the grown nanostructures. Variation in band gap has also been observed at substrate temperature. The slight change in band gap has also been observed at LN₂ temperature. From the above studies, it is found that these types of ZnO nanostructures are suitable for various applications like solar cell, supercapacitor and energy storage applications.

References

1. A.A. Khan, V.A. Fonoberov, M. Shamsa, A.A. Balandina, et al. *J. Appl. Phys.* **97**, 124313 (2005)
2. V.A. Fonoberov, A.A. Balandin, et al. *J. Nanoelect. Optoele.* **1**, 19 (2006)
3. B. Sunandan, J. Dutta et al., *Sci. Technol. Adv. Mater.* **10**, 013001 (2009)
4. Y. Boqian, F. Peterxian, A. Kumar, R.S. Katiyar, M. Achermann, et al. *J. Phys. D: Appl. Phys.* **42**, 195402 (2009)
5. L.I. Yang, M.W. Paul, L. Yin, T.B. Scott et al., *Nanotechnology* **18**, 215602 (2007)
6. A. Umar, C. Ribeiro, A.-Al. Hajry, Y. Masuda, Y.B. Hahn et al. *J. Phys. Chem. C*, **113**, 14715 (2009)
7. M.C. Newton, S. Firth, T. Matsuura, P.A. Warburton, et al. *J. Phys.: Conf. Ser.* **26**, 251 (2006)
8. S. Shishiyana, L. Chowb, O. Lupana, T. Shishiyana et al., *ECS Trans.* **3**, 65 (2006)
9. V.V. Ursaki, I.O. Lupan, L. Chow, L.M. Tiginyanu, V.V. Zalamai, et al. *Solid State Comm.* **143**, 437 (2007)
10. H. Zeng, W. Cai, B. Cao, J. Hu, Y. Li, P. Liu et al., *Appl. Phys. Lett.* **88**, 181905 (2006)
11. S. Chaudhary, A. Umar, K.K. Bhasin, S. Bakoutas et al., *Materials* **11**, 1–38 (2018)
12. H.H. Cheng, H.M. Cheng, C.Y. Wu, H.S. Huang, Y.C. Lee, W.F. Hsieh et al., *Nanotechnology* **17**, 1404 (2006)
13. T.S. Ko, S. Yang, H.C. Hsu, C.P. Chu, H.F. Lin, S.C. Liao, T.C. Lu, H.C. Kuo, W.F. Hsieh, C.S. Wang et al., *Mat. Sci. Engg. B* **134**, 54 (2006)
14. M. Lucas, Z.L. Wang, E. Riedo et al., *Appl. Phys. Lett.* **95**, 051904 (2009)
15. D.D. Wang, J.H. Yang, L.L. Yang, Y.J. Zhang, J.H. Lang, M. Gao et al., *Cryst. Res. Tech.* **43**, 1041 (2008)
16. J. Fan, H.R. Scholz, F.M. Kolb, M. Zacharias, U. Gösele, F. Heyroth, C. Eisenschmidt, T. Hempel, et al. *J. Christen, Appl. Phys. A*, **79**, 1895 (2004)
17. D. Pradhan, M. Kumar, Y. Ando, K.T. Leung et al., *Nanotechnology* **19**, 035603 (2008)
18. H.J. Fan, B. Fuhrmann, R. Scholz, C. Himcinschi, A. Berger, H. Leipner, A. Dadgar, A. Krost, S. Christiansen, U. Gösele, M. Zacharias et al., *Nanotechnology* **17**, S231–S239 (2006)
19. M. Laurenti, V. Cauda et al., *Nanomaterials* **7**, 1–34 (2017)
20. S.S. Bhat, A. Qurashi, F.A. Khanday et al., *TrAc Trend Anal. Chem.* **86**, 1–13 (2017)
21. R. Wahab, Y.S. Kim, D.S. Lee, J.M. Seo, H.S. Shin et al., *Sci. Adv. Mater.* **2**, 35–42 (2010)
22. D.P. Singh et al., *Sci. Adv. Mater.* **2**, 245–272 (2010)

23. R. Ding, J. Liu, J. Jiang, X. Ji, X. Li, F. Wu, X. Huang, et al. *Sci. Adv. Mater.* **2**, 396–401 (2010)
24. A. Khan, S.N. Khan, W.M. Jadwisienczak et al., *Sci. Adv. Mater.* **2**, 572–577 (2010)
25. Y. Zhu, Y. Chen, C. Jia, X. Zhang et al., *J. Nanosci. Nanotechnol.* **10**, 8204–8209 (2010)
26. H. Ghayour, A.A. Nourbakhsh, S. Mirdamadi, R.H. Rezaei, et al. *J. Nanosci. Nanotechnol.* **10**, 7455–7458 (2010)
27. L. Irimpan, N.P.V. Nampoore, P. Radhakrishnan et al., *Sci. Adv. Mater.* **2**, 578–582 (2010)
28. F.G. Guo, Y. Wang, Q. Liu et al., *J. Nanosci. Nanotechnol.* **10**, 7167–7170 (2010)
29. H. Zeng, J. Cui, B. Cao, U. Gibson, Y. Bando, D. Golberg et al., *Sci. Adv. Mater.* **2**, 336–358 (2010)
30. N.T. Soitah, Y. Chunhui, S. Liang et al., *Sci. Adv. Mater.* **2**, 534–538 (2010)
31. H.Y. Ko, S.J. Yu et al., *J. Nanosci. Nanotechnol.* **10**, 8095–8101 (2010)
32. W. Wu, S. Bai, N. Cui, F. Ma, Z. Wei, Y. Qin, E. Xie et al., *Sci. Adv. Mater.* **2**, 402–406 (2010)
33. K.S. Mohanta, C.D. Kim, H.B. Kong, K.H. Cho, W. Liu, S. Tripathy, et al. *Sci. Adv. Mater.* **2**, 64–68 (2010)
34. K.B. Sharma, N. Khare, M. Kumar, et al. *J. Nanosci. Nanotechnol.* **10**, 8424–8431 (2010)
35. T. Han, X. Li, X. Zahang, J. Liu, J. Li et al., *Adv. Cond. Matter. Physics* **2017**, 4859863–4859870 (2017)
36. S.J. Young, C.C. Yang, L.T. Lai et al., *J. Electrochem. Soc.* **164**, B3013–B3028 (2017)
37. K.W. Guo et al., *J. Appl. Biotechnol. Bioeng.* **2**, 197–202 (2017)

Chapter 20

Role of Nanostructures in Development of Energy-Efficient Electrochemical Non-enzymatic Glucose Sensors



Vijay Kumar Anand, B. Archana, Amit Wason, G. S. Virdi
and Rakesh Goyal

Abstract There are various complexities involves with enzymatic glucose sensors such as poor shelf life due to the inherent instability of an enzyme, a fabrication complexity included in enzyme immobilization procedures and interference caused by soluble redox mediators. Therefore, research towards enzymeless glucose sensing has increased. Further, the integration of photovoltaic or alternate energy harvesting methods with glucose sensors results in the development of cost-effective and energy-efficient biosensor systems. Continuous technological advancements of novel materials having distinctive nanostructures assist in understanding the fundamentals of enzymeless glucose detection. In this paper, we have discussed the electrochemical method of glucose detection and the role of nanostructures in development of energy-efficient electrochemical non-enzymatic glucose sensors.

Keywords Non-enzymatic · Nanostructures

20.1 Introduction

In a human body, if the pancreas is not able to produce an adequate amount of insulin or if the body is unable to effectively utilize the produced insulin, a disease known as diabetes is said to exist. In the recent decade, diabetes has become much prevalent [1, 2]. The number of diabetic patients was 415 million in 2015, and this number would become 642 million in 2040 as predicted by the International Diabetes Foundation (IDF) [3]. The mortality rate due to diabetes is also increasing at an alarming rate [3, 4]. People with diabetes must maintain their blood glucose level within the physiological range that is why an accurate monitoring of blood glucose level becomes very important; consequently, the use of blood glucose monitoring

V. K. Anand (✉) · G. S. Virdi · R. Goyal
IKG Punjab Technical University, Kapurthala, Punjab, India
e-mail: ervijay2222@gmail.com

V. K. Anand · B. Archana · A. Wason
Microelectronics/MEMS R&D Laboratory, ECE Department, Ambala College of Engineering
and Applied Research, Ambala, Haryana, India

© Springer Nature Singapore Pte Ltd. 2020
V. K. Jain et al. (eds.), *Advances in Solar Power Generation
and Energy Harvesting*, Springer Proceedings in Energy,
https://doi.org/10.1007/978-981-15-3635-9_20

devices is very common these days. Some of the leading manufacturers of blood glucose monitoring devices are Abbott Laboratories, Medtronic, Roche Diagnostics, Bayer, Bionime, Dexcom and LifeScan [5]. The latest self-monitoring devices have excellent features like minimal sample volume (μL), reduced testing time and a wide glucose detection range, etc. Among the various glucose detection methods, continuous glucose monitors (CGM) provide more comprehensive understanding of fluctuating glucose trends. CGM systems monitor interstitial glucose levels all the time. Abbott's FreeStyle Libre Pro CGM system is more helpful to those diabetic patients who fear from fingersticks as it does not require the same. It measures the interstitial glucose level using a small sensor attached on the arm, in every 15 min for up to 14 days. For medical records, a doctor can download the recorded information [6, 7].

20.2 Enzymatic Glucose Detection

Enzyme-based electrochemical glucose sensors are commercially used for blood glucose measurement. Glucose oxidase (GOx) and glucose dehydrogenase (GDH) enzymes are mostly used for this purpose [8, 9]. The high selectivity towards glucose molecules and high stability of GOx make it a strong candidate, but at a temperature above $40\text{ }^{\circ}\text{C}$ or solution pH below 2 and above 8, it rapidly loses its activity. The exposure to unstable humidity critically affects the GOx-based sensors. The activity of GOx is also dependent on oxygen concentration in its surrounding [10]. GDH is most commonly utilized with cofactors such as pyrroloquinoline quinone (PQQ) and flavin adenine dinucleotide (FAD) [8]. In comparison with GOx, GDH with its cofactors has higher activity. However, GDH-PQQ-based blood glucose monitors can be affected by galactose and maltose, and GDH-FAD blood glucose monitors respond to xylose. Except glucose, maltose, galactose and xylose are different forms of sugar which may exist in blood. The reactivity of a GDH system towards these may lead to an incorrect measurement of glucose [11, 12]. Various groups are working worldwide to overcome the limitations associated with the GDH system. Efforts are going on to make GDH-FAD system less reactive towards xylose [13–15].

20.3 Non-enzymatic Glucose Detection

Currently, the enzyme-based sensor dominates glucose sensor industry. Nevertheless, non-enzymatic glucose sensors are being researched so as to overcome the above-mentioned boundaries of enzyme-based glucose sensors. Complicated enzyme immobilization procedures make the fabrication of enzymatic glucose sensors very difficult. On the other hand, the absence of biological functional units in most non-enzymatic sensors can be beneficial in respect of simple structures and better quality. The response of enzymatic glucose sensors is dependent on oxygen

concentrations. The deficiency of oxygen in the absence of mediator produces a nonlinear and less sensitive response. However, in enzymeless glucose sensors, the electrical current is produced due to glucose oxidation on the electrode surface, thus eliminating the oxygen limitations. Another serious problem in enzyme-based sensors is the stability of an enzyme. An enzyme loses its activity at a temperature above 40 °C or solution pH below 2 and above 8; the high or low value of humidity may also damage the stored or in-use sensors. As a result, there has been a considerable interest in developing non-biological electrode materials. The rapid advancement in nanotechnology is persistently opening new prospective for enzymeless glucose sensing. Particularly, nanoporous platinum-based non-enzymatic glucose sensors can overcome the limitations associated with temperature, humidity and solvent, etc. By looking at the merits of enzymeless glucose sensors, it is expected that the cost of CGM system can be cut down to a large extent. Sensing behaviour of enzymeless glucose sensors can be viewed in terms of mechanism or material used. This paper discusses the role of nanostructures in the development of sensors used in enzymeless glucose sensing.

20.4 Direct Glucose Oxidation

In an electrocatalytic process, the active sites of the metallic electrode adsorb reactant molecules. Factors affecting the adsorption mechanism include incomplete d-orbitals, plentiful defects in catalysts and encouraging electronic states of the redox centre. According to the chemisorption model proposed by Pletcher [16, 17], in the glucose oxidation reaction, initially, the glucose is adsorbed onto the electrode surface and a bond formation takes place between them. Then, the hydrogen atom attached to C-1 carbon atom in the glucose molecule (see Fig. 20.1a) is extracted and creates a bond with electrode surface [16, 18, 19] resulting into change in oxidation state of the glucose molecule, leading to a lowering of glucose–metal bond strength which ultimately results in desorption of the glucose molecule. Incipient Hydrrous Oxide Adatom Mediator (IHOAM) model (see Fig. 20.1b) is also used to explain the direct glucose oxidation. According to this model, incipient hydrrous oxide, OH_{ads} , layer is formed when the active metal atoms on the surface of the electrode undergo a premonolayer oxidation [18, 20, 21]. This OH_{ads} layer is supposed to mediate the further glucose oxidation. The electrocatalytic activity of noble metals can be easily explained with the help of chemisorption and IHOAM models. However, the activity of various transition metals or metal oxide-based electrodes is not in agreement with these models. The oxidation of glucose in materials such as Ni [22, 23], Cu [24, 25] and Co [26, 27] is obtained when the transition metal centre go through a redox reaction. The metal oxide having a higher oxidation state has a strong power to produce surface bound OH_{ads} radicals at anodic bias. These OH_{ads} radicals have a capability to oxidize organic reactants. The first step in glucose oxidation is the

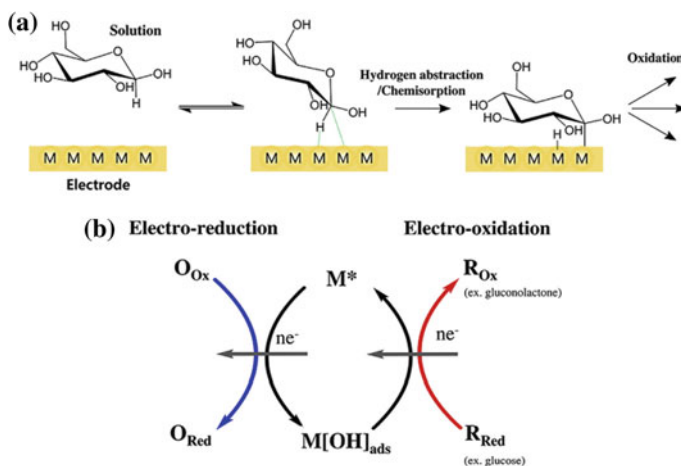


Fig. 20.1 **a** Chemisorption model of glucose oxidation. **b** Incipient Hydrus Oxide Adatom Mediator (IHOAM) model [17]

abstraction of a C-1 hydrogen atom; subsequently, the reaction intermediates oxidizes into glucono-d-lactone. The abstraction of a hydrogen atom sets the rate of glucose oxidation.

The amperometric techniques are most commonly used to study direct glucose oxidation on the electrode surface. The glucose oxidation reaction is mostly performed in alkaline conditions due to the availability of OH_{ads}. Also, the transition metal and metal oxide-based electrodes may be unstable in acidic conditions.

20.5 Nanostructures for Glucose Detection

The nanostructures like nanoparticle, nanorod, nanowire, nanotube, mesoporous particles and films are commonly used in electrocatalysis [28–35], energy applications [28, 30–39] and sensors (including glucose sensors) [40–44]. A nanostructured electrode material can act like a catalyst in three different ways, i.e. by generating sites which are electrocatalytic active, enhancement of active surface area and the creation of nanospace surrounded by conducting surfaces [45]. As per our previous discussion, the oxidation of glucose requires either sites for surface adsorption or reactive OH_{ads} radicals, which facilitate the electrochemical glucose oxidation. In nanostructures, the existence of high indexed planes, adatoms and edges is very common, and these defects are responsible for electrocatalysis on the electrode surface. Together with the surface morphology, nanomaterials also possess different electronic band structure as compared to their bulk counterparts. The large number of electrocatalytic active sites present on the surface of nanomaterials is considered to assist the

oxidation of glucose electrocatalytically. The high surface roughness of nanomaterials greatly enlarges the electrochemically active surface area (ECSA) leading to the generation of large currents which makes the nanostructured electrodes more sensitive. However, the wider electrode surface could increase the background signals including capacitive current. Alongside the sensitivity, selectivity is another important performance parameter for glucose sensors. The role of nanostructured surfaces would be worth if the enlarged ECSA or catalytic active sites can make sensor highly selective by amplifying the glucose signals only. A highly selective nanostructured glucose sensor exclusively oxidizes glucose on its surface while rejecting all other interferents. In this regard, electrodes with nanopores are not only sensitive but also selective in nature [46, 47]. The porous structure creates nanospaces which help in catalysis. A field gradient in the range equivalent to Debye length is created within a nanoporous electrode when subjected to an electric field. The pore size and electrolyte concentration, for which nanoporous electrode with its complete surface takes part in the faradaic reaction, can be determined for a maximum value of ECSA-to-apparent area ratio. With small pores having thickness less than electric double layer, the potential required to oxidize the glucose is high. Large pore size results in a poor ECSA-to-apparent electrode area ratio leading to a reduced sensitivity. The sensitivity of glucose sensors is inversely proportional to the pore size and attains a maximum value for a particular pore size. The nanoporous electrode thickness also affects the ECSA-to-apparent electrode area ratio which increases with increase in thickness of nanoporous electrode. The interfering molecules such as 4-acetamidophenol and ascorbic acid oxidize much faster than glucose which may result in the generation of high current at a very low concentration of interfering reactants. Large current is obtained at a flat Pt electrode, not from glucose, but from interfering molecules because of their fast reaction kinetics. Due to sluggish glucose oxidation reaction, the current keeps on increasing with the increasing ECSA-to-apparent electrode area. In general, the concentration of glucose in blood dominates any other electroactive potential reactants due to which the contribution of glucose is high in signal output as compared to other interfering molecules. Another factor which affects the kinetics of glucose oxidation is surface roughness; a nanostructured electrode with a high roughness factor is more sensitive to glucose, while the current response remains unchanged with fast oxidizable substances [46]. At an adequately high potential, in a diffusion-controlled system, the reactant inside the nanoporous electrode should deplete immediately due to fast electrochemical oxidation. This fast oxidation results in currents from flat and nanoporous electrodes identical to each other. It is also observed that the faradaic current due to interfering molecules is influenced by the apparent geometric area rather than the ECSA [48].

Another study reveals that in diffusion-controlled system, the current due to oxidation of glucose is an increasing function of nanoporous electrode thickness, i.e. high RF, but this current saturates with an excessively thick nanoporous electrode. In an electrocatalysis experiment, nanoporous noble metal electrodes reflect enhanced anti-interference capability when used in phosphate buffer saline (PBS) solution enriched with chloride ions.

20.6 Conclusion

The factors which generally affect the performance of electrochemical non-enzymatic glucose sensors are catalytic active sites, ECSA-to-apparent electrode area ratio, etc. However, in case of mesoporous electrodes having small pore size, the current due to glucose oxidation is more than expected from the ECSA. The factor which seems to enhance the performance of [49–54] small mesopores is the formation of a nanospace by surrounding electrode surfaces. The reactants in this nanospace are expected to experience exceptional conditions, e.g. the strong electric field gradient, different dielectric properties of solvent, very confined dynamic diffusion and so on. The electrocatalytic enhancement in nanostructures still needs to be investigated.

The use of nanomaterials in the development of biosensors has significantly enhanced the resolution and detection limits. Renewable energy sources are gaining much attention as an alternative to conventional energy sources. Therefore, a biosensor system integrated with nanomaterials and photovoltaics, which can detect a variety of biomolecules with high accuracy at a relatively low cost and no battery pollution, is a perfect biosensor system of the future. The electrochemical non-enzymatic glucose sensors based on nanostructures are able to produce large electric currents corresponding to small changes in glucose concentration at relatively small working potentials. The low working potential and high sensitivity of nanostructure-based electrochemical non-enzymatic glucose sensor make them highly energy efficient.

Acknowledgements The authors are thankful to IKG Punjab Technical University, Kapurthala, Punjab, India and Microelectronics/MEMS R&D Laboratory, Ambala College of Engineering and Applied Research, Ambala, Haryana, India, for providing the necessary resources.

References

1. K.G.M.M. Alberti, P.Z. Zimmet, World Health Organization Consultation, Definition, diagnosis and classification of diabetes mellitus and its complications part 1: diagnosis and classification of diabetes mellitus provisional report of a WHO consultation. *Diabet. Med.* **15**, 539–553 (1998)
2. World Health Organization, *Definition and Diagnosis of Diabetes Mellitus and Intermediate Hyperglycemia: Report of a WHO/IDF Consultation* (2006)
3. K. Ogurtsova, J.D.R.R. Fernandes, Y. Huang, U. Linnenkamp, L. Guariguata, N.H. Cho, D. Cavan, J.E. Shaw, L.E. Makaroff, IDF diabetes atlas: global estimates for the prevalence of diabetes for 2015 and 2040. *Diabetes Res. Clin. Pract.* **128**, 40–50 (2017)
4. World Health Organization, *Global Report on Diabetes Geneva*. Switzerland (2016)
5. Med device tracker Report, *Global Diabetes Management Devices Market* (Informa, London, 2017)
6. Abbott's freestyle libre system becomes first CGM to be FDA Cleared for Use Without Fingersticks (2017). <http://www.mobihealthnews.com/content/abbotts-freestyle-libre-system-becomes-first-cgm-be-fda-cleared-usewithout-fingersticks>

7. FDA approves first continuous glucose monitoring system for adults not requiring blood sample calibration. U.S. FOOD & DRUG Administration (2017). <https://www.fda.gov/NewsEvents/Newsroom/PressAnnouncements/ucm577890.htm>
8. S. Ferri, K. Kojima, K. Sode, Review of glucose oxidases and glucose dehydrogenases: a Bird's eye view of glucose sensing enzymes. *J Diabetes. Sci. Technol.* **5**, 1068–1076 (2011)
9. S.K. Vashist, D. Zheng, K. Al-Rubeaan, J.H.T. Luong, F.S. Sheu, Technology behind commercial devices for blood glucose monitoring in diabetes management: a review. *Anal. Chim. Acta* **703**, 124–136 (2011)
10. R. Wilson, A.P.F. Turner, Glucose-oxidase—an ideal enzyme. *Biosens. Bioelectron.* **7**, 165–185 (1992)
11. J.P. Frias, C.G. Lim, J.M. Ellison, C.M. Montandon, Review of adverse events associated with false glucose readings measured by GDHPQQ- based glucose test strips in the presence of interfering sugars. *Diabetes Care* **33**, 728–729 (2010)
12. T.G. Schleis, Interference of maltose, icodextrin, galactose, or xylose with some blood glucose monitoring systems. *Pharmacotherapy* **27**, 1313–1321 (2007)
13. K. Mori, M. Nakajima, K. Kojima, K. Murakami, S. Ferri, K. Sode, Screening of Aspergillus-derived FAD-glucose dehydrogenases from fungal genome database. *Biotechnol. Lett.* **33**, 2255–2263 (2011)
14. G. Sakai, K. Kojima, K. Mori, Y. Oonishi, K. Sode, Stabilization of fungi-derived recombinant FAD-dependent glucose dehydrogenase by introducing a disulfide bond. *Biotechnol. Lett.* **37**, 1091–1099 (2015)
15. H. Yoshida, G. Sakai, K. Mori, K. Kojima, S. Kamitori, K. Sode, Structural analysis of fungus-derived FAD glucose dehydrogenase. *Sci. Rep.* **5** (2015)
16. D. Pletcher, Electrocatalysis—present and future. *J. Appl. Electrochem.* **14**, 403–415 (1984)
17. K.E. Toghiani, R.G. Compton, Electrochemical non-enzymatic glucose sensors: a perspective and an evaluation. *Int. J. Electrochem. Sci.* **5**, 1246–1301 (2010)
18. J. Wang, J. Pharm, Amperometric biosensors for clinical and therapeutic drug monitoring: a review. *Biomed. Anal.* **19**, 47–53 (1999)
19. M.M. Rahman, A.J.S. Ahammad, J.H. Jin, S.J. Ahn, J.J. Lee, A comprehensive review of glucose biosensors based on nanostructured metal-oxides. *Sensors* **10**, 4855–4886 (2010)
20. L.D. Burke, Premonolayer oxidation and its role in electrocatalysis. *Electrochim. Acta* **39**, 1841–1848 (1994)
21. S. Ernst, J. Heitbaum, C.H. Hamann, The electrooxidation of glucose in phosphate buffer solutions: Part I. Reactivity and kinetics below 350 mV/RHE. *J. Electroanal. Chem. Interfacial Electrochem.* **100**, 173–183 (1979)
22. S. Berchmans, H. Gomathi, G.P. Rao, Electrooxidation of alcohols and sugars catalyzed on a nickel-oxide modified glassy-carbon electrode. *J. Electroanal. Chem.* **394**, 267–270 (1995)
23. M. Fleischmann, K. Korinek, D. Pletcher, Oxidation of organic compounds at a nickel anode in alkaline solution. *J. Electroanal. Chem.* **31**, 39–49 (1971)
24. J.M. Marioli, T. Kuwana, Electrochemical characterization of carbohydrate oxidation at copper electrodes. *Electrochim. Acta* **37**, 1187–1197 (1992)
25. K. Kano, M. Torimura, Y. Esaka, M. Goto, T. Ueda, Electrocatalytic oxidation of carbohydrates at copper(ii)-modified electrodes and its application to flow-through detection. *J. Electroanal. Chem.* **372**, 137–143 (1994)
26. T.R.I. Cataldi, A. Guerrieri, I.G. Casella, E. Desimoni, Study of a cobalt-based surface-modified glassy-carbon electrode—electrocatalytic oxidation of sugars and alditols. *Electroanalysis* **7**, 305–311 (1995)
27. T.R.I. Cataldi, I.G. Casella, E. Desimoni, T. Rotunno, Cobalt-based glassy-carbon chemically modified electrode for constant-potential amperometric detection of carbohydrates in flow-injection analysis and liquid chromatography. *Anal. Chim. Acta* **270**, 161–171 (1992)
28. E.J. Popczun, J.R. McKone, C.G. Read, A.J. Bacci, A.M. Wiltrot, N.S. Lewis, R.E. Schaak, Nanostructured nickel phosphide as an electrocatalyst for the hydrogen evolution reaction. *J. Am. Chem. Soc.* **135**, 9267–9270 (2013)

29. J.Y. Chen, B. Lim, E.P. Lee, Y.N. Xia, Shape-controlled synthesis of platinum nanocrystals for catalytic and electrocatalytic applications. *Nano Today* **4**, 81–95 (2009)
30. L.T. Qu, Y. Liu, J.B. Baek, L.M. Dai, Nitrogen-doped graphene as efficient metal-free electrocatalyst for oxygen reduction in fuel cells. *ACS Nano* **4**, 1321–1326 (2010)
31. J.F. Xie, H. Zhang, S. Li, R.X. Wang, X. Sun, M. Zhou, J.F. Zhou, X.W. Lou, Y. Xie, Defect-rich MoS₂ ultrathin nanosheets with additional active edge sites for enhanced electrocatalytic hydrogen evolution. *Adv. Mater.* **25**, 5807–5813 (2013)
32. P. Trogadas, V. Ramani, P. Strasser, T.F. Fuller, M.O. Coppens, Hierarchically structured nanomaterials for electrochemical energy conversion. *Angew. Chem. Int. Ed.* **55**, 122–148 (2016)
33. M. Zhou, H.L. Wang, S.J. Guo, Towards high-efficiency nanoelectrocatalysts for oxygen reduction through engineering advanced carbon nanomaterials. *Chem. Soc. Rev.* **45**, 1273–1307 (2016)
34. P. Strasser, Free electrons to molecular bonds and back: closing the energetic oxygen reduction (ORR)-Oxygen evolution (OER) cycle using coreshell nanoelectrocatalysts. *Accounts Chem. Res.* **49**, 2658–2668 (2016)
35. Z. Dasdelen, Y. Yildiz, S. Eris, F. Sen, Enhanced electrocatalytic activity and durability of Pt nanoparticles decorated on GO-PVP hybride material for methanol oxidation reaction. *Appl. Catal. B Environ.* **219**, 511–516 (2017)
36. J.P. Giraldo, M.P. Landry, S.M. Faltermeier, T.P. McNicholas, N.M. Iverson, A.A. Boghossian, N.F. Reuel, A.J. Hilmer, F. Sen, J.A. Brew, M.S. Strano, Plant nanobionics approach to augment photosynthesis and biochemical sensing. *Nat. Mater.* **13**, 400–408 (2014)
37. J.T. Abrahamson, B. Sempere, M.P. Walsh, J.M. Forman, F. Sen, S. Sen, S.G. Mahajan, G.L.C. Paulus, Q.H. Wang, W. Choi, M.S. Strano, Excess thermo power and the theory of thermo power waves. *ACS Nano* **7**, 6533–6544 (2013)
38. Y.M. Li, G.A. Somorjai, Nanoscale advances in catalysis and energy applications. *Nano Lett.* **10**, 2289–2295 (2010)
39. A. Hagfeldt, G. Boschloo, L.C. Sun, L. Kloo, H. Pettersson, Dye sensitized solar cells. *Chem. Rev.* **110**, 6595–6663 (2010)
40. N.M. Iverson, P.W. Barone, M. Shandell, L.J. Trudel, S. Sen, F. Sen, V. Ivanov, E. Atoia, E. Farias, T.P. McNicholas, N. Reuel, N.M.A. Parry, G.N. Wogan, M.S. Strano, In vivo biosensing via tissue-localizable near-infrared-fluorescent single-walled carbon nanotubes. *Nat. Nanotechnol.* **8**, 873–880 (2013)
41. Y. Koskun, A. Savk, B. Sen, F. Sen, Highly sensitive glucose sensor based on monodisperse palladium nickel/activated carbon nanocomposites. *Anal. Chim. Acta* **1010**, 37–43 (2018)
42. G. Baskaya, Y. Yildiz, A. Savk, T.O. Okay, S. Eris, H. Sert, F. Sen, Rapid, sensitive, and reusable detection of glucose by highly monodisperse nickel nanoparticles decorated functionalized multi-walled carbon nanotubes. *Biosens. Bioelectron.* **91**, 728–733 (2017)
43. C. Yang, M.E. Denno, P. Pyakurel, B.J. Venton, Recent trends in carbon nanomaterial-based electrochemical sensors for biomolecules: a review. *Anal. Chim. Acta* **887**, 17–37 (2015)
44. C.Z. Zhu, G.H. Yang, H. Li, D. Du, Y.H. Lin, Electrochemical sensors and biosensors based on nanomaterials and nanostructures. *Anal. Chem.* **87**, 230–249 (2015)
45. D.W. Hwang, S. Lee, M. Seo, T.D. Chung, Recent advances in electrochemical non-enzymatic glucose sensors: a review. *Anal. Chim. Acta* **1033**, 1–34 (2018)
46. S. Park, T.D. Chung, H.C. Kim, Nonenzymatic glucose detection using mesoporous platinum. *Anal. Chem.* **75**, 3046–3049 (2003)
47. S. Park, Y.J. Song, J.H. Han, H. Boo, T.D. Chung, Structural and electrochemical features of 3D nanoporous platinum electrodes. *Electrochim. Acta* **55**, 2029–2035 (2010)
48. A.J. Bard, L.R. Faulkner, *Electrochemical Methods: Fundamentals and Applications*, 2nd edn. (Wiley, New York, 2001)
49. J.H. Bae, J.H. Han, D. Han, T.D. Chung, Effects of adsorption and confinement on nanoporous electrochemistry. *Faraday Discuss.* **164**, 361–376 (2013)
50. J.H. Bae, Y.R. Kim, R.S. Kim, T.D. Chung, Enhanced electrochemical reactions of 1,4-benzoquinone at nanoporous electrodes. *Phys. Chem. Chem. Phys.* **15**, 10645–10653 (2013)

51. J.H. Han, J.H. Bae, D. Han, T.D. Chung, Confined molecular dynamics for suppressing kinetic loss in sugar fuel cell. *Electrochim. Acta* **187**, 457–464 (2016)
52. M. Seo, J.H. Bae, D.W. Hwang, B. Kwak, J. Yun, S.Y. Lim, T.D. Chung, Catalytic electron transfer at nanoporous indium tin oxide electrodes. *Electrochim. Acta* **258**, 90–97 (2017)
53. S.H. Kim, J.B. Choi, Q.N. Nguyen, J.M. Lee, S. Park, T.D. Chung, J.Y. Byun, Nanoporous platinum thin films synthesized by electrochemical dealloying for nonenzymatic glucose detection. *Phys. Chem. Chem. Phys.* **15**, 5782–5787 (2013)
54. S. Park, H.C. Kim, T.D. Chung, Electrochemical analysis based on nanoporous structures. *Analyst* **137**, 3891–3903 (2012)

Correction to: Study and Analysis of Parameters Affecting Tubular Daylighting Device



Devendra Singh Bisht, Harry Garg, R. R. Shravana Kumar
and Vinod Karar

Correction to:
Chapter 9 in: V. K. Jain et al. (eds.),
Advances in Solar Power Generation and Energy Harvesting,
Springer Proceedings in Energy,
https://doi.org/10.1007/978-981-15-3635-9_9

The original version of the book was inadvertently published with an incorrect affiliation of the authors. The affiliation (CSIR-Central Scientific Instruments Organisation, Sector 30C, Chandigarh 160030, India) of the authors in chapter 9 has been amended. The chapter and book have been updated with the changes.

The updated version of this chapter can be found at
https://doi.org/10.1007/978-981-15-3635-9_9

© Springer Nature Singapore Pte Ltd. 2020
V. K. Jain et al. (eds.), *Advances in Solar Power Generation
and Energy Harvesting*, Springer Proceedings in Energy,
https://doi.org/10.1007/978-981-15-3635-9_21